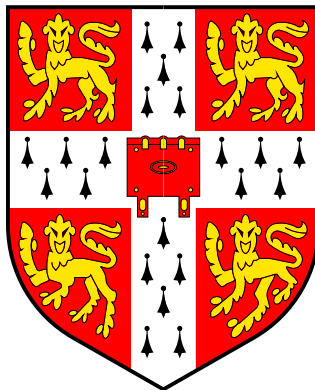# Collective phenomena in correlated semiconductors, degenerate Fermi gases, and ferroelectrics

G.J. Conduit

Selwyn College

University of Cambridge

April 2009

This thesis is submitted for the degree of Doctor of Philosophy

Collective phenomena in correlated semiconductors, degenerate Fermi gases, and ferroelectrics

G.J. Conduit, Selwyn College

WE are surrounded by materials that are comprised of electrons and nuclei which not only feel particle-particle electromagnetic forces but also obey the long-accepted laws of quantum mechanics. The interplay of strong interactions and quantum mechanics can cause the constituent particles to display collective behaviour which is markedly different from that of the separate particles. In this thesis, collective phenomena in *semiconductors*, *atomic gases*, and around *quantum critical points* have inspired separate research projects.

Degenerate semiconductors: Assuming that there is a large number of degenerate conduction band minima provides a useful route to developing an exact analytical treatment of semiconductors. The new formalism, which was also verified computationally, gives an exact expression for the total electron energy, and provides convenient access to the electron dynamical response.

Ultracold atomic gases: These are a new tool that offer investigators an exquisite level of control over a many-body system. Firstly we show how an atomic gas could be used to unravel a long-standing mystery about textured superconductors, secondly we explore the properties of collective modes, and thirdly we investigate a novel form of ferromagnetism.

Critical phenomena in correlated quantum systems: As the temperature falls thermal excitations give way to quantum fluctuations. These can couple leading to unexpected phases; firstly we search for a putative textured phase that could preempt the first order ferromagnetic transition, and secondly predict a metaelectric phase transition in ferroelectrics.

Preface

THIS thesis describes work done between October 2006 and April 2009 in the Theory of Condensed Matter (TCM) group at the Cavendish Laboratory, Cambridge, under the supervision of Dr P.D. Haynes and Prof. B.D. Simons. Chp. 1 reviews the field and introduces the tools used in this thesis. Subsequent chapters contain original material that is in preparation for submission to peer review or is published elsewhere as follows:

Chapter 2: G.J. Conduit, *A many-flavor electron gas approach to electron-hole drops*, Phys. Rev. B, **78**:035111, 2008 [1].

Chapter 3: G.J. Conduit and P.D. Haynes, *Diffusion Monte Carlo study of a valley-degenerate electron gas and application to quantum dots*, Phys. Rev. B, **78**:195310, 2008 [2].

Chapter 4: G.J. Conduit, P.H. Conlon and B.D. Simons, *Superfluidity at the BEC-BCS crossover in two-dimensional Fermi gases with population and mass imbalance*, Phys. Rev. A, **77**:053617, 2008 [3].

Chapter 6: G.J. Conduit and B.D. Simons, *Itinerant ferromagnetism in atomic Fermi gases: Influence of population imbalance*, Phys. Rev. A, **79**:053606, 2009 [4].

This thesis is my own work and contains nothing which is the outcome of work done in collaboration with others, except as specified in the text and Acknowledgements. This thesis does not exceed 60,000 words, including tables, footnotes, bibliography and appendices, but excluding photographs and diagrams.

G.J. Conduit

Cambridge, April 2009

Acknowledgements

Contents

Chapter One

Scope of this thesis

PHYSICISTS try to uncover the basic axioms of nature by studying a wide range of phenomena that lay the foundations of the physical sciences. One important aspect of real-life systems is that they are made up of multitudinous component particles. A good example of such a many-body system is a metal in which a mobile sea of electrons moves amongst a rigid background lattice of ions. The behaviour of the electrons is particularly interesting because each one interacts with all of the other electrons according to the long-standing laws of electromagnetism. Since the electrons all interact with each other, they can all move together and display new collective or cooperative behaviour that one electron by itself cannot achieve. One example of collective behaviour is the alignment of electron spins in ferromagnetism. Another crucial facet is that an electron's motion is governed by the well-established laws of quantum mechanics, which causes the electrons to have counterintuitive properties such as wave-particle duality. However, in *condensed matter physics* the *interplay* of strong interactions between the particles and quantum mechanics leads to novel phenomena that are the subject of cutting edge research.

The foundations of condensed matter physics [5] were laid down by Bloch in the 1930's through a revolutionary understanding of non-interacting electrons in a periodic potential. Following developments in the band theory of electrons, the next stage in furthering a description of electrons moving through a lattice

1

was the formulation of the nearly free and tight binding theories. A perturbative approach to dealing with electron-electron interactions developed through the 50's, 60's, and 70's where a tool borrowed from high energy physics – Feynman diagrams – was applied to perform infinite order summations over the electron-electron interactions. Following in the historical development of condensed matter physics from no interactions, to weak interactions and then perturbative summations, from the 70's strong interactions became the main focus of theorists. The consequences of strong particle-particle interactions were found to lie in two main categories that unite the research described in this thesis:

Renormalise the properties of the particles: In this arena I have harnessed the traditional vehicle of condensed matter physics – the study of electrons in solids. In Sec. 1.2 I introduce a project that exposes how the interactions between electrons in semiconductors changes their energy and dynamical response.

Drive the system into new phases of matter: This thesis pursues two themes of research in this domain. Firstly, in Sec. 1.3 I describe how to take advantage of the opportunity presented by a novel many-body system, an ultracold atomic gas, to unravel long-standing mysteries in the solid state, as well as to explore fundamentally new many-body physics. Secondly, in Sec. 1.4, inspired by recent experiments, I introduce two projects that study how quantum fluctuations change the behaviour of strongly correlated systems in the vicinity of a phase transition.

Condensed matter physics is typically studied either through experiment, computer simulations, or analytics. Before describing the separate research projects I briefly review the universal transferable theoretical tools employed throughout this thesis.

1.1   Analytical toolkit

A major roadblock in condensed matter physics is how to approach the many-body Schrödinger equation. Though in general it cannot be solved exactly, a number of useful approximate methods to tackle it are outlined in Table 1.1. Those at the top

Table 1.1: Some analytical and computational approaches to studying condensed matter physics. The system properties and typical size are shown.

Application	Analytical approach	Computational approach	Particles present
Macroscopic and topological effects	Linear response functions [6]	Newtonian [7]	> 10000
	Ginzburg-Landau (GL) theory [8] Scaling theory and renormalisation group [8]		
Atomic dynamics	Nearly free electrons [9]	Pair potentials [10]	1000
	Tight binding [9]	Semi-empirical tight binding [10] HF [9]	
Electronic states	$\mathbf{k} \cdot \mathbf{p}$ perturbation theory [9]	DFT [11] DMFT [12] GW [13]	100
Binding energies	Infinite order perturbation theory [14] Functional path integral [8, 16, 17] Exact analytical solution [18]	QMC [15]	10

of the table can describe macroscopic and topological effects in large systems. Those at the bottom are suitable for systems containing only a few particles (that could be periodically repeated through the system), but can predict electronic structure and achieve chemical accuracy (~ 0.01eV). In this thesis we adopt three independent approaches whose basic features are outlined below: a functional integral formalism to derive analytic results, and complementary Quantum Monte Carlo (QMC) and DFT computational methods that were used to study the system numerically.

The functional integral approach aims to calculate the quantum partition function, which is a summation over all possible states of the system. In general this is not tractable, but one approach is to focus attention on those terms which make the most significant contribution to the summation over the states. First one identifies the dominant term, and then accounts for a small subset of related terms, but discards the less relevant high energy contributions. This powerful method is introduced more fully in App. A.2.

Computer simulations allow investigators to perform experiments without their apparatus. They also have other advantages over traditional experiments; firstly, quantities inaccessible to an experiment can be probed; and secondly system parameters, for example lattice spacing, can be changed at will. The QMC calculations [15] we use are *ab initio*, meaning that they calculate the wave function

from first-principles following an algorithm outlined in App. A.4. Another approach is to use some already-known information about the state to simplify the calculation; a common method is to assume that the system is locally uniform and use a well-established functional for the dependence of local energy with electron density. The implementation of DFT that is employed in this thesis is described in App. A.5.

Having reviewed the tools we now describe the backdrops for the three research arenas presented in this thesis: semiconductors, ultracold atomic gases, and critical phenomena.

1.2   Electron gases of many flavours

Our first arena in which to explore the consequences of strong interactions is the correlations between electrons in semiconductors. Here we will find that the interactions of the electrons with the background ionic lattice will, rather than complicate the system, instead change the dynamics of the electrons dramatically. This enables a powerful approximation that will provide an efficient vehicle with which to model the correlations between the electrons.

An electron moving through a vacuum has a dispersion relation $p^2/2m_e$, where p is momentum and m_e is the electron mass. However, an electron moving inside a solid interacts with the periodic background ionic lattice which introduces a renormalisation of the electron energy that depends on the electron's momentum. In fact, around a minimum of the energy we can do away with having to consider the ions by replacing their effect on the energy of each electron with a single renormalisation of the electron mass, giving it a new *effective mass* given by $1/m^* = \mathrm{d}^2\epsilon/\mathrm{d}k^2/\hbar^2$ for an electron at wave vector k; in the non-interacting case the electron simply has the dispersion $\epsilon = \hbar^2 k^2/2m_e$, and so we would recover the bare electron mass.

Semiconductors are an intermediary between metals and insulators – they contain relatively few thermally excited conducting electrons. The effective mass of these *conduction band* electrons is controlled not only by the interaction of the electrons with the lattice, but also the interaction of the conduction band electrons with all the other electrons present – the *valence band* electrons. These flow out of
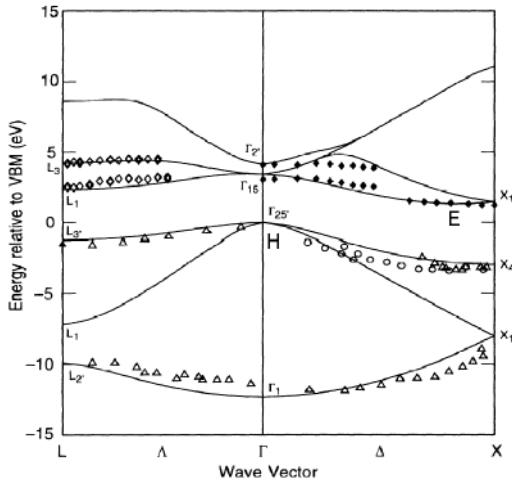
Figure 1.1: The Si band structure highlighted by points that were found with inverse-photoemission (above Fermi surface) and photoemission (below Fermi surface), taken from Ortega and Himpsel [19]. The solid curve shows the results of an *ab initio* quasiparticle calculation by Zhu and Louie [20]. The Fermi energy is at $E = 0$ eV; below are valence bands with holes at "H"; above conduction bands with degenerate minima at "E".

the way of a conduction band electron, acting like the *backflow* of a fluid. The effective mass now changes with momentum, so is best summarised by a non-parabolic dispersion profile for the electrons, which is shown for Silicon (Si) in Fig. 1.1. For the conduction band electrons, the minimum in the energy dispersion is no longer at $p = 0$, but is now six-fold degenerate and part-way out to the Brillouin zone boundary.

Si is not unique in having degenerate conduction band valleys; in fact many semiconductors have degenerate minima. The number of valleys presents a new parameter, which we call the number of "*flavours*", with which to analyse the materials. Additional motivation to study many-flavour electron-hole liquids stems from the opportunity to probe the formation of electron-hole drops in, for example, the Germanium (Ge) crystal in Fig. 1.2. A many-flavour approximation presents a new handle to probe strongly correlated physics. In Chp. 2 we derive analytical results for the correlation energy and electron dynamical response. Then, in Chp. 3 we verify those results computationally, and apply the method to analyse quantum dots and also the electron-hole drop shown in Fig. 1.2.

1.3 Strongly correlated phases in atomic gases

Eighty years after Bose-Einstein Condensation (BEC) was predicted it was revealed in the velocity distribution of an ultracold atomic gas [22–24], which is shown in Fig. 1.3. Since then, research in atomic gases has grown explosively, driven forwards

Figure 1.2: Photograph of a long-lived electron-hole drop in Ge. The width of the photo corresponds to 1.5mm on the crystal. Taken from Wolfe et al. [21].
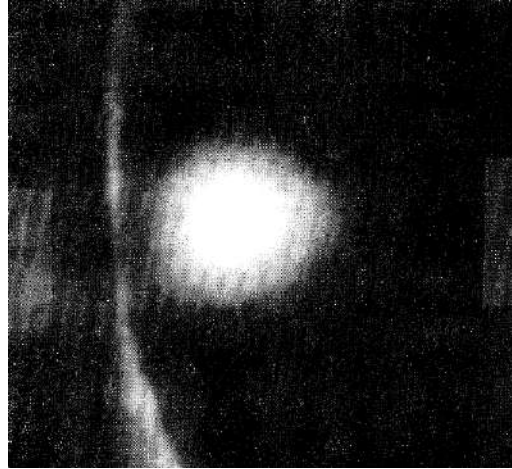
Figure 1.3: Velocity-distribution of a gas of Rubidium atoms; left: just warmer than a BEC; centre: at the appearance of the condensate; right: deep in the BEC regime. Taken from Anderson et al. [22].
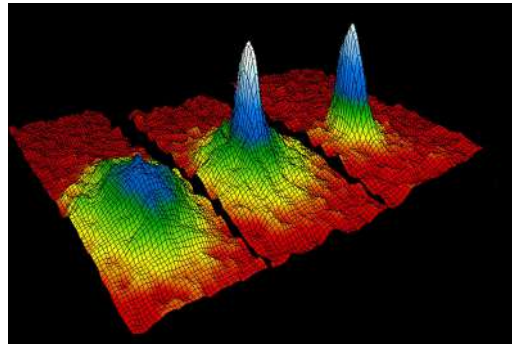
by two key developments which have enlarged the range of physics that can be investigated with the system:

1. The ability to tune the interaction strength by a Feshbach resonance [25–28]. This tool gives investigators unprecedented control over interactions and has enabled the observation of the BEC-BCS crossover [29–31] in fermionic atomic gases. The mechanism of the Feshbach resonance is outlined in Sec. 1.3.1.

2. The gas can be constrained into either one, two, or three dimensions with a strong optical potential [32], or alternatively could be held in a periodic potential [33, 34]. This readily adaptable external potential has enabled manipulation and control of a many-body system beyond that currently achievable in solid state systems. For example, an atomic gas in an optical lattice can now be used to simulate the dynamics of another complex quantum system [35, 36].
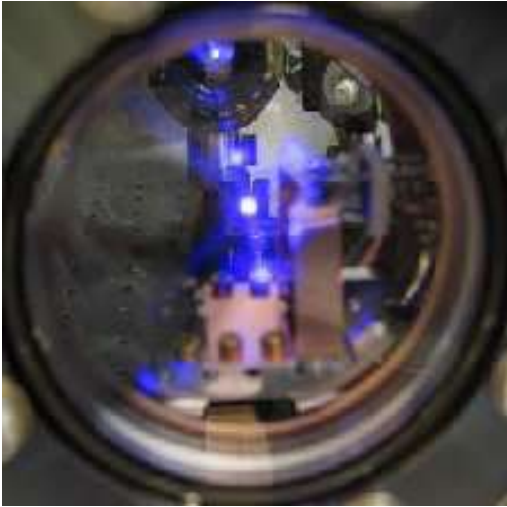
Figure 1.4: A cloud of Strontium atoms taken during cooling. The atoms are visible because they are still photoluminescent and have not yet reached quantum degeneracy. Taken from the MIT & Harvard Center for Ultracold Atoms.

Atomic gases now offer investigators a unique level of control over a many-body system. There are two ways to take advantage of this exquisite regulation: firstly, in Sec. 1.3.2 and Sec. 1.3.3, I introduce two projects that demonstrate how atomic gases place experimentalists in the unique position to unravel a long-standing mystery about solid state superconductivity, and secondly, in Sec. 1.3.4, I take advantage of the opportunity atomic gases pose to explore new many-body physics. To motivate these projects further, I first outline the typical experimental setup used to study atomic gases.

The atomic gas is created by liberating a hot (~ 800K) gas of atoms from the surface of a solid. Cooling then takes place in two phases. Firstly, the gas is cooled using a detuned laser, from which each photon absorbed delivers an impulse that reduces the kinetic energy of atoms. This technique can achieve temperatures down to $\sim 10^{-7}$K, such as the gas shown in Fig. 1.4. This is not yet cold enough to reach the regime of quantum degeneracy, and further cooling requires the atoms to collide with each other. Because collisions exchange energy, some atoms are allowed to escape from the trap and evaporate, leaving the remainder cooled. Although bosons can collide, fermions cannot, so require a second sympathetic atomic species to carom. This technique allows the regime of quantum degeneracy to be reached, with temperatures as low as $\sim 10^{-9}$K. Although the ground state at such low temperatures is an uninspiring solid, its formation requires three-body collisions and the atomic gas is so rarefied that such collisions occur infrequently.
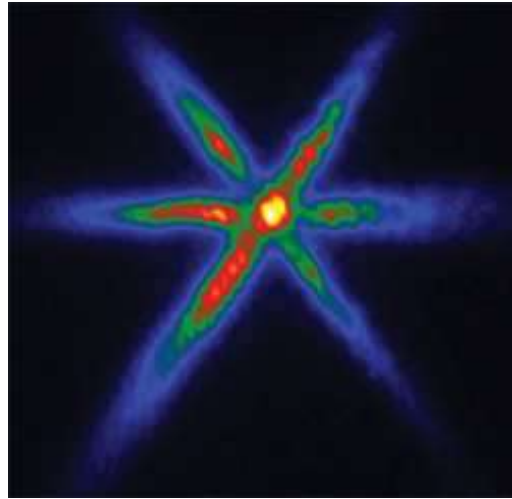
Figure 1.5: Atomic gas confined to the intersection of three laser beams. The atoms are observed from low-light fluorescence after brief illumination with resonant laser light. Taken from Chapman Research Labs.

As the atoms are not charged they are difficult to trap. One way of imposing an external potential is an Optical Lattice (OL), which is a periodic potential set up by two or more interfering laser beams[1] [33]. This can allow a potential to be created that is similar to the periodic potential in a solid, but allows the periodicity and potential strength to take a large range of values. Alternatively, the atoms can be confined at the intersection of three laser beams as shown in Fig. 1.5. One final possibility is that those atoms with a magnetic moment may be contained by a magnetic field gradient[2], generated by an anti-Helmholtz configuration of coils.

Before describing the two systems studied in this thesis I also outline the Feshbach resonance, which has enabled the full control of the interaction strength in atomic gases.

1.3.1 Feshbach resonance

One remarkable capability that ultracold atom gases give to researchers is the complete control of particle-particle interactions. This is achieved by taking advantage of a *Feshbach resonance*, by which the relative internal energy level of the atoms are tuned by varying an external magnetic field [37].

---

[1]The atoms feel the dipole force $\mathbf{F} = \alpha(\omega_{\mathrm{L}})\nabla(|\mathbf{E}(\mathbf{r})|^2)/2$. This is due to the spatially varying Alternating Current (ac)-Stark effect shift of the atoms in an off-resonant laser beam.

[2]The atoms with magnetic moment $\mathbf{m}$ feel force $\mathbf{F} = \nabla(\mathbf{m} \cdot \mathbf{B})$. Earnshaw's theorem states that there is neither a global minimum nor a global maximum in a magnetic field, therefore the weak-field seeking atoms can be trapped only where the magnitude of the magnetic field has a local minimum.
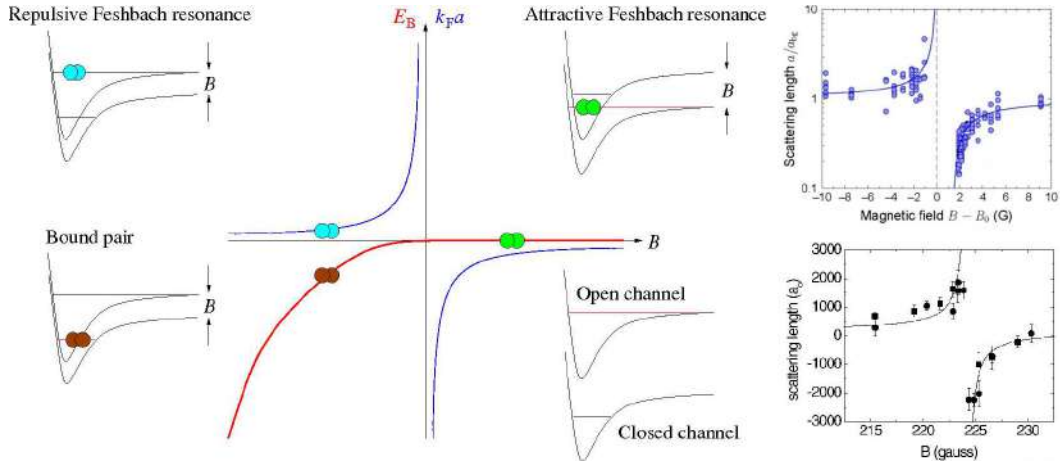
Figure 1.6: Left: the two-channel model for Feshbach resonance. The state energies vary with interatomic separation. There are two channels: in the open channel the particles are free whereas those in the closed channel are bound. The energy spacing between the channels can be controlled by an external magnetic field **B**. Three different possibilities for the particles are shown, that lead to binding energy E_B and scattering length $k_F a$ as shown by the red and blue lines respectively. Right, upper: experimental measurement of scattering length of Cr atoms, taken from Physikalisches Institut, Universität Stuttgart; right lower: scattering length of K atoms from Regal and Jin [38].

To understand the Feshbach resonance we need to consider both the open and closed channels in a *two-channel model*, as shown in Fig. 1.6. The atoms are prepared so that they are unbound in an *open-channel* state, whilst they would be bound in the *closed-channel* state. The open-channel and closed-channel state magnetic moments differ by μ so that the relative energy of closed and open-channel states μB can be shifted by varying the external magnetic field B. If the magnetic field is chosen so that the energy of one particular closed-channel bound state is near to the open-channel energy then resonant coupling occurs and the scattering between the two opposite spin particles is modified. As shown, backed-up by experimental measurements in Fig. 1.6, the scattering can be either repulsive, attractive, or the particles can form a bound pair at the BEC-BCS crossover [39, 40]. As described in App. A.1, the scattering is naturally described in terms of a scattering length a, which is positive for repulsion and negative for attraction.

Having laid down the key principles that underpin how to use ultracold atomic gases to probe many-body physics, we now proceed to describe the three projects researched in this thesis.

Figure 1.7: The formation of a Cooper pair in (a) a BCS state, (b) a FFLO instability caused by an imbalance between the two Fermi surfaces. The two particle species are denoted by different shading, the Fermi surfaces by the solid lines and pairing momentum **q** by the dotted line.
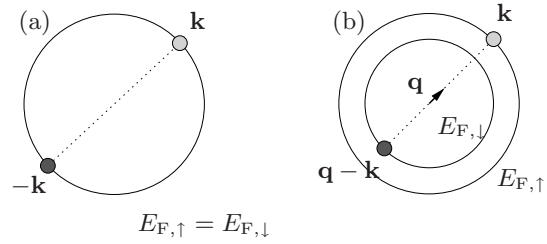
1.3.2 Introduction to the FFLO state

Ever since the discovery of the Meissner effect [9], an external magnetic field has been an important probe of the superconducting state. When a superconductor is placed in a magnetic field set to the upper Chandrasekhar-Clogston limit [41, 42] the Bardeen, Cooper, and Schrieffer (BCS) state can be destroyed and the total energy lowered by the gas becoming polarised, with the spins aligned along the magnetic field.

This heuristic picture was not bettered until the proposal of a modulated superconducting phase at the Chandrasekhar-Clogston cross-over. According to the BCS theory of superconductivity, Cooper pairs are formed of two fermions with different spins from opposite sides of the Fermi surface so that the pair overall has zero total momentum, as shown in Fig. 1.7. If the Fermi surfaces of the two species have different radii because of an external magnetic field then pairing is not so straightforward. A majority spin particle with momentum **k** couples to a minority spin particle with momentum $\mathbf{q}-\mathbf{k}$. The pair has non-zero total momentum $\mathbf{k} + (\mathbf{q} - \mathbf{k}) = \mathbf{q}$ whose magnitude is equal to the difference in Fermi momenta $|\mathbf{q}| = k_{F,\uparrow} - k_{F,\downarrow}$; the case $\mathbf{q} = \mathbf{0}$ corresponds to the standard BCS theory. The Cooper pair now has a finite centre-of-mass momentum **q**, which is fed through to the gap parameter having a spatial modulation with wave vector **q**, this Fulde-Ferrel-Larkin-Ovchinnikov (FFLO) state was first predicted by Fulde and Ferrell [43] and Larkin and Ovchinnikov [44]. The FFLO state has never been unambiguously experimentally observed [45] as it is easily disrupted by scattering off impurities.

Although the FFLO state might be difficult to observe in the solid state, in Chp. 4 we show how ultracold atomic gases now offer a unique opportunity to unravel this long-standing mystery. The ultracold atom gas is free from the impurities that plague the solid state. Additional motivation to use ultracold atom gases arises
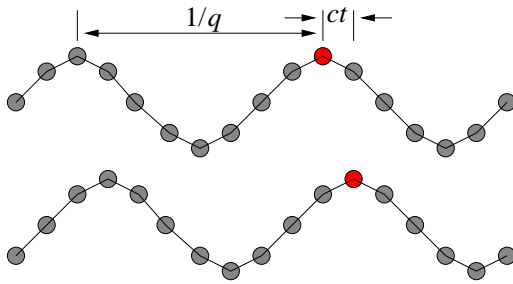
Figure 1.8: The collective mode of a string of particles at two sequential instants separated by time t. The red particle highlights a crest as it moves to the right.

because they offer an exquisite level of control over the Fermi surfaces of the two species, adjusted through either population or mass imbalance.

1.3.3   Collective modes

The microscopic details of the particle behaviour are often not readily accessible by looking at their individual excitations. Instead, if the particles are in a strongly correlated state then their macroscopic properties provide a window into their microscopic behaviour. One way to probe the macroscopic action of the particles is to study their *collective modes*. These are the fundamental collective excitations of the particles, much like the transverse motion of particles in a rope highlighted in Fig. 1.8, which travels to the right with a characteristic speed c. This velocity is an important property of the collective modes of a superfluid state of an atomic gas as it is allied to the Landau critical velocity of the superfluid – the maximum speed of dissipationless flow.

In Chp. 5 we are motivated by our study of the FFLO state presented in Chp. 4 and the ongoing experiments of John Thomas at Duke University to search for the collective modes in a two-dimensional atomic gas with both population and mass imbalance.

1.3.4   Introduction to itinerant ferromagnets

The two projects just described address the impact of attractive interactions on pair correlations. However, a conjugate research arena is to study whether repulsive interactions acting between particles can lead to magnetic phases. In this thesis we address this question in two projects, firstly here with an ultracold atomic gas, and later in Sec. 1.4.1 we examine putative textured ferromagnetism in the solid state.

Each electron in a solid carries a spin, which has an associated magnetic field. When the spins of all the electrons in a solid align they generate a macroscopic magnetic field. There are two broad classes of ferromagnetism [46], in the first the electrons are confined to particular atoms and so become localised in real space. The second type of ferromagnetism is due to the alignment of the magnetic moments of the conduction band electrons, that is the *itinerant* electrons that are free to move between atomic sites, and so are localised in momentum space. This type of magnetism occurs, for example, in Zirconium 2-Zinc ($ZrZn_2$) [47, 48], Uranium Digermanide (UGe_2) [49], MnSi [50, 51], and Cobalt (II) Sulphide (CoS_2) [52]. It has recently been established that at low temperatures the onset of itinerant ferromagnetism is unexpectedly first order rather than second order [53–58]. The solid state system is still beset with complications due to coupling to the lattice, however, as outlined in Chp. 6 atomic gases now provide a vehicle to study in detail how the quantum fluctuations affect the ferromagnetic transition.

Atomic gases not only allow us to probe ferromagnetism in a controlled environment but to introduce an additional twist that will enable even richer physics to be studied in Chp. 6. One feature of cold atom gases is that they may be created with an unequal spin population. There is no mechanism by which the spins can flip, so the population imbalance is a conserved quantity, which is preserved throughout the experiment. This has important ramifications; for example, when favourable, the ferromagnetic moment must be formed in-plane.

1.4   Critical phenomena in correlated quantum systems

The final major research theme in this thesis is critical phenomena that emerge in strongly correlated solid state systems. At high temperatures thermal excitation causes fluctuations that drive the phase transition. At low temperatures, however, the phase transition is driven by the quantum fluctuations that now dominate the system. Near to existing phase transitions, quantum fluctuations can push the system into novel phases of matter that are the subject of cutting edge research [59], an early example of which is the emergence of superconductivity in Cerium Palladium Silicon ($CePd_2Si_2$), as reproduced in Fig. 1.9 [60, 61]. A chief reason
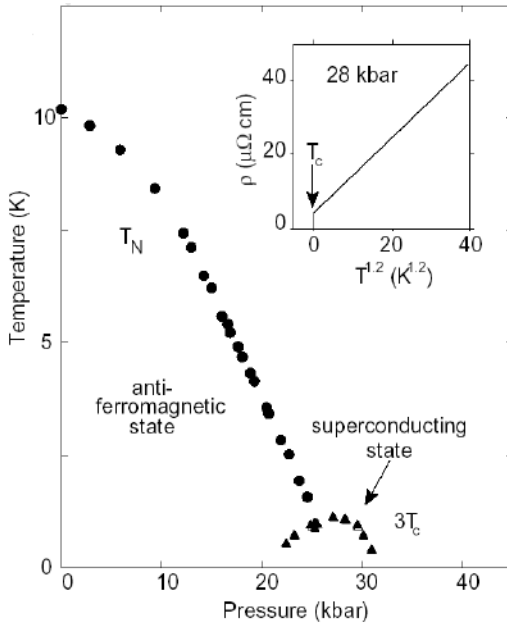
Figure 1.9: Emergence of superconductivity in the antiferromagnet $CePd_2Si_2$, taken from Mathur et al. [61].

is that close to a transition the relevant excitations become highly degenerate so new phases of matter emerge. However, before the system can enter the novel phase, a different physics of the fluctuation dynamics might dominate, namely the fluctuations might couple leading to a first order phase transition. There is a strong precedent [62–64] to study the coupling of a fluctuating field ψ to the principal field ϕ. If the two fields couple through a parameter a then the total action might be described by a Landau expansion (see App. A.3.1)

$$
\begin{aligned}
S[\phi,\psi] &= r\phi^2 + u\phi^4 + a\phi^2\psi + b\psi^2 \\
&= r\phi^2 + (u - a^2/4b)\phi^4 + b(\psi + a\phi^2/2b)^2 \\
S[\phi] &= r\phi^2 + (u - a^2/4b)\phi^4 \,,
\end{aligned}
\tag{1.1}
$$

where to go from the second to third line we have integrated out the field ψ using the tools described in App. A.2. Whatever the sign of the coupling a, we see that it always tends make the fourth order term coefficient ϕ^4 more negative and so drive the phase transition first order. Here we look for a similar mechanism, but focus on the coupling of the relevant field to orthogonal components of itself. We will concentrate our research on two topical solid state systems, itinerant ferromagnets and ferroelectrics, which are both introduced below.
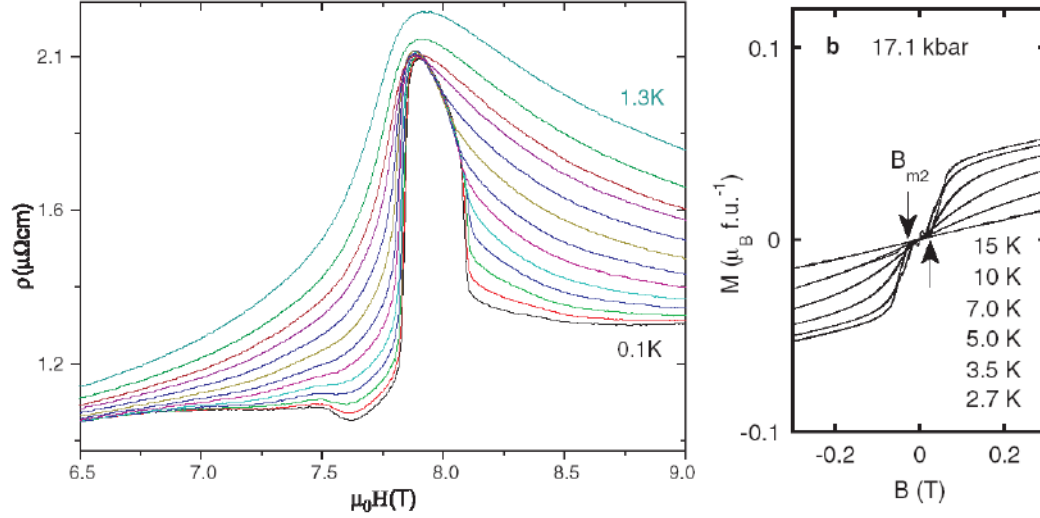
Figure 1.10: Left: resistance anomaly in $Sr_3Ru_2O_7$ that is indicative of scattering off a spin crystal, taken from Grigera et al. [65]. Right: kink of magnetisation in $ZrZn_2$ that is indicative of a metamagnetic phase, taken from Uhlarz et al. [47].

1.4.1 Textured itinerant ferromagnetism

This project focuses on recent experimental evidence highlighted in Fig. 1.10 that hints at anomalous phase behaviour at the first order ferromagnetic phase transition in $Sr_3Ru_2O_7$ [65] and $ZrZn_2$ [47]. Inspired by the atomic gas study in Chp. 6, in Chp. 7 we go onto ask whether the first order ferromagnetic phase transition might be preempted by a textured ferromagnetic phase that is consistent with the experimental evidence.

Additional motivation to search for a textured phase arises from an analogy to the FFLO state studied in Chp. 4 [66, 67] which provides a precedent for searching for a putative textured phase that preempts a first order transition. This is highlighted by the Ginzburg-Landau expansion of the action that, for both the FFLO state and the itinerant ferromagnet, is expected to take the form

$$S[\phi] = r\phi^2 + u\phi^4 + v\phi^6 + \frac{2}{3}u(\nabla\phi)^2 - h\phi \, , \tag{1.2}$$

where ϕ is the magnetisation. The coefficient u of the fourth-order term and the lowest order gradient term are inextricably linked as both stem from a product of four Green functions dominated by contributions from around the Fermi surface.

Both terms are expected to turn negative together, and so the first order transition, driven by a negative quartic term, is expected to be preempted by a textured phase caused by a negative gradient term.

1.4.2   Displacive ferroelectrics

Ferroelectricity is the spontaneous electric polarisation of a material that can be reversed by the application of an external electric field. There are two main classes of ferroelectric, which are referred to as order-disorder and displacive. In an order-disorder ferroelectric there is a dipole moment in each unit cell, but at high temperatures they are pointing in random directions. Upon lowering the temperature and going through the phase transition the dipoles rotate to all point in the same direction within a domain. In a displacive ferroelectric, such as Barium Titanate ($BaTiO_3$), Strontium Titinate ($SrTiO_3$), and Potassium Tantalate ($KTaO_3$), at high temperature each unit cell has no dipole moment. On lowering the temperature the unit cells all spontaneously polarise leading to an asymmetric shift in the equilibrium ion positions and hence a permanent dipole moment. Here we focus on the displacive ferroelectric transition, which the prevailing theory predicts remains second order down to low temperatures. However, in Chp. 8 we are motivated by the recent work of Taniguchi et al. [68] that provides strong evidence for a first order ferroelectric transition and recent experimental results [69] shown in Fig. 1.11 that show that the inverse dielectric constant has an unexpected minimum consistent with coupling between phonon modes. Inspired by the mechanism of the first order ferroelectric transition explored in Chp. 6, we consider how orthogonal optical phonon modes couple in order to search for a putative first order displacive ferroelectric phase transition.
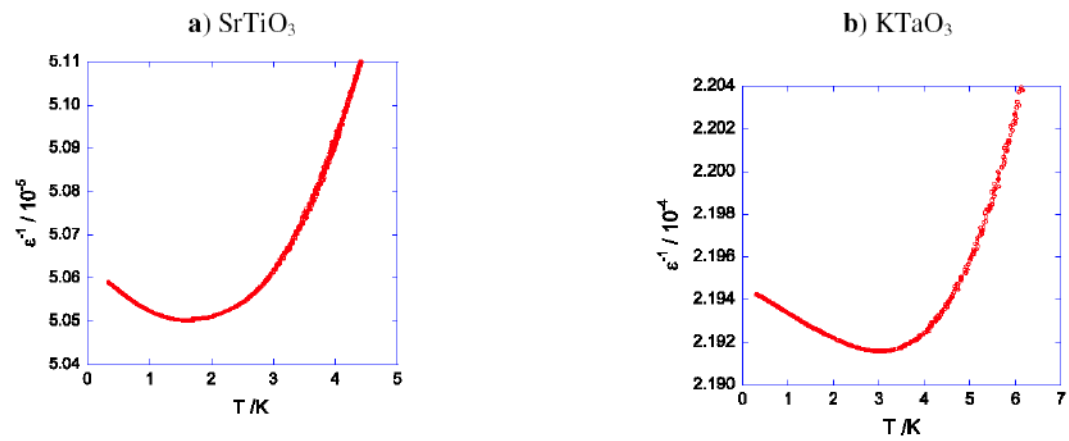
Figure 1.11: Observation of a minimum in the inverse dielectric constant in both (a) SrTiO$_3$, and (b) KTaO$_3$ in the neighbourhood of the quantum critical point on the paraelectric side. Taken from Rowley et al. [69].

Part I

Electron gases of many flavours

Electron gases in multivalley semiconductors and semimetals have an unusual dispersion that distinguishes between electrons with the same momentum. This allows us to associate a new quantum number, the flavour, with each electron. In the limit of many flavours being present new analytical results for the properties of the electron gas can be derived, which are presented in Chp. 2. We take advantage of the opportunity to computationally verify these results and apply the formalism to quantum dots in Chp. 3.

Chapter Two

Many-flavour electron gas approach to electron-hole drops

$\mathbf{I}$ N this chapter a Many-Flavour Electron Gas (MFEG) is analysed, such as could be found in a multi-valley semiconductor or semimetal. Using the re-derived polarisability for the MFEG an exact expression for the total energy of a uniform MFEG in the many-flavour approximation is found; the interacting energy per particle is shown to be $-0.574447(E_{\mathrm{h}} a_0^{3/4} m^{*3/4}) n^{1/4}$ with E_{h} being the Hartree energy, a_0 Bohr radius, and m^* particle effective mass. The short characteristic length-scale of the MFEG motivates a local density approximation, allowing a gradient expansion in the energy density, and the expansion scheme is applied to electron-hole drops, finding a new form for the density profile and its surface scaling properties.

The content of this chapter stems from the recent publication Conduit [1].

2.1 Introduction

For some semiconductors, at low temperatures and high density, electrons and holes condense into electron-hole drops, which provide a good testing ground for understanding effects of electron-electron interactions [70]. Some of the

semiconductors (and also semimetals) that electron-hole drops form in [71, 72], such as Si, Ge, and diamond have conduction band minima near the Brillouin zone boundary, for example Si has six degenerate valleys, see Fig. 2.1, a Ge-Si alloy has ten degenerate valleys, and $Pb_{1-x-y}Sn_xMn_yTe$ has twelve valleys in the Σ band [73]. When the material is strained, valley degeneracy reduces [74–78], which can be experimentally probed [79–88], meaning that valley degeneracy could be regarded as a control parameter. Because of this, as well as degeneracy being large in some semiconductors, valley degeneracy might be a good parameter with which to formulate a theory of electron-hole drops.

Previous theoretical analyses of electron-hole drops [78, 89–94] used an expansion of the energy density with parameters found from separate energy calculations [77]. An alternative approach is to assume that each valley contains a different type of fermion, denoted by an additional quantum number, which we shall call the *flavour*, the total number of flavours (valleys) is ν. Further motivation to study flavours stems from the fact that in some previous studies of multiply degenerate systems the number of flavours has not been well defined, for example heavy fermions [95–97], charged domain walls [98], a super-strong magnetic field [72], and spin instabilities [99, 100]. Cold atom systems in optical lattices [101–103] have a well defined number of flavours but weak interactions between particles. In electron-hole drops however the number of flavours is well defined and interactions are strong.

The ground state energy and pair correlation function of a free MFEG were examined using a numerical self-consistent approach for the local field correction by Gold [104], and superconductivity was studied by Cohen [105]. Following the method of Keldysh and Onishchenko [72], Andryushin et al. [71] studied the behaviour of the free MFEG by summing over all orders of Green's function contributions, they found an exact expression for the correlation energy of a MFEG (which dominates the interacting energy in the extreme many-flavour limit). This chapter describes the derivation of a more versatile formalism, based on a path integral, which gives an exact expression for the total energy of the MFEG; the theory could apply with as few as six flavours where the exchange energy assumed small by Andryushin et al. [71] would be significant.
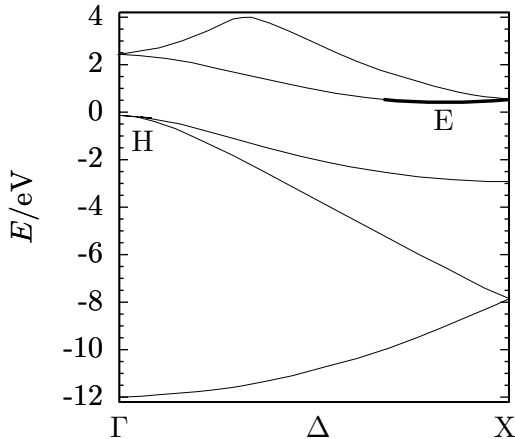
Figure 2.1: The Si band structure in the [100] direction generated with a LDA-DFT approximation by a plane-wave pseudopotential method [106]. The Fermi energy is at $E = 0$ eV; below are valence bands with holes at H; above conduction bands, the bold parabolic curve signifies the first conduction band valley with electrons at E.

As well as studying the uniform case, the previously unstudied density response of a MFEG not constrained to be uniform is investigated. The screening length-scales of the MFEG are shown to be short relative to the inverse Fermi momentum, suggesting that a Local Density Approximation (LDA) might be a good approximation, motivating a gradient approximation. This gradient expansion is then applied to analyse the electron-hole drop density profile, and to simulate effects of strain the scaling of drop surface thickness and tension with number of flavours is examined.

In a MFEG with ν flavours at low temperatures the relationship between the number density of electrons n and Fermi momentum p_F is

$$n = \frac{\nu p_F^3}{3\pi^2}. \tag{2.1}$$

When the electrons have multiple flavours, each Fermi surface encloses fewer states so $p_F \propto \nu^{-1/3}$. The local band curvature governs the electron effective mass, the band structure is often such that the holes relax into a single valence band minimum at the Γ point (see Fig. 2.1); here holes are assumed to be heavy and spread out uniformly providing a jellium background.

The Thomas-Fermi approximation predicts a screening length $\kappa^{-1} = (4\pi e^2 g)^{-1/2}$, where g is the Density of States (DOS) at the Fermi surface. The DOS is dependent on the number of flavours as $g \propto \nu\sqrt{E_F} \propto \nu^{2/3}$ and so $\kappa^{-1} \propto \nu^{-1/3}$. The ratio of the inverse Fermi momentum length-scale to the screening length varies with number of flavours as $p_F/\kappa \propto \nu^{-2/3}$. This chapter takes the many flavour limit

Figure 2.2: The dark grey ellipsoids show Fermi surfaces of electrons in the six degenerate conduction band valleys in Si. $E(\mathbf{q})$ is the energy with momentum $\mathbf{q}$ measured with respect to the Γ point, $\epsilon_i(\mathbf{p})$ is energy with momentum $\mathbf{p}$ measured with respect to the centre of the ith valley.
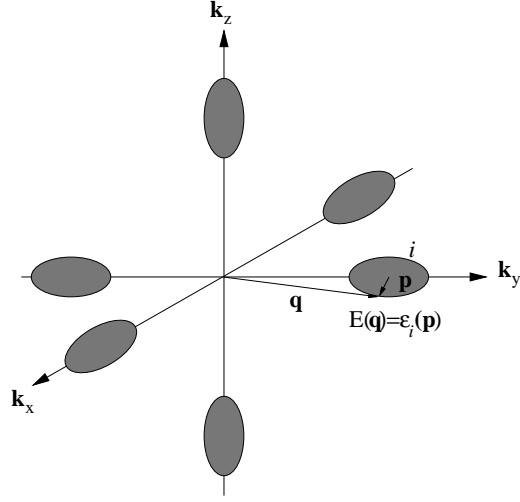
$\nu \gg 1$, in which the screening length is smaller than the inverse Fermi momentum, $\kappa^{-1} \ll p_{\mathrm{F}}^{-1}$, the many-flavour limit therefore means that the wave vectors of the strongest electron-electron interactions obey $q \gg p_{\mathrm{F}}$, this is the opposite limit to the Random-Phase Approximation (RPA) which assumes that $p_{\mathrm{F}} \gg \kappa$. Physically this means the characteristic length-scales of the MFEG are short so a LDA can be used in Sec. 2.3 to develop a gradient expansion.

The conduction band energy spectrum is characterised by two spectra $E(\mathbf{q})$ and $\epsilon_i(\mathbf{p})$ as shown in Fig. 2.2. There are two energy functions: $E(\mathbf{q})$ gives the energy in the band structure at momentum $\mathbf{q}$; $\epsilon_i(\mathbf{p}) = p^2/2m$ denotes the kinetic energy at momentum $\mathbf{p}$ with respect to the centre of the ith valley (the dispersions of all valleys are assumed to be the same and isotropic so that $\epsilon_i(\mathbf{p}) = \epsilon(\mathbf{p})$. Andryushin et al. [71] have outlined a method of calculating a scalar effective mass for anisotropic valleys).

Physical manifestations of the many-flavour limit include effects where the DOS at the Fermi surface (energy E_{F}) is important; from Eqn. (2.1) the DOS of a particular flavour i shrinks as $g_i(E_{\mathrm{F}}) \propto p_{\mathrm{F}} \propto \nu^{-1/3}$ whereas the DOS of all flavours grows since $g(E_{\mathrm{F}}) = \sum_{i=1}^{\nu} g_i(E_{\mathrm{F}}) = \nu g_1(E_{\mathrm{F}}) \propto \nu^{2/3}$. With increasing flavours, more electrons are within $\sim k_{\mathrm{B}}T$ of the Fermi surface hence are able to be thermally excited, therefore the heat capacity of the MFEG, $C = 12k_{\mathrm{B}}^2 T(\nu/3\pi^2 n)^{2/3}/5$, increases with number of flavours. The Stoner criterion [107, 108] for band ferromagnetism states that for opposite spin electrons interacting with positive

exchange energy U, ferromagnetism occurs when $g(E_F)U \geq 1$. With increasing number of flavours the total DOS $g(E_F) \propto \nu^{2/3}$ increases so that the Stoner criterion becomes more favourable. However, this analysis does not take into account the curvature of the DOS at the Fermi surface which can be an important factor in determining whether ferromagnetism occurs [109, 110]. The effect of the total DOS is also seen in the paramagnetic susceptibility, this is proportional to the total DOS at the Fermi surface so is expected to increase with number of flavours. Analogously one can compare a transition metal with narrow d-bands that leads to a large DOS at the Fermi surface with a simple metal that has broader free electron conduction bands and so a lower DOS at the Fermi surface. Similar to many flavour systems, transition metals are experimentally observed [111] to have a significantly higher specific heat capacity and greater magnetic susceptibility than typical simple metals. The simple scaling relationships with number of flavours for heat capacity and magnetisation provide additional motivation to analyse a MFEG in more detail.

This chapter uses the atomic system of units, that is $e^2 = \hbar = m = 1/(4\pi\epsilon_0) = 1$, but is modified so that m denotes an appropriate effective mass for the electron-hole bands, which is the same for all valleys. This mass $m = m_e m^*$ can be expressed as a multiple of the electron mass m_e and the dimensionless effective mass m^*. The units of length are then $a_0^* = a_0/m^*$ where a_0 is the Bohr radius, units of energy are those of an exciton, $E_h^* = E_h m^*$, where E_h is the Hartree energy. These six quantities, defined to be unity, give the standard atomic units when $m^* = 1$. For the important relationships that are derived in this chapter particular to the MFEG, the full units are shown explicitly for clarity. Throughout this chapter density is denoted by both n (number density of particles) and r_s (Wigner-Seitz radius).

In this chapter, firstly a new formalism for the uniform system is derived. In Sec. 2.1.1 the system polarisability is found, in Sec. 2.2.1 the general quantum partition function is derived, and in Sec. 2.2.2 the uniform MFEG total energy is calculated. Secondly, we examine the system with non-uniform density: in Sec. 2.3 a gradient expansion in the density for the total energy is found and is applied to electron-hole drops in Sec. 2.4, whose density profile and surface properties are calculated.

2.1.1 Polarisability

In this section the MFEG polarisability is derived. Though the result for the
polarisability is the same as previous work [71, 112], the derivation is presented here
since an assumption made leads to an applicability constraint on the many-flavour
theory (in Sec. 2.2.3), and the MFEG polarisability is an important quantity that
will feature prominently in two main results of this chapter: the Sec. 2.2 derivation
of the MFEG interacting energy and the derivation of the gradient expansion (see
Sec. 2.3).

The polarisability $\Pi_0^{\mathrm{MF}}(\mathbf{q},\omega)$, where the superscript "MF" (many-flavour)
denotes this is only for a MFEG, at wave vector $\mathbf{q}$ and Matsubara frequency ω
is given by the standard Lindhard form

$$\Pi_0^{\mathrm{MF}}(\mathbf{q},\omega) = \sum_{i,j=1}^{\nu} \frac{\delta_{i,j}}{4\pi^3} \int \frac{n_{\mathrm{F}}\left(\epsilon_i\left(\mathbf{p}\right)\right) - n_{\mathrm{F}}\left(\epsilon_j\left(\mathbf{p}+\mathbf{q}\right)\right)}{i\omega + \epsilon_i\left(\mathbf{p}\right) - \epsilon_j\left(\mathbf{p}+\mathbf{q}\right)} d\mathbf{p}\,, \qquad (2.2)$$

where $n_{\mathrm{F}}(\epsilon_i) = 1/(e^{\beta(\epsilon_i-\mu)}+1)$ is the Fermi-Dirac distribution, $\beta = 1/k_{\mathrm{B}}T$, and μ is
the chemical potential. In the standard expression for the polarisability the Fermi-
Dirac distribution would contain the energy spectrum $E(\mathbf{p})$ but in the MFEG each
electron is in a particular valley so the polarisability should be re-expressed in terms
of the energy dispersion of each valley $\epsilon_i(\mathbf{p})$ (see Fig. 2.2) and the contributions
must be summed over the valleys i and j. Eqn. (2.13) shows that a large Coulomb
potential energy penalty $V(\mathbf{q}) \propto 1/q^2$ inhibits exchange between different valleys so
that the Kronecker delta $\delta_{i,j}$ removes cross-flavour terms, and as all of the conduction
valleys have the same dispersion a factor of ν will replace the remaining summation
over valleys. Supposing each conduction valley has a locally quadratic isotropic
dispersion relationship (with effective mass m), symmetrising results in

$$\Pi_0^{\mathrm{MF}}(\mathbf{q},\omega) = \frac{\nu}{4\pi^3} \int \frac{n_{\mathrm{F}}\left(\left|\frac{1}{2}\mathbf{q}-\mathbf{p}\right|^2/2\right) - n_{\mathrm{F}}\left(\left|\frac{1}{2}\mathbf{q}+\mathbf{p}\right|^2/2\right)}{i\omega - \mathbf{p}\cdot\mathbf{q}} d\mathbf{p}\,. \qquad (2.3)$$

In Sec. 2.2.2 it is shown that the typical momentum exchange $q \sim (\hbar a_0^{-1/4})n^{1/4}$
is large relative to the Fermi momentum, therefore the two volumes in momentum
space of integration variable $\mathbf{p}$, defined by the two Fermi-Dirac distributions are far

apart relative to their radii $q/2 \gg p_{\mathrm{F}}$, and the temperature is sufficiently low so that the high energy tails of the two distributions have negligible overlap. Within these approximations the simple form for the polarisability is

$$\Pi_0^{\mathrm{MF}}(\mathbf{q},\omega) = -\frac{n}{(\omega/q)^2 + q^2/4}\,, \tag{2.4}$$

this expression agrees with the many-flavour polarisability found by Andryushin et al. [71] and Beni and Rice [112].

The standard Lindhard form for the polarisability, when taken in the same $q \gg p_{\mathrm{F}}$ limit as imposed by the many-flavour system agrees with Eqn. (2.4). In the static limit where frequencies are small compared to the momentum transfer $q^2 \gg (\hbar^3/a_0^{*2}E_{\mathrm{h}}^*)\omega$, the polarisability varies as q^{-2}. In this limit, one Green's function is restricted by the sum over Matsubara frequencies to lie inside the Fermi surface whilst the other gives the polarisability dependence of $1/\epsilon(\mathbf{q}) \sim q^{-2}$ due to the excited electron's kinetic energy.

The derivation of the polarisability accounted only for intra-valley scattering, which means that in the MFEG the same terms contribute [71] as in the RPA for the standard electron gas. Therefore diagrammatically, as detailed in App. A.6, in the polarisability all electron loops are empty, the polarisability contains only reducible diagrams, which is denoted by the polarisability subscript "0".

2.2 Analytic formulation

Having reviewed the derivation of the polarisability of the system it is now used to formulate two complementary components of the many-flavour theory. The first is the derivation of the energy of a uniform system; we begin by calculating the general quantum partition function in Sec. 2.2.1 and continue for the homogeneous case in Sec. 2.2.2. The validity of the many-flavour approach for a uniform MFEG is investigated in Sec. 2.2.3. The second part of the formalism is a gradient expansion of the energy density, looked at in Sec. 2.3. Finally, the uniform and gradient expansion parts of the formalism will be brought together to study the model system of electron-hole drops in Sec. 2.4.

2.2.1   Partition function

To derive an expression for the total energy of the system a functional path integral method is followed, which is a flexible approach that should be extendable to investigate further possibilities such as modulated states and inter-valley scattering. The derivation of the functional integral phenomenology is outlined in App. A.2. Fermion field variables ψ are used to describe the electrons irrespective of flavour in the dispersion $E(\hat{\mathbf{p}})$. Overall the system is electrically neutral, so in momentum representation the $\mathbf{q} = \mathbf{0}$ element is ignored. The repulsive charge-charge interaction acting between electrons is $V(\mathbf{r}) = e^2/r$, we explicitly include the dependence on electron charge e (even though it is defined to be unity) so that the charge can be set equal to zero to recover the non-interacting theory. For generality we consider stationary charges $Q(\mathbf{r})$ embedded in the MFEG which have a corresponding static potential $U(\mathbf{r})$. The quantum partition function for the MFEG written as a Feynman path integral is then

$$
\mathcal{Z} = \iint \mathcal{D}\bar{\psi}\mathcal{D}\psi \exp\left(\iint \bar{\psi}(\mathbf{r},\tau)\left(-\mathrm{i}\hat{\omega} + E\left(\hat{\mathbf{p}}\right) - \mu\right)\psi(\mathbf{r},\tau)\mathrm{d}\mathbf{r}\mathrm{d}\tau\right)
$$
$$
\times \exp\left\{\frac{1}{2}\iiint \left[\bar{\psi}(\mathbf{r}',\tau)\psi(\mathbf{r}',\tau) - Q(\mathbf{r}')\right]V(\mathbf{r}-\mathbf{r}')\left[\bar{\psi}(\mathbf{r},\tau)\psi(\mathbf{r},\tau) - Q(\mathbf{r})\right]\mathrm{d}\mathbf{r}'\mathrm{d}\mathbf{r}\mathrm{d}\tau\right\}.
$$
$$
(2.5)
$$

This expression for the quantum partition function differs from that used for an electron gas (which has just a single flavour) only by the operator $E(\hat{\mathbf{p}})$ which gives the appropriate energy dispersion. To recover the standard electron gas result, which has a free particle dispersion relationship centred at the Γ point, one should set $E(\mathbf{p}) = p^2/2m_{\mathrm{e}}$. For the MFEG, as outlined in Fig. 2.2, $E(\mathbf{p})$ represents the dispersion relationship of the whole conduction band, but no approximation concerning the flavours has yet been made, so the formalism applies for any number of flavours with a suitable energy dispersion relationship.

To make the action quadratic in the fermion variable ψ, the Hubbard-

Stratonovich transformation [113] introduces an auxiliary boson field $\phi(\mathbf{r},\tau)$

$$
\mathcal{Z} = \int \mathcal{D}\phi \exp\left(-\frac{\beta\Omega}{2} \sum_{\mathbf{q}\neq\mathbf{0},\omega} \phi(\mathbf{q},\omega)(q^2/4\pi)\phi(-\mathbf{q},-\omega) + \overbrace{\frac{\pi e^2 \beta n}{2} \sum_{\mathbf{q}\neq\mathbf{0}} \frac{4\pi}{q^2}}^{\dagger}\right)
$$
$$
\times \iint \mathcal{D}\bar{\psi}\mathcal{D}\psi \exp\left(\iint \bar{\psi}(\mathbf{r},\tau)\left(-\mathrm{i}\hat{\omega} + E\left(\hat{\mathbf{p}}\right) + \hat{U} - \mu + \mathrm{i}e\hat{\phi}\right)\psi(\mathbf{r},\tau)\mathrm{d}\mathbf{r}\mathrm{d}\tau\right). \quad (2.6)
$$

Following the prescription laid out in App. A.2.5, the direct decoupling channel [113] was chosen as the relevant contributions come from a RPA-type contraction of operators.

The term labelled with a ($\dagger$) exclusive of both fermion variables ψ and the auxiliary field ϕ, physically removes the electron self-interaction included when expressing the auxiliary field in a Fourier representation. Integrating over the fermion variables ψ and using $\ln(\det\hat{A}) = \mathrm{Tr}(\ln\hat{A})$ gives $\mathcal{Z} = \int \mathrm{e}^{-S[\phi]}\mathcal{D}\phi$, where the action $S[\phi]$ is

$$
S[\phi] = \frac{\beta\Omega}{2\pi} \sum_{\mathbf{q}\neq\mathbf{0},\omega} \phi(\mathbf{q},\omega)(q^2/4\pi)\phi(-\mathbf{q},-\omega) - 2\pi e^2 \beta n \sum_{\mathbf{q}\neq\mathbf{0}} \frac{1}{q^2}
$$
$$
- \mathrm{Tr}\Big(\ln\big(\underbrace{-\mathrm{i}\hat{\omega} + E\left(\hat{\mathbf{p}}\right) + \mathrm{i}e\hat{\phi} + \hat{U} - \mu}_{\hat{G}_\phi^{-1}}\big)\Big). \quad (2.7)
$$

Due to its similarity to an inverse Green function, $\hat{G}_\phi^{-1}$ is used to denote the argument of the logarithm, the subscripts "ϕ" or "0" denote whether the inverse Green's function includes the auxiliary field or is free.

Finally, we note for use later that the ground state total energy per particle $E_\mathrm{G} = E_\mathrm{int} + E_0$ can be split into two components. The interacting energy is E_int (found in Sec. 2.2.2) and the non-interacting energy is

$$
E_0 = \frac{3}{10}\left(3\pi^2\frac{n}{\nu}\right)^{2/3}, \quad (2.8)
$$

which is the energy with interaction between charges switched off ($e = 0$). It falls with increasing number of electron flavours due to the shrinking Fermi surface.

2.2.2   Homogeneous Coulomb gas

So far, up to Eqn. (2.7), the formalism is exact, however to perform the functional integral over bosonic variable ϕ an approximation must be made. To proceed one notes that with no external potential $U(\mathbf{r}) = 0$ the saddle-point auxiliary field of the action (Eqn. (2.7)) is $\phi = 0$, fluctuations in the action are expanded about the saddle point solution in ϕ giving the expression

$$S[\phi] = \ln(\hat{G}_0^{-1}) + \operatorname{Tr}\left(\hat{\phi}\hat{V}^{-1}\hat{\phi} - \frac{1}{2}\overbrace{\hat{\phi}\hat{G}_0\hat{\phi}\hat{G}_0}^{\ddagger}\right)$$
$$- \frac{1}{4}\operatorname{Tr}\left(\hat{\phi}\hat{G}_0\hat{\phi}\hat{G}_0\hat{\phi}\hat{G}_0\hat{\phi}\hat{G}_0\right) + \mathcal{O}(\phi^6) - \frac{e^2}{2}\beta n \sum_{\mathbf{q}\neq\mathbf{0}}\frac{4\pi}{q^2}. \qquad (2.9)$$

Terms are now kept to quadratic order in ϕ, this is equivalent to the RPA, analogous to the terms kept in the derivation of the many-flavour polarisability, see Sec. 2.1.1. This approximation will place a constraint on the validity of the formalism that is further examined in Sec. 2.2.3.

The product of two Green's functions in the quadratic term in ϕ, labelled ($\ddagger$), is identified with the polarisability Π_0, this is still expressed in terms of the general energy spectrum $E(\mathbf{p})$ so is not yet necessarily many-flavour and does not carry the superscript "MF" used in Sec. 2.1.1. Following a multi-dimensional Gaussian integral over the fluctuating field ϕ (to quadratic order) the quantum partition function is

$$\mathcal{Z} = \prod_{\mathbf{q},\omega}\left(q^2/4\pi - e^2\Pi_0(\mathbf{q},\omega)\right)^{-\frac{1}{2}}\exp\left(\frac{\beta}{2}\sum_{\mathbf{q}\neq\mathbf{0}}\frac{4\pi e^2}{q^2}n\right). \qquad (2.10)$$

In the low temperature limit we consider the free energy to get $E_{\mathrm{G}} = -\lim_{\beta\to\infty}(\ln(\mathcal{Z})/\beta) = E_0 + E_{\mathrm{int}}$ to get the interacting energy per particle, normalised so that $E_{\mathrm{int}} = 0$ with no interactions ($e = 0$),

$$E_{\mathrm{int}} = \frac{1}{2n}\left(\iint \ln\left(1 - \frac{4\pi e^2}{q^2}\Pi_0(\mathbf{q},\omega)\right)\frac{\mathrm{d}\omega\mathrm{d}\mathbf{q}}{(2\pi)^4} - e^2 n\sum_{\mathbf{q}\neq\mathbf{0}}\frac{4\pi}{q^2}\right). \qquad (2.11)$$

This equation remains general and is not necessarily in the many-flavour limit, it is

in agreement with previous expressions for the interacting energy [74] studied not in the many-flavour limit, but which use alternative forms for the polarisability. If the standard (single flavour) electron gas form for the polarisability, the Lindhard function, is used then it is possible to recover, in the high density limit, the Gell-Mann Brückner [114] expression for the total energy.

However, to proceed, one should now assume many-flavours and use the appropriate polarisability, Eqn. (2.4). The many-flavour polarisability summed over all Matsubara frequencies in the zero temperature limit $\beta \to \infty$ satisfies $\frac{1}{\beta}\sum_\omega \Pi_0^{\mathrm{MF}}(\mathbf{q},\omega) = -n$. This is used to substitute for the electron density n in the final term in Eqn. (2.11) to yield the many-flavour result

$$E_{\mathrm{int}} = \frac{1}{2n} \iint \left(\ln\left(1 - \frac{4\pi e^2}{q^2}\Pi_0^{\mathrm{MF}}(\mathbf{q},\omega)\right) + \frac{4\pi e^2}{q^2}\Pi_0^{\mathrm{MF}}(\mathbf{q},\omega) \right) \frac{\mathrm{d}\omega\mathrm{d}\mathbf{q}}{(2\pi)^4} . \qquad (2.12)$$

To evaluate the interacting energy one first substitutes for the many-flavour polarisation using Eqn. (2.4), makes the change of variables $\Omega = \omega/q^2$ and $Q = q/n^{1/4}$, and re-arranges to get

$$E_{\mathrm{int}} = -n^{1/4} \overbrace{\frac{1}{(2\pi)^3} \iint \frac{16\pi e^2}{1 + 4\Omega^2} - Q^4 \ln\left(1 + \frac{16\pi e^2/Q^4}{1 + 4\Omega^2}\right) \mathrm{d}\Omega\mathrm{d}Q}^{A_{\mathrm{3D}}} . \qquad (2.13)$$

The integral is independent of density and number of flavours, so is the numerical factor $A_{\mathrm{3D}} = (E_{\mathrm{h}}^* a_0^{*3/4})\Gamma(-5/4)\Gamma(3/4)/(2\pi^{5/4}) \approx 0.574447(E_{\mathrm{h}}^* a_0^{*3/4})$ that was evaluated analytically[1]. The interacting energy is therefore

$$E_{\mathrm{int}} = -A_{\mathrm{3D}}n^{1/4} , \qquad (2.14)$$

which is independent of the number of flavours. In evaluating Eqn. (2.13) the main contribution to the integral over $Q = q/n^{1/4}$ is at a momentum $q \propto (\hbar a_0^{*-1/4})n^{1/4}$, so the interaction and screening length-scale in a MFEG is $\lambda \sim \hbar/q \propto a_0^{*1/4}n^{-1/4} \ll \hbar/p_{\mathrm{F}}$, which is shorter than the Fermi momentum length-scale.

---

[1]This differs from the value reported by Andryushin et al. [71] and Keldysh and Onishchenko [72] of $A_{\mathrm{3D}} = 32(2\pi)^{3/4}2^{1/2}(E_{\mathrm{h}}^* a_0^{*3/4})/(5\Gamma^2(1/4))$ by a factor of $2^{9/4}$. The result presented here was confirmed by three separate methods: analytically, numerically, and by comparing with the results of QMC simulations on the many-flavour system that are described in more detail in Chp. 3 [2].

The interacting energy $E_{\text{int}} = E_{\text{ex}} + E_{\text{corr}}$ can be split into exchange energy E_{ex} and correlation energy E_{corr}. The interacting energy is independent of number of flavours, the exchange energy, $E_{\text{ex}} = -(3/2)(3n/\pi\nu)^{1/3}$ [104], falls with number of flavours, therefore the correlation energy dominates over the exchange energy in the interacting energy in the many-flavour limit. In terms of the total energy, the correlation energy also dominates over the non-interacting energy, the kinetic energy that falls with number of flavours as $E_0 \propto \nu^{-2/3}$. The increasing importance of the correlation energy can be understood further by considering the electron pair correlation function. With increasing number of flavours the length-scales between electrons of the same flavour increase as $\propto \nu^{1/3} r_{\text{s}}$ and thus exchange energy and kinetic energy reduce whereas the correlation energy depends only on the distance r_{s} between electrons so is unaffected by the number of flavours present. Andryushin et al. [71] and Keldysh and Onishchenko [72] found the Eqn. (2.14) expression to be the correlation rather than interacting energy, neglecting the exchange energy which is small in the extreme many flavour limit. In Sec. 2.2.3 the expression for the interacting energy is compared with self-consistent numerical calculations [104] on a MFEG with up to six flavours.

The interacting energy of a standard electron gas with a single flavour [104] is more negative than that of a MFEG, which in turn is more negative than that of a Bose condensate [115], this could be due to the reducing negativity of the exchange energy, important in the single flavour system, but zero in the Bose condensate. In these two extreme systems, the single flavour electron gas and the Bose condensate, there is no notion of valley degeneracy, and therefore the intermediate system, the MFEG, might be expected at most to have only a weak dependence on number of valleys. In fact, the interacting energy of the MFEG, over the range of density found in Sec. 2.2.3, contains no dependence on the number of valleys. The absence of flavour dependence is also present in the universal behaviour for the exchange-correlation energy in electron-hole liquids proposed by Vashishta and Kalia [116].

The non-interacting energy term $E_0 \propto (n/\nu)^{2/3}$ favours low electron density, the interacting term $E_{\text{int}} = -A_{\text{3D}} n^{1/4}$ favours high electron density, therefore the total energy per particle has a minimum as a function of density of $E_{\text{Gmin}} \propto -\nu^{2/5}$ at

$n_{\min} \propto \nu^{8/5}$. The presence of a minimum in energy with density of the MFEG is consistent with the results of Andryushin et al. [71] and Brinkman and Rice [74] who analysed conduction electrons in a semiconductor. One consequence of this minimum is the possibility of a low density phase coexisting with excitons.

Before analysing the non-uniform system in detail in Sec. 2.3 we can make qualitative arguments about its expected behaviour within a potential well. According to Thomas-Fermi theory, an electron gas in a slowly varying attractive potential has a constant chemical potential. The electron gas is least dense at the edges of the potential and is densest at the centre of the well. In a MFEG, due to the negative interacting energy $E_{\text{int}} = -A_{\text{3D}} n^{1/4}$ favouring high electron density, the density is expected to further reduce at the edges of the attractive potential and increase at the centre of the well. In a repulsive potential the opposite should occur.

2.2.3 Density limits

In this section we will derive approximate expressions for the upper and lower density limits over which the many-flavour limit applies, these will be used to check the theory against numerical results [104] and to predict a lower bound on the number of flavours required for the theory to apply.

To find the upper density limit one notes that Eqn. (2.13) implies that an acceptable upper limit to the momentum integral would scale as $q = \alpha(\hbar a_0^{*-1/4})n^{1/4}$, the constant $\alpha \approx 4$ was determined numerically and was chosen to give the q upper limit on the integral that recovered 95% of the interacting energy. Additionally, the two regions of integration defined by the Fermi Dirac distributions in Eqn. (2.3) must not overlap, requiring that $q/2 \geq p_{\text{F}}$. Combining these requires that for the many-flavour limit to apply the density must satisfy $n a_0^{*3} \ll (\alpha^{12}\nu^4)/(2^{12}3^4\pi^8)$. Physically the breakdown at high density is due to the strongest interactions taking place on length-scales longer than the inverse length p_{F}^{-1}.

The low density limit is derived by considering the expansion of the action in the auxiliary boson field ϕ, Eqn. (2.9). In order to evaluate the Gaussian functional integral over the bosonic variable ϕ it is necessary to neglect the quartic term in ϕ, valid only when investigating the system with respect to its long-range behaviour,

that is $p_\mathrm{F} \hbar a_0^* \gg 1$ [113], and therefore $n a_0^{*3} \gg \nu / 3\pi^2$. The breakdown at low density can be understood because the MFEG is effectively a boson gas, all electrons will be in the Γ state ($\mathbf{k} = \mathbf{0}$) and there is no exchange energy.

The upper and lower critical density limits can be combined to conclude that the many-flavour limit result for interacting energy applies for densities that obey $0.03\nu \ll n a_0^{*3} \ll 0.005\nu^4$; this density range increases as ν^4 with number of flavours, the scaling relationship is the same as the applicable density range of the correlation energy found by Andryushin et al. [71], though they did not provide estimates of numerical factors.

Using the above high and low density limits it is possible to estimate the minimum number of flavours required for the theory to apply. This is done by setting the lower and upper estimates for the allowable density to be equal, which gives $\nu \gtrapprox 2$, this estimate is approximate due to the possible inaccuracies in the upper and lower critical densities used in its derivation. As the upper and lower critical densities have been set equal, the many-flavour theory will apply here only over a very narrow range of densities, but this range widens with increasing number of flavours as ν^4. An alternative limit can be found by comparing the interaction energy predicted by the theory over the expected density range of applicability with the results of Gold [104]. Their numerical self-consistent approach gives interaction energies accurate to approximately $3\,\%$ when compared with single-flavour electron gas QMC calculations [117, 118] and some initial many-flavour QMC calculations [2]. At two flavours the interacting energy predicted by the many-flavour theory is $\sim 10\,\%$ more positive than the self-consistent numerical results [104] indicating the many-flavour theory does not apply at two flavours. For six flavours over the predicted allowed density range the many-flavour theory is between $\sim 0\,\%$ and $\sim 4\,\%$ more positive than the numerical results, which indicates that the many-flavour theory can be applied within the predicted range of applicability ($0.5 < r_\mathrm{s}/a_0^* < 1$). The theory should be applicable in common multi-valley compounds, such as silicon which has six conduction band valleys, and to those with more valleys [73]. This result is corroborated by the results of QMC calculations on systems with between 6 and 24 flavours, which are described in more detail in Chp. 3 [2].

In the first half of this chapter a new versatile formalism to describe a MFEG has been developed that could apply in systems containing approximately six or more degenerate conduction valleys. An exact expression for the total energy of the uniform MFEG was found and the applicable density range derived. The next step is to investigate the response of the MFEG to an external potential. A gradient approximation is developed in Sec. 2.3 and this is applied to electron-hole drops in Sec. 2.4.

2.3 Gradient correction

In Sec. 2.1 it was shown that the typical length-scales of the MFEG are short $q \gg p_{\mathrm{F}}$, motivating a LDA. This motivation is in addition to the usual reasons for the success of the LDA in DFT [11] – that the LDA exchange-correlation hole need only provide a good approximation for the spherical average of the exchange-correlation hole and obey the sum rule [119]. In this section the LDA is used with the polarisability derived in Sec. 2.1.1 to develop a gradient correction to the energy density that allows the theory to be applied to a non-uniform MFEG.

The typical momentum transfer in the MFEG is $q \sim (\hbar a_0^{*-1/4}) n^{1/4}$ hence the shortest length-scale over which the LDA may be made is approximately $(a_0^{*1/4}/\hbar) n^{-1/4}$ and the maximum permissible gradients in electron density are $|\nabla n|_{\max} \sim qn \sim (\hbar a_0^{*-1/4})) n^{5/4}$. The gradient expansion will break down for short scale phenomena, for example a Mott insulator transition. To derive an energy density gradient expansion we follow Hohenberg and Kohn [120] and Rice [90] and consider an external charge distribution $n_{\mathrm{ext}}(\mathbf{q})$ that couples to the induced charge distribution $n_{\mathrm{ind}}(\mathbf{q})$ with Coulomb energy density

$$-\frac{1}{2} \sum_{\mathbf{q}} \frac{4\pi e^2}{q^2} n_{\mathrm{ext}}(\mathbf{q}) n_{\mathrm{ind}}(\mathbf{q}) . \tag{2.15}$$

One now substitutes for $n_{\mathrm{ext}}(\mathbf{q})$ using the relative permittivity $1/\epsilon(\mathbf{q}) = 1 + n_{\mathrm{ind}}(\mathbf{q})/n_{\mathrm{ext}}(\mathbf{q}) = 1/(1 - 4\pi\Pi_0^{\mathrm{MF}}/q^2)$ and the many-flavour polarisability Eqn. (2.4). The highest order term in $1/q^2$ gives the induced charge Coulomb energy, the term of order q^2 is associated with a gradient expansion, in real space this gives the

expansion for the total energy per particle

$$E_{\mathrm{G}} + \frac{(\nabla n)^2}{8n^2} + \mathcal{O}\left((\nabla n)^4\right) , \tag{2.16}$$

here E_{G} is ground state energy of the uniform system found in Sec. 2.2.2. The form of the energy correction is similar to the von Weizsäcker term [121], although here it is larger, having a coefficient of $1/8$ rather than $1/72$ as in the von Weizsäcker case. The difference can be qualitatively understood by considering the Fermi surfaces involved in the two cases for a given wave vector q, in the many-flavour case the Fermi surfaces involved in the integral of Eqn. (2.3) do not overlap as $q/2 \gg p_{\mathrm{F}}$ so there is a large volume in Fermi space available hence a large coefficient of $1/8$, whereas in the ordinary electron gas (single flavour) the same Fermi surfaces do overlap, as now $q/2 \ll p_{\mathrm{F}}$, reducing the volume available for integration so reducing the coefficient to $1/72$.

The gradient correction for the energy could be used in analytical approximations or as a DFT functional. This energy density expansion allows the MFEG to be applied to a variety of systems, its use for studying electron-hole drops is demonstrated in Sec. 2.4.

2.4   Electron-hole drops

In this section the MFEG is used to investigate the properties of electron-hole drops. An electron-hole drop is a two-phase system: a spherical region of a MFEG surrounded by an exciton gas [112]. The density profile, surface thickness and surface tension of drops are investigated; the scaling of surface thickness and tension with number of flavours is also found since this can be experimentally probed through externally imposed strain reducing the valley degeneracy [76].

There have been four main theoretical methods used to analyse an electron-hole drop in silicon and germanium, semiconductors which have six and four flavours respectively. Rice [91] fitted an analytic form to the energy density minimum and included the lowest order of a local gradient correction, from the equation for energy density an analytic form for the density profile was derived. A similar

approach was used by Sander et al. [89] and Rice [90] to study the surface structure in more detail. The second approach [92, 93], which was also applicable to situations with an external magnetic field and uniaxial strain, conserved momentum, particle number and pressure balance at the drop surface, the resulting equations were then solved numerically. A third approach followed by Kalia and Vashishta [78] used a Padé approximant for the energy density [77] derived specifically for silicon and germanium but did not include a gradient correction factor. The fourth approach of Reinecke et al. [94] again used a Padé approximant for the energy density and also included a gradient correction factor. The latter two approaches assumed an exponential density profile for the drop. These four methods all use approximate forms for the energy density, an advantage of the many-flavour approach is that the exact form for the analytic energy density (within the many flavour assumption) can be used to solve for the drop density profile. Whilst analytic forms for the inner and outer density profile as well as a model for the entire profile can be derived, the general problem must be solved numerically. With an exact form for the density profile, electron-hole drop surface effects can be studied.

Local charge neutrality is assumed so that the density of electrons and holes are everywhere identically equal. A LDA with gradient correction is used so the drop energy density is written as the sum of the local non-interacting, local interacting and the lowest order term in a gradient expansion,

$$\varepsilon(\mathbf{r}) = \frac{3}{10}\left(\frac{3\pi^2}{\nu}\right)^{2/3} n(\mathbf{r})^{5/3} - A_{3D}n(\mathbf{r})^{5/4} + \frac{(\nabla n(\mathbf{r}))^2}{8n(\mathbf{r})}. \qquad (2.17)$$

The total energy of a drop is $\int \varepsilon(\mathbf{r})\mathrm{d}\mathbf{r}$ and the total number of electrons in the drop is $\int n(\mathbf{r})\mathrm{d}\mathbf{r}$. The total energy is minimised with respect to electron density $n(\mathbf{r})$ whilst keeping a constant number of electrons in the drop by applying the Euler-Lagrange equation with a Lagrange multiplier μ, which represents the chemical potential. If the drop has spherical symmetry the density must satisfy

$$2rn\frac{\mathrm{d}^2n}{\mathrm{d}r^2} + 4n\frac{\mathrm{d}n}{\mathrm{d}r} - r\left(\frac{\mathrm{d}n}{\mathrm{d}r}\right)^2 = 16\left(\frac{3\pi^2}{\nu}\right)^{2/3} rn^{8/3} - 40A_{3D}rn^{9/4} - 32\mu rn^2. \quad (2.18)$$

The boundary conditions are specified at the centre of the drop, where the density

takes the equilibrium homogeneous MFEG value and the density is smooth, namely $n(0) = \bar{n}$ and $n'(0) = 0$. The differential equation Eqn. (2.18) cannot be solved analytically for $n(\mathbf{r})$, but a solution, $n(\mathbf{r}) = \bar{n}$, exists for $\mu = 0$ which corresponds to the homogeneous MFEG, that is a drop containing an infinite number of electrons. Before solving the differential equation numerically, two approximate schemes are developed, one that applies near the drop centre and the other near the drop edge, and their predictions are compared with existing density profile forms.

Near the centre of the drop a perturbation solution about the equilibrium density, $n(\mathbf{r}) = \bar{n} + \Delta n(\mathbf{r})$ where $\Delta n(\mathbf{r}) \ll \bar{n}$, is considered. The solution to Eqn. (2.18) for the density is then

$$n(r) = \bar{n} + \frac{8\mu\bar{n}}{Q^2} \left(1 - \frac{\sinh(Qr)}{Qr} \right). \tag{2.19}$$

This density profile is characterised by an exponential reduction of the density away from $\bar{n}$ at the centre. The energy Q^2 is physically the rate of change of energy per unit volume with respect to changing particle density, with

$$Q^2 = \frac{64}{3} \left(\frac{3\pi^2}{\nu} \right)^{2/3} \bar{n}^{2/3} - 45A_{3D}\bar{n}^{1/4} - 32\mu. \tag{2.20}$$

The second approximation scheme applies in the drop tail where electron density is low, $n(\mathbf{r}) \ll \bar{n}$. The term containing the chemical potential is disregarded as it is arbitrarily small for the large drops under investigation, the non-interacting and interacting energy terms contain higher powers of density so are negligibly small. In this regime the solution to Eqn. (2.18) is

$$n(r) = \begin{cases} n_0 \left(\frac{1}{r} - \frac{1}{r_0} \right)^2 & r < r_0, \\ 0 & r \geq r_0. \end{cases} \tag{2.21}$$

Here n_0 and r_0 are variational parameters which must be fitted to a numerical solution. This analytic form shows that the electron-hole drop has a definite outer radius r_0, which is approached parabolically, it is also noted that in the drop tail

the solution obeys the differential equation

$$\frac{1}{r^2}\frac{\mathrm{d}}{\mathrm{d}r}\left(r^2\frac{\mathrm{d}n^{1/2}}{\mathrm{d}r}\right) = \nabla^2 n^{1/2} = 0\,. \tag{2.22}$$

If electron density is mapped onto a wave function ψ through $n = |\psi|^2$ then the solution Eqn. (2.21) obeys Schrödinger's equation at low energy, that is $\nabla^2\psi = 0$. The implied Schrödinger equation is for a low density MFEG with negligible interaction between electrons due to their large separation, consistent with the original assumption of low density in the drop tail.

Previous studies of electron-hole drops [78, 91, 94] had a solution with the same exponential form both inside and outside of the drop, our inner functional form, an exponential, agrees with previous work [78, 91, 94], but our outer functional form, a quadratic-like polynomial, does not agree with the exponential decay seen in previous work. However, at the outside of the drop density is low and the arguments of Sec. 2.2.3 show the many flavour theory, which requires that the density satisfies $n \gg 0.03\nu$, does not apply here. The other theories [78, 91, 94] also do not apply in the low density region so both the many-flavour and previous theories fail to agree only where they are not applicable.

Using just the solution for the density in the drop tail Eqn. (2.21), a reasonable analytical approximation for the density profile of the whole drop is

$$n(r) = \left(\frac{1}{n_0(1/r - 1/r_0)} + \frac{1}{\bar{n}}\right)^{-1}\,. \tag{2.23}$$

This solution has the correct functional form at both the inside $(n(r) \to \bar{n})$ and outside of the drop and extrapolates smoothly in between. It can be fitted to the actual solution using parameters n_0 and r_0. However, the general differential equation is solved numerically giving the density profile shown in Fig. 2.3. The numerical solution is well approximated in the inner and outer regions by Eqn. (2.19) and Eqn. (2.21) respectively, and the model Eqn. (2.23) provides a good fit to the numerical solution, having just a slightly too shallow gradient around the median density but it agrees at both the centre and outside of the well.

To allow us to compare properties of electron-hole drops predicted using many-

Figure 2.3: The density profile of a 12 flavour electron-hole drop with density parameter $r_\mathrm{s} = 1$. The numerical solution is shown by the dotted line, analytical approximations to the inside (outside) of the drop by the dashed (dot-dashed) lines, and a best fit model fitted to the numerical solution by the solid line.
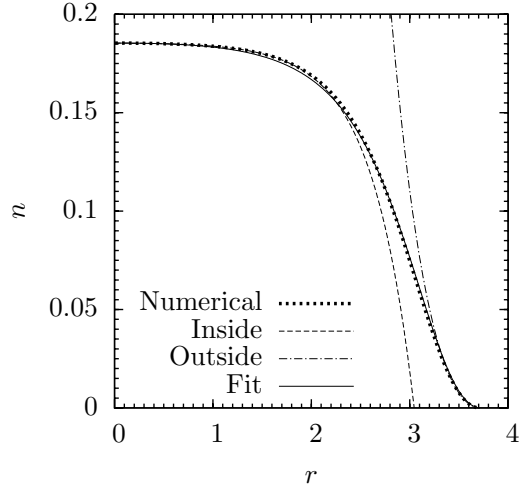
Figure 2.4: The surface tension γ of the 12 flavour drop of radius r_m is shown using the solid line and pluses based on the left-hand y-axis. The variation of the surface thickness D is shown using the dashed line and crosses based on the right-hand axis, each point represents a separate simulation.
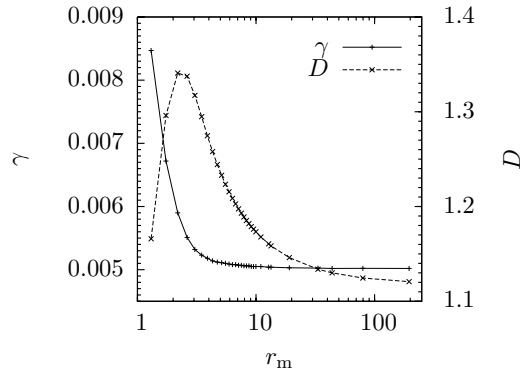
flavour theory with other work [78, 94], one can characterise the electron-hole drop properties through its surface thickness D and tension γ. The surface thickness D is the width over which the density falls from $90\,\%$ to $10\,\%$ of its homogeneous equilibrium value $\bar{n}$. The total surface energy is the difference between the energy per unit area of the MFEG in the drop and the energy of the same number of particles at equilibrium density in a homogeneous system. The surface tension γ is the total surface energy divided by the characteristic drop surface area, here taken to be the area of the spherical surface at the median density, which corresponds to a characteristic drop radius r_m. The results of numerical calculations in Fig. 2.4 show both the surface tension and surface thickness of the drop tend to constant values as the drop size increases. For large drops the boundary becomes approximately flat so the surface thickness becomes independent of drop radius, as does the surface tension since its major contribution comes from the drop boundary. We now examine the surface thickness and tension more carefully in turn.
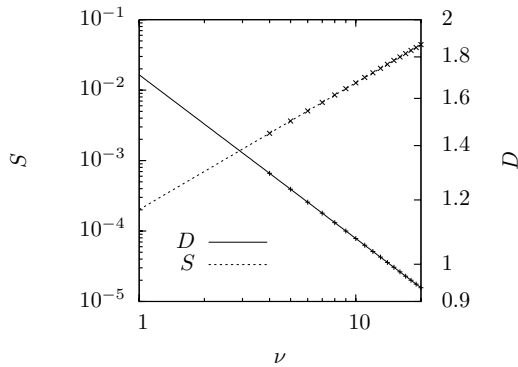
Figure 2.5: The variation of surface tension (dashed line and crosses) and surface thickness (solid line and pluses) with number of flavours present, the straight line fits are used to give the exponents of the scaling parameters.

To derive an approximate expression for the surface thickness we use the analytical approximation Eqn. (2.19) to the density profile of the inside of the drop, which gives the density reduction from the drop centre

$$\Delta n(r) = -\frac{4\mu\bar{n}}{Q^{3/2}r}e^{Qr}\,. \tag{2.24}$$

From this, the surface thickness D over which density falls from $90\,\%$ to $10\,\%$ is given in the large drop limit $r_{\mathrm{m}} \gg D$ by

$$D \approx \frac{\ln 9}{Q}\,. \tag{2.25}$$

In the given example in Fig. 2.3 (12 flavours) this predicts that the surface thickness is $D \approx 0.8a_0^*$, which is of similar size to the result found by numerical solution of Eqn. (2.18) of $\sim 1.1a_0^*$, but indicates that the approximation for surface thickness in Eqn. (2.25) is not able to produce accurate results. The values for surface thickness of drops found using the many-flavour theory can be compared with results from other approximations. For the six flavour gas in the large drop limit the many-flavour theory approximation Eqn. (2.25) predicts a thickness of $1.2a_0^*$, and exact numerical integration of the many-flavour theory Eqn. (2.18) predicts thickness $1.6a_0^*$. The silicon six flavour result of Kalia and Vashishta [78] has a surface thickness of $1.6a_0^*$, which is in good agreement with the many-flavour result.

Having used many-flavour theory to predict the density profile and surface thickness of an electron-hole drop, it is interesting to examine their scaling relationships with number of flavours. This is because the scaling relationships

can be experimentally probed [76] by comparing the surface thickness before and after putting the material under a strain which reduces the valley degeneracy, for example in silicon from six to two flavours. These scaling relations will also allow the many-flavour results to be further compared with previous theoretical work. In Sec. 2.2.2 it was shown that the expected MFEG uniform density is $\bar{n} \propto \nu^{8/5}$, and from Eqn. (2.20) $Q^2 \propto \nu^{2/5}$, which with Eqn. (2.25) predicts surface thickness to scale as $D \propto \nu^{-1/5}$. This scaling prediction for surface thickness can be compared with numerical results for the variation of surface thickness with number of flavours in Fig. 2.5, found by solving the differential equation Eqn. (2.18). The coefficient for surface thickness $D \propto \nu^{\alpha}$ is $\alpha = -0.19995(7)$ in good agreement with the predicted value of $-1/5$. We can also qualitatively compare our scaling result with numerical results [78, 94] from studies of the electron-hole drop in silicon. These studies compared results for silicon found at the unstrained six flavour with the results at two flavours to attempt to model the effect of stress reducing valley degeneracy. Though two flavour calculations cannot be accurately given by the many-flavour theory, the qualitative variation of surface tension and surface thickness should be. The variation of surface thickness with number of flavours $D \propto \nu^{-1/5}$ is weak, for silicon from six to two flavours the many-flavour theory, assuming it is valid, predicts that the thickness increases by a factor of 1.2. This compares reasonably with the numerical results of Ref. [78], which predicts an increase in surface thickness by a factor of ~ 1.1.

The dominating contribution to surface energy is at the boundary of the drop so the surface tension in large drops is approximately the gradient term in the energy density, Eqn. (2.16) (the main contribution to the surface tension) multiplied by the surface thickness D

$$\gamma \approx \frac{(\nabla n)^2}{8\bar{n}} D \approx \frac{\bar{n}}{8D} \,, \tag{2.26}$$

where we use the additional approximation $\nabla n \approx \bar{n}/D$. Finally, with the relationship found above, $D \propto \nu^{-1/5}$, and $\bar{n} \propto \nu^{8/5}$ found in Sec. 2.2.2, this predicts surface tension varies with number of flavours as $\gamma \propto \nu^{9/5}$. The numerical results of Fig. 2.5, found by solving the differential equation Eqn. (2.18) exactly, predict a

coefficient for $\gamma \propto \nu^\alpha$ of $\alpha = 1.8004(3)$ in good agreement with the analytical result, $9/5$. For silicon, reducing the number of flavours from six to two, the above result predicts that surface tension reduces by a factor of 7. This qualitatively agrees with the variation seen by Refs. [78, 94] of a reduction by a factor of 3, though comparison is difficult due to the presence of holes and there being too few flavours present for the many-flavour theory to be fully applicable.

2.5 Conclusions

This chapter describes a new formalism for calculating the behaviour of a MFEG. In the many-flavour limit the Fermi momentum reduces as $p_\mathrm{F} \propto \nu^{-1/3}$ so is small compared with the momenta associated with the strongest interactions. Intra-valley interactions are more significant than inter-valley.

The behaviour of a homogeneous MFEG in the limit of many-flavours was derived. Specifically the exact interacting energy per particle is $E_\mathrm{int} = -0.574447(E_\mathrm{h}^* a_0^{*3/4} m^{*1/4}) n^{1/4}$; making it energetically favourable for the MFEG to be dense. The formalism was found to apply with as few a six flavours over the density range $0.03\nu \ll na_0^{*3} \ll 0.005\nu^4$.

The MFEG has short characteristic length-scales which motivates a LDA. A gradient expansion of the energy density with the lowest order term $|\nabla n|^2/8n$ was derived, which was applied to electron-hole drops to study their density profile and surface properties. Surface thickness was found to scale as $D \propto \nu^{-1/5}$, surface tension as $\gamma \propto \nu^{9/5}$.

In Chp. 3 [2] we compare our analytical results with those from computer simulations to verify our findings for the uniform MFEG, its polarisability and the gradient expansion. This allows the limits over which the many-flavour limit applies to be derived more accurately, which in turn enables the formalism to be applied to more physical systems.

Chapter Three

Diffusion Monte Carlo study of a valley degenerate electron gas and application to quantum dots

I N this chapter a MFEG in a semiconductor with a valley degeneracy ranging between 6 and 24 is analysed using Diffusion Monte Carlo (DMC) calculations. The DMC results compare well with an analytic expression derived in Chp. 2 for the total energy to within $\pm 1\,\%$ over an order of magnitude range of density, which increases with valley degeneracy. For Bi_2Te_3 (six-fold valley degeneracy) the applicable charge carrier densities are between $7 \times 10^{19} cm^{-3}$ and $2 \times 10^{20} cm^{-3}$. DMC calculations distinguished between an exact and a useful approximate expression for the 24-fold degenerate MFEG polarisability for wave numbers $2p_F < q < 7p_F$. The analytical result for the MFEG is generalised to inhomogeneous systems by means of a gradient correction, the validity range of this approach is obtained. Employed within a density-functional theory calculation this approximation compares well with DMC results for a quantum dot.

The material making up this chapter was recently published in Conduit and Haynes [2].

3.1 Introduction

Good quantum numbers, that describe conserved quantities as a quantum system evolves, derive their significance from their connection to the powerful conservation laws of physics. In addition to the familiar examples of spin and crystal momentum, under some circumstances electrons in solids can have an additional quantum number that distinguishes them, which we call the *flavour*; we denote the total number of flavours by ν. One example of such a system are semiconductors and semimetals that have degenerate conduction-band valleys, where the flavour denotes the electron's valley. Examples of multi-valley semiconductors include Ge, which as shown in Fig. 3.1 has four degenerate valleys (N.B. not eight, as valleys at the Brillouin zone vertices overlap), Si has six degenerate valleys, a Ge-Si alloy has ten degenerate valleys, and $Pb_{1-x-y}Sn_xMn_yTe$ has twelve valleys in the Σ band [73]. The system has been experimentally realized as an electron-hole liquid that forms in drops [1, 71]. In these systems the number of flavours (the number of valleys) is well defined and there are strong Coulomb interactions between particles which motivates the analysis. This is in contrast to several other systems in which the number of flavours is poorly defined such as heavy fermions [95–97], charged domain walls [98], a super-strong magnetic field [72], and spin instabilities [99, 100]; or where the number of flavours is well defined but interactions between particles are weak such as ultracold atoms in optical lattices [101–103].

The properties of a MFEG in a semiconductor were first studied analytically for the normal phase by Andryushin et al. [71], and for the superconducting phase by Cohen [105]. In Chp. 2 [1] we extended the MFEG analysis by finding an energy functional and gradient expansion, which allowed the study of inhomogeneous systems. However, the analytical treatment was limited to consider the same contributions to the energy as in the random phase approximation (these contributions dominate in the many-flavour limit). To go further requires numerical calculations, the only example of which for a MFEG to date [104] used a self-consistent approach for the local field correction formulated by Singwi et al. [122] Singwi, Tosi, Land & Sjölander (STLS), see also Ref. [123]. The method was later applied to charge impurities by Bulutay et al. [124]. The calculations of Ref. [104]
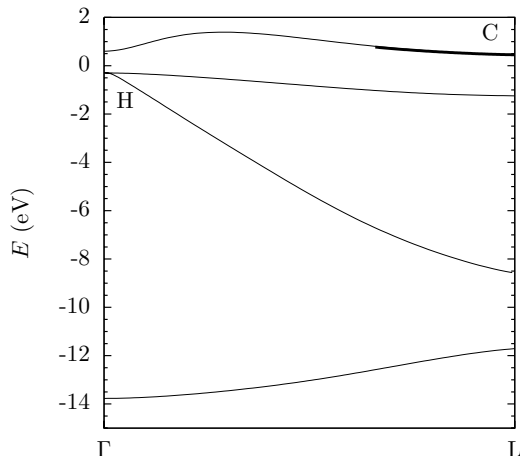
Figure 3.1: The Ge band-structure in the [111] direction calculated using a plane-wave pseudopotential method [106]. The Fermi energy is at $E = 0$eV; below are valence bands with the holes centred around H, above are conduction bands. The first conduction band valley is highlighted in bold, low-lying conduction-band electrons are centred around C.

were performed for $\nu \leq 6$, too few flavours to gauge the applicability of the analytic many-flavour approximation, which in Chp. 2 [1] we estimated to apply at around six or more flavours.

In this chapter we follow the suggestion of Gold [104], and present the results of what are expected to be more accurate DMC [15, 125–127] calculations on the MFEG for $\nu \leq 24$, which should allow us to verify the analytical MFEG approach. We then examine aspects of the many-flavour approximation that have not yet been studied computationally: in Sec. 3.4 we compare the analytical density-density response function derived in Sec. 3.1.2 with that predicted using DMC. Once verified this allows us in Sec. 3.5 to employ a gradient expansion within DFT to find the ground state of a quantum dot, we compare results with DMC calculations and examine the validity of the gradient expansion.

We adopt the atomic system of units: that is $e^2 = \hbar = m = 1/(4\pi\epsilon_0) = 1$. The mass $m = m_{\mathrm{e}}m^*$ is defined to be the electron mass, m_{e}, multiplied by a dimensionless effective mass m^* appropriate for the conduction-band valleys, which when $m^* = 1$ will recover standard atomic units. We assume the valleys all have the same dispersion profile and so the same effective mass, Andryushin et al. [71] outlined a method of calculating a scalar effective mass for anisotropic valleys. With the above definitions, energy is given in terms of an exciton $E_{\mathrm{h}}^* = E_{\mathrm{h}}m^*$, where E_{h} is the Hartree energy, and length $a_0^* = a_0/m^*$ in terms of the Bohr radius a_0. To denote density we use both the number density of conduction-band electrons n and the Wigner-Seitz radius r_{s}.

Before presenting the numerical results, to orient the discussion, we describe the basic physics of the MFEG and review the analytical results of Chp. 2 [1] that will be computationally verified in this chapter.

3.1.1   Introduction to a MFEG

In a low temperature MFEG, the number of flavours ν, number density of conduction-band electrons n, and Fermi momentum p_F are related through

$$n = \frac{\nu p_\mathrm{F}^3}{3\pi^2} \,.$$
(3.1)

At fixed electron density, the Fermi momentum reduces with increasing number of flavours as $p_\mathrm{F} \propto \nu^{-1/3}$, so each Fermi surface encloses fewer states. The semiconductor hole band-structure often has a single valence-band minimum at the Γ point, such as in Ge, see Fig. 3.1, hence we assume the holes are heavy and are uniformly distributed, providing a jellium background.

For a constant number density of particles, the density of states at the Fermi surface, g, rises with increasing number of flavours as $g \propto \nu\sqrt{E_\mathrm{F}} \propto \nu^{2/3}$. Therefore, the screening length estimated with the Thomas-Fermi approximation [9] is $\kappa^{-1} = (4\pi e^2 g)^{-1/2} \propto \nu^{-1/3}$, and the ratio of the screening to Fermi momentum length-scale varies with number of flavours as $p_\mathrm{F}/\kappa \propto \nu^{-2/3}$. In the many-flavour limit $\nu \gg 1$, the screening length is much smaller than the inverse Fermi momentum, $\kappa^{-1} \ll p_\mathrm{F}^{-1}$, and so the dominant electron-electron interactions have characteristic wave vectors which obey $q \gg p_\mathrm{F}$. This is in direct contrast to the RPA where $p_\mathrm{F} \gg \kappa$, although in both the many-flavour and the RPA, the same Green function contributions with empty electron loops dominate diagrammatically [1, 71]. As is outlined in App. A.6, these diagrams contain the greatest number of different flavours of electrons, and as $\nu \gg 1$ therefore have the largest matrix element. Since $q \gg p_\mathrm{F}$, the typical length-scales of the MFEG are short, this indicates that a LDA could be applied. This motivation is in addition to the usual reasons for the success of the LDA in DFT [11], namely that the LDA exchange-correlation hole need only provide a good approximation for the spherical average of the exchange-correlation hole and obey

the sum rule [119].

3.1.2 Polarisability

In the many-flavour limit the exact result for the polarisability of a MFEG at wave vector $\mathbf{q}$, and Matsubara frequency ω is [1, 71, 112]

$$
\Pi_0(\omega,q) = \frac{\nu}{2\pi^2} \left\{ \frac{\omega}{q} \left[\tan^{-1}\left(\frac{q/2 + p_{\mathrm{F}}}{\omega/q} \right) - \tan^{-1}\left(\frac{q/2 - p_{\mathrm{F}}}{\omega/q} \right) \right] \right.
$$
$$
\left. - \frac{(\omega/q)^2 + p_{\mathrm{F}}^2 - q^2/4}{2q} \ln\left[\frac{(\omega/q)^2 + (q/2 + p_{\mathrm{F}})^2}{(\omega/q)^2 + (q/2 - p_{\mathrm{F}})^2} \right] - p_{\mathrm{F}} \right\}, \tag{3.2}
$$

which in the many-flavour limit is approximately

$$
\Pi_0(\omega,q) = -\frac{n}{(\omega/q)^2 + q^2/4} + \mathcal{O}(\nu^{-2/3}). \tag{3.3}
$$

This quantity governs the density-density response of the MFEG so is important to verify. Since Eqn. (3.3) has a simple form it can be used to calculate further properties of the MFEG [1], such as homogeneous energy in Sec. 3.1.3 and the gradient expansion in Sec. 3.1.4, which further motivates its numerical verification.

3.1.3 Homogeneous energy

Starting from the approximate expression for polarisability, Eqn. (3.3), it can be shown that the total energy of a MFEG, including all the exchange and correlation contributions is [1]

$$
E = \frac{3}{10} \left(\frac{3\pi^2}{\nu} \right)^{2/3} n^{5/3} - \overbrace{A_{3\mathrm{D}} n^{5/4}}^{E_{\mathrm{int}}}, \tag{3.4}
$$

where $A_{3\mathrm{D}} = \Gamma(-5/4)\Gamma(3/4)/(2\pi^{5/4})(E_{\mathrm{h}}^* a_0^{*3/4}) \approx 0.574447(E_{\mathrm{h}}^* a_0^{*3/4})$ and E_{int} denotes the interacting energy (which would be zero if electron-electron interactions were ignored).

In Chp. 2 [1] it was suggested that this relation for the total energy applies over a density range, at 99% accuracy, $0.03\nu \ll na_0^{*3} \ll (0.074\nu)^4$, which widens with

number of flavours as ν^4 (see also Ref. [71]). Considering the number of flavours where the range of validity vanishes indicates that the many-flavour limit will apply if there are ten or more flavours. An alternative estimate for the density range is found in Sec. 3.4.1 by comparing the analytical result with DMC calculations.

3.1.4 Gradient correction

The applicability of the LDA in a MFEG motivates the search for a gradient expansion to the energy Eqn. (3.4) as a way to analyse inhomogeneous systems such as electron-hole drops and quantum dots. The typical momentum transfer in the MFEG is $q \sim 4(\hbar a_0^{*-1/4})n^{1/4}$, which defines the shortest length-scale over which a LDA can be made, therefore, the maximum permissible gradient in electron density is $|\nabla n|_{\max} \sim qn \sim 4(\hbar a_0^{*-1/4})n^{5/4}$. A gradient expansion will break down for phenomena with short length-scales, for example mass enhancement [128]. If electron density is smoothly varying then starting from Eqn. (3.3), the gradient correction to the energy for a MFEG is [1]

$$E = E_0 + \frac{1}{8}\frac{(\nabla n)^2}{n} \, , \tag{3.5}$$

where E_0 is the energy of a homogeneous MFEG with density n, see Eqn. (3.4). As discussed in Sec. 3.1.1, this gradient expansion would be useful for DFT calculations and so its computational verification is important.

3.2 Computational method

In this section we briefly describe the two computational methods that we used, Variational Monte Carlo (VMC) and DMC [15], which are introduced in more detail in App. A.4. They are both QMC methods, chosen since DMC gives the exact ground state energy subject to the fixed node approximation, and both are expected to give more accurate results than the STLS approach used by Gold [104].

The VMC method uses a normalisable and differentiable trial wave function Ψ_T, of the form discussed below. The Metropolis algorithm [129] is used to sample the wave function probability density $|\Psi_T|^2$ using a random walk, and make an estimate

of the local energy $E_L(\mathbf{r}) = \Psi_T(\mathbf{r})^{-1} \hat{H} \Psi_T(\mathbf{r})$. In order to obtain the ground state one could minimise the spatial average of the local energy with respect to the free parameters in the trial wave function. However, it is computationally more stable to minimise the variance in the estimates of the local energy. As VMC obeys the variational principle by construction, it yields an upper bound to the true ground state energy.

The more accurate DMC algorithm is a stochastic method that begins with a trial or guiding wave function, in this case the optimised VMC trial wave function. The DMC method is based on imaginary time evolution, which when using the operator $e^{-t(\hat{H} - E_T)}$ projects out the ground state wave function from the trial wave function, and yields an estimate of the ground state energy, E_T. The nodal surface on which the wave function is zero (and across which it changes sign) is fixed [127, 130] to be that of the trial wave function, this ensures that the fermionic exchange symmetry is maintained. The DMC algorithm produces the exact ground state energy subject to the fixed node approximation, and is also variational so gives an accurate upper bound to the true ground state energy once the population control bias and finite time-step bias are eliminated. The algorithm used closely follows that described in Ref. [131].

In our QMC calculations we use a Slater-Jastrow [15, 132, 133] trial wave function. The Slater part of the wave function is a product of determinants, each one corresponding to a different electron spin or flavour. Each determinant is over the spatial orbitals of electrons occupying the lowest energy levels. The determinant changes sign when rows or columns are swapped, this ensures that the wave function is antisymmetric under exchange of electrons with the same flavour and spin. The Slater wave function itself is not the ground state of an interacting electron gas, so to improve the wave function, variational degrees of freedom that account for two-body correlations are included within a Jastrow factor. The Jastrow factor is symmetric under particle exchange so does not alter the particle exchange symmetry of the wave function. Furthermore, the Jastrow factor is always positive so does not alter the wave function nodal surface. The Jastrow factor contains a two-body polynomial term $u(r_{ij}) = F(r_{ij}) \sum_{l=2}^{6} \alpha_l r_{ij}^l$, a power series form [133] in electron separation

r_{ij} with optimisable parameters, α_l. The term $F(r_{ij})$ ensures that the Kato cusp conditions are satisfied [134]. To ensure that electron-electron correlations do not extend beyond the simulation cell, the term is cutoff at the Wigner-Seitz radius. To treat longer-ranged correlations, the Jastrow factor includes a two-body plane-wave expansion, $p(\mathbf{r}_{ij}) = \sum_{A,\mathbf{G}_A} a_A \cos(\mathbf{G}_A \cdot \mathbf{r}_{ij})$. Those reciprocal lattice vectors, $\{\mathbf{G}_A\}$, that are related by the point group symmetry (denoted by A) of the Bravais lattice share the same optimisable parameters, a_A. To ensure accuracy we checked the stability of the VMC results when the expansion order of the u and p terms was increased. At all densities the Jastrow factor optimised cutoff lengths took the maximum allowed value (the Wigner-Seitz radius).

The DMC calculations were performed with 57 different reciprocal lattice vectors and, following Ortiz and Ballone [135], Ceperley [117], and Ceperley and Alder [118], further VMC calculations were performed at other system sizes (27, 33, 57, and 81 reciprocal lattice vectors) to derive the parameters to extrapolate the DMC energy to infinite system size. Additionally, all the DMC results were extrapolated to have zero time-step between successive steps in the electron random walk. In DMC simulations the acceptance probability of a proposed step in the random walk exceeded 99 %. We used 300 DMC configurations, comparable to the 200-300 used by Ortiz and Ballone [135], and checked for population control bias by ensuring that ground state energy estimates did not vary with a changing number of configurations. All the QMC calculations were performed using the CASINO computer program [136].

3.3   Homogeneous MFEG

We start with the simplest possible system to analyse numerically, the homogeneous MFEG, this provides not only a suitable system to validate both theory (Sec. 3.1.3) and the QMC many-flavour calculations, but should also confirm the range of densities over which the many-flavour approximation applies. The 3D homogeneous electron gas ($\nu = 1$) has been studied before using QMC [117, 118, 135] and these studies provide a useful guide to the method we should follow.

To calculate the interaction energy E_{int} we subtracted the theoretical Thomas-Fermi kinetic energy from the DMC ground state energy (see Eqn. (3.4)). At each

of 6, 12, 18, and 24 flavours we performed five DMC calculations and interpolated to find where theory and DMC results agree to within $\pm 1\%$. Results in Fig. 3.2 show that for $\nu > 6$ the theory applies over at least an order of magnitude in density to an accuracy of $\pm 1\,\%$ – the theory can be applied at fewer flavours than expected. For fewer than ~ 12 flavours the valid logarithmic range of the theory increases with ν, the 18 and 24 flavour results show a dramatic increase in the range of validity, especially on the high density side. In the limit of many flavours ($\nu > 12$) the expected $99\,\%$ range of validity $0.03\nu \ll na_0^{*3} \ll (0.074\nu)^4$ is approximately consistent with the computationally predicted $\pm 1\,\%$ region, therefore the minimum number of flavours required for all aspects of the many-flavour theory to be valid is approximately ten.

For Si with $m^* = 1.08$ the many-flavour limit applies to an accuracy of $\pm 1\,\%$ for a charge carrier concentration between $4 \times 10^{23} \text{cm}^{-3}$ and $1 \times 10^{24} \text{cm}^{-3}$, this is greater than the typical maximum carrier density $\sim 1 \times 10^{21} \text{cm}^{-3}$ and so in Si the formalism is not applicable. In systems with a low effective mass, for example the $\nu = 6$ material Bi_2Te_3 used in thermoelectric cooling, which has $m^* = 0.06$ [137–139], the required charge carrier concentration is between $7 \times 10^{19} \text{cm}^{-3}$ and $2 \times 10^{20} \text{cm}^{-3}$, which compares favourably with the typical maximum carrier density $\sim 1 \times 10^{21} \text{cm}^{-3}$ and so the many-flavour limit formalism could be applied to low effective mass materials.

The STLS estimates for the ground state energy [104] at $\nu = 1$ were $\sim 3.4\%$ less negative than the DMC results of Ortiz and Ballone [135], and at $\nu = 6$ were $\sim 3.1\%$ less negative than our DMC results. This represents a significant difference between our and the STLS results when looking for the 1% range of validity, highlighting the need for the more accurate DMC calculations. The range of validity at $\pm 1\,\%$ up to at least 24 flavours is to the high density side of the minimum in the total energy seen in Fig. 3.2, but the minimum $n_{\min} \propto \nu^{8/5}$ lies within the region of validity for higher ν. $n_{\min}$ is the density expected to be seen in physical systems such as electron-hole drops, the good agreement of the theory with DMC results at this density indicates that the theory could be usefully applied to investigate the properties of physical systems, one example pursued in Chp. 2 [1] was the application to electron-hole

Figure 3.2: The lower panel shows the fractional difference of DMC interaction energy E_{DMC} from the model E_{int} with MFEG density n (and Wigner-Seitz radius r_s) for different numbers of flavours, the dotted lines show $\pm 1\%$ disagreement. The central panel bars highlight the numerical region of applicability, the gray shaded area represents the analytically predicted region of $\pm 1\%$ applicability. The upper panel shows the total energy for 6, 12, 18 and 24 flavour electron gases.
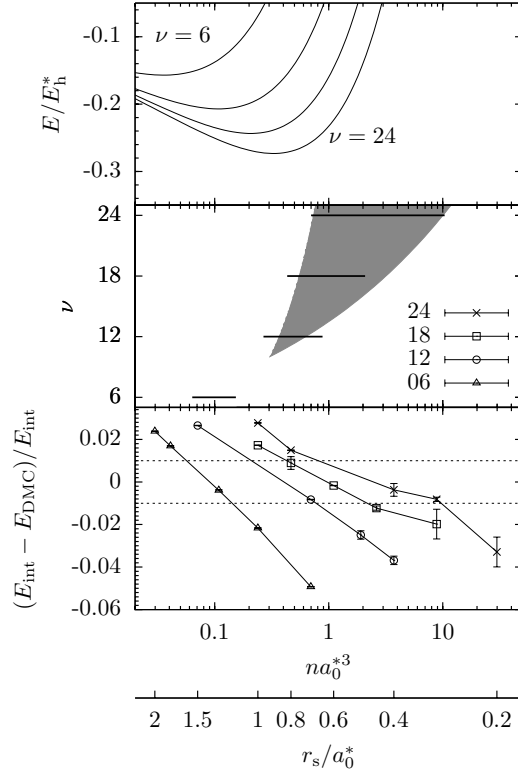
drops.

3.4   Static density-density response

Having verified the homogeneous system behaviour we may now proceed and computationally examine inhomogeneous behaviour through the static density-density (linear) response function Eqn. (3.3). The polarisability is an important quantity that was used in Chp. 2 [1] to develop both homogeneous theory and the gradient correction, the density-density response function itself also governs the electrical response properties, for example polarisation, screening, and behaviour in an external potential; it is therefore useful to verify this response before applying the theory to model systems. We examine $1/\epsilon(\mathbf{q})$, the quantity that is probed experimentally [140].

DMC has previously been used to find the static density-density response of single-flavour systems: Sugiyama et al. [141] applied the method to charged bosons, the density-density response of the electron gas was calculated by Moroni et al.

[142] (in two dimensions), and Bowen et al. [143] and Moroni et al. [144] (three dimensions). However, density-density response has not been studied numerically in a many-flavour system. Here we employ two methods to find the density-density response function. The more accurate and computationally efficient method of calculating the response is to examine the ground state energy, calculated using DMC. A VMC energy based estimate and an estimate using the induced electron density are used to check the accuracy of the trial wave function.

Before the results are described in Sec. 3.4.3, we outline the theory behind the two methods used to estimate the response, firstly in Sec. 3.4.1 by using the ground state energy variation, and secondly in Sec. 3.4.2 through the magnitude of the periodic density modulation.

3.4.1 Ground state energy variation

To calculate the density-density response we use a weak probe so that the density response is solely due to the properties of the homogeneous system. We apply a static ($\omega = 0$) monochromatic perturbative external potential $U(\mathbf{r}) = U_{\mathbf{q}} \cos(\mathbf{q} \cdot \mathbf{r})$ to the homogeneous MFEG, corresponding to the background charge having an additional sinusoidal variation $n_{\text{ext}}(\mathbf{r}) = n_{\mathbf{q}} \cos(\mathbf{q} \cdot \mathbf{r})$. The external potential and external charge are linked [141] through Poisson's equation by

$$n_{\text{ext}}(\mathbf{k}) = \frac{U_{\mathbf{q}} q^2}{8\pi} (\delta_{\mathbf{k},\mathbf{q}} + \delta_{\mathbf{k},-\mathbf{q}}). \tag{3.6}$$

We assume that different Fourier components are independent, the density response to an external potential with wave vector $\mathbf{q}$ and frequency ω is only at that wave vector and frequency so the induced charge is $n_{\text{ind}}(\mathbf{k}) = \left(\langle \hat{n}_{\mathbf{k}} \rangle_{U_{\mathbf{q}}} - \langle \hat{n}_{\mathbf{k}} \rangle_0 \right) (\delta_{\mathbf{k},\mathbf{q}} + \delta_{\mathbf{k},-\mathbf{q}})$. Here $\langle \hat{n}_{\mathbf{k}} \rangle_{U_{\mathbf{q}}}$ is the expectation value of the charge density Fourier component at wave vector $\mathbf{k}$ with an applied external potential $U_{\mathbf{q}}$, and $\langle \hat{n}_{\mathbf{k}} \rangle_0$ is the same but in the homogeneous case with no external potential. Linear response theory gives the static density-density response function as the ratio of the induced charge density

and the perturbing external charge density so

$$\frac{1}{\epsilon(\mathbf{q})} = 1 + \frac{8\pi}{U_{\mathbf{q}}q^2} \left(\langle \hat{n}_{\mathbf{q}} \rangle_{U_{\mathbf{q}}} - \langle \hat{n}_{\mathbf{q}} \rangle_0 \right) . \tag{3.7}$$

If the external potential is small relative to other typical energies the density response is determined solely by the properties of the homogeneous MFEG. We can expand in small $U_{\mathbf{q}}$ so that

$$\langle \hat{n}_{\mathbf{k}} \rangle_{U_{\mathbf{q}}} - \langle \hat{n}_{\mathbf{k}} \rangle_0 \approx U_{\mathbf{q}} \frac{\mathrm{d} \langle \hat{n}_{\mathbf{k}} \rangle}{\mathrm{d} U_{\mathbf{q}}} \bigg|_{U_{\mathbf{q}}=0} = U_{\mathbf{q}} \frac{\mathrm{d}^2 E}{\mathrm{d} U_{\mathbf{q}}^2} \bigg|_{U_{\mathbf{q}}=0} , \tag{3.8}$$

where the induced charge density is calculated by considering the dependence of the ground state energy E on the magnitude of the external field. Substituting this into Eqn. (3.7) gives an expression for the density-density response

$$\frac{1}{\epsilon(\mathbf{q})} = 1 + \frac{8\pi}{q^2} \frac{\mathrm{d}^2 E}{\mathrm{d} U_{\mathbf{q}}^2} \bigg|_{U_{\mathbf{q}}=0} . \tag{3.9}$$

To recover the density-density response function at a particular wave vector, several QMC calculations were performed at that wave vector for different amplitudes of the external field. A polynomial fit was made to the ground state energy so as to extract the second derivative. To investigate the lowest order polarisability the applied external field should be as small as possible yet still give statistically significant results, to ensure this we checked that the ground state energy showed only quadratic behaviour with applied field amplitude. A further convenient way to check the perturbing field is sufficiently small is to ensure the electric field of the external potential is less than the typical electric field strength between two neighbouring electrons, e/r_{s}^2.

3.4.2 Induced charge density measurement

As the external potential is perturbative we use the same plane-wave basis set as employed for the calculations on the homogeneous MFEG described in Sec. 3.3. To account for the modulating density, following Moroni et al. [142], Bowen et al. [143], and Moroni et al. [144] we introduce a new q term into the Jastrow factor of the

form

$$q(\mathbf{r}_i) = b \cos(\mathbf{q} \cdot \mathbf{r}_i) , \tag{3.10}$$

where b is an optimisable parameter, $\mathbf{r}_i$ the position of the ith electron, and the wave vector $\mathbf{q}$ corresponds to that of the perturbative external potential. As b is small, the charge density induced by the perturbative external potential is $n_{\text{ind}} \approx 2b \cos(\mathbf{q} \cdot \mathbf{r}_i)$. From Eqn. (3.6) and Eqn. (3.7) it follows that

$$\frac{1}{\epsilon(\mathbf{q})} = 1 + \frac{8\pi b}{q^2 U_{\mathbf{q}}} . \tag{3.11}$$

The optimised value of b was found by variance minimisation during a VMC calculation. The relationship then allows us to derive an estimate for the density-density response function for each separate $U_{\mathbf{q}}$, typically four values were averaged to give a final estimate for the density-density response.

3.4.3   Results

We chose to find the polarisability for a MFEG with $\nu = 24$ and $r_{\text{s}} = 0.6a_0^*$. This lies at the lower bound of the range of validity near to the minimum in the energy (see Fig. 3.2) at a density expected to be seen in physical systems. This density was also chosen since it had most of the polarisability curve $0.25 < 1/\epsilon \leq 1$ in the region of applicability $q \geq 2p_{\text{F}}$. Boundary conditions mean that the external potential must be periodic over the simulation cell, therefore the external potential wave vector $\mathbf{q}$ must be a reciprocal lattice vector. We checked that if the Jastrow factor q term wave vector was changed so that it was incommensurate with the external potential then following optimisation $b = 0$ within statistical errors; this verified the linear response assumption that Fourier components are independent.

The results of the calculation are shown in Fig. 3.3. The DMC results obtained by considering the variation in ground state energy (see Sec. 3.4.1) better fits the exact than approximate expression for the polarisability, and though error bars are large can distinguish between the two within one standard deviation. This shows that QMC results can exceed the accuracy of the approximation made in Eqn. (3.3),

Figure 3.3: The density-density response $1/\epsilon$ versus the wave vector $|\mathbf{q}|$ of a MFEG with $\nu = 24$ and $r_\mathrm{s} = 0.6a_0^*$. The solid curve shows the exact result $1/\epsilon_\mathrm{exact}$ (Eqn. (3.2)), the dotted curve the Eqn. (3.3) approximation. The shaded grey region $|\mathbf{q}|/2 < p_\mathrm{F}$ is where the many-flavour limit breaks down. The points show the values for the permittivity calculated from QMC results, the circle is from charge modulated, the triangle from VMC energy and the cross from DMC energy. The lower panel plots the actual response, the upper panel shows the deviation of response from the exact theoretical result Eqn. (3.2) with standard error bars.
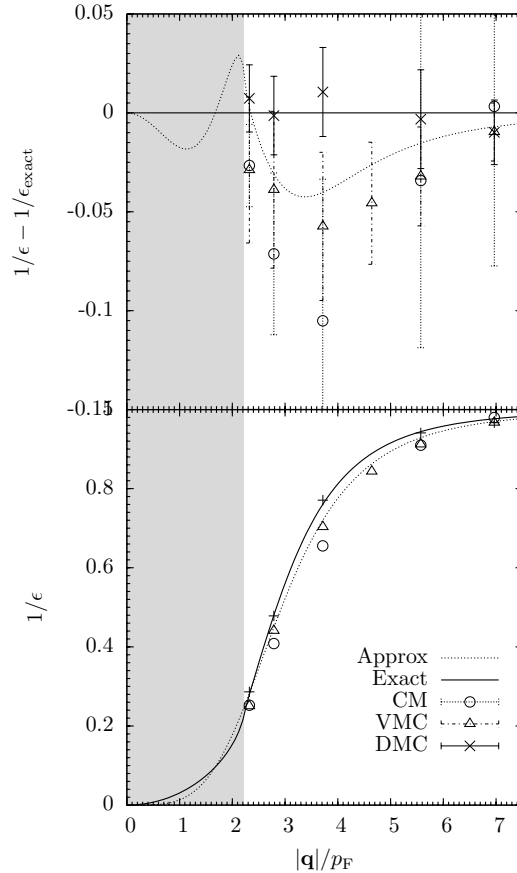
though that estimate remains useful. The positive agreement verifies the theory and confirms the accuracy of the CASINO simulations.

The ground state energies calculated by VMC were used in the same way as the DMC results to find the density response and provide a reasonable fit, though here error bars are large so comparison is difficult. Following the prescription in Sec. 3.4.2 we also derived values for the density-density response function using the charge density modulation at the wavelength of the perturbing potential, $U_\mathbf{q}$. These values agreed within statistics though carried a larger uncertainty than those derived using the ground state energy. Both of these alternative methods appear to underestimate the density-density response. These results are consistent, a smaller charge density response gives a smaller coefficient in the Jastrow factor q term and a smaller reduction in ground state energy. Nevertheless, the reasonable agreement of both VMC estimates and to the DMC results indicates that the trial wave function had an adequate nodal surface.

3.5 Gradient correction

It was important to verify the density-density response as it is a key component to the many-flavour formalism and could be applied to other many-flavour systems where density is expected to be inhomogeneous, for example junctions and the response to defects and impurities. Now that it has been verified, we may proceed to consider a quantity derived from it: the gradient expansion, Eqn. (3.5), which is also useful for analysing systems with inhomogeneous density. Once we have investigated the validity of such an expansion we can apply the formalism to quantum dots, chosen since they have a large controllable variation in electron density so should provide a good test of the gradient expansion. Quantum dots are commonly made in many-flavour semiconductor materials so can be modelled using a many-flavour formalism, and are a system in which there is current research interest.

Quantum dots [145, 146] have not previously been studied in the many-flavour limit though there have been several previous computational studies of a single-flavour electron gas confined in a quantum dot. Previous QMC simulations of quantum dots include Pollock and Koch [147], Harju et al. [148] performed VMC calculations for parabolically confined electrons in circular dots. Bolton [149] performed fixed-phase DMC simulations. Path-integral QMC calculations have also been performed [150–152], these showed poor agreement with results from exact diagonalisation [153]. Benedict et al. [154], Williamson et al. [155], Puzder et al. [156] all compared the optical band-gap between DMC calculations and results from other methods. For circular quantum dots Pederiva et al. [157] found the ground-state using both DMC, a local spin density approximation method, and Hartree-Fock, they then directly compared the ground-state energy, correlation energy, and spin density profiles. Ghosal et al. [158] also used DMC to investigate circular quantum dots. Quantum dots have successfully been investigated using DFT [157, 159–161], Pederiva et al. [157] found the local spin density approximation method predicted ground-state energies that were typically 2% greater than DMC energies, Ferconi and Vignale [159] obtained a 3% agreement between current-density-functional theory and exact diagonalisation results.

3.5.1   Method

Before describing the study of quantum dots using a many-flavour functional in detail we first outline the general strategy of the numerical calculations. Firstly, a DFT calculation using the many-flavour functional (including the gradient approximation) was performed using a plane-wave basis set. This produced an estimate of the ground-state energy and density according to the many-flavour theory. It also provided a trial wave function that was converted to a B-spline basis set and, with Jastrow factor, was optimised in a VMC calculation, in preparation for a DMC calculation. Finally, the DMC calculation gave a second estimate of the ground state energy and density, exact only for the fixed node approximation. This estimate was compared with the DFT calculation, and also gave an insight into the accuracy of the many-flavour theory.

Here we carried out simulations on a quantum dot with a harmonic external potential of the form $V = kr^2/2$, where r is the distance to the centre of the quantum dot containing a MFEG with 12 flavours. This potential was chosen as it is simple, continuous, realistic [162, 163], and has been used in previous computational studies [148, 157, 159–161, 164–166]. Filled shells in this potential correspond to $1, 4, 10, 20, 35, \ldots$ orbitals (whose degeneracy may be reduced by electron-electron interactions). In DFT we used a supercell containing a single dot to model the aperiodic system with periodic boundary conditions, in DMC non-periodic calculations with just a single quantum dot were performed. The cubic cell was large enough that the trial wave functions had reduced by at least a factor of 10^{-4} at its boundary.

Trial wave functions were generated using the DFT program 3Ddotdft, an extended version of DOTDFT [167]; the background theory behind the algorithms employed is described in App. A.5. The program used the many-flavour functional with gradient approximation so had energy density

$$\varepsilon(n(\mathbf{r})) = -A_{\text{3D}} n^{5/4} + \xi \frac{|\nabla n|^2}{8n} \,. \tag{3.12}$$

A new parameter ξ was introduced that multiplies the gradient term, which allowed

us to adjust its size; $\xi = 1$ gives the correct analytical expression, and $\xi = 0$ the functional without a gradient expansion.

The VMC simulations, run in CASINO, used a B-spline basis set [168, 169] because a localised basis set offers significant performance advantages over plane-waves. The wave function was optimised in VMC with a Jastrow factor containing the two-body polynomial u term and two-body plane-wave term p with the same form as used in Sec. 3.3 and Sec. 3.4, and a one-body electron-potential term $\chi(r_i) = F(r_i) \sum_{m=2}^{6} \beta_m r_i^m$ with F determining behaviour at the cutoff length, r_i the distance of the ith electron from the centre of the potential, and the β_m being optimisable parameters; we also note that the χ term has no central cusp.

The many-flavour functional incorrectly adds in the *self-interaction* energy of each electron to its own Coulomb potential. One way to correct for this is to add an additional term to the density functional [170, 171]. However, as the number of flavours is increased the ratio of the correct interaction ($\propto \nu^2$) to incorrect self-interaction ($\propto \nu$) increases as $\sim 2\nu - 1$ so in the many-flavour limit the self-interacting energy error may be neglected. To ensure the B-spline grid was sufficiently fine, we compared the trial wave function kinetic and external potential energy before and after conversion the B-spline basis set. We also checked the choice of DMC time-step was sufficiently small, the number of configurations was suitably large, and the simulation cell size was adequately large. On changing these variables the variation in the ground state energy was $\Delta E \approx 0.02 E_{\text{h}}^*$, sufficiently small to allow us to compare the ground state energy as the potential strength and gradient expansion coefficient were varied.

3.5.2   Results

We analysed a quantum dot containing a MFEG of 12 flavours and 4 bands (shells), containing a total of 96 electrons. This was chosen since it had a full shell so is expected to have a zero spin ground-state [146] that can be analysed with the many-flavour functional, was computationally feasible, and contained enough electrons to be in the LDA regime, where the many-flavour functional is expected to apply.

Two different investigations were carried out to probe effects of changing the
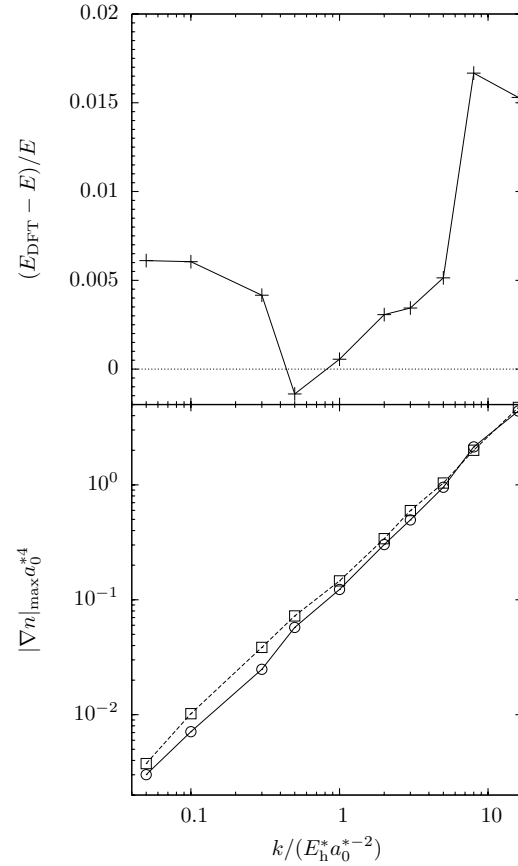
Figure 3.4: In the upper plot the crosses and solid line show the difference between DFT (E_{DFT}) and DMC (E) energies with varying external potential strength k, if agreement were exact, points would lie along the horizontal dotted line. In the lower plot the circles and solid line show the maximum density gradient of the dots with varying k, and the squares and dashed line the gradient at which the theory breaks down.

density gradient, firstly strength of the dot confining potential k was changed, and secondly the gradient expansion coefficient ξ was varied.

Varying the external potential strength k

At the strong external potential $k = 8$, corresponding to steep gradients, Fig. 3.4 shows the DFT energy is overestimated compared with the DMC result, indicating that the gradient approximation is not applicable and that the next order term in a gradient expansion is negative. Fig. 3.5 shows that the DFT density profile underestimates the true density towards the centre of the dot and overestimates density in the outer regions, indicating that the DFT functional does not favour steep enough gradients. This is consistent with the next term in the gradient expansion being negative. The breakdown corresponds to a coefficient of $\alpha \approx 1.8$ in $q_{\max} = \alpha(\hbar a_0^{*-1/4})n^{1/4}$, close to the $\alpha \approx 4$ which corresponds to the maximum contribution to the interacting energy.
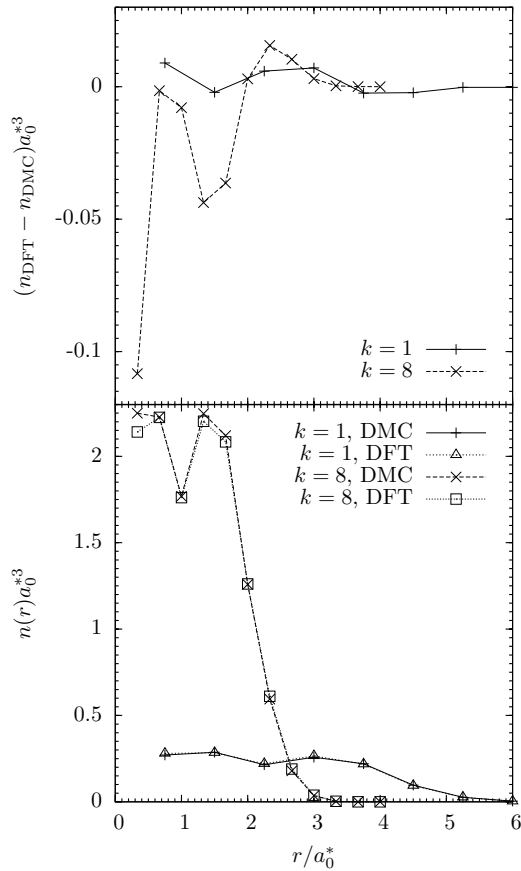
Figure 3.5: The lower panel shows the density profile of quantum dots estimated using both DFT and DMC at external potential strengths of $k = 1$ and $k = 8$. The difference between the DFT and DMC results at $k = 1$ and $k = 8$ is shown in the upper panel. The DMC statistical error is less than the size of the points.

At the intermediate potential $k = 1$ the DFT and DMC estimates of energy and the density profile agree, in this region the gradient approximation applies. The DFT density profile shows a slight over-density at the centre, consistent with self-interaction energy being included in the DFT calculation. At the weak potential $k = 0.1$ electron densities are low meaning the homogeneous interacting energy is outside of its region of applicability (see Fig. 3.2), therefore the DFT energy is an overestimate.

Varying the gradient term coefficient ξ

Fig. 3.6 shows results of simulations on dots, chosen to have a potential strength $k = 1$, which is at the centre of agreement of the previous results. The best agreement between the DFT and DMC ground state energy is at $\xi \sim 0.9$. This is in good agreement with the expected $\xi = 1$, the difference may be due to systematic errors such as the self-interacting energy or higher order gradient terms. As expected,

Figure 3.6: The upper panel shows, for dots with external potential strength $k = 1$, the density profile maximum gradient as a function of ξ. The central panel shows the variation of external potential DFT energy based on the primary y-axis using square points and the solid line, the secondary y-axis shows electron-electron DFT energy using crosses and the dashed line. The lower panel solid line shows the variation of DFT ground state energy with ξ, and the horizontal dotted line the ground-state energy predicted using DMC from the $\xi = 1$ trial wave function. The DMC statistical error is less than the size of the points.
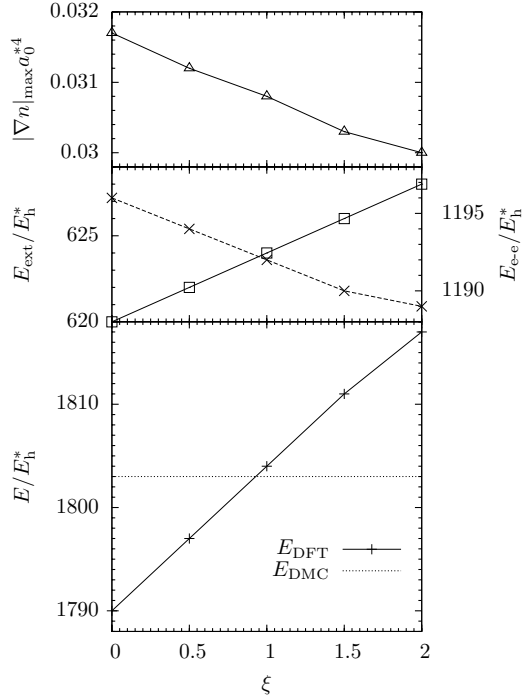
the energy is overestimated for dots with too large a gradient expansion term, and underestimated for dots with too small a gradient correction term.

The maximum gradient seen in the dot density profile decreases as ξ increases (see Fig. 3.6). The dot becomes more spread out so the external energy E_{ext} increases whilst the total electron-electron Coulomb energy $E_{\text{e-e}}$ decreases. Overall the total DFT energy increases. Three quantum dot electron density profiles for gradient term coefficients $\xi = 1$, 2, and 3 are shown in Fig. 3.7. Compared with the dot calculated with $\xi = 1$, the dot generated with no energy penalty for gradients, $\xi = 0$, has a high central and low outer density showing that it has a higher gradient in the density. Conversely dot with increased energy cost for gradients, $\xi = 2$, has a more shallow profile.

The density profiles seen in Fig. 3.5 and Fig. 3.7 can be further analysed in light of other theoretical studies of quantum dots reviewed in Ref. [146]. The density profile calculated using the many-flavour functional is not flat at the centre, but instead has correlation-induced density inhomogeneity evidenced by a characteristic minimum in the density at $r \approx 2a_0^*$. The intermediate density regime in which this occurs is consistent with the strong correlations causing a minimum in the total
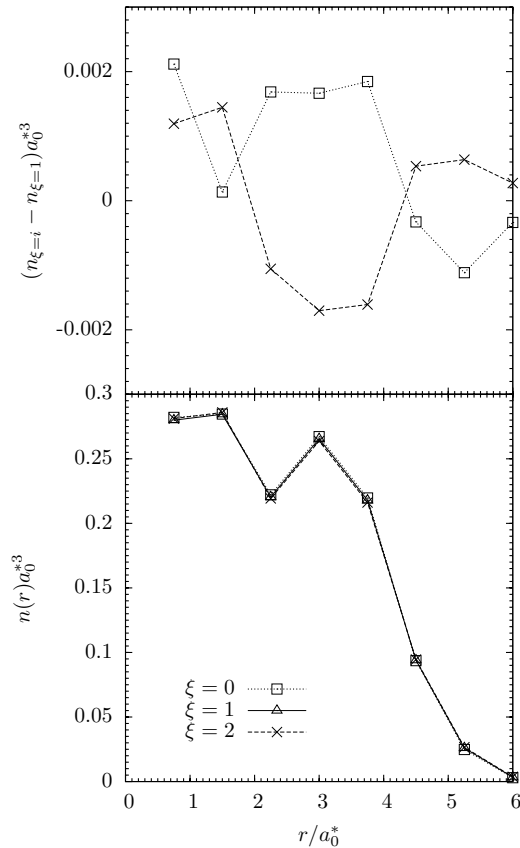
Figure 3.7: The upper panel shows the variation of the $\xi = 0$ (dotted line, squares) and the $\xi = 2$ (dashed line, crosses) DFT density profiles from the $\xi = 1$ DFT density profile. The lower panel shows DFT density profiles for $\xi = 0$, $\xi = 1$ (solid line, triangles), and $\xi = 2$ in a $k = 1$ dot.

many-flavour energy density found in Chp. 2 [1]. It is also akin to the intermediate density regime seen in other quantum dot systems [146, 152, 158, 172], in the high density limit the quantum dot has properties like a Fermi liquid with de-localised electrons [146, 152, 173], whereas in the low density limit the electrons become crystalline [146, 150, 152, 174–176] inside the dot. As the many-flavour functional was successful in predicting correlation-induced inhomogeneities, it could be used to investigate other many-flavour quantum dot effects including the Kondo effect in multi-valley semiconductors [177, 178], the reduction of valley degeneracy of coupled quantum dots [179–181], and harmonically trapped cold atoms with an additional quantum number denoting energy level [101–103, 182].

3.6 Conclusions

We have computationally verified the theory of the MFEG presented in Chp. 2 [1] using QMC simulations. In a homogeneous system, DMC estimates for the ground

state energy are consistent with theory and the theoretically estimated density range over which the theory applies is consistent with numerical results. The applicable density for Bi_2Te_3 ($\nu = 6$) corresponds to a charge carrier density between 7×10^{19}cm^{-3} and 2×10^{20}cm^{-3}.

The density response function for a MFEG with 24 flavours was found using three methods: density modulation predicted by VMC, and the variation in ground state energy predicted by VMC and also by DMC. The two VMC results underestimated the response $1/\epsilon$, but the DMC results agreed with theory and could distinguish between the exact and a useful approximate expression for polarisability.

We used a many-flavour functional including a local gradient approximation in DFT calculations of large quantum dots. The DFT calculation estimated the ground-state energy and wave function, which were verified by a DMC calculation. We found the high gradient breakdown of the expansion was at $q_{\max} \approx 1.8(\hbar a_0^{*-1/4})n^{1/4}$, the low gradient breakdown was consistent with the homogeneous MFEG lowest applicable density, and that the gradient expansion was applicable in the intermediate regime. The many-flavour functional, used as part of DFT calculations, could be a useful tool for analysing other multi-valley semiconductor systems.

Part II

Strongly correlated phases in atomic gases

In recent years a new way to study condensed matter physics has come to the fore: an ultracold atomic gas. The atomic gas now offers investigators an exquisite level of control over a many-body system, which allows them to be used to not only unravel long-standing mysteries in the solid state but also study phenomena that could not be envisioned in the solid state. In Chp. 4 we show how experimentalists could take advantage of this unique opportunity to for the first time observe the Fulde-Ferrel-Larkin-Ovchinnikov phase, we explore observable collective modes in Chp. 5, and in Chp. 6 demonstrate how an ultracold atomic gas could be used to shed new light on itinerant ferromagnetism.

Chapter Four

Superfluidity at the BEC-BCS crossover in two-dimensional Fermi gases with population and mass imbalance

I N this chapter we explore the zero temperature phase behaviour of a two-dimensional two-component atomic Fermi gas with population and mass imbalance in the regime of the BEC-BCS crossover. Working in the mean-field approximation, we show that the normal and homogeneous balanced superfluid phases are separated by an inhomogeneous superfluid phase of FFLO type. We obtain an analytical expression for the line of continuous transitions separating the normal and inhomogeneous FFLO phases. We further show that the transition from the FFLO phase to the homogeneous balanced superfluid is discontinuous leading to phase separation. If the species have different masses, the superfluid phase is favoured when the lighter species is in excess. We explore the implications of these findings for the properties of the two-component Fermi gas in the atomic trap geometry. Finally, we compare and contrast our findings with the predicted

phase behaviour of the electron-hole bilayer system.

The contents of this chapter draw upon the recent publication Conduit et al. [3].

4.1   Introduction

By controlling interaction through a magnetically-tuned Feshbach resonance, ultracold atomic Fermi gases have provided a versatile arena in which to explore pairing phenomena and superfluidity [37, 183, 184]. Already the crossover between the BEC phase of strongly bound diatomic molecules to the BCS phase of weakly bound Cooper pairs has been observed experimentally [183, 185–189]. In recent years, much attention has been focused on the phase behaviour of two-component Fermi gases with population imbalance [190–208], and generalised mass ratios between different species [206, 209–216]. The symmetry breaking effect of population and mass imbalance destabilises the condensate leading to an enriched phase diagram characterised by tricritical point behaviour with first order transitions separating normal and superfluid phases at low temperatures [217]. More detailed studies have shown that, on the weak coupling side of the crossover, the transition into a homogeneous superfluid phase at low temperatures is preempted by the development of an inhomogeneous superfluid phase [190, 195, 199, 218–224]. This is a manifestation of the FFLO phase predicted to occur in superconducting electron systems subject to a Zeeman field [43, 44, 225]. In the three-dimensional system, the FFLO phase is predicted to occupy only a small region of the phase diagram making its experimental identification in the atomic trap geometry challenging. Indeed, even in solid state systems, the FFLO phase has only recently been observed [226].

The potential for an FFLO instability at a single wave vector in a three-dimensional ultracold atomic gas with only population imbalance was explored by Hu and Liu [198] and Zhang and Duan [205]. They found a stable FFLO phase only on the BCS side of the resonance. Additionally, Wu and Yip [227] showed the three-dimensional system is unstable to FFLO superfluid currents, but these were not found in the non-uniform three-dimensional trap experiments of Shin et al. [228].

Lately, efforts have been made to explore the effects of population imbalance on pairing in two-component Fermi gases in two-dimensions. Although the phase

diagram of the zero temperature system has been explored in the regime of BEC-BCS crossover in the mean-field approximation [204], the potential for FFLO phase formation has not yet been addressed. By contrast, motivated by potential applications to strongly anisotropic layered systems, several theoretical studies have explored the potential for superconducting FFLO phase formation in two-dimensional electron systems [229–231]. A quasiclassical analysis by Combescot and Mora [232], involving a GL expansion of the free energy in Fourier components of the superconducting order parameter, found that the FFLO transition in two dimensions was continuous at low temperatures. In a separate study of condensation in electron-hole bilayers, Pieri et al. [230] argued that the FFLO phase can occupy a significant part of the two-dimensional phase diagram. Motivated by these investigations, and the potential impact on the atomic gas system, in the following we will investigate the potential for FFLO phase formation in the two-dimensional two-component Fermi gas addressing both population imbalance and generalised mass ratios.

In the context of ultracold atomic Fermi gases, a two-dimensional system can be experimentally realized by confining the gas with a one-dimensional optical lattice consisting of two counter-propagating laser beams [233–236]. These impose a periodic potential, with antinodes spaced every half wavelength. The interwell barrier energy, and therefore the tunnelling rate, depends on the laser intensity, which should be chosen to be much higher than the species chemical potential and the superfluid gap [237, 238]. This inhibits transfer of atoms between layers and the Fermi gas separates into stacked quasi two-dimensional layers. The depth of the optical potential can always be varied independently of the external harmonic trapping potential and species chemical potentials so it should always be possible to reduce the tunnelling rate sufficiently that the cold atom gas can be regarded as being two-dimensional gas. Within a layer, the short-ranged interaction of the atoms can be adjusted by exploiting a Feshbach resonance. It has been suggested [239] that due to the possible formation of dressed molecules a single band theory could incorrectly predict cloud size in the strong coupling limit. However, here we are interested in the weak coupling limit and the behaviour at the BEC-BCS crossover where we believe that a single band theory will encompass the essential

behaviour allowing us to capture the qualitative phase structure.

Finally, further motivation for the investigation of superfluidity in the mass imbalanced system comes from studies of exciton condensation in bilayer electron-hole systems. In recent years, attempts to realize a condensed exciton phase have focused on quantum well structures where electrons and holes are restricted to neighbouring two-dimensional layers [229–231]. The range of the Coulomb interaction between the particles can be shortened by introducing a screening layer. As with the two-component Fermi gas, the electron-hole system affords the possibility of tuning between a superfluid of tightly-bound pairs (excitons) to a condensate phase of an electron-hole plasma. Moreover, while one can, in principle, engineer a balanced electron-hole population, the effective masses of the electron and hole quasi-particles in the semiconductor are typically quite different. In GaAs, the ratio of the hole to electron mass is ca. $m_h/m_e = 4.3$. Condensation phenomena in mass imbalanced systems have also been explored in the context of quantum chromodynamics, where the particles represent different species of quarks [240].

The remainder of the chapter is organised as follows: In Sec. 4.2 we begin by deriving an expression for the thermodynamic potential in the mean-field approximation for the two-component Fermi gas allowing for the development of an inhomogeneous condensate phase. In Sec. 4.3 we use this result to elucidate the zero-temperature phase diagram of the system for a uniform order parameter both at fixed chemical potential and fixed number density. In Sec. 4.4 we explore the tendency of the system to condense into an inhomogeneous superfluid phase. In particular we combine the results of a GL expansion with the numerical analysis of the thermodynamic potential to infer the region over which the inhomogeneous phase persists. Finally, in Sec. 4.5, we examine the properties of the atomic Fermi gas in the harmonic trap geometry, concluding our discussion in Sec. 4.6.

4.2 Mean-field theory

Our starting point is a two-component Fermi gas with each species indexed by a pseudo-spin $\sigma \in \{\uparrow, \downarrow\} \equiv \{+1, -1\}$. The single-particle dispersion $\epsilon_{\mathbf{k},\sigma} = k^2/2m_\sigma$ depends on the different effective masses of the two species m_σ, throughout we set

$\hbar = 1$. Introducing the reduced mass, $1/m_R = (1/m_\uparrow + 1/m_\downarrow)/2$ and the mass ratio $r = m_\downarrow/m_\uparrow$ we have $m_\uparrow = m_R(1 + 1/r)/2$ and $m_\downarrow = m_R(1 + r)/2$. To enforce a population imbalance, each species must be associated with its own chemical potential, $\mu_\sigma = \mu + \sigma h$. With these definitions, one may see that the phase diagram of the system is symmetric under the transformation, $(h,r) \mapsto (-h,1/r)$.

In the following, we will focus on the zero temperature phase behaviour of the system as predicted by mean-field theory. In doing so, we will miss non-perturbative effects that appear at large mass ratios. In particular, when the ratio of masses is greater than 13.6, it is known that, in three-dimensions, two heavy and one light fermion can form a three-body weakly bound state [241–243]. Our analysis does not include the possibility of such a state.

To explore the regime of BEC-BCS crossover, we will focus our attention on a single-channel Hamiltonian describing a wide Feshbach resonance where the closed channel population remains small throughout [205, 244, 245]. The quantum partition function for the system can then be expressed as a functional field integral over fermionic fields ψ_σ and $\bar{\psi}_\sigma$, $\mathcal{Z} = \int e^{-S[\bar{\psi},\psi]}\mathcal{D}\psi\mathcal{D}\bar{\psi}$ (for further details see App. A.2), with the action

$$S\left[\psi,\bar{\psi}\right] = \int_0^\beta \mathrm{d}\tau \left[\sideset{}{'}\sum_{\mathbf{k},\sigma} \bar{\psi}_{\mathbf{k},\sigma} \left(\partial_\tau + \xi_{\mathbf{k},\sigma}\right) \psi_{\mathbf{k},\sigma} - \frac{1}{2} \sideset{}{'}\sum_{\mathbf{k},\mathbf{k}',\mathbf{q}} \bar{\psi}_{\mathbf{k},\uparrow}\bar{\psi}_{\mathbf{q}-\mathbf{k},\downarrow}V_{\mathbf{k}'-\mathbf{k}}\psi_{\mathbf{k}',\downarrow}\psi_{\mathbf{q}-\mathbf{k}',\uparrow}\right],$$

$$(4.1)$$

where V denotes the two-body interaction potential, $\beta = 1/k_B T$ is the inverse temperature, and the primed summation denotes a cutoff corresponding to the length-scale of the contact potential, k_c. Here, for brevity, we have set $\xi_{\mathbf{k},\sigma} = \epsilon_{\mathbf{k},\sigma} - \mu_\sigma$. Anticipating the development of pair correlations, as expounded in App. A.2.5 we introduce a Hubbard-Stratonovich decoupling of the interaction in the Cooper channel, with $\mathcal{Z} = \int e^{-S[\psi,\bar{\psi},\Delta,\bar{\Delta}]}\mathcal{D}\psi\mathcal{D}\bar{\psi}\mathcal{D}\Delta\mathcal{D}\bar{\Delta}$, where the action now

takes the form,

$$
S\left[\psi,\bar{\psi},\Delta,\bar{\Delta}\right] = \sideset{}{'}\sum_{\omega,\mathbf{k},\mathbf{k}'} \bar{\Delta}_{\omega,\mathbf{k}} \left(V^{-1}\right)_{\mathbf{k}'-\mathbf{k}} \Delta_{\omega,\mathbf{k}'}
$$
$$
+ \sideset{}{'}\sum_{\omega,\mathbf{k},\mathbf{q}} \left(\bar{\psi}_{\omega,\mathbf{q}/2-\mathbf{k},\uparrow} \ \psi_{\omega,\mathbf{q}/2+\mathbf{k},\downarrow} \right) \begin{pmatrix} -\mathrm{i}\omega + \xi_{\mathbf{k}-\mathbf{q}/2,\uparrow} & \Delta_{0,\mathbf{q}} \\ \bar{\Delta}_{0,\mathbf{q}} & -\mathrm{i}\omega - \xi_{\mathbf{k}+\mathbf{q}/2,\downarrow} \end{pmatrix} \begin{pmatrix} \psi_{\omega,\mathbf{q}/2-\mathbf{k},\uparrow} \\ \bar{\psi}_{\omega,\mathbf{q}/2+\mathbf{k},\downarrow} \end{pmatrix} .
$$

$$(4.2)$$

Anticipating that the transition to the Superfluid (SF) from the normal phase is continuous (a property already established in the weak coupling limit of the two-dimensional system by Combescot and Mora [232]), we will suppose that the order parameter is characterised by a single plane-wave state corresponding to the stationary saddle-point solution, $\Delta_{\omega,\mathbf{q}} = \Delta_{\mathbf{Q}}\delta_{\mathbf{q},\mathbf{Q}}\delta_{\omega,0}$ [198, 205, 246]. In this case, $\mathbf{Q} = \mathbf{0}$ describes the homogeneous SF state while, for $\mathbf{Q} \neq \mathbf{0}$, the condensate is of FFLO type. If the transition to the inhomogeneous phase is first order, the single wave vector assumption necessitates some degree of approximation that will underestimate the width of the FFLO region in the phase diagram.

Then, approximating the functional integral over fields Δ by its mean-field value, and taking the interaction to be contact, $V(\mathbf{r}) = g\delta^2(\mathbf{r})$, integration over the fermionic fields gives the thermodynamic potential,

$$
\Omega = \frac{|\Delta_{\mathbf{Q}}|^2}{g} + \sideset{}{'}\sum_{\mathbf{k}} (\xi_{\mathbf{k},+} - \overbrace{E_{\mathbf{k}}}^{\ddagger}) - \frac{1}{\beta} \operatorname{Tr}\ln\left(1 + \mathrm{e}^{-\beta(E_{\mathbf{k}}+\sigma\xi_{\mathbf{k},-})}\right) , \qquad (4.3)
$$

where $\xi_{\mathbf{k},\pm} = (\xi_{\mathbf{k}-\mathbf{Q}/2,\uparrow} \pm \xi_{\mathbf{k}+\mathbf{Q}/2,\downarrow})/2$, and $E_{\mathbf{k}} = (\xi_{\mathbf{k},+}^2 + |\Delta_{\mathbf{Q}}|^2)^{1/2}$. From this expression, one can obtain the polarisation or "magnetisation",

$$
m \equiv n_\uparrow - n_\downarrow = -\mathrm{d}\Omega/\mathrm{d}h = n_{\mathrm{F}}\left(E_{\mathbf{k}} - \xi_{\mathbf{k},-}\right) - n_{\mathrm{F}}\left(E_{\mathbf{k}} + \xi_{\mathbf{k},-}\right) , \qquad (4.4)
$$

and the total number density,

$$
n \equiv n_\uparrow + n_\downarrow = -\mathrm{d}\Omega/\mathrm{d}\mu = 1 + \frac{\xi_{\mathbf{k},+}}{E_{\mathbf{k}}}\left(n_{\mathrm{F}}\left(E_{\mathbf{k}} - \xi_{\mathbf{k},-}\right) + n_{\mathrm{F}}\left(E_{\mathbf{k}} + \xi_{\mathbf{k},-}\right) - 1\right) , \quad (4.5)
$$

where $n_{\mathrm{F}}(E) = 1/(1 + \mathrm{e}^{-\beta E})$ denotes the Fermi function.

Finally, because of the issues outlined in App. A.7, to regularise the unphysical Ultraviolet (UV) divergences associated with the δ-function form of contact interaction (and contained within the term labelled by ‡ in Eqn. (4.3)), we will set

$$\frac{1}{g} = \int_0^{E_{\mathrm{c}}} \frac{1}{2E + E_{\mathrm{b}}} \mathrm{d}E \, . \tag{4.6}$$

where E_{b} denotes the energy of the two-body bound state and $E_{\mathrm{c}} = k_{\mathrm{c}}^2/2m$ the energy cutoff on the length-scale of the contact potential [204, 247]. E_{b} will then be used as a control parameter to tune through the BEC-BCS crossover. As E_{b} is increased, the system evolves continuously from the weak coupling BCS phase to the strong coupling BEC phase of tightly-bound pairs.

Having obtained the thermodynamic potential in the mean-field approximation, we now outline our strategy for calculating the zero temperature phase diagram. As a platform to address the potential for inhomogeneous phase formation, in the following section we begin by establishing the phase diagram associated with a uniform order parameter, i.e. $\mathbf{Q} = \mathbf{0}$. In this case, the integrations associated with the thermodynamic potential Eqn. (4.3) can be evaluated analytically and many key features of the generalised phase diagram understood. Then, in Sec. 4.4, we return to the more general situation, exploring the capacity for inhomogeneous phase formation. After confirming that, in the single wave vector approximation, the transition to the SF phase is always continuous, we develop a GL expansion of the action to determine the locus of the normal-FFLO phase boundary analytically. Combining these results, we determine the phase diagram for a spatially uniform system as a function of fixed chemical potential and, separately, as a function of fixed particle number. Finally, in Sec. 4.5, we apply these results to the problem of resonance superfluidity in the physically realizable harmonically trapped system.

4.3   Uniform superfluid

In this section we focus on the phase diagram of a system in which the order parameter is constrained to be uniform. At zero temperature, setting $\mathbf{Q} = \mathbf{0}$, the thermodynamic potential can be evaluated analytically for arbitrary population imbalance and mass ratio,

$$
\begin{aligned}
\frac{2\Omega}{\nu} &= |\Delta_\mathbf{0}|^2 \left[\ln \left(\frac{\sqrt{\mu^2 + |\Delta_\mathbf{0}|^2} - \mu}{E_\mathrm{b}} \right) - \frac{1}{2} \right] - \mu \left(\sqrt{\mu^2 + |\Delta_\mathbf{0}|^2} + \mu \right) \\
&\quad - \theta \left(h'^2 - |\Delta_\mathbf{0}|^2 \right) \left[\theta \left(\mu_\mathrm{f} - Rh' - \mu_\mathrm{c} \right) \left(2|h'|\mu_\mathrm{c} - |\Delta_\mathbf{0}|^2 \ln \left| \frac{\mu_\mathrm{c} + |h'|}{\mu_\mathrm{c} - |h'|} \right| \right) \right. \\
&\quad + \theta \left(\mu_\mathrm{c} + \mu_\mathrm{f} - Rh' \right) \theta \left(\mu_\mathrm{c} - \mu_\mathrm{f} + Rh' \right) \\
&\quad \times \left(|h'|(\mu_\mathrm{c} + 2\mu_\mathrm{f}) - \mu \sqrt{\mu^2 + |\Delta_\mathbf{0}|^2} - |\Delta_\mathbf{0}|^2 \ln \left| \frac{\mu_\mathrm{c} + |h'|}{\sqrt{\mu^2 + |\Delta_\mathbf{0}|^2} - \mu} \right| \right. \\
&\quad \left. \left. + \operatorname{sgn}(h') \left(R(\mu^2 - h'^2) + \frac{|\Delta_\mathbf{0}|^2}{2} \ln(r) \right) \right) \right] .
\end{aligned}
\tag{4.7}
$$

Here θ denotes the Heaviside step function, $\nu = m_\mathrm{R}/2\pi$ the two-dimensional density of states of the reduced mass system and, for clarity, we have defined the set of parameters,

$$
R \equiv \frac{r-1}{r+1}, \qquad h' \equiv \frac{h - \mu R}{\sqrt{1 - R^2}}, \qquad \mu_\mathrm{c} \equiv \sqrt{h'^2 - |\Delta_\mathbf{0}|^2}, \qquad \mu_\mathrm{f} \equiv \mu\sqrt{1 - R^2}. \tag{4.8}
$$

By minimising the thermodynamic potential with respect to $\Delta_\mathbf{0}$, one obtains the loci of phase boundaries shown in Table 4.1. When the mass ratio is unity ($R = 0$), these results coincide with those obtained in Ref. [204]. In particular, one may note that, in the SF phase, the order parameter takes the form

$$
|\Delta_\mathbf{0}| = \sqrt{E_\mathrm{b}(2\mu + E_\mathrm{b})} \, ,
$$

implying a thermodynamic potential, $\Omega = -\nu(\mu + E_\mathrm{b}/2)^2$, independent of the chemical potential difference, h. As a result, one may infer that the magnetisation, $m = -\mathrm{d}\Omega/\mathrm{d}h$, is zero. For the uniform condensate, the SF phase always involves a balanced population of fermions. Drawing on these results, let us now comment on the implications for the phase diagram of the system for, respectively, fixed chemical

Table 4.1: Summary detailing the loci of phase boundaries for $\mu/E_{\rm b}$ as a function of $h/E_{\rm b}$ and $R = (r-1)/(r+1)$. Results labelled ($\bigstar$) are found in, and are relevant for, Sec. 4.4.

PP-FFLO$\bigstar$	$\dfrac{1 + (h/E_{\rm b})R \pm \sqrt{1 + 2(h/E_{\rm b})R - R^2 - 2(h/E_{\rm b})R^3}}{R^2}$
FFLO-SF$\bigstar$ and PP-SF	$\dfrac{1 + 2(h/E_{\rm b})R - R^2 - \sqrt{(1 - R^2)(1 + 4(h/E_{\rm b})R)}}{2R^2}$
FP-SF	$\dfrac{\sqrt{2}(h/E_{\rm b}) + \sqrt{1 - R}}{\sqrt{2} - 2\sqrt{1 - R}}$
ZP-FP	$\pm(h/E_{\rm b})$
FP-FFLO$\bigstar$ and FP-PP	$\mp(h/E_{\rm b})$
ZP-SF	$-1/2$
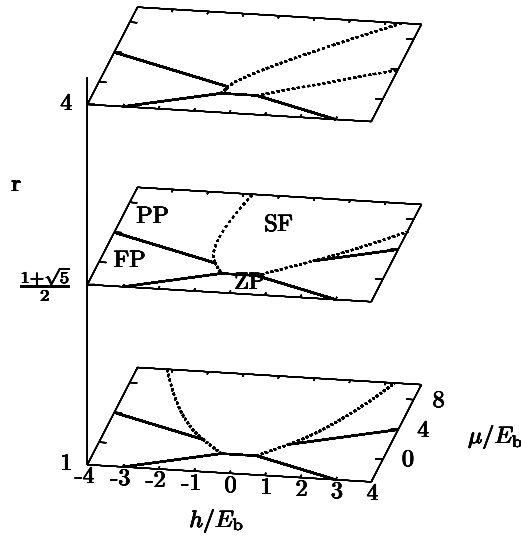
Figure 4.1: The phase diagram shown as a function of $(h/E_{\rm b}, \mu/E_{\rm b})$ for three different values of the mass ratio, r. The diagrams were constructed assuming a uniform order parameter, neglecting the potential for inhomogeneous phase formation. The solid lines represent continuous phase boundaries, while the dashed lines denote first order transitions into the balanced SF phase.

potential and fixed particle number.

4.3.1 Fixed chemical potentials

When the chemical potentials, μ and h, are held constant, minimisation of the thermodynamic potential leads to the phase diagram depicted in Fig. 4.1. The equal mass case is consistent with the result of Tempere et al. [204]. For μ smaller than either the molecular binding energy per particle, $-E_{\rm b}/2$, or the chemical potential shift associated with the majority species, $-h$, (corresponding to an empty Fermi surface), the equilibrium phase hosts no particles (the Zero Particles (ZP) state). On increasing the chemical potential, μ, a second order phase transition into either a balanced SF, or a Fully Polarised (FP) normal phase occurs. The transfers from the ZP phase to a FP normal phase, and from a FP phase to a Partially Polarised (PP) normal phase are both continuous. The phases have boundaries where the Fermi
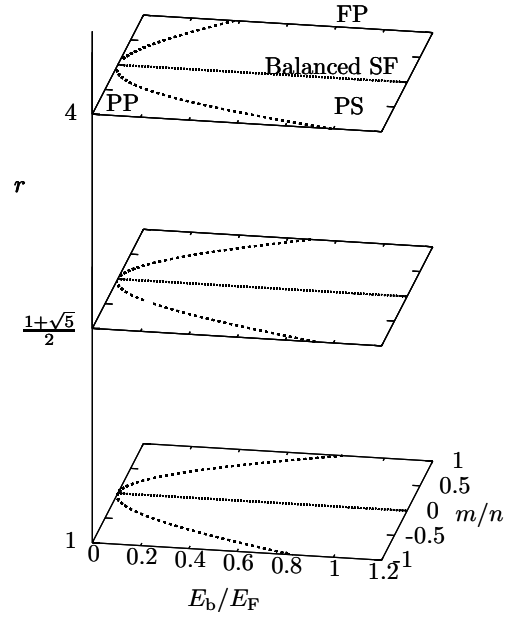
Figure 4.2: The phase diagram as a function of m/n and interaction strength, $E_{\rm b}/E_{\rm F}$, of the two-dimensional system with fixed majority and minority particle densities for three different mass ratios, r. The SF phase (dotted line) is the line of zero population imbalance. Between the balanced SF and PP/FP phase (dashed line) lies a region of phase separation (PS).

surface shrinks to zero at $\mu = -h$ and $\mu = +h$ respectively (for $h > 0$). At fixed $E_{\rm b}$, an increase in chemical potential, μ, leads to an increase in the order parameter of the balanced superfluid system, $|\Delta_0| \propto \sqrt{\mu}$, and an attendant increase in the critical h required to destroy the condensate. The phase transition from the normal state, both FP and PP, into the SF is first order.

As the ratio of masses is increased, as shown in Fig. 4.1 on the side $r > 1$, the phase diagram becomes skewed. This can be understood by tracking the locus of the line where the Fermi surfaces of the two species are perfectly matched, approximately along the centre of the SF phase. The central superfluid locus is $\mu/h = 1/R$, which is consistent with the skew. Superfluidity is therefore more favourable if the "light" species has a greater chemical potential than the "heavy" species.

4.3.2 Fixed number densities

In the canonical ensemble, where the number densities n and m are held constant, the chemical potentials, μ and h, must be inferred self-consistently. In this case, a first order transition in the $(\mu/E_{\rm b}, h/E_{\rm b})$ phase diagram (Fig. 4.1) implies Phase Separated (PS) [190] in the (n,m) phase diagram. At each point along the PP-SF phase boundary in $(\mu/E_{\rm b}, h/E_{\rm b})$ one can evaluate the corresponding polarisation and total number density. From this result, one can infer the boundaries between

the normal and phase separated regions as functions of E_b/E_F and polarisation, m/n. Here we have defined a "Fermi energy" scale $E_F = n/\nu$, where $\nu = m_R/2\pi$ denotes the constant two-dimensional density of states of the reduced mass system. The resulting phase diagram is shown in Fig. 4.2.

As expected, in the BEC limit of large E_b/E_F, one finds phase separation, with the development of a condensate of tightly-bound molecular pairs coexisting with a FP phase containing excess fermions. The phase diagram shows that this behaviour persists into the weak coupling BCS limit, with the system phase separating into a balanced SF phase (i.e. with $m/n = 0$), and the excess particles forming a non-interacting PP Fermi gas. In the BCS limit of weak pairing, a small population imbalance is sufficient to destroy pairing and enter the PP normal phase region.

When the species have unequal masses, the phase diagram is skewed, similar to the fixed chemical potential case in Sec. 4.3.1. If there is a mass imbalance then the Fermi energy of each spin species scales as $E_{F,\sigma} = n_\sigma/\nu_\sigma \equiv \pi(n + \sigma m)/m_\sigma \propto 1/m_\sigma$ implying that it is energetically more beneficial for the "heavy" rather than "light" particles to be in the normal state. Therefore, at a given mass imbalance, the phase diagram loses its symmetry in m/n and superfluidity is favoured if the "lighter" species is in excess whereas the normal state is favoured if the "heavy" species is in excess.

4.4 Inhomogeneous superfluid

With the properties of the uniform SF phase in place, we now turn to the question of inhomogeneous phase formation. To characterise the nature of the PP-FFLO transition, we adopt two methodologies: firstly, utilising the general phenomenology of phase transitions described in App. A.3, in Sec. 4.4.1 we will develop a GL expansion of the action to explore the locus of putative continuous transitions from the normal PP phase into the inhomogeneous FFLO phase. Secondly, in Sec. 4.4.2, we will assess the validity of the GL expansion by investigating the global minimum of the thermodynamic potential for a mean-field order parameter field involving a single wave vector. Using these results, we will infer the phase diagram of a system with fixed chemical potentials in Sec. 4.4.3, and fixed particle densities in Sec. 4.4.4.

4.4.1   Ginzburg-Landau theory

With the ansatz that the transition from the normal to condensed phase is continuous, close to the transition we may expand the action in fluctuations, $|\Delta_{\mathbf{q}}|$. In doing so, one obtains

$$S_{\text{eff}} = \sum_{\mathbf{q}} \alpha_{\mathbf{q}} |\Delta_{\mathbf{q}}|^2 + \mathcal{O}\left(|\Delta|^4\right) , \tag{4.9}$$

where

$$\alpha_{\mathbf{q}} = \sum_{\mathbf{k}} \left(\frac{1}{2\epsilon_{\mathbf{k}} + E_{\text{b}}} - \frac{1 - n(\xi_{\mathbf{k}-\mathbf{q}/2,\uparrow}) - n(\xi_{\mathbf{k}+\mathbf{q}/2,\downarrow})}{\xi_{\mathbf{k}-\mathbf{q}/2,\uparrow} + \xi_{\mathbf{k}+\mathbf{q}/2,\downarrow}} \right) \tag{4.10}$$

denotes the static pair susceptibility. The locus of continuous transitions may be determined from the value of $\mathbf{q}$ at which $\alpha_{\mathbf{q}}$ is both minimised and passes through zero. Within the condensed phase, higher order terms in $\Delta_{\mathbf{q}}$ determine the crystalline structure of the FFLO state [248].

The corresponding phase boundary then translates to the largest allowable chemical potential shift, h, which occurs when the Fermi surfaces just touch but do not cross [232]. From this condition, one finds a phase boundary along the line,

$$\frac{h}{E_{\text{b}}} = \left(\frac{\mu}{E_{\text{b}}} - 1 \right) R \pm \sqrt{ \left(\frac{2\mu}{E_{\text{b}}} - 1 \right) (1 - R^2) } . \tag{4.11}$$

Minimising $\alpha_{\mathbf{q}}$ with respect to $|\mathbf{q}|$, one obtains the further condition $\epsilon_{\mathbf{q}} \equiv q^2/(2m_{\text{R}}) = 2E_{\text{b}}/(1 - R^2)$. Measured in units of the Fermi momentum of the reduced mass system, this translates to a wave vector,

$$\frac{|\mathbf{q}|}{k_{\text{F}}} = \sqrt{ \frac{E_{\text{b}}}{E_{\text{F}}} \frac{(m_{\uparrow} + m_{\downarrow})}{2m_{\text{R}}} } , \tag{4.12}$$

where $k_{\text{F}}^2 = 2m_{\text{R}} E_{\text{F}}$ and, inverting Eqn. (4.11), $E_{\text{b}} = \mu - hR \pm \sqrt{(\mu^2 - h^2)(1 - R^2)}$. In the weak coupling limit, $E_{\text{b}} \ll E_{\text{F}}$, so that, at equal masses, $E_{\text{b}} = h^2/2\mu$ giving $|\mathbf{q}| = 2h/v_{\text{F}}$, where v_{F} is the Fermi velocity, agreeing with the findings of Burkhardt and Rainer [249], Shimahara [250], and Combescot and Mora [232]. In the same
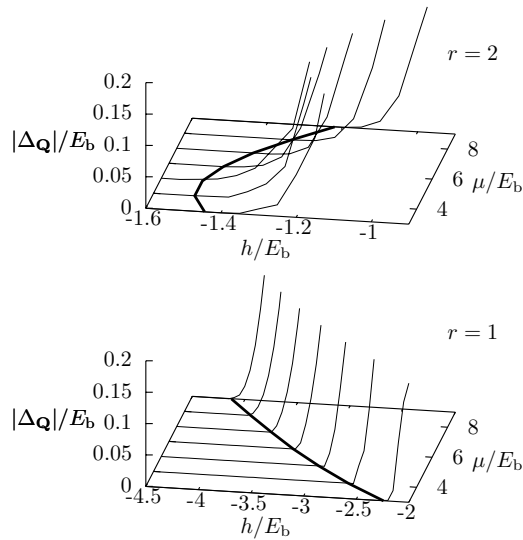
Figure 4.3: Variation of the order parameter $|\Delta_{\mathbf{Q}}|/E_b$ with chemical potential difference, h/E_b, and chemical potential, μ/E_b. The upper panel is at a mass ratio $r = 2$, and the lower panel at equal masses, $r = 1$. The thin black lines trace out the $|\Delta_{\mathbf{Q}}|/E_b$ variation, found by minimising the thermodynamic potential Eqn. (4.3), for several different chemical potentials. The thick black line is the locus of the second order transition predicted by GL theory.

limit, the pair susceptibility takes the form, $\Re(\ln(1 + \sqrt{1 - (|\mathbf{q}|v_F/2h)^2}))$, collapsing to that found in previous works.

4.4.2 FFLO instability phase boundaries

To assess whether the transition from the PP phase to the FFLO phase is really continuous, one can instead minimise the thermodynamic potential Eqn. (4.3) with respect to the wave vector $\mathbf{Q}$ and the mean-field value of the order parameter $\Delta_{\mathbf{Q}}$. For several values of chemical potential, μ, and two different mass ratios $r = 1$ and $r = 2$, numerical minimisation of the thermodynamic potential confirms that the order parameter changes continuously, falling to zero along a line of instability, see Fig. 4.3. The locus of the transition also agrees with that obtained from the GL expansion in Sec. 4.4.1. This result is in accord with that found in Ref. [232] in the weak coupling limit of the equal mass system, and shows that the transition remains continuous across the entire range of the FFLO phase.

We are now in a position to evaluate all phase boundaries associated with the FFLO instability. The agreement described above between GL theory and direct minimisation allows us to use the analytic GL boundary between the PP and FFLO phases. The minimum in the thermodynamic potential that gives rise to the FFLO phase is shallow relative to that of the SF phase. We are therefore able to approximate the actual FFLO-SF phase boundary by the $\mathbf{Q} = 0$ result for the
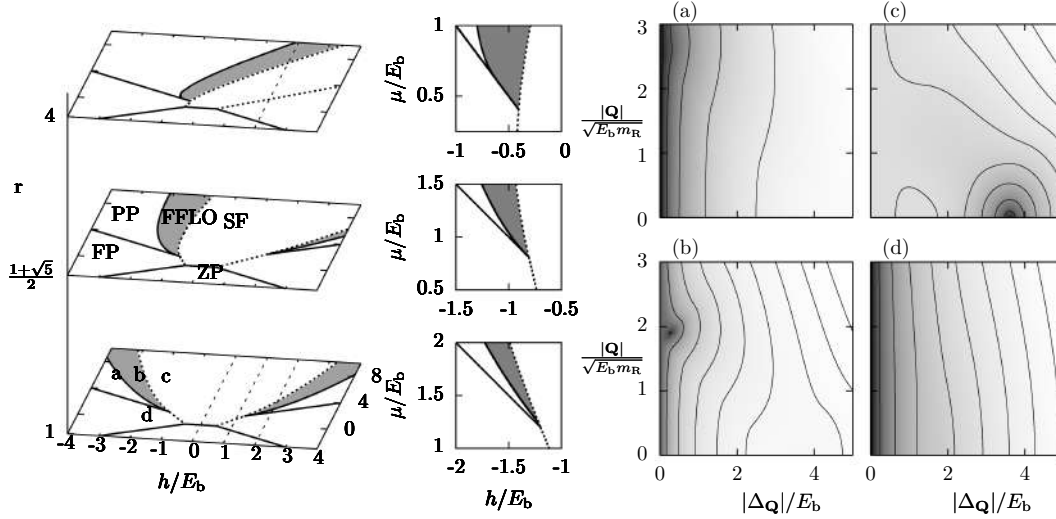
Figure 4.4: The left-hand column shows the phase diagram in $(\mu/E_{\rm b}, h/E_{\rm b})$ at three different mass ratios r. The solid lines represent second order phase boundaries, the dashed line denotes first order phase transitions into the balanced SF phase. The FFLO phase is highlighted in grey. The trajectories followed in the sample traps in Sec. 4.5 are shown by thin dashed lines. The central column of diagrams focus more closely on the topology of the phase diagram close to the tricritical point region for $h/E_{\rm b} < 0$. Thermodynamic potential surfaces are shown in the right-hand column; the darker the more negative and so more favourable; label (a) is a PP normal state, (b) a FFLO state, (c) a SF state, and (d) a FP state. Different plots have different shading calibrations, (unequally spaced) contour lines are also shown.

PP-SF boundary described in Sec. 4.3. A summary of the phase boundaries is shown in Table 4.1, the additional boundaries due to the presence of the FFLO phase are labelled ($\bigstar$). As the extent of the SF region is only reduced by the presence of the FFLO phase, the SF is balanced, as was shown for the $\mathbf{Q} = \mathbf{0}$ study in Sec. 4.3.

4.4.3   Fixed chemical potentials

Let us now apply these results to the problem of a uniform system with constant chemical potentials. The corresponding phase diagram is shown in Fig. 4.4. While the general topology of the phase diagram mirrors that discussed in Sec. 4.3.1, the transition to the balanced SF phase is preempted by the formation of an inhomogeneous FFLO phase. The FFLO instability occurs mainly on the PP side of the PP-SF phase boundary of the uniform condensate shown in Fig. 4.1 with just a small intrusion on the balanced SF side. The FFLO instability does not occur within the FP state as there are no minority state particles with which to pair. The FFLO-PP boundary is second order, while the FFLO-SF boundary is first order.

The FFLO-PP phase boundary terminates at the SF phase for small mass ratios and at the FP phase for large mass ratios on the side of the majority "heavy" species. The movement of the boundary terminus with increasing mass ratio r is in the opposite direction on the majority "light" species side – it moves further up the SF phase boundary. The special mass ratio where it terminates at the SF-FP phase boundary on the majority "heavy" species side is at $r_c = (1 + \sqrt{5})/2$.

The thermodynamic potential variation is also shown in Fig. 4.4 at four different points (a), (b), (c), (d) for $r = 1$. Since the wave vector dependence of the thermodynamic potential enters through the order parameter, in both the PP (a) and FP (d) normal phases the minimum is $|\mathbf{Q}|$-independent. At the highlighted FFLO phase point (b), the global minimum lies at $|\Delta_{\mathbf{Q}}| \approx 0.2 E_b$ with $|\mathbf{Q}| \approx 2\sqrt{m_R E_b}$, while a local minimum also develops at $|\Delta_{\mathbf{Q}}| \approx 3.8 E_b$ with $|\mathbf{Q}| = 0$ corresponding to the putative uniform SF phase. At the highlighted SF point (c), the global minimum lies at $|\Delta_{\mathbf{Q}}| \approx 3.8 E_b$ and $|\mathbf{Q}| = 0$.

4.4.4 Fixed number densities

Let us now address the implications of the phase diagram for a spatially uniform system held at fixed number densities. Obtaining the corresponding density, n, and magnetisation, m, gives the phase diagram shown in Fig. 4.5. Once again, the topology of the phase diagram mirrors that discussed for the homogeneous condensate in Sec. 4.3.2. However, between the phase separated SF phase and normal phase, the system exhibits an inhomogeneous FFLO phase over a wide region of the phase diagram.

In the weak coupling BCS limit, even a small population imbalance is sufficient to enter the FFLO phase region. We note that in a population balanced system the Fermi momenta of the populations are equal so no shift of the Fermi surfaces is required to form Cooper pairs and a modulated phase is not seen.

The effects of the moving PP-FFLO phase boundary terminus, described in Sec. 4.4.3, are also apparent. For equal masses, the FFLO phase never meets the FP normal state. For mass ratios in excess of $r_c = (1 + \sqrt{5})/2$, the FFLO phase meets the FP state on the majority "heavy" species side, but is further from the

Figure 4.5:   The phase diagram in $(m/n, E_b/E_F)$ of the two-dimensional system with fixed majority and minority particle densities for three different mass ratios r. The SF phase (dotted line) is represented by the line of zero population imbalance $m/n = 0$. The PP phase is separated from the FFLO phase (highlighted in grey) by a second order phase boundary (solid line). In the PS region bordered by the dashed line, the system separates into a balanced SF and either a normal phase or, depending on the composition, an inhomogeneous FFLO phase. The right-hand column of graphs focus on the terminus of the PP-FFLO phase boundary on the side of negative polarisation for the three featured mass ratios.
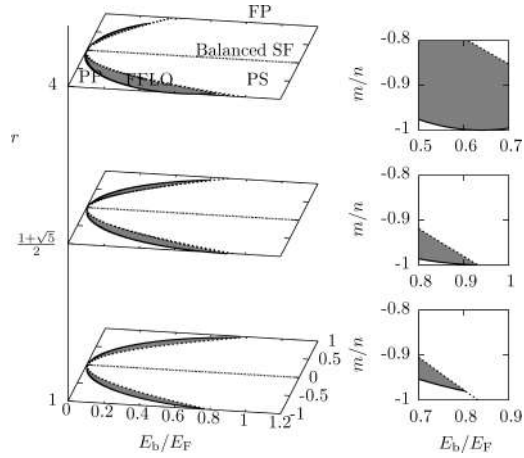
FP state on the "light" species side. For high mass ratios, this is evidenced by the much broader FFLO region on the heavy species side.

To conclude this section, it is interesting to compare the phase diagram of the ultracold atom system with contact interaction and the problem of electron-hole bilayers with long-ranged Coulomb interaction. In particular, we focus our discussion on the study in Ref. [230] of Gallium(III) Arsenide (GaAs) bilayers where the mass ratio $r = 4.3$. In this case, it is more natural to characterise the strength of interaction by $r_s = r_0/a_0$, where $r_0 = 1/\sqrt{\pi n}$ denotes the interparticle spacing, and a_0 is the effective Bohr radius of the two-body bound state. The latter is related to the dimensionless ratio E_b/E_F through the relation, $E_b/E_F = 0.381 r_s^2$. As a result, we find that the system enters the BCS phase with the appearance of FFLO phase behaviour for r_s values of ca. 1.5 (4) compared with that found for the unscreened electron-hole bilayer of $r_s \sim 1.5$ (16) for the "light" ("heavy") species. More qualitatively, in both cases, the systems show a preference towards the superfluid phase when the "light" species is in excess, and the normal phase when the "heavy" species is in excess. Although the topology of the phase diagram is quantitatively the same, two significant differences appear. The first is that, with the electron-hole bilayer, the FFLO-SF phase boundary on the "heavy" species side penetrates further into the BEC regime than in the ultracold atomic gas. The second difference is that, with the electron-hole bilayer, the FFLO region existed from the
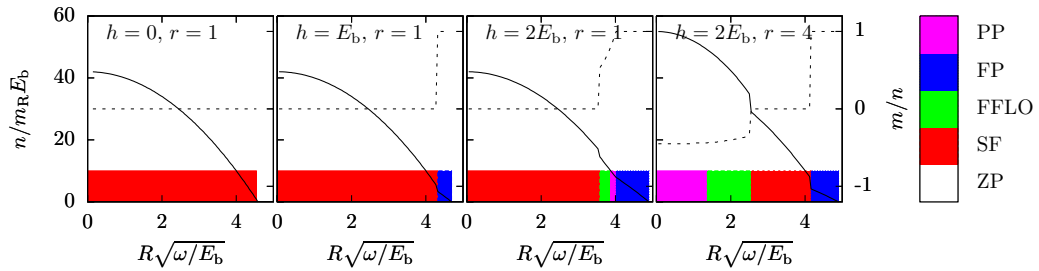
Figure 4.6: Radial density profiles of four systems in identical harmonic traps with different values of population imbalance, h, and mass ratio, r. The solid line shows the radial density based on the primary y-axis. The dashed line shows the local population imbalance based on the secondary y-axis. The band shows where different phases exist with colours labelled on the right-hand side of the figure. With changing radial coordinate, the separate panels are associated with the trajectories highlighted in the $(h/E_b, \mu/E_b)$ phase diagram shown in Fig. 4.4.

normal phase to $m = 0$, and no phase separation between FFLO and SF was seen, except for the deep in the BEC regime. However in the ultracold atomic gas, phase separation of the SF was seen into a balanced SF and a FFLO phase. Both of these differences indicate that, with the electron-hole bilayer, the FFLO phase was more stable relative to the SF than in the ultracold atomic gas. This could be due to the long-range forces that act in the electron-hole bilayer whereas the ultracold atomic gas experiences only contact forces that would favour formation of tightly-bound BEC pairs.

4.5 Harmonically trapped system

Finally, focusing on applications to ultracold atomic gases, we now address the influence of the trap geometry on the phase behaviour. Here we make use of the local density approximation in which the chemical potential of both species, $\mu_\sigma(\mathbf{R}) = \mu_\sigma - V(\mathbf{R})$, are renormalised by the same local trapping potential $V(\mathbf{R})$, the chemical potential difference, h, remains fixed across the trap. Moreover, we further assume that the spatial coordinates are rescaled to ensure a spherically symmetric trapping potential, $V(\mathbf{R}) = \omega R^2/2$. Although there is some experimental evidence [251, 252] that the local density approximation might not be valid [196, 253] in some setups, we believe that its application here will correctly address the qualitative phase structure.

To identify the phases present, one may consider a trajectory of changing μ with constant h and r in the phase diagram of fixed chemical potentials. To find the total

magnetisation and number of particles in the trap, one may make use of the local relations $m = -\mathrm{d}\Omega/\mathrm{d}h$ (Eqn. (4.4)) and $n = -\mathrm{d}\Omega/\mathrm{d}\mu$ (Eqn. (4.5)) respectively, and then integrate over the trap. All trajectories will end up, at large enough radius, in the ZP regime, which is the edge of the particle distribution.

The profiles in four sample traps are shown in Fig. 4.6, which follow trajectories highlighted in Fig. 4.4. The first three have species with equal masses, $r = 1$. At zero population imbalance only the SF state is observed. With a population imbalance, firstly there is a central balanced SF region surrounded by a ring of FP majority spin particles. On increasing the population imbalance yet further, between the ring of FP particles and the central SF, an FFLO instability adjacent to a PP region is seen. The first order transition between the SF and FFLO region (and FP state) leads to a discontinuity in density and polarisation. The second order transitions between FFLO, PP and FP states have continuous variation of density and polarisability but discontinuous changes in their gradients.

The final profile in Fig. 4.6 is at an unequal mass ratio, $r = 4$. The inclusion of mass imbalance causes the SF region in Fig. 4.4 to be biased towards the "lighter" species. This means that it is possible to have a ring of superfluidity remote from the trap centre, or an isolated ring of FFLO instability not at the centre and no accompanying SF region. When there are two rings of normal phase bounding the SF they may either both be the "heavy" particle normal phase if we are crossing the extrusion of the FFLO phase, or alternatively one might be "light" and the other "heavy" if traversing right across the skewed SF phase. In the latter case, shown in Fig. 4.6, the species favoured by the chemical potential shift dominates at the outside of the trap. At the centre of the trap, the normal state is of the "heavy" species as superfluidity favours the "lighter" species.

4.6   Conclusions

We have derived an analytic expression for the thermodynamic potential of a two-dimensional two-component atomic Fermi gas in the mean-field approximation with population imbalance and general mass ratio at zero temperature. A complementary GL analysis was used to examine the PP-FFLO transition. Analytical expressions

for the phase boundaries separating normal and inhomogeneous superfluid phases have been obtained while the properties of the FFLO phase have been addressed numerically. Within the mean-field approximation, the SF phase does not sustain a population imbalance. The region of FFLO instability exhibits a second order phase transition from the PP normal phase, and first order phase transition into the balanced SF. In the BCS limit, a small population imbalance is sufficient to destroy pairing. In the BEC limit, there is phase separation between tightly-bound molecules and a FP normal phase. If there is a mass imbalance, the SF phase is favoured if the majority particles are the "lighter" species, while the polarised normal state is favoured if the "heavy" species are in excess.

A trapped geometry leads to a rich range of possible density profiles. If there is no mass imbalance, a SF phase is seen at the trap centre surrounded by a PP followed by a FP normal phase of the majority spin species. If there is mass imbalance, then a ring of the SF and/or the FFLO state could be seen bordered both inside and outside by either species of normal phase particles.

————— Chapter Five —————

Collective modes of a two-dimensional superfluid Fermi gases with population and mass imbalance

Iɴ this chapter we study the superfluid collective mode spectrum across the BEC-BCS crossover for a two-dimensional fermionic gas at zero temperature. We allow for the possibility of both a population and a mass imbalance between the species. The linear behaviour of the collective mode spectrum persisted from the BCS regime down to unitarity. We carefully studied a pronounced anticrossing of the collective mode spectrum with the continuum of single fermionic excitations that gave rise to a significant plateau in the BCS regime. Using the collective mode dispersion we determined that the Landau critical velocity has a sharp maximum near to unitarity, and we also examined the healing length.

5.1   Introduction

Ultracold atomic Fermi gases now provide investigators with an unprecedented level of control over a many-body system. By tuning the atoms through a Feshbach resonance the interaction strength between atoms can be controlled right across the spectrum of strongly attractive to repulsive, providing a window to explore the crossover from the BEC phase of strongly bound diatomic molecules to the BCS phase of weakly bound Cooper pairs [37, 183–189]. One facet of the exquisite level of control is the ability to investigate physics in reduced dimensions, for example, counter-propagating laser beams [233–236] can be used to set up a periodic potential with antinodes spaced every half wavelength. These provide barriers between the stacked two-dimensional layers of ultracold atomic gases whose inter-layer tunnelling rate is prohibited [237, 238] by the strong optical potential. In this chapter we focus on the properties of such a trapped two-dimensional ultracold atomic gas.

One unique possibility offered by two-component ultracold atom gases is the opportunity to study the consequences of either a mass ratio between the two species [206, 209–214, 254, 255] or a population imbalance [190–208]. These two parameters provide a powerful handle to enrich the phase diagram, leading to the emergence of a tricritical point separating the normal and superfluid phase [217]. Just as a magnetic field in a solid can cause a mismatch between the electron Fermi surfaces, a mass ratio or population imbalance can result in a disparity that can drive the system into the textured FFLO phase that was described in Chp. 4 [3].

Collective modes offer a macroscopic window into the microscopic details of the BEC-BCS crossover. The dispersion profile observed reflects fundamental properties of the microscopic physics, but should be more readily accessible to experiment than single particle excitations. In this chapter, we transcend the BEC-BCS crossover and focus on how the Bogoliubov collective mode, the elementary excitation of BEC state, transforms into the Anderson-Bogoliubov mode in the BCS state. Although the phase diagram of the zero temperature system has been explored in the regime of BEC-BCS crossover in the mean-field approximation [3, 204], the potential for collective modes has only been considered in three-dimensions with equal populations and equal species masses [256] or with a mass imbalance [257];

here we present a detailed analysis of the collective modes in a two-dimensional atomic gas with population and mass imbalance.

Our analysis of the collective mode spectrum invokes dynamical BCS theory. This model well describes the physics either side of the crossover [256] and has been extensively used in the literature in partial studies of collective modes [258–262], as well as the three-dimensional study of collective modes by Combescot et al. [256]. Although at unitarity it is considered as an interpolation model, it provides a firm base to build on and should be trusted qualitatively at the crossover. One further obstacle is the potential formation of dressed molecules that could [239] lead to quantitatively wrong results, however, we are interested primarily in the behaviour at the BEC-BCS crossover where we believe the single band theory should capture the qualitative collective mode dispersion relationship. The remainder of this chapter is organised as follows: We introduce the formalism to analyse collective modes in Sec. 5.2, and in Sec. 5.3 we present the collective modes spectra and consider the critical velocity. Finally, we conclude our discussion in Sec. 5.4.

5.2   Formalism

A two-component atomic Fermi gas contains two atomic species that are indexed by the pseudo-spin $\sigma \in \{\uparrow, \downarrow\} \equiv \{+1, -1\}$. In general the species with differing masses m_σ have a ratio of masses $r = m_\downarrow/m_\uparrow$, and we use $1/m = (1/m_\uparrow + 1/m_\downarrow)/2$ to denote the reduced mass. Additionally, the atomic gas can sustain a population imbalance with each species having a separate chemical potential $\mu_\sigma = \mu + \sigma h$. A Feshbach resonance can be used to tune the attractive contact interaction of strength g that acts between a pair of opposite spin fermions. The interaction strength can be related to the binding energy E_b of a pair by $1/g = \int_0^\infty (2E + E_\mathrm{b})^{-1} \mathrm{d}E$. The binding energy E_b itself can be re-expressed in terms of the natural experimental parameter to describe the interaction, the three-dimensional scattering length a (for further details see App. A.1), using the relation [204, 263] $E_\mathrm{b} = 0.291\hbar\omega_\mathrm{L} \exp(\sqrt{2\pi}l/a)$ where $\omega_\mathrm{L} = \sqrt{8\pi^2 V_0/m\lambda^2}$, $l = \sqrt{\hbar/m\omega_\mathrm{L}}$, and λ is the periodicity of the laser potential confining the atomic gas to two dimensions, which has depth V_0. Throughout the remainder of this chapter we adopt the atomic units $\hbar = k_\mathrm{B} = 1$.

5.2.1   Collective mode dispersion

Our starting point is the single-channel Hamiltonian that describes a wide Feshbach resonance. Deploying the formalism outlined in App. A.2, we write the quantum partition function as a functional field integral over the fermionic fields ψ_σ and $\bar{\psi}_\sigma$, $\mathcal{Z} = \int e^{-S[\bar{\psi},\psi]} \mathcal{D}\psi \mathcal{D}\bar{\psi}$, with the action

$$S[\bar{\psi},\psi] = \int_0^\beta d\tau \left(\sum_{\mathbf{k},\sigma} \bar{\psi}_{\mathbf{k},\sigma} \left(\partial_\tau + \xi_{\mathbf{k},\sigma} \right) \psi_{\mathbf{k},\sigma} - \frac{g}{2} \sum_{\mathbf{k},\mathbf{q}} \bar{\psi}_{\mathbf{k},\uparrow} \bar{\psi}_{\mathbf{q}-\mathbf{k},\downarrow} \psi_{\mathbf{k},\downarrow} \psi_{\mathbf{q}-\mathbf{k},\uparrow} \right) , \quad (5.1)$$

where $\beta = 1/k_{\mathrm{B}}T$ is the inverse temperature and we have set $\xi_{\mathbf{k}}^\sigma = k^2/m_\sigma - \mu_\sigma$. Anticipating the condensation of Cooper pairs, following the prescription laid out in App. A.2.5 we decouple the quartic interaction term in the Hubbard-Stratonovich channel with the bosonic field Δ. To study the collective modes of the system we consider the response function for a perturbation to the mean-field BCS gap parameter $\Delta = \Delta_0 + \delta$, where $\Delta_0 = \sqrt{E_{\mathrm{b}}(2\mu + E_{\mathrm{b}})}$ is the mean-field solution in the superfluid phase derived in Chp. 4 [3] and δ represents the collective mode under consideration. The dispersion relation for the collective mode is the frequency Ω and momentum $\mathbf{q}$ where the coefficient of δ^2 in the action first changes sign. Following functional integration over the fermionic variables we obtain the action

$$S = \frac{\beta}{g} \left(|\Delta_0|^2 + \mathrm{Tr}\, |\delta|^2 \right) - \frac{1}{2} \mathrm{Tr} \ln \left(\hat{\mathsf{G}}^{-1} + \hat{\delta} \right) , \quad (5.2)$$

where the Bogoliubov Green function is defined as

$$\mathsf{G}^{-1}(\mathbf{k} \pm \mathbf{q}/2) = \begin{pmatrix} F_\pm^\uparrow & \Delta_0 \\ \overline{\Delta}_0 & F_\pm^\downarrow \end{pmatrix} , \quad (5.3)$$

with the components $F_\pm^\uparrow = i\omega \pm \Omega/2 + \xi_{\mathbf{k}\pm\mathbf{q}/2}^\uparrow$ and $F_\pm^\downarrow = i\omega \pm \Omega/2 - \xi_{\mathbf{k}\pm\mathbf{q}/2}^\downarrow$. The action is then expanded to second order in the collective mode δ to give the action

$$S = \frac{\beta|\Delta_0|^2}{g} + \frac{\beta}{2} \mathrm{Tr} \left[\bar{\delta} \begin{pmatrix} \frac{1}{g} + N_+ F_+^\downarrow N_- F_-^\uparrow & N_+ \Delta N_- \Delta \\ N_+ \overline{\Delta} N_- \overline{\Delta} & \frac{1}{g} + N_+ F_+^\uparrow N_- F_-^\downarrow \end{pmatrix} \delta \right] , \quad (5.4)$$

where we introduce the normalisation stemming from the inversion of the Green function denoted by $N_\pm = (F_\pm^\uparrow F_\pm^\downarrow - |\Delta_0|^2)^{-1}$. The action now needs to be diagonalised in order to determine the eigenvalues, we focus here on the lowest eigenvalue which corresponds to the collective mode $\Omega(\mathbf{q})$ that emerges when the eigenvalue changes sign. To numerically determine the bands we follow the prescription of first finding the matrix elements for a given Ω and $\mathbf{q}$, diagonalise to recover the eigenvalues, and then refine our choice of Ω until that eigenvalue is zero which yields the collective mode frequency.

Having formally calculated the collective mode spectrum we now outline our strategy to analyse it. Firstly, we consider the low energy limit and derive the linear dispersion relation for the sound velocity in Sec. 5.2.2. Secondly, in Sec. 5.2.3 using the formalism above we derive analytical expressions for an upper bound on the spectrum corresponding to the destruction of pairs. We then verify that these are in close agreement with the numerical calculation of the collective mode spectrum, and analyse its mass ratio, population imbalance, and interaction strength dependence in Sec. 5.3.1. Finally, in Sec. 5.3.2 we use our collective mode spectra to calculate the superfluid critical velocity and healing length.

5.2.2 Sound velocity

At low energy the collective modes spectrum is linear, whose gradient corresponds to the velocity of sound propagation in the superfluid. Previous studies of the sound velocity [8, 16, 264] focused on the equal mass and population case, or just mass imbalance [257] in three dimensions; here we aim to expand to generalised mass ratio and population imbalance in two dimensions. At low energy the collective modes manifest themselves through a spatially changing phase θ of the order parameter $\Delta(\mathbf{r}) = \Delta_0 e^{2i\theta(\mathbf{r},t)}$ and $\overline{\Delta}(\mathbf{r}) = \Delta_0 e^{-2i\theta(\mathbf{r},t)}$. To examine the properties of these Goldstone mode degrees of freedom we follow the established method outlined by Nagaosa [16] and impose a gauge transformation of the Grassmann fields $\psi'_\sigma(\mathbf{r}) = \psi_\sigma(\mathbf{r})e^{i\theta(\mathbf{r},t)}$ and $\overline{\psi}'_\sigma(\mathbf{r}) = \overline{\psi}_\sigma(\mathbf{r})e^{-i\theta(\mathbf{r},t)}$ that renders the gap parameter uniform and time independent. To address the excitations we aim to develop an expansion of the form $S = S_1(\nabla\theta)^2 + S_2(\partial_t\theta)^2$. The spatial gradient term appears

to quadratic order inside the logarithm in Eqn. (5.2) so only needs to be expanded to first order; this term will therefore be preceeded by a Green function that gives the total density of particles, and therefore yields $S_1 = 2\mu + E_b$. The temporal term however appears to just first order inside the logarithm that therefore needs to be expanded to second order, so the temporal term is preceeded by two Green functions. Separate approximations in either the BEC or BCS limit yield the same expression for $S_2 = m_\uparrow + m_\downarrow$. Therefore, the linear collective mode spectrum is $\Omega = q\sqrt{(2\mu + E_b)/(m_\downarrow + m_\uparrow)}$. In the BEC limit this physically reflects that the particles are tightly bound so that their dynamics depends only on their total mass, whereas in the BCS limit the particles are weakly bound and their velocity is separable $v = \sqrt{v_\uparrow v_\downarrow}$ into the velocities of a homogeneous gas of just up-spin mass particles $v_\uparrow$ and down spin $v_\downarrow$ [257]. The dispersion profile should follow the linear dispersion calculated in this section until we approach the single particle excitation threshold.

5.2.3   Fermion excitation threshold

Having considered the low momentum limit for the spectrum, we now focus on the complementary high energy limit. Rather than propagating sound, the pairs now break apart and two single fermions are excited that escape separately. This process will place an upper bound on the collective mode spectrum, which approaches that bound at high momentum and correspondingly high energy. In order to derive the threshold for excitation of single fermions we follow the method of Combescot et al. [256] and search for the first emergence if a singularity in the action Eqn. (5.4). We find that, after the summation over Matsubara frequencies, the singularity is at

$$
\Omega = \sqrt{\left(\frac{\xi^\uparrow_{\mathbf{k+q}/2} + \xi^\downarrow_{\mathbf{k+q}/2}}{2}\right)^2 + \Delta^2} + \sqrt{\left(\frac{\xi^\uparrow_{\mathbf{k-q}/2} + \xi^\downarrow_{\mathbf{k-q}/2}}{2}\right)^2 + \Delta^2}
$$
$$
+ \frac{\xi^\uparrow_{\mathbf{k-q}/2} + \xi^\downarrow_{\mathbf{k+q}/2} - \xi^\uparrow_{\mathbf{k+q}/2} - \xi^\downarrow_{\mathbf{k-q}/2}}{2} \, . \tag{5.5}
$$

In calculating this expression the chemical potential shifts h appear in tandem so always cancel, therefore the excitation threshold is independent of population

imbalance. The singularity first emerges where Ω is minimised with respect to $\mathbf{k}$. Though this cannot be found in general, three limits are tractable:

Balanced masses: The minimum is at $k = 0$ which gives the threshold in agreement with Ref. [256], $\Omega = 2\sqrt{(q^2/8m - \mu)^2 + |\Delta_0|^2}$.

Large momentum limit: When $q^2/8m \gg |\Delta_0|$ the minimum is at $k = q(r - 1)/[2(r + 1)]$. Deep in the BEC limit the two particles have momenta $q_\uparrow = q/(1 + r)$ and $q_\downarrow = q/(1 + 1/r)$ which, as they are free particles have the dispersion $\Omega = q^2/[m(1 + r)(1 + 1/r)] - \mu$.

Zero momentum: If $q = 0$ then the minimum occurs at $k = 0$ and $\Omega = 2\sqrt{\mu^2 + \Delta^2} = 2(\mu + E_b)$. This is independent of the mass ratio since it corresponds to the energy to just overcome the binding energy and then leave the two remnant atoms stationary.

5.3 Results

We now put the general numerical (Sec. 5.2.1), sound velocity (Sec. 5.2.2), and the excitation threshold (Sec. 5.2.3) results together to firstly calculate the collective modes spectrum, and secondly examine the critical velocity of the system.

5.3.1 Collective modes

The collective modes spectra shown in Fig. 5.1 are split into three classes, namely the BCS limit where $E_b \ll \mu$, the BEC limit at which $E_b \gg \mu$, and the intermediate unitarity regime at $E_b \approx 2\mu$ [204, 247] which we describe separately below. In our discussion firstly we make contact with the three-dimensional analysis [256, 257] by considering equal masses and no population imbalance, and then turn to the general two-dimensional case with a general mass ratio and/or population imbalance.

Weak coupling BCS regime: In the limit $q \ll \sqrt{m}(\mu + E_b)/\sqrt{\mu + E_b/2}$ the spectrum has an extended linear regime with the gradient being determined by the sound velocity $\sqrt{(\mu + E_b/2)/m}$. Then at $q = \sqrt{m}(\mu + E_b)/\sqrt{\mu + E_b/2}$ where the linear spectrum would cross the pair breaking continuum the
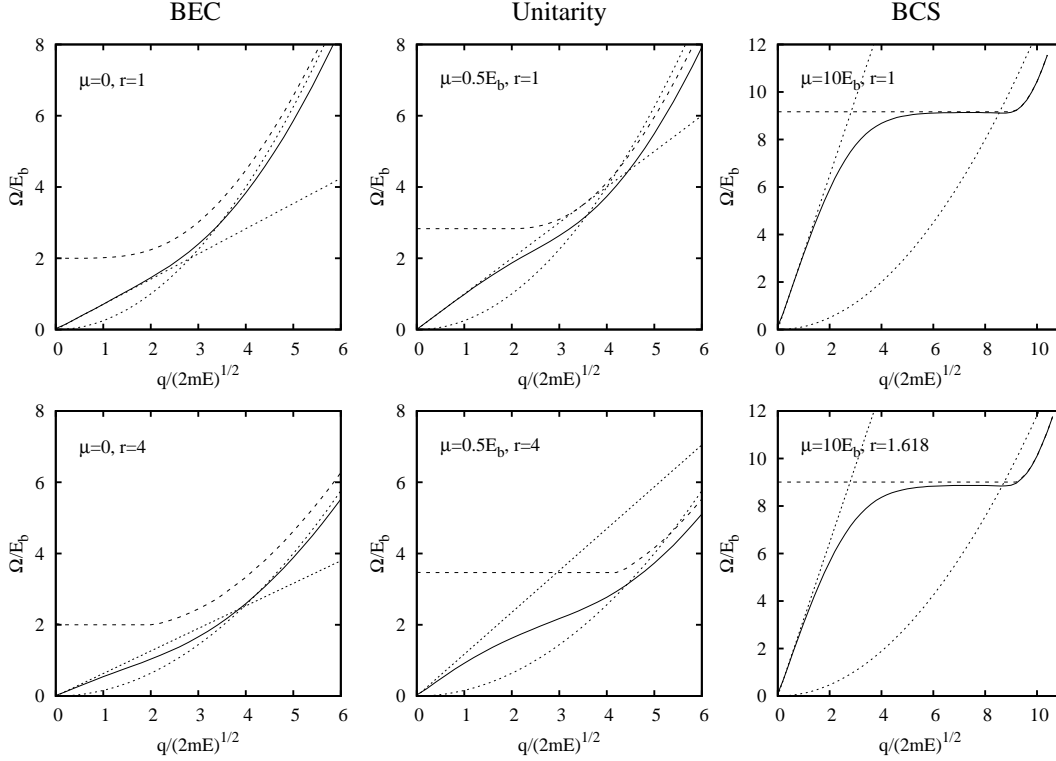
Figure 5.1: The collective modes spectra are shown by the solid lines, the asymptotic limits of the linear sound velocity and free particle kinetic energy are denoted by the dotted lines, and the upperbound imposed by the pair-breaking continuum by the dashed line. The variation with chemical potential imbalance h is not explicitly shown as the superfluid was always balanced.

dispersion curves over to a flat plateau with $\Omega = 2(\mu + E_{\rm b})$. This situation is analogous to an anti-crossing in a two level system, with the collective mode being one level, and the pair breaking continuum the second level. This dispersion is unique to cold atomic gases, in superfluid Helium-3 (^{3}He) hard core repulsion between ^{3}He atoms means that the sound velocity is faster and the mode merges into the pair-breaking continuum, whereas, in a superconductor the collective mode frequency merges into the plasma frequency as electrons carry charge. The plateau in the dispersion is maintained until it meets the free kinetic energy of two remnant fermions at $q = [2m(1+r)(1+1/r)(\mu + E_{\rm b}/2)]^{1/2}$ when the dispersion curves upwards corresponding to the free kinetic energy $\Omega = q^2/[m(1+r)(1+1/r)]$.

Collective mode at unitarity: At unitarity, similar to the BCS limit, the spectrum is linear until it comes into the vicinity of the pair breaking

continuum. The dispersion then displays behaviour analogous to two level anti-crossing, though the horizontal plateau is less pronounced than in the BCS regime. At very large momentum the dispersion curves upwards corresponding to the kinetic energy of the two remnant particles.

BEC limit: In this limit the two crossover momenta derived in the BCS regime, from linear to plateau, and plateau to free particle coincide (for equal mass ratios) at $q \sim 2\sqrt{2mE_{\rm b}}$. The horizontal plateau in the dispersion profile is therefore lost and we recover the clean Bogoliubov behaviour [8, 16, 264] of linear sound $\sqrt{(\mu + E_{\rm b}/2)/m}$ at low momenta and free particle $\Omega = q^2/[m(1 + r)(1 + 1/r)]$ at high momentum.

Mass ratio: Though the plateau threshold energy $\Omega = 2(\mu + E_{\rm b})$ is independent of mass ratio, both the sound velocity and the free particle kinetic energy $\Omega = q^2/[m(1 + r)(1 + 1/r)]$ do depend on the ratio of masses. Therefore, the flat plateau shifts to higher momentum q with increasing mass ratio since the sound velocity decreases and the heavier particle can carry the majority of the momentum with relatively small kinetic energy cost.

Population imbalance: As shown in Chp. 4 [3] the superfluid is always balanced so the introduction of chemical potential shift does not alter the collective modes dispersion.

5.3.2 Critical velocity

The critical velocity of a superfluid is given by Landau's criterion, $v_{\rm c} = \min(\Omega(q)/q)$. There are two sorts of excitations in the system that could give the minimum in $\Omega(q)/q$: the bosonic collective modes (analysed in Sec. 5.2.2), and secondly fermionic pair breaking (studied in Sec. 5.2.3). If the dispersion relation always has an upwards curvature, reminiscent of the Bogoliubov dispersion relation, then the minimum of $\omega(q)/q$ is given at $q \to 0$ by the sound velocity $\sqrt{(2\mu + E_{\rm b})/(m_\uparrow + m_\downarrow)}$. However, in the BCS limit the single fermionic particle excitations produce the horizontal anticrossing feature of the spectrum which can result in a lower minimum of $\Omega(q)/q$, approximately at the high momentum end of that horizontal plateau. The critical
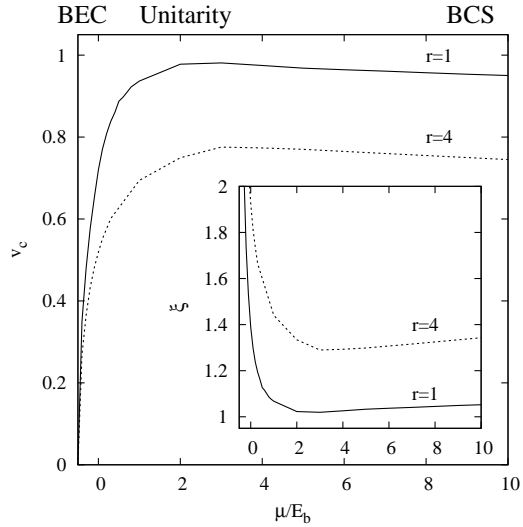
Figure 5.2: The critical superfluid velocity v_c for $r = 1$ is shown by the solid line, and for $r = 4$ by the dashed line as a function of μ/E_b. The inset graph shows the healing length given by the critical velocity (solid line for $r = 1$ and dashed line for $r = 4$).

velocity at two different mass ratios is highlighted in Fig. 5.2. In the BEC limit the critical velocity depends only on total mass, but on passing through unitarity into the BCS limit the critical velocity falls with an increasing ratio of masses. This is because the heavier particle of the pair can carry the majority of the momentum with relatively little kinetic energy cost so the pair-breaking continuum occurs at higher momentum, extending the range of the horizontal plateau. Near unitarity the critical velocity has a maximum, as it switches from bosonic to fermionic excitations.

We also examined the quantity $\xi = 1/mv_c$ [256, 265]. Physically it is the healing length in the BEC limit, and in the BCS limit is the coherence length that sets the size of Cooper pairs. Near unitarity the healing length sets the core size of quantised vortices. As $\xi = 1/mv_c$ it displays the same physical behaviour as has already been discussed for the critical velocity.

5.4   Summary and discussion

In this chapter we have investigated the collective modes across the BEC-BCS crossover for a fermionic ultracold atomic gas held at zero temperature. In the BEC limit we found good agreement with the Bogoliubov dispersion which depended on the total mass of a pair, and in the BCS regime an extended linear region, which increased with a ratio of masses. This was ascribed to the heavier particle carrying the majority of the momentum with relatively little energy cost. The critical velocity

fell with mass ratio both in the BEC and the BCS regime.

Our investigation has uncovered qualitative behaviour that merits both further theoretical investigation and experimental verification. One particularly interesting facet is the interaction between the collective mode and excitation continuum, analogous to anti-crossing in two-level systems. This behaviour occurs mainly on the BCS side though it continues slightly beyond unitarity on the BEC side which might provide a useful probe into molecule formation at the crossover. Finally, we assembled our results to recover the Landau critical velocity which was found to have a pronounced maximum near to unitarity. This feature should be experimentally verifiable.

As one goal of the study is to demonstrate the opportunity that collective modes present to probe microscopic physics, we now discuss three possible experimental approaches to study the dispersion of the collective modes. The first method is to study the Goldstone mode via the resonance it causes in the spectrum of the density-density correlation function [266], which can be monitored either directly as a density fluctuation pulse or through two-photon Bragg scattering. A second probe is to measure the speed of sound by monitoring the damping rate of a radial breathing mode by studying Time of Flight (TOF) measurements [267, 268]. A third powerful probe of the superfluid critical velocity would be to drag a single ionic impurity through the atomic gas whose motion would become damped as vortices are created when the superfluid critical velocity is exceeded.

One important avenue of future research is the ramifications of a trap on our results. The confined geometry imposes discrete low-energy collective modes, which should have interesting behaviour at the BEC-BCS crossover. In the BCS limit, established theory [269, 270] predicts that if the quadrupole mode frequency is greater than the Cooper pair breaking threshold then the mode is damped so has small spectral weight. As one approaches the crossover the pairs become more strongly bound shifting the spectral weight to the quadrupole mode frequency which corresponds to the oscillation of a trapped BEC gas [271]. In the crossover regime the persistence of the linear dispersion profile should be apparent in trapped geometry, albeit with a modified spectral weight and damping. Another further consideration is

how the spectrum would be affected by the fermion self energy arising from coupling to non-Bose-condensed bosons [272] that we neglected since these two-particle modes are strongly damped.

—————— Chapter Six ——————

Itinerant ferromagnetism in atomic Fermi gases: Influence of population imbalance

I~N~ this chapter we investigate ferromagnetic ordering in an itinerant ultracold atomic Fermi gas with repulsive interactions and population imbalance. In a spatially uniform system, we show that at zero temperature the transition to the itinerant magnetic phase transforms from first to second order with increasing population imbalance. Drawing on these results, we elucidate the phases present in a trapped geometry, finding three characteristic types of behaviour with changing population imbalance. Finally, we outline the potential experimental implications of the findings.

The work in this chapter is the subject of the recent publication Ref. [4].

6.1   Introduction

Feshbach resonance phenomena provide unprecedented control of pair interactions in degenerate atomic Fermi gases [273, 274]. This feature has allowed extensive studies of pairing phenomena in two-component Fermi gases providing access to

the entire range of BEC-BCS crossover [183, 186–188]. Although the emphasis of experimental investigations has been primarily on the problem of resonance superfluidity, interacting Fermi gases support other strongly-correlated phases including itinerant ferromagnetism.

In solid state condensed matter systems, the problem of itinerant ferromagnetism has a long history dating back to the pioneering studies by Stoner [275] and Wohlfarth [109]. These early investigations proposed that, at low enough temperatures, a Fermi gas subject to a repulsive interaction potential could undergo a continuous phase transition into an itinerant spin polarised phase [276]. This Stoner transition reflects the shifting balance between the potential energy gained in spin polarisation through Pauli exclusion statistics, and the associated cost in kinetic energy. Subsequent studies showed that fluctuations in the magnetisation at low temperatures drive the second order transition first order at low enough temperatures [53–58]. Such behaviour is born out around quantum criticality in a variety of experimental solid state systems including $ZrZn_2$ [47, 48], UGe_2 [49], Manganese Silicide (MnSi) [50, 51, 277–279], CoS_2 [52], Ytterbium-Rhodium-Silicon ($YbRh_2Si_2$) [280], and Strontium Ruthenium Oxide ($SrRuO_3$) [281]. When subject to a magnetic field, the attendant increase in Zeeman energy results in the bifurcation of the tricritical point separating the region of first and second order ferromagnetic transitions into two lines of metamagnetic critical points.

In the following, we will explore the potential implications of this itinerant magnetic phase behaviour on the equilibrium properties of strongly interacting two-component atomic Fermi gases; here we refer to the pseudo-spin associated with the hyperfine states characterising the two atomic populations. However, in contrast to the solid state system, the application of these ideas to the atomic Fermi gas must address the features imposed by the trap geometry, and the constraints resulting from the inability of particles to transfer between different spin states [201]. As a result, in the general case, one must consider atomic Fermi mixtures in which an effective spin polarisation is imposed by population imbalance [282, 283]. The potential for itinerant ferromagnetism in atomic Fermi gases has been already addressed in the literature, the work of Sogo and Yabu [284] studied a trapped

system in the Thomas-Fermi approximation. Subsequently, Duine and MacDonald [285] developed a diagrammatic perturbative expansion in interaction strength to address the phase behaviour of the balanced two-component Fermi system. In the following, we will develop a functional integral formulation to explore the phase behaviour of the general population imbalanced system. As well as providing access to the mean-field phase behaviour of the system, such an approach allows for future considerations of the collective low energy spin dynamics of the spin polarised phase. Moreover, the theory provides a platform to explore the potential for the development of an equilibrium spin textured phase recently conjectured in relation to the solid state system [54, 286–289] that is pursued in Chp. 7.

The chapter is organised as follows: In Sec. 6.2 we derive an expression for the thermodynamic potential of the system as a function of the local density and in-plane magnetisation fields. To address the important effects of spin-wave fluctuations on the nature of the equilibrium phase diagram, we will explore the renormalisation of the mean-field equations keeping those terms that are second order in the coupling strength, g. Using this result, in Sec. 6.3.1 we analyse the phase diagram of the spatially uniform system as a function of the interaction strength, g, and chemical potential shift. Finally, in Sec. 6.3.2 we explore in detail the phase behaviour of the magnetic system in the atomic trap geometry.

6.2   Field integral formulation

Expressed in the coherent state path integral formalism that is expounded in App. A.2, the quantum partition function of a population imbalanced two-component Fermi gas is

$$\mathcal{Z} = \int \mathcal{D}\psi \exp\left[-\int_0^\beta d\tau\, d\mathbf{r} \sum_{\sigma=\{\uparrow,\downarrow\}} \bar{\psi}_\sigma(-\mathrm{i}\partial_\tau + \hat{\xi} - \sigma\Delta\mu)\psi_\sigma - \bar{\psi}_\uparrow\bar{\psi}_\downarrow\psi_\downarrow\psi_\uparrow\right] , \quad (6.1)$$

where $\bar{\psi}_\sigma(\tau,\mathbf{r})$ and $\psi_\sigma(\tau,\mathbf{r})$ denote Grassmann fields, $\beta = 1/k_\mathrm{B}T$ is the inverse temperature, and $\hat{\xi} = \hat{p}^2/2m - \mu$. Here we have used a pseudo-spin index, $\sigma \in \{\uparrow, \downarrow\}$, to discriminate the two components. As independent particles (with

no interconversion), the density of the two majority/minority degrees of freedom must be specified by two chemical potentials. For convenience, it is helpful to separate the chemical potentials into their sum and difference; $\mu + \Delta\mu$ for up-spin and $\mu - \Delta\mu$ for down-spin. In this representation, population imbalance may be adjusted through the chemical potential shift, $\Delta\mu$. Note that, although population imbalance is synonymous with a global pseudo-spin magnetisation, a spontaneous symmetry breaking into an itinerant ferromagnetic phase can still develop with the appearance of a non-zero in-plane component of the magnetisation. Finally, we suppose that the strength of the repulsive s-wave contact interaction, $g\delta^3(\mathbf{r})$, can be tuned using a Feshbach resonance.

6.2.1   Hubbard-Stratonovich decoupling

To develop an effective low-energy theory for the Fermi gas, it is convenient to decouple the quartic contact interaction by introducing auxiliary bosonic fields, ρ and ϕ, conjugate to the local density $\sum_{\alpha=\{\uparrow,\downarrow\}} \bar{\psi}_\alpha \psi_\alpha$ and magnetisation $\sum_{\alpha,\beta=\{\uparrow,\downarrow\}} \bar{\psi}_\alpha \boldsymbol{\sigma}_{\alpha\beta} \psi_\beta$ respectively, setting

$$
\begin{aligned}
\mathcal{Z} = \int \mathcal{D}\boldsymbol{\phi}\mathcal{D}\rho\mathcal{D}\psi \exp\bigg\{ &- \int d\tau d\mathbf{r} \bigg[g(\phi^2 - \rho^2) \\
&+ \sum_{\alpha,\beta=\{\uparrow,\downarrow\}} \bar{\psi}_\alpha \left[(\hat{G}_0^{-1} + g\rho)\delta_{\alpha\beta} - (\Delta\mu\mathbf{e}_z + g\boldsymbol{\phi}) \cdot \boldsymbol{\sigma}_{\alpha\beta} \right] \psi_\beta \bigg] \bigg\}.
\end{aligned}
\tag{6.2}
$$

Here $\hat{G}_0 = (-\mathrm{i}\partial_t + \hat{\xi})^{-1}$ defines the Green's function of the non-interacting system, and $\boldsymbol{\sigma}$ denotes the vector of Pauli spin matrices. As outlined in App. A.2.5, without decoupling in both the Hartree and Fock channels one would subsequently encounter unphysical diagrammatic contributions to the perturbative scheme developed below [290–292]. It is also the simplest approach that maintains spin rotational invariance of the Hamiltonian, and leads to the correct set of Hartree-Fock equations [293, 294]. Then, integrating over the Fermi fields, one obtains the

expression

$$\mathcal{Z} = \int \mathcal{D}\phi \mathcal{D}\rho \mathcal{D}\psi\, \mathrm{e}^{-\int d\tau d\mathbf{r}\, g(\phi^2 - \rho^2)} \exp\left[\mathrm{Tr}\ln\left(\hat{G}_0^{-1} + g\rho - \boldsymbol{\sigma}\cdot(\Delta\mu\mathbf{e}_{\mathrm{z}} + g\boldsymbol{\phi})\right)\right]. \tag{6.3}$$

At this stage the analysis is exact, but to proceed further one must employ an approximation. To orient our discussion and make contact with conventional Stoner theory, let us first consider a direct saddle-point approximation scheme.

6.2.2 Stoner mean-field theory

As well as the "effective" magnetisation imposed by population imbalance, we anticipate the development of a spontaneous magnetisation which will drive the axis of quantisation away from the z-axis. We re-orient the axis of quantisation to lie parallel to the net magnetisation, denoted in mean-field theory (with over-bars) $\overline{\boldsymbol{\phi}} = \overline{\boldsymbol{\phi}}_\perp + \overline{\phi}_{\mathrm{z}}\mathbf{e}_{\mathrm{z}}$, $\overline{\boldsymbol{\phi}}_\perp = (\overline{\phi}_{\mathrm{x}}, \overline{\phi}_{\mathrm{y}})$, and with this definition, the total magnetisation of the system is given by $\overline{\mathbf{M}} = \Delta\mu\mathbf{e}_{\mathrm{z}}/g + \overline{\boldsymbol{\phi}}$. Separately varying the action with respect to $\overline{\boldsymbol{\phi}}_\perp$ and $\overline{\phi}_{\mathrm{z}}$ one obtains, respectively, the saddle-point equations,

$$\begin{pmatrix} \overline{\boldsymbol{\phi}}_\perp \\ \overline{\phi}_{\mathrm{z}} \end{pmatrix} = -\frac{(\beta V)^{-1}\,\mathrm{Tr}(\hat{G}_+ - \hat{G}_-)}{\sqrt{(g\overline{\boldsymbol{\phi}}_\perp)^2 + (g\overline{\phi}_{\mathrm{z}} + \Delta\mu)^2}} \begin{pmatrix} g\overline{\boldsymbol{\phi}}_\perp \\ g\overline{\phi}_{\mathrm{z}} + \Delta\mu \end{pmatrix}, \tag{6.4}$$

where $\hat{G}_\pm^{-1} = \hat{G}_0^{-1} + g\overline{\rho} \mp |\Delta\mu\mathbf{e}_{\mathrm{z}} + g\overline{\boldsymbol{\phi}}|$, and V denotes the total volume of the system. Together, these equations admit two possible solutions:

$\overline{\boldsymbol{\phi}}_\perp = \mathbf{0}$ and $\overline{M} = \overline{\phi}_{\mathbf{z}}$: The total magnetisation of the system can be ascribed to population imbalance with no spontaneous magnetisation in-plane. Within this solution, $\overline{M}$ is a function of $|g\overline{\phi}_{\mathrm{z}} + \Delta\mu|$, so it can be used to infer the chemical potential shift, $\Delta\mu$.

$\overline{\boldsymbol{\phi}}_\perp \neq \mathbf{0}$: The total magnetisation takes the form $\overline{M} = (\overline{\boldsymbol{\phi}}_\perp^2 + \overline{\phi}_{\mathrm{z}}^2)^{1/2}$. Along the z-axis, the magnetisation is fixed due to population imbalance, with the additional magnetisation developing within the x-y plane. In this case, the saddle-point solution translates to the condition $\Delta\mu = 0$, i.e. no chemical

potential shift is required to recover the fixed z-component of the magnetisation due to the population imbalance; it is simply given by the resolved component of the total magnetisation.

The total population $N = N_\uparrow + N_\downarrow$ can in turn be obtained from the variation $\delta\overline{S}/\delta\overline{\rho} = 0$.

Expanding the action in interaction strength, g, $\overline{S} = g\phi_z^2 \operatorname{Tr}(1 + g\hat{G}_0\hat{G}_0) = g\phi_z^2(1 - g\nu)$, and one can extract the familiar Stoner criterion [107, 108] for a population balanced system, with ν being the density of states. For $g\nu < 1$ the state is unmagnetised, $\overline{M} = 0$, and chemical potentials of the two Fermi surfaces remain equal. If $g\nu > 1$ then the state is magnetised with $\overline{M} = \sqrt{(g\nu - 1)/g^3\nu''}$. We also note that the Stoner criterion can be reformulated to account for population imbalance giving $\overline{S} = g\phi^2(1 - g\nu) - g^2\Delta\mu^2$, leading to a transition at the same value of interaction strength as for the balanced system. Although, at this order, the saddle-point approximation predicts a continuous transition to a ferromagnetic phase for the balanced system, it is well-established that fluctuations of the magnetisation field drive the transition first order at low temperature [295]. This effect can be captured by retaining fluctuation contributions to second order in the interaction. In the following, we will explore the impact of fluctuations on the equations of motion associated with the uniform mean-field.

6.2.3   Integrating out auxiliary field fluctuations

To implement this program, it is convenient to parameterise the Hubbard-Stratonovich fields into some, as yet undetermined, stationary (spatially uniform) values ϕ_0 and ρ_0, and fluctuations around them, ϕ_{fl} and ρ_{fl}. Integrating out these fluctuations, the goal is to obtain the renormalised mean-field equations for ϕ_0 and ρ_0 retaining contributions to second order in g. Substituting $\phi = \phi_0 + \phi_{\text{fl}}$ and $\rho = \rho_0 + \rho_{\text{fl}}$ into Eqn. (6.3), and rotating the z-axis from the quantisation direction to lie along the direction of uniform magnetisation using the constant matrix T, one

obtains

$$\mathcal{Z} = e^{-\beta V g(\phi_0^2 - \rho_0^2)} \int \mathcal{D}\rho_{\text{fl}} \mathcal{D}\phi_{\text{fl}} \exp\left[-\int d\tau d\mathbf{r} \, g(\phi_{\text{fl}}^2 - \rho_{\text{fl}}^2)\right]$$
$$\times \exp\left[\text{Tr}\ln\mathsf{G}^{-1} + \text{Tr}\ln(\mathsf{I} + g\mathsf{G}\mathsf{T}^{-1}(\mathsf{I}\rho_{\text{fl}} + \boldsymbol{\sigma}\cdot\boldsymbol{\phi}_{\text{fl}})\mathsf{T})\right], \quad (6.5)$$

where now $\hat{G}_{\pm}^{-1} = \hat{G}_0^{-1} + g\rho_0 \mp |\Delta\mu\mathbf{e}_z + g\phi_0|$ denotes the elements of the inverse Green's function of the system at the level of the renormalised mean-field, $\hat{\mathsf{G}} = \text{diag}(\hat{G}_+, \hat{G}_-)$. Then, expanding the action to second order in fluctuations, $\rho_{\text{fl}}(\mathbf{r},\tau)$ and $\boldsymbol{\phi}_{\text{fl}}(\mathbf{r},\tau)$, and performing the functional integral, one obtains the thermodynamic grand potential from the quantum partition function using $\Phi_{\text{G}} = -\beta^{-1}\ln\mathcal{Z}$,

$$\Phi_{\text{G}} = \overbrace{\text{Tr}\ln\hat{G}_+^{-1} + \text{Tr}\ln\hat{G}_-^{-1}}^{\dagger} + g\left(\phi_0^2 - \rho_0^2\right)$$
$$+ \underbrace{\frac{1}{2}\text{Tr}\ln\left(1 - g^2\Pi_{++}\Pi_{--}\right)}_{\parallel} + \underbrace{\frac{1}{2}\text{Tr}\ln\left(1 + g\Pi_{+-} + g\Pi_{-+} + g^2\Pi_{+-}\Pi_{-+}\right)}_{\perp}, \quad (6.6)$$

a result that is independent of the transformation T. Here we have defined the spin-dependent polarisation operator,

$$\Pi_{ss'}(\omega,\mathbf{q}) = \frac{2}{\beta V}\sum_{\omega',\mathbf{k}} G_s(\omega',\mathbf{k})G_{s'}(\omega' - \omega, \mathbf{k} - \mathbf{q}), \quad (6.7)$$

where the sum on ω' runs over fermionic Matsubara frequencies. The term labelled ($\dagger$) simply represents the thermodynamic potential of a non-interacting Fermi gas with shifted chemical potentials. The term labelled ($\perp$) is due to transverse fluctuations of the magnetisation field and coincides with that obtained in Ref. [296]. By contrast, the term labelled ($\parallel$), corresponding to longitudinal fluctuations, differs from that obtained in Ref. [296] by the additional contributions from density fluctuation effects.

To proceed, we now expand the potential Φ_{G} to second order in g and perform the summations over Matsubara frequencies. Rearranging the momenta summations,

one obtains

$$\Phi_{\mathrm{G}} = -\frac{1}{\beta V} \sum_{\substack{\mathbf{k} \\ s=\{+,-\}}} \ln\left(1 + \mathrm{e}^{-\beta(\epsilon_{\mathbf{k}}-\mu_s)}\right) + g\left(\phi_0^2 - \rho_0^2\right) + gN_+N_-$$

$$+ \frac{2g^2}{V} \sum_{\mathbf{k}_{1,2,3}} \frac{\overbrace{n_+(\epsilon_{\mathbf{k}_1})n_-(\epsilon_{\mathbf{k}_2})}^{\diamondsuit}(1 - n_+(\epsilon_{\mathbf{k}_3}))(1 - n_-(\epsilon_{\mathbf{k}_4}))}{\epsilon_{\mathbf{k}_1} + \epsilon_{\mathbf{k}_2} - \epsilon_{\mathbf{k}_3} - \epsilon_{\mathbf{k}_4}}, \qquad (6.8)$$

where $\mu_s = \mu - g\rho_0 + s|\Delta\mu\mathbf{e}_{\mathrm{z}} + g\phi_0|$, $n_s(\epsilon) = (1 + \exp(-\beta(\epsilon - \mu_s)))^{-1}$, and $N_s = \sum_{\mathbf{k}} n_s(\epsilon_{\mathbf{k}})$. Conservation of momentum requires that $\mathbf{k}_1 + \mathbf{k}_2 = \mathbf{k}_3 + \mathbf{k}_4$. Physically, the numerator of the second order term indicates that the matrix element associated with the transition $(\mathbf{k}_1,\mathbf{k}_2) \to (\mathbf{k}_3,\mathbf{k}_4)$ is proportional to the probability that states $\mathbf{k}_1$ and $\mathbf{k}_2$ are occupied, whilst states $\mathbf{k}_3$ and $\mathbf{k}_4$ are unoccupied. Following Pathria [297] (and the earlier discussion of Abrikosov and Khalatnikov [295]), to renormalise the unphysical divergence of the term in $n^2(\epsilon)$, labelled $(\diamondsuit)$ close to resonance, we regularise the effective interaction at second order in scattering length a (see App. A.1),

$$g(\mathbf{k}_1,\mathbf{k}_2) \mapsto \frac{2k_{\mathrm{F}}a}{\pi\nu} - \frac{8k_{\mathrm{F}}^2 a^2}{\pi^2\nu^2 V^2} \sum_{\mathbf{k}_{3,4}} \frac{1}{\epsilon_{\mathbf{k}_1} + \epsilon_{\mathbf{k}_2} - \epsilon_{\mathbf{k}_3} - \epsilon_{\mathbf{k}_4}}, \qquad (6.9)$$

where $\nu = \sqrt{\mu}/\sqrt{2}\pi^2$ and $k_{\mathrm{F}} = \sqrt{2m\mu}$. In a population imbalanced system the definition for the chemical potential is that which gives the same total number of particles in the population balanced system, that is $k_{\mathrm{F}} = \sqrt[3]{3\pi^2(n_\uparrow + n_\downarrow)}$, where $n_\uparrow$ and $n_\downarrow$ are the number of up and down-spin particles; this definition holds true in both the canonical and grand canonical ensembles. This regularisation of the contact interaction exactly cancels the divergent terms in $n^2(\epsilon)$, labelled $(\diamondsuit)$. Furthermore, the terms in $n^4(\epsilon)$ are zero by symmetry. Finally, making use of the symmetry in

$\mathbf{k}_3$ and $\mathbf{k}_4$, one obtains

$$\Phi_{\mathrm{G}} = -\frac{1}{\beta V} \sum_{\substack{\mathbf{k} \\ s=\{+,-\}}} \ln\left(1 + \mathrm{e}^{-\beta(\epsilon_\mathbf{k} - \mu_s)}\right) + \frac{2k_{\mathrm{F}}a}{\pi\nu}\left(\phi_0^2 - \rho_0^2\right) + \frac{2k_{\mathrm{F}}a}{\pi\nu}N_+N_-$$
$$-\frac{8k_{\mathrm{F}}^2 a^2}{\pi^2 \nu^2 V^3} \sum_{\mathbf{k}_{1,2,3}} \frac{n_+(\epsilon_{\mathbf{k}_1})n_-(\epsilon_{\mathbf{k}_2})\left(n_+(\epsilon_{\mathbf{k}_3}) + n_-(\epsilon_{\mathbf{k}_3})\right)}{\epsilon_{\mathbf{k}_1} + \epsilon_{\mathbf{k}_2} - \epsilon_{\mathbf{k}_3} - \epsilon_{\mathbf{k}_4}} . \tag{6.10}$$

From the thermodynamic potential we can compute the free energy per unit volume $F = \Phi_{\mathrm{G}} + \sum_{\sigma=\{\uparrow,\downarrow\}}(\mu + \sigma\Delta\mu)N_\sigma$. To consolidate terms entering the free energy we switch from the population imbalance pseudo-spin basis to the magnetisation basis, retain contributions to order $\mathcal{O}((k_{\mathrm{F}}a)^2)$, recall that if $\Delta\mu = 0$ then $M \neq 0$, whereas if $\Delta\mu \neq 0$ then $M = 0$, and affect the rearrangement

$$\frac{2k_{\mathrm{F}}a}{\pi\nu}\left(\phi_0^2 - \rho_0^2\right) + \sum_{\sigma=\{\uparrow,\downarrow\}}(\mu + \sigma\Delta\mu)N_\sigma$$
$$= \overbrace{\left(\mu - \frac{2k_{\mathrm{F}}a}{\pi\nu}\rho_0 + \left|\Delta\mu\mathbf{e}_{\mathrm{z}} + \frac{2k_{\mathrm{F}}a}{\pi\nu}\phi_0\right|\right)}^{\mu_+}N_+ + \overbrace{\left(\mu - \frac{2k_{\mathrm{F}}a}{\pi\nu}\rho_0 - \left|\Delta\mu\mathbf{e}_{\mathrm{z}} + \frac{2k_{\mathrm{F}}a}{\pi\nu}\phi_0\right|\right)}^{\mu_-}N_-$$
$$\left.\begin{array}{l} +\frac{2k_{\mathrm{F}}a}{\pi\nu}\left(\phi_0^2 - \rho_0^2\right) + \left(\frac{2k_{\mathrm{F}}a}{\pi\nu}\rho_0 + \Delta\mu - \left|\Delta\mu\mathbf{e}_{\mathrm{z}} + \frac{2k_{\mathrm{F}}a}{\pi\nu}\phi_0\right|\right)N_+ \\ +\left(\frac{2k_{\mathrm{F}}a}{\pi\nu}\rho_0 - \Delta\mu + \left|\Delta\mu\mathbf{e}_{\mathrm{z}} + \frac{2k_{\mathrm{F}}a}{\pi\nu}\phi_0\right|\right)N_- \end{array}\right\} \varnothing . \tag{6.11}$$

Then, if we set $\phi_0 = \overline{\phi} + \Delta\phi$ and $\rho_0 = \overline{\rho} + \Delta\rho$, an expansion in $\Delta\phi$ and $\Delta\rho$ shows that the terms labelled ($\varnothing$) sum to zero to the accuracy of the free energy, $\mathcal{O}((k_{\mathrm{F}}a)^2)$. Retaining the remaining contribution, the free energy reduces to the form,

$$F = \overbrace{-\frac{1}{\beta V} \sum_{\substack{\mathbf{k} \\ s=\{+,-\}}} \ln\left(1 + \mathrm{e}^{-\beta(\epsilon_\mathbf{k} - \mu_s)}\right) + \sum_{s=\{+,-\}} \mu_s N_s}^{\ddagger} + \frac{2k_{\mathrm{F}}a}{\pi\nu}N_+N_-$$
$$-\frac{8k_{\mathrm{F}}^2 a^2}{\pi^2 \nu^2 V^3} \sum_{\mathbf{k}_{1,2,3}} \frac{n_+(\epsilon_{\mathbf{k}_1})n_-(\epsilon_{\mathbf{k}_2})\left(n_+(\epsilon_{\mathbf{k}_3}) + n_-(\epsilon_{\mathbf{k}_3})\right)}{\epsilon_{\mathbf{k}_1} + \epsilon_{\mathbf{k}_2} - \epsilon_{\mathbf{k}_3} - \epsilon_{\mathbf{k}_4}} . \tag{6.12}$$

This expression coincides [1] with that obtained in Ref. [285]. The method employed

---

[1]The result of Ref. [285] was a perturbation expansion to second order in the scattering length a considering all Green's function contributions. The term labelled ($\ddagger$) corresponds to the "$e^{(0)} - Ts$" term of Ref. [285] — i.e. the difference between the kinetic energy and entropy. The $\Delta\mu = 0$ limit has also been derived elsewhere [295, 297].

in the numerical calculation of the summation over three momenta is described in App. A.8.

6.2.4   Magnetisation

To minimise the free energy and obtain the net magnetisation it is convenient to take the expression for the thermodynamic potential (6.10) and affect the shift of the field $\Phi_z \mapsto \Phi_z - \Delta\mu\pi\nu/2k_{\mathrm{F}}a$. As a result, the thermodynamic potential takes the form

$$
\Phi_{\mathrm{G}} = -\frac{1}{\beta V} \sum_{\substack{\mathbf{k} \\ s=\{+,-\}}} \ln\left(1 + \mathrm{e}^{-\beta(\epsilon_{\mathbf{k}} - \mu_s)}\right) + \frac{2k_{\mathrm{F}}a}{\pi\nu}\left|\boldsymbol{\phi}_0 - \frac{\Delta\mu\mathbf{e}_z\pi\nu}{2k_{\mathrm{F}}a}\right|^2 - \frac{2k_{\mathrm{F}}a}{\pi\nu}\rho_0^2
$$
$$
+ \frac{2k_{\mathrm{F}}a}{\pi\nu}N_+N_- - \frac{8k_{\mathrm{F}}^2 a^2}{\pi^2\nu^2 V^3}\sum_{\mathbf{k}_{1,2,3}} \frac{n_+(\epsilon_{\mathbf{k}_1})n_-(\epsilon_{\mathbf{k}_2})\left(n_+(\epsilon_{\mathbf{k}_3}) + n_-(\epsilon_{\mathbf{k}_3})\right)}{\epsilon_{\mathbf{k}_1} + \epsilon_{\mathbf{k}_2} - \epsilon_{\mathbf{k}_3} - \epsilon_{\mathbf{k}_4}} \,, \quad (6.13)
$$

where, in response to the shift of Φ_z, the factors of $\mu_s = \mu - 2k_{\mathrm{F}}a\rho_0/\pi\nu + 2k_{\mathrm{F}}as|\boldsymbol{\phi}_0|/\pi\nu$ entering the definitions of $N_\pm$ and $n_\pm$ are now independent of $\Delta\mu$. The thermodynamic potential can be rewritten in terms of a function of just the auxiliary fields and the chemical potential shift as $\Phi_{\mathrm{G}} = F(|\boldsymbol{\phi}_0|) + 2k_{\mathrm{F}}a|\boldsymbol{\phi}_0 - \Delta\mu\mathbf{e}_z\pi\nu/2k_{\mathrm{F}}a|^2/\pi\nu - 2k_{\mathrm{F}}a\rho_0^2/\pi\nu$.

In the grand canonical ensemble, the thermodynamic potential must be minimised with respect to the components of the auxiliary field giving

$$
\frac{F'(|\boldsymbol{\phi}_0|)}{|\boldsymbol{\phi}_0|}\begin{pmatrix} \boldsymbol{\phi}_\perp \\ \phi_z \end{pmatrix} + \frac{4k_{\mathrm{F}}a}{\pi\nu}\begin{pmatrix} \boldsymbol{\phi}_\perp \\ \phi_z - \Delta\mu\pi\nu/2k_{\mathrm{F}}a \end{pmatrix} = \mathbf{0}\,, \quad (6.14)
$$

where $\boldsymbol{\phi}_\perp = (\phi_x, \phi_y)$ so $\boldsymbol{\phi}_0 = \boldsymbol{\phi}_\perp + \phi_z\mathbf{e}_z$. Following Sec. 6.2.2 one may now identify the magnetisation with the field $\boldsymbol{\phi}_0 - \pi\nu\Delta\mu\mathbf{e}_z/2k_{\mathrm{F}}a$. If $\Delta\mu = 0$, then the system of equations is solved by either $F'(|\boldsymbol{\phi}_0|)/|\boldsymbol{\phi}_0| + 4k_{\mathrm{F}}a/\pi\nu = 0$ (the direction of spontaneous ferromagnetism in-plane remains undetermined), or $\boldsymbol{\phi}_0 = \mathbf{0}$. If $\Delta\mu \neq 0$ then $\boldsymbol{\phi}_\perp = \mathbf{0}$, and the magnetisation is set by the equation $F'(\phi_z) = 2(\Delta\mu - 2k_{\mathrm{F}}a\phi_z/\pi\nu)$ and is oriented along the z-axis. This behaviour is analogous to what we saw in the mean-field analysis in Sec. 6.2.2. Finally, as a consistency check, one may note that the expected degree of population imbalance can be recovered

(a)

(b)
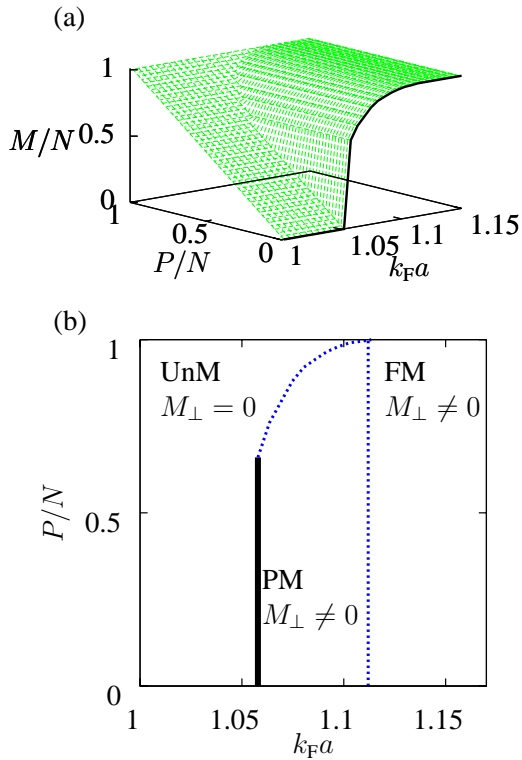
Figure 6.1: (a) shows the magnetisation M as a function of population imbalance, P and interaction strength $k_{\mathrm{F}}a = \sqrt[3]{3\pi^2(n_\uparrow + n_\downarrow)}$ in the canonical ensemble at $T = 0$ at fixed species populations. The thick line traces system variation at $P = 0$ which corresponds to trap profile ($P/N = 0$) in Fig. 6.3. (b) shows the phase boundary between "unmagnetised" (UnM) and partially magnetised (PM) region and the line of saturation before the fully-magnetised (FM) region. Note that, by unmagnetised, we refer to the not in-plane magnetisation. The solid line denotes first order transitions, the dashed second order and saturation.

from the grand potential $M = -\ \partial\Phi_{\mathrm{G}}/\partial\Delta\mu|_{T,V,N}$.

6.3   Population imbalance

With the formal part of the analysis complete, we will now apply these results to explore the implications of ferromagnetism in the atomic Fermi gas. To begin, let us consider the phase behaviour of the system in the canonical ensemble working at fixed particle number. The variation of the total magnetisation, $|M|$, as a function of interaction strength and particle imbalance can be found by minimising the free energy at fixed particle number. The results are shown in Fig. 6.1. To ensure that the free energy is locally *minimised* rather than just being at a *stationary value* [298], the curvature was examined numerically. In the balanced Fermi gas, $P = 0$, the results shown in Fig. 6.1(a) recapitulate those discussed by Duine and MacDonald [285]. In particular at zero temperature, when the interaction strength is small, $k_{\mathrm{F}}a \lesssim 1.05$, there is no net magnetisation. As the interaction strength is increased, at $k_{\mathrm{F}}a \approx 1.05$ there is a first order phase transition into a magnetised phase with $M/N \approx 0.6$. As $k_{\mathrm{F}}a$ is increased further the magnetisation rises until it is saturated

at $k_\mathrm{F}a \approx 1.11$.

With increasing population imbalance, P, at $k_\mathrm{F}a \lesssim 1.05$, where it is not energetically favourable for a spontaneous magnetisation to develop, the magnetisation is forced to stay pinned to the minimum value set by the imbalance. With increasing interaction strength, at $k_\mathrm{F}a \approx 1.05$ there is a first order transition and the magnetisation jumps to $M/N \approx 0.6$. This feature is consistent with the findings of the Stoner mean-field theory that the transition interaction strength found is independent of population imbalance. If the population imbalance is greater than $P/N \gtrsim 0.6$ then the magnetisation takes the value of the spontaneous magnetisation projected onto the sheet of minimum magnetisation caused by the population imbalance.

From these results, one can infer the corresponding zero temperature phase diagram Fig. 6.1(b). Characterising the phase behaviour by the strength of the in-plane magnetisation and the degree of polarisation, the phase diagram divides into three distinct regions. At low interaction strength the system is not spontaneously unmagnetised, though there can be a magnetisation fixed by the population imbalance. Then, at increased interaction strength the system become partially magnetised either through a first order (at low population imbalance) or a second order phase transition. At interaction strength above $k_\mathrm{F}a \gtrsim 1.11$ the magnetisation saturates.

To address the properties of the population imbalanced system in the grand canonical regime, we will divide our discussion between the uniform and trap geometries. In Sec. 6.3.1 we will address the properties of a uniform system where the chemical potential μ and shift $\Delta\mu$ are held constant (allowing the species populations to effectively interchange). Drawing on these results, we will then discuss the phase behaviour in a harmonic trap in Sec. 6.3.2.

6.3.1   Uniform system

In the spatially uniform system, when the chemical potentials of the two species are fixed, for each value of the interaction strength $k_\mathrm{F}a$ and relative shift in chemical potential $\Delta\mu/\mu$, from the free energy one can obtain the phase corresponding to
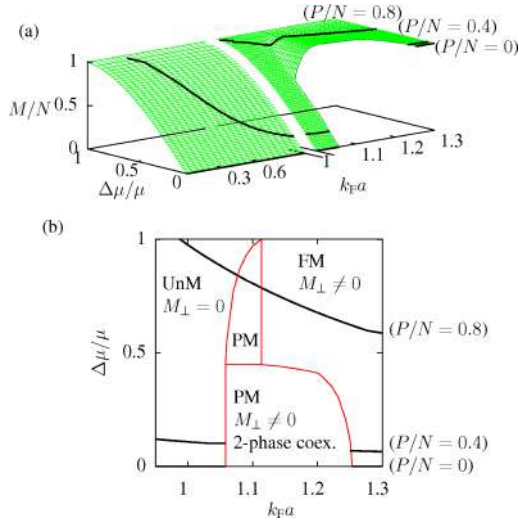
Figure 6.2: (a) shows the variation of magnetisation M as a function of chemical potential shift $\Delta\mu$ and interaction strength $k_{\mathrm{F}}a$ in the grand canonical ensemble at $T = 0$. The thick lines correspond to trap profiles at $P/N = 0$, $P/N = 0.4$, and $P/N = 0.8$ in Fig. 6.3. In the region where magnetisation is undefined there is phase separation. The lower set of diagrams show the phase boundaries (and saturation line) between "unmagnetised" (UnM), partially magnetised (PM) and fully-magnetised (FM) regions, as well as the region of phase separation.

minimal thermodynamic potential. Applying this procedure, the resulting phase behaviour is shown in Fig. 6.2. For $\Delta\mu/\mu = 0$ and small interaction strength $k_{\mathrm{F}}a \lesssim$ 1.05 there is no magnetisation. As the interaction strength is increased, at $k_{\mathrm{F}}a \approx$ 1.05 in the canonical regime Fig. 6.1 there is a first order phase transition into a fully-magnetised state. Working at fixed chemical potential [Fig. 6.2(a)], the phase transition straight into a saturated state increases the number of particles, which in turn increases the effective interaction strength to $k_{\mathrm{F}}a \approx 1.25$ (calculated using the chemical potential for a non-interacting system with the same total number of particles). This leads to an intermediate region of phase separation in the grand canonical regime. At $k_{\mathrm{F}}a \lesssim 1.05$ as the chemical potential shift is increased up to $\Delta\mu/\mu = 1$, the magnetisation increases up to its maximum saturated value as the Fermi surfaces become more unbalanced. At $\Delta\mu/\mu > 1$ the chemical potential of the minority spin species is negative so only the majority spin species remain and the system is fully magnetised. With a chemical potential shift the region of phase separation corresponds to the first order phase transition in Fig. 6.1. The corresponding phase diagram showing the regime of two-phase coexistence is shown in Fig. 6.2(b).

Finally, if the system has an imposed density and population imbalance, and the chemical potentials are free to vary, then there are two possibilities: Firstly, the spontaneous ferromagnetism is sufficient to provide the population imbalance and any excess magnetisation lies in the plane. This corresponds to a point on the line

$\Delta\mu = 0$ in Fig. 6.2. The second possibility is that spontaneous ferromagnetism is not sufficient, and so there is an additional chemical potential shift $\Delta\mu \neq 0$. In this case the magnetisation then points along the direction of population imbalance. This is consistent with the findings in Sec. 6.2.4. For a given interaction strength, the magnetisation increases with chemical potential shift to saturation, so there is always a chemical potential shift that will give a suitable population imbalance.

6.3.2   Trapped system

Using the insight gained from the study of the uniform system, we can now explore an atomic Fermi gas in the physical system — a potential trap. Without loss of generality we take $\uparrow$ ($\downarrow$) to represent the majority (minority) species of atoms. We focus on a harmonic trap, with rescaled spatial coordinates to ensure a spherically symmetric trapping potential, $V(\mathbf{r}) \sim r^2$. Furthermore, we make use of the local density approximation in which the chemical potential of both species $\mu_{\mathrm{eff},\sigma}(\mathbf{r}) = \mu_{0,\sigma} - V(\mathbf{r})$ are renormalised by the same trapping potential. Although there is some experimental evidence [251, 252] that the local density approximation might not be valid [196, 253] in some setups, we believe that its application here will correctly address the qualitative phase structure. The chemical potentials are regarded to be locally fixed, therefore the local phase is that of the uniform system in the grand canonical regime examined in Sec. 6.3.1. With a constant chemical potential shift $\Delta\mu$ and interaction strength g, but varying effective chemical potential μ, the system follows the trajectory $k_{\mathrm{F}}a \propto \sqrt{\mu}$ and $\Delta\mu/\mu \propto 1/\mu$ in the grand canonical regime shown in Fig. 6.2. If the chemical potential is large, the system spontaneously becomes ferromagnetic, and the magnetisation is saturated; if the chemical potential is small, the relative chemical potential shift is large ensuring the magnetisation is again near saturation. The locus in Fig. 6.2 shows that, in the intermediate region, the magnetisation can develop a minimum depending on the degree of population imbalance.

To understand the behaviour in the trap geometry, one should note the following: If the degree of equilibrium pseudo-spin magnetisation is in excess of that imposed by total population imbalance alone, the analysis of Sec. 6.2.4 tells us that some
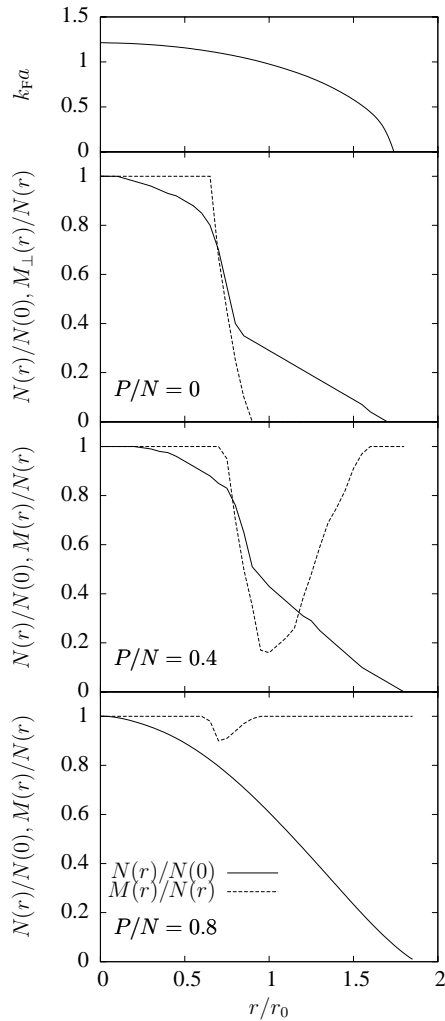
Figure 6.3: The density of particles at radius r in a trap potential profile at three different values of total population imbalance. The variation in the local particle density N is shown by the solid line, and the variation in the local magnetisation M is shown by the dashed line. The plot densities are renormalised by their central density, N_0, radii by the outer radius, r_0, of non-interacting particles with the same average inner chemical potential, μ_0. The upper panel shows the effective $k_F a$ in the $P/N = 0$ case.

component of the spontaneous magnetisation lies along the z-axis with the remainder oriented in the x-y plane. If, however, net population imbalance is large, then $\Delta\mu \neq 0$ and no in-plane magnetisation develops. Here one may identify three characteristic behaviours with radial density profiles shown in Fig. 6.3. The first ($P/N = 0$) has in-plane magnetisation, and the others do not. The second ($P/N = 0.4$) has a first order transition and non-zero phase separation whereas the third ($P/N = 0.8$) is always fully magnetised due to strong interactions. The three plots all have the same central chemical potential.

The first possibility shown in Fig. 6.3($P/N = 0$) is at small population imbalance, involving the development of a spontaneous magnetisation which is in excess of what can be absorbed by population imbalance alone, in this case $\Delta\mu = 0$ and

some magnetisation lies in the plane. At small radii, where the interaction strength $k_{\mathrm{F}}a > 1.25$ is greater than the limit for ferromagnetism, the results of the uniform system (Sec. 6.3.1) show that there is saturated ferromagnetism in the plane and a normal component that provides the fixed population imbalance. Following this there is a region of phase separation and then at $k_{\mathrm{F}}a \approx 1.05$ there are equal particle densities and no magnetisation. The outer edge of the particle distribution of both species is where $\mu_0 = V(r_0)$.

In the second scenario shown in Fig. 6.3($P/N = 0.4$) the spontaneous magnetisation is not sufficient to provide population imbalance alone, in this case we require $\Delta\mu \neq 0$, and all magnetisation is oriented along the axis of population imbalance. From the trap centre the population imbalance is first fully saturated, followed by a region of phase separation, into a region of partial magnetisation. This causes the minority spin particles to have a sharp maximum number density at $r/r_0 \approx 0.6$, and the magnetisation to have a corresponding minimum; this counters the intuitive expectation that number density should rise towards the trap centre due to the increasing effective chemical potential. As the effective chemical potential continues to fall with increasing radius, the minority spin species population falls more rapidly than the majority and magnetisation increases. At a large radius, the chemical potential of the minority spin particles reaches zero before the majority spin so there is a thin shell containing only majority spin particles at the outside and so is fully magnetised.

The third possibility shown in Fig. 6.3($P/N = 0.8$) is that the locus in Fig. 6.2 does not cross the first order transition and region of phase separation. At $\Delta\mu/\mu < 1$ the system is fully magnetised due to the strong interactions between particles. At $\Delta\mu/\mu > 1$ the system is fully magnetised due to there being no minority spin particles. In the intermediate regime there is a narrow band where the system is partially polarised. The majority spin species exists out to greater radius than in cases ($P/N = 0$) and ($P/N = 0.4$) because $\Delta\mu$ is larger so a greater potential at a larger radius is required to give the majority spin species zero effective chemical potential.

6.4 Discussion

To conclude, let us now consider four methods of how spin magnetisation could be detected experimentally. Firstly, the interaction energy can be estimated by studying the expansion of the gas [31]. Time of flight measurements of the expanding cloud with no external magnetic field $B = 0$ are ballistic and so can provide the initial kinetic energy. If the magnetic field is present, $B \neq 0$, then interactions are significant during the expansion. Collisions ensure that all of the interaction energy is converted into kinetic energy so the measurements reflect the total released energy. Taking the difference between the $B \neq 0$ and $B = 0$ measurements therefore probes the interaction energy. An unmagnetised gas has interaction energy whereas the fully magnetised gas has zero interaction energy so time of flight measurements should allow the ferromagnetic state to be detected.

Radio frequency spectroscopy [37] allows one to probe the spatial variations of scattering lengths by exciting the atoms from one spin state $|1\rangle$ into some other state $|3\rangle$ whilst leaving the atoms in the second spin state $|2\rangle$ unaffected. The presence of atoms in state $|2\rangle$ shifts the resonance ν_{13} by $\Delta\nu_{13} = 2n_2(a_{23} - a_{21})$, where a_{ij} is the scattering length between states $|i\rangle$ and $|j\rangle$. Measurement of the resonance shift could allow the spatial distribution of the individual species to be probed. The presence of the ferromagnetic state could be inferred by looking for the characteristic density profiles outlined in Sec. 6.3.1.

A third simple method of detecting a ferromagnetic transition could be to monitor the size of the atomic cloud. In a harmonic trap the cloud size is proportional to the square root of the Fermi energy. Therefore, the size of the fully-magnetised state is $2^{1/3}$ larger than the unmagnetised.

On the repulsive side of the Feshbach resonance three-body collisions can result in the formation of a molecular bound state of two atoms that might destroy the atomic gas before it has time to undergo ferromagnetic ordering. To overcome this obstacle an atomic gas spin could be polarised along the magnetic field direction and an RF $\pi/2$ pulse applied to rotate all the spins into the plane [37]. The rate of precession of the spins is set by the magnetic field strength, which varies across the atomic gas due to field inhomogeneities. The precession rate of the atoms would however be kept

locked together by the ferromagnetic interaction. Furthermore the ferromagnetic phase has an antisymmetric wave function which inhibits collisions and so prevents the formation of molecular bound states. A signature of ferromagnetism is therefore the absence of molecular bound state formation.

We now outline two possible ways to further our analysis. The first order phase transition leads to discontinuities in the density and magnetisation leading to phase separation. Such behaviour could lead to a breakdown of the local density approximation, a potential source of inaccuracy in our analysis. This could be fixed through inclusion of a surface energy.

The second is to investigate the possibility that magnetic texture could develop. Textured modes may have been seen via the possible formation of a CDW/SDW in experimental results on the analogous solid state systems of itinerant electron ferromagnets UGe_2 [286, 287], Calcium Ruthenate ($Ca_3Ru_2O_7$) [299], and MnSi [50]. In Chp. 7 our general formalism is extended to include the possibility of a textured phase which lies beyond the first order line in the putative paramagnetic regime.

In conclusion we have developed a general formalism to describe itinerant ferromagnetic transitions in two-component fermionic cold atom systems with repulsive interactions, and potential population imbalance. At low population imbalance, we predict that the first order transition that characterises the balanced system persists. However, when the imbalance is large the transition becomes continuous. In the trap geometry we found the first order phase transition led to discontinuities in density and magnetisation. Up to a critical total population imbalance, set by the possible total magnetisation following a first order transition, the phases in the trap had the same density and magnetisation profiles with increasing population imbalance, but in-plane magnetisation fell. With population imbalance above this level, the system requires a chemical potential shift to generate a population imbalance; however there is still a small range over which a first order phase transition is seen. In the two latter cases the local population imbalance displayed a characteristic minimum with radius.

Part III

Critical phenomena in correlated quantum systems

As experimentalists gain access to ever lower temperatures, the thermal fluctuations in a system die away as quantum fluctuations take over. Coupling between these quantum fluctuations can lead to a new paradigm of quantum phase transitions. In Chp. 7 we apply the formalism developed in Chp. 6 to predict a textured ferromagnetic phase that preempts the first order ferromagnetic transition, and in Chp. 8 we study the consequences of quantum critical fluctuations on ferroelectric phenomena.

Chapter Seven

Textured itinerant ferromagnetism

MANY analytical techniques suggest that quantum fluctuations lead to a fundamental instability of the Fermi liquid that drives ferromagnetic transitions first order at low temperatures. We present both analytical and numerical evidence that this first order transition is preempted by the formation of an inhomogeneous spin phase in a manner that is closely analogous to the formation of the inhomogeneous superconducting FFLO state. To conclude we discuss the experimental systems in which these effects may be seen.

7.1 Introduction

Many magnetic materials, for example iron, display second order ferromagnetic phase transitions. The temperature at which this transition occurs can be tuned using external parameters such as doping and pressure. Hertz realized that tuning such a transition to zero temperature could give rise to a new type of critical universality – for which he coined the term quantum criticality [300]. This proposal has led to a tremendous experimental and theoretical effort that has had notable successes. The universal scaling for the quantum critical regime are seen in a variety

of materials [301].

However, in all systems that have been investigated so far, new behaviour intervenes before the transition can be tuned to absolute zero. In heavy fermion materials, the second order transition will often become first order before the quantum critical point is reached [58, 302, 303]. Example materials include $ZrZn_2$ [47, 48], UGe_2 [49], MnSi [50, 51], and CoS_2 [52]. Recent experimental evidence points to novel phenomena that go beyond the first order transition, with materials such as $ZrZn_2$ [47], UGe_2 [286, 287], $Ca_3Ru_2O_7$ [299], Iron-Niobium ($NbFe_2$) [304] and $Sr_3Ru_2O_7$ all displaying unusual behaviour in the vicinity of the putative quantum critical point. This universal failure to find a naked quantum critical point has lead to speculation that it represents a fundamental principle [305]. Diagrammatic calculations that extend beyond the standard Moriya-Hertz-Millis theory of itinerant quantum criticality suggest a fundamental breakdown of the GL expansion around the quantum critical point. Indeed, older results [306, 307] using straightforward second order perturbation theory, can be used to show that quantum fluctuations of particle-hole pairs lead to a first order transition [285]. An alternative field theoretical approach detailed in Chp. 6 [4] unifies these two pictures.

We show that in situations where a linearisation of the electron dispersion about the Fermi surface is permissible, the first order magnetic transition is always preempted by the formation of a spatially modulated or inhomogeneous magnetic phase, This is closely analogous to the inhomogeneous superconducting FFLO state [43, 44] that was explored in the context of ultracold atomic gases in Chp. 4. This modulated phase was presaged by non-analyticities in the gradient expansion that appear in extensions to the Moriya-Hertz-Millis theory [58, 302, 303, 308, 309]. Here, we use the alternative field theoretical approach developed in Chp. 6 [4] to provide analytical evidence for our picture. This has two advantages: i) it avoids non-analyticities; ii) it allows us to develop a simple and appealing picture of how quantum fluctuations drive the reconstruction of the phase diagram. These analytical considerations are supported by numerical QMC simulations that we also report here.

The remainder of this chapter is organised as follows: we begin in Sec. 7.2 by

stating our model Hamiltonian and give a brief exposition of our analytical approach, followed by the details of our QMC simulations in Sec. 7.3. Finally in Sec. 7.4, we suggest how our mechanism might be probed in future theoretical and experimental studies.

7.2 Ginzburg-Landau expansion

Our analysis is based on a model of electrons with a contact interaction of strength g

$$\hat{H} = \sum_{\mathbf{p},\sigma} \frac{p^2}{2m} a^\dagger_{\mathbf{p}\sigma} a_{\mathbf{p}\sigma} + \frac{g}{2} \sum_{\{\mathbf{p}_i\},\{\sigma_i\}} a^\dagger_{\mathbf{p}_1\sigma_1} a^\dagger_{\mathbf{p}_2\sigma_2} a_{\mathbf{p}_3\sigma_3} a_{\mathbf{p}_4\sigma_4} , \qquad (7.1)$$

where the second summation is carried out under the conservation of momentum $(\mathbf{p}_1 + \mathbf{p}_2 = \mathbf{p}_3 + \mathbf{p}_4)$ and spin $(\sigma_1 + \sigma_2 = \sigma_3 + \sigma_4)$. One simple approximation is to replace the particle creation and annihilation operators with their mean field estimates which leads to the Stoner model. This model describes a playoff between kinetic and potential energy which predicts a second order ferromagnetic phase transition such as that seen in iron. However, the mean-field approximation neglects the important consequences of quantum fluctuations; when these were summed over in Ref. [4, 58, 302, 303], the coupling between transverse fluctuations and the magnetisation leads to the presence of a non-analytic term $m^4 \ln m^2$ in the free energy that is responsible for driving the ferromagnetic transition first order.

Our strategy is to build upon the analysis of the first order homogeneous transition developed in Chp. 6 [4]. We extend the analysis by postulating that a textured ferromagnetic phase will develop by a continuous transition, which will initially develop at a single wave vector, allowing the ansatz that it is a spin spiral. This is the same ansatz used in the original analysis of the FFLO state and we shall revisit it in the discussion. To analyse the inhomogeneous spin phase, we take the Hamiltonian Eqn. (7.1) and using the tools expounded in App. A.2.5 we perform a Hubbard-Stratonovich transformation in both density ρ and magnetisation ϕ

channels to give the action

$$S[\phi] = \beta g(\phi^2 - \rho^2) - \operatorname{Tr}\ln(\mathsf{I}G_0^{-1} + g(\mathsf{I}\rho + \boldsymbol{\sigma}\cdot\boldsymbol{\phi})),\qquad(7.2)$$

where $G_0^{-1} = \mathrm{i}\omega + \epsilon_{\mathbf{p}} - \mu$ and $\epsilon_{\mathbf{p}} = p^2/2m$. We then consider a general spin spiral, built up from a constant magnetisation $\mathbf{m}_{\mathrm{c}}$ and a spiral modulated component $\mathbf{m}$ with wave vector $\mathbf{q}$ that rotates around axis $\hat{\mathbf{n}}$ (which without loss of generality is assumed to be along $\hat{\mathbf{z}}$). Following a gauge transformation that renders the magnetisation spatially homogeneous we obtain

$$S[\phi] = \beta g(m^2 + m_{\mathrm{c}}^2 + \phi_{\mathrm{fl}}^2 - \rho^2) - \operatorname{Tr}\ln\left(G_{\sigma_{\mathrm{z}}}^{-1} + g(\mathsf{I}\rho + \boldsymbol{\sigma}\cdot\boldsymbol{\phi}_{\mathrm{fl}} + \boldsymbol{\sigma}\cdot\boldsymbol{m}_{\mathrm{c}} + \sigma_{\mathrm{x}}m)\right),$$
$$(7.3)$$

with $G_{\pm}^{-1} = \mathrm{i}\omega + \epsilon_{\mathbf{p}\pm\mathbf{q}/2} - \mu$. Under this formalism the different classes of planar spin spiral (with $m_{\mathrm{c}} = 0$) have the same energy. Though the expression is not tractable with $m_{\mathrm{c}} \neq 0$ we note that in an expansion $F = t(q)m^2 + t(0)m_{\mathrm{c}}^2 + um^2m_{\mathrm{c}}^2$ that, if a modulated phase does preempt the uniform phase (which will be verified later), then $t(q)$ will become negative at smaller interaction strength than $t(0)$. Therefore, irrespective of the sign of u, the planar spin spiral will be favoured over any spin spiral with $m_{\mathrm{c}} \neq 0$. We therefore proceed with $m_{\mathrm{c}} = 0$ and expand to second order in both the auxiliary field m and also to second order in the quantum fluctuations of the magnetisation $\boldsymbol{\phi}_{\mathrm{fl}}$ and density ρ_{fl}

$$
\begin{aligned}
S[\boldsymbol{\phi}] &= \beta g m^2 + g^2 \operatorname{Tr}\left(G_+ m G_- m\right) \\
&+ \beta g \operatorname{Tr}\left(\rho_{\mathrm{fl}}^2 + \phi_{\mathrm{fl,x}}^2 + \phi_{\mathrm{fl,y}}^2 + \phi_{\mathrm{fl,z}}^2\right) - 2g^3 \operatorname{Tr}\left[G_+ m \left(G_-\rho_{\mathrm{fl}}G_-\phi_{\mathrm{fl,x}} + G_-\phi_{\mathrm{fl,x}}G_-\rho_{\mathrm{fl}}\right)\right] \\
&+ g^2\Big[\operatorname{Tr}\left(-G_0\rho_{\mathrm{fl}}G_0\rho_{\mathrm{fl}} - 2g^2G_+\rho_{\mathrm{fl}}G_+\rho_{\mathrm{fl}}G_+ m G_- m - g^2 G_+\rho_{\mathrm{fl}}G_+ m G_-\rho_{\mathrm{fl}}G_- m\right) \\
&+ \operatorname{Tr}\left(G_0\phi_{\mathrm{fl,x}}G_0\phi_{\mathrm{fl,x}} + 2g^2G_+\phi_{\mathrm{fl,x}}G_+\phi_{\mathrm{fl,x}}G_+ m G_- m + g^2 G_+\phi_{\mathrm{fl,x}}G_+ m G_-\phi_{\mathrm{fl,x}}G_- m\right) \\
&+ \operatorname{Tr}\left(G_0\phi_{\mathrm{fl,y}}G_0\phi_{\mathrm{fl,y}} + 2g^2G_+\phi_{\mathrm{fl,y}}G_+\phi_{\mathrm{fl,y}}G_+ m G_- m - g^2 G_+\phi_{\mathrm{fl,y}}G_+ m G_-\phi_{\mathrm{fl,y}}G_- m\right) \\
&+ \operatorname{Tr}\left(G_0\phi_{\mathrm{fl,z}}G_0\phi_{\mathrm{fl,z}} + 2g^2G_+\phi_{\mathrm{fl,z}}G_+\phi_{\mathrm{fl,z}}G_+ m G_- m - g^2 G_+\phi_{\mathrm{fl,z}}G_+ m G_-\phi_{\mathrm{fl,z}}G_- m\right)\Big].
\end{aligned}
$$
$$(7.4)$$

After integrating out the Gaussian quantum fluctuations, and re-expanding the

resulting energy to quadratic order in the auxiliary field m we find that the quadratic coefficient in a Landau expansion $S(\mathbf{q}) = \alpha_{0,0} + t(\mathbf{q})m^2 + u(\mathbf{q})m^4 + \cdots$ is

$$
t(\mathbf{q}) = \overbrace{\frac{1}{g} - g\Pi(\mathbf{q})}^{\dagger} + g^2\Pi(\mathbf{q})\left(\Pi(\mathbf{q}) - 2N^2\right) + 4g^3\sum_{\mathbf{p},\mathbf{p}'}\Pi(\mathbf{p}')G^2(\mathbf{p})G(\mathbf{p}+\mathbf{p}')G(\mathbf{p}+\mathbf{q})
$$
$$
- 4g^3\sum_{\mathbf{p}}\left(\sum_{\mathbf{p}'}G(\mathbf{p}')G(\mathbf{p}'+\mathbf{p})G(\mathbf{p}'-\mathbf{q})\right)^2, \tag{7.5}
$$

where $G(\mathbf{p}) = (i\omega - \varepsilon(\mathbf{p}) + \mu)^{-1}$, N is the particle density, and $\Pi(\mathbf{q}) = \sum_{\mathbf{p}} G(\mathbf{p} + \mathbf{q})G(\mathbf{p})$. The term labelled "$\dagger$" corresponds to the Stoner model of the transition. In order to remove unphysical ultraviolet divergences we re-regularise the interaction parameter which allows us to make the link $g \mapsto 2k_{\mathrm{F}}a/\pi\rho_{\mathrm{F}}$, where ρ_{F} is the density of states at the Fermi surface and a in the physically observable scattering length that is introduced in App. A.1. We note that, at $q = 0$, the free energy agrees, within the scope of the expansion, with the uniform phase derived in Chp. 6 [4]. The momentum integrals at zero temperature for the uniform phase are possible only for the balanced case as described in Chp. 6 [4], so the finite temperature and inhomogeneous phase integrals demanded here were calculated numerically.

As shown in Fig. 7.1 the Landau expansion predicts that a second order transition into an inhomogeneous spin phase preempts the first order phase transition. The expansion cannot however describe how far the textured phase penetrates into the uniform ferromagnetic phase. Using the Landau expansion formalism we also verify that at $q = 0$ if the transition were restricted to be second order then the system becomes ferromagnetic only after the first order transition and joins smoothly to the second order phase boundary at temperatures above the tricritical point. Furthermore, this putative second order phase boundary has negative slope at $T = 0$, consistent with Refs. [310, 311].

In analogy to FFLO [66, 67], the presence of the tricritical point immediately hints at the possibility of a textured phase. The most straightforward way to uncover this link is to consider the free energy as a functional of the up and down-spin Green functions $G_\uparrow$ and $G_\downarrow$; $F[G_\uparrow, G_\downarrow]$. Using the GL phenomenology described in App. A.3, we aim to derive the parameters in the GL expansion

Figure 7.1: The lower graph shows the development of modulated ferromagnetism, the solid line shows the first order and the dashed line the second order transition into the homogeneous ferromagnetic state. The dotted line shows the assumed second order phase transition into a modulated ferromagnetic state, that is the spinodal line. The textured and uniform phases are shaded, and the putative penetration of the textured into the uniform phase is highlighted by the intermediate shaded tone, labelled "?". The upper graph shows the wave vector q of the modulated phase boundary, plotted along the second order phase boundary between the normal and textured phase.
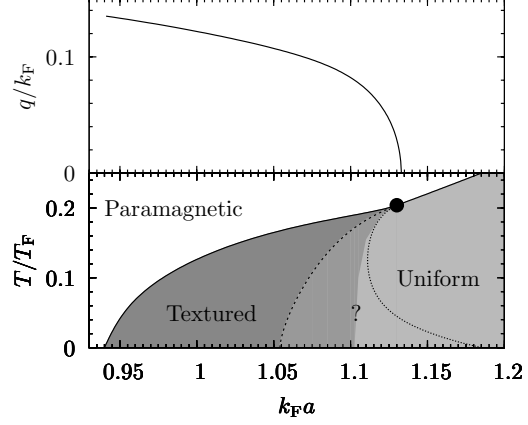
$F = \sum_{i,j=0}^{\infty} \alpha_{i,j} m^{2i} q^{2j}$ we first need to evaluate the operators $\partial G_{\uparrow\downarrow}/\partial q = \pm p \cos\theta$ and $\partial G_{\uparrow\downarrow}/\partial m = \pm 1$. We note that the second order differential with respect to q yields a factor of $p^2 \cos^2\theta$ relative to the second order differential with respect to m, that, in the pole dominated regime near to the tricritical point, will average to $2p_F^2/3$. Therefore $3\partial^2 F/\partial q^2 = 2p_F^2 \partial^2 F/\partial m^2$, and so in the GL expansion this implies the relationship between terms $3\alpha_{i+1,0} = 2\alpha_{i,1}p_F^2$. In particular this means that the coefficients of the terms m^4 and $q^2 m^2$ are directly related and therefore we expect that the tricritical point where $u(0)$ changes sign has an accompanying inhomogeneous spin phase driven by a switching sign of $t(q)$.

Using the theory developed above we can estimate the temperature at which the tricritical point and appearance of spatial modulation occur. The mean-field contribution to the M^4 coefficient in the expansion of energy is $\sim (g^3/T^2)e^{-\epsilon_F/T}$ and the quantum fluctuation correction to this coefficient is $\sim -\rho_F^3 g^6/\epsilon_F^2$. To logarithmic accuracy, therefore, one may estimate the tricritical temperature to be $T \sim -\epsilon_F/3\ln(\rho_F g)$. This temperature is a significant fraction of the Fermi temperature, which is typically two orders of magnitude greater than the tricritical point temperature seen in typical materials. The cause of this discrepancy is not known, though could be due to the approximation that electron-electron screening renders their interactions to be contact-like.

7.3   Quantum Monte Carlo

We now turn now to the numerical Quantum Monte Carlo analysis of the Stoner Hamiltonian (7.1) making use of the CASINO program [312] that is introduced in App. A.4. These methods are based upon optimising a trial wave function and are restricted to zero temperature. Our approach mirrors that used in previous studies of itinerant ferromagnetism [118, 313, 314]. The variational wave function used in our simulation, $\psi = D\mathrm{e}^{-J}$, is a product of a Slater determinant, D, that takes account of the Fermion statistics and occupation of single particle orbitals, and a Jastrow factor, J, that accounts for electron correlations.

The Slater determinant consists of plane-wave spinor orbitals containing both spin-up and spin-down electrons, $D = \det(\{\psi_{\mathbf{k}\in k_\uparrow}, \bar{\psi}_{\mathbf{k}\in k_\downarrow}\})$. As detailed in App. A.4.8, this is not an exact eigenstate of the total spin, but the Slater determinant contains many more states with low than high spin so the low spin state provides the dominant contribution to the variational state energy. In the case of uniform magnetisation, for computational efficiency, we factorise the Slater determinant into an up and a down-spin determinant [312]. With more up than down-spin orbitals present the wave function adopts an overall magnetisation set by that ratio. At first calculations were performed within the simple setting of the unmagnetised system to determine how the ground state energy varies with system size, and twist averaging was employed as a second tool to reduce finite size errors. Once the energy scaling with system size was determined for the unmagnetised system the same correction factor could be applied to the magnetised system. The wave function can contain only a discrete number of orbitals, here 19, 27, 33, 57, 81, 93, or 123 of a given spin type. As the magnetisation can only take on set values calculations could not be repeated at the same magnetisation for different system sizes, so finite size effects had to be removed using the calibration derived in the unmagnetised regime.

The spin textured phase is described by non-collinear spins, which have only recently been studied within Variational Monte Carlo (VMC) [315]. These studies lead us to describe a planar spin spiral with a trial wave function that contains the spinors $\psi_{\mathbf{k}} = \mathrm{e}^{\mathrm{i}\mathbf{q}\cdot\mathbf{r}/2}(\mathrm{e}^{\mathrm{i}\mathbf{k}\cdot\mathbf{r}}, \mathrm{e}^{-\mathrm{i}\mathbf{k}\cdot\mathbf{r}})$ and $\bar{\psi}_{\mathbf{k}} = \mathrm{e}^{-\mathrm{i}\mathbf{q}\cdot\mathbf{r}/2}(-\mathrm{e}^{\mathrm{i}\mathbf{k}\cdot\mathbf{r}}, \mathrm{e}^{-\mathrm{i}\mathbf{k}\cdot\mathbf{r}})$ which explicitly

Figure 7.2: The lower panel shows the ground state magnetisation M with interaction strength $k_F a$, the solid line corresponds to the uniform phase, the dashed line is the textured phase. The upper panel shows the wave vector of the inhomogeneous spin phase, and the discrete values of q sampled in the investigation are highlighted by the horizontal dotted lines.
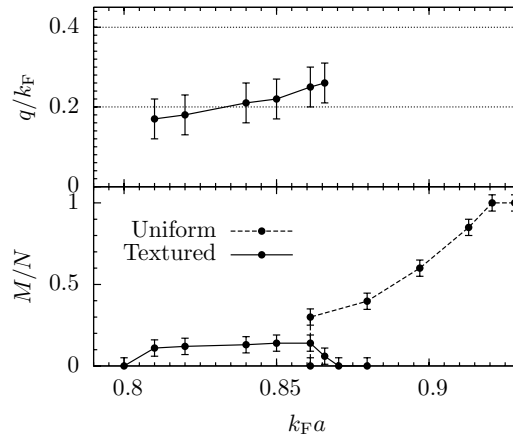
fix the spin spiral orientation. The energy was interpolated from QMC runs at $q/k_F = 0$, 0.2, and 0.4; at $q = 0$ this would recover the factorised form for the Slater determinant employed in the uniform case. Our simulations are carried out in a unit cell with periodic boundary conditions commensurate with the pitch of the spiral.

The Jastrow factor, J, accounts for electron-electron correlations. It consists of the polynomial and plane-wave expansions in electron-electron separation proposed in Ref. [133] and detailed in App. A.4.4. To further optimise the wave function the orbitals in the Slater determinant were evaluated at quasiparticle positions related to the electrons through a polynomial backflow function [316]. In the spiral case, the Jastrow factor is restricted to be spin independent to maintain the spin spiral orientation and the wave function antisymmetry. The impact of this constraint was tested by comparing the result of calculations on the uniform system with a restricted Jastrow factor to a calculation with the unrestricted Jastrow factor. Typically the unrestricted Jastrow factor required a polynomial expansion of six terms, whereas the restricted Jastrow factor required that eight terms be present. The trial wave functions were optimised using QMC methods. In the uniform case, the optimisation was performed in two steps using VMC and Diffusion Monte Carlo, whereas only VMC calculations were performed for the textured state.

To model the repulsive contact potential between the electrons we employ the modified Pöschl-Teller interaction [39, 317–319]

$$U(r) = \frac{2\mu U_0}{\cosh^2(\mu r)}, \tag{7.6}$$

where U_0 is the well depth and $1/\mu$ the well width. This form was chosen because it has smooth edges that the QMC configurations can sample faithfully. To ensure that the well was a suitable model for the contact interaction we checked that the results did not depend on different well parameters that have the same scattering length, and that a square well potential gives the same result.

To analyse the system we first constrained the magnetisation to be spatially uniform. At each interaction strength the energy at nine different values of the magnetisation was found and then interpolated to find the minimum ground state energy. The statistical error in the energy estimates produced by QMC led to the uncertainty in the ground state magnetisation at each interaction strength sampled in Fig. 7.2. The plot reveals a first order phase transition into the itinerant ferromagnetic phase at $k_\mathrm{F}a = 0.86$. The discrepancy from the analytic prediction of $k_\mathrm{F}a = 1.054$ arises because the analytics were based on perturbing in an interaction strength that in reality is not small. However, the confirmation of the first order transition indicates that the analytics capture the essence of the transition and provide confidence in using them to explore the possibility of a textured ferromagnetic phase.

The verification of the first order transition into a uniform phase provides a platform upon which to construct the full textured phase diagram. Calculations were performed at three different values for the magnetisation $M/N = 0, 0.1, 0.2$ and three different texture wave vectors $q/k_\mathrm{F} = 0, 0.2, 0.4$ at each interaction strength. Interpolating between the results showed that an inhomogeneous magnetic phase pre-empts the transition into the uniform phase with $q \approx 0.2k_\mathrm{F}$ and $M/N = 0.15$. The resulting textured phase has similar extent and wave vector to the analytical prediction lending support to the conclusions of the perturbative field theoretic analysis. Furthermore the results indicate that the textured phase penetrates into the uniform phase between $k_\mathrm{F}a = 0.85$ and $k_\mathrm{F}a = 0.86$, which we were not able to estimate analytically.

7.4 Discussion

We have shown that quantum fluctuations can lead to a reconstruction of the itinerant electron ferromagnetic phase transition to produce an intermediate spatially modulated or inhomogeneous phase. We have restricted our analysis to the consideration of the simplest modulated phase that can be formed from a ferromagnet – the spin spiral. In the same way as the FFLO state might consist of a patterned phase formed by the superposition of several such spirals, so the inhomogeneous phase might harbour spin crystalline order. Neither the computational nor the analytical study are able to shed light upon whether there is a more patterned textured phase that beats the spin spiral, or whether the transition into it from the normal state is continuous. However, should a more patterned phase be favourable, or the transition into the textured phase not be continuous, then this will in both cases result in the textured phase occupying a larger region of the phase diagram than predicted here. This will not invalidate the main conclusion of this work that a textured phase preempts the first order ferromagnetic phase transition.

In other contexts, it has been shown that features in the density of states due to an electronic band dispersion can lead to a first order ferromagnetic transition [109, 320, 321] and to the formation of an inhomogeneous magnetic phase [322]. It is natural to ask what is the relationship between the lattice-driven and fluctuation-driven reconstructions of the magnetic phase diagram. This is largely an open question. We have made preliminary investigations using an extension of the Wohlfarth-Rhodes criterion [109]. This criterion determines when rigid features in the electron density of states may drive a ferromagnetic transition first order. It consists of a requirement that the fourth order term in the expansion of free energy in magnetisation becomes negative. Allowing the electron dispersion to change self-consistently due to interactions, the density of states acquires a magnetisation dependence and the requirement that the quartic term be negative leads to an extended Wohlfarth-Rhodes criterion that takes the form

$$\int_{|\mathbf{k}| \leq k_F} \left(\frac{1}{\rho(\epsilon_{\mathbf{k}})} \partial_{\epsilon_{\mathbf{k}}} + \partial_M \right)^4 \epsilon(\mathbf{k}, M) \frac{d\mathbf{k}}{(2\pi)^3} \leq 0 \qquad (7.7)$$

Neglecting the magnetisation dependence recovers the conventional Wohlfarth-Rhodes criterion. Applying this extended Wohlfarth Rhodes criterion to the energy spectrum of the interacting electron gas developed in Chp. 6 [4] shows that the transition is driven first order by an increase in density of states near to the Fermi surface with increasing magnetisation. We have also used this extended Wohlfarth-Rhodes criterion to check the robustness of our results to a perturbative change in the electron dispersion of the form $\varepsilon(p) = p^2/2 + \alpha|p| + \beta p^2 + \gamma|p|^3$. We find that the topology of the phase diagram is unaffected by this perturbation although the positions of the various phase boundaries do move in response to it[1]. The question of how fluctuation corrections and singular features in the density of states interplay with one another remains open. There remains the possibility of some interesting effects, not least because the two mechanisms lead to spatial modulation in potentially different regions of the phase diagram: at the zero-field tricritical point in the case of fluctuation correction and at a new, finite-field tri-critical point in the case of the latter.

We comment briefly upon the possibility of alternative types of order for the intervening phase. In the context of lattice-driven magnetic phase reconstruction, there has been speculation whether the intervening phase consists of spatially modulated magnetism [322] or a d-wave distortion of the Fermi-surface – the so-called electron nematic [323, 324]. In the lattice-driven case these phases have a similar energetic drive. In the case of fluctuations, one might anticipate that a d-wave distortion of the Fermi surface will lead to a similar enhancement of the phase space for particle-hole virtual intermediate states to that due to a spatial modulation of magnetisation. This may result in a similar phase diagram to that shown in Fig. 7.1 where the intervening phase has a d-wave distorted Fermi surface. This question warrants further consideration.

Finally, one might ask in what experimental context are the effects discussed in this chapter likely to be seen. There has been speculation that these effects have already been seen in some solid-state systems. It is difficult to resolve whether this

---

[1]For the first order transition we find a shift in the transition interaction strength of $\Delta(k_F a) = 0.9\alpha + 1.1\beta + 1.3\gamma$. For the inhomogeneous spin phase the lowest order correction in the interaction strength to the GL expansion is $\Delta(k_F a) = 0.4\alpha + 0.8\beta + 1.1\gamma$.

is indeed the case at present, since we do not have a clear understanding of the interplay of lattice and fluctuation effects. For this reason, perhaps the clearest context in which to investigate these effects would be in atomic condensates which was explored in Chp. 6 [4].

Chapter Eight

Theory of quantum paraelectrics and the metaelectric transition

I N this chapter we present a microscopic model of the quantum paraelectric-ferroelectric phase transition with a special focus on the influence of transverse-optical phonon modes. These drive the continuous phase transition first order through a metaelectric transition. We discuss two further consequences of fluctuations, firstly for the heat capacity, and secondly we show that the inverse paraelectric susceptibility displays $\chi^{-1} \sim T^2$ quantum critical behaviour, and that fluctuations can cause the inverse susceptibility to have a characteristic minimum with temperature. Finally, we discuss the observable consequences of our results.

8.1 Introduction

Ferroelectric materials feature in many modern day electronic devices including computer memory and sensors, and are a simple setting for studying quantum criticality [68, 69, 325]. Here we focus on the family of displacive ferroelectrics where the transition is driven by zone-centre soft modes that conspire to enable the optical lattice modes to condense, forming a structural distortion. An important point is that near to quantum criticality excitations can become highly degenerate

and new phases of matter can emerge. Motivated by the emergence of a first order phase transition near criticality in itinerant ferromagnetism that was explored in Chp. 6 [4], and recent experimental evidence for a first order phase transition in ferroelectrics [68], we explore the possibility that polar transverse-optic phonons couple to drive a first order displacive metaelectric transition and investigate the implications for the inverse susceptibility.

The soft-mode optical phonons in ferroelectrics can be well-described by a bosonic field theory. If the dynamics were undamped and the interactions short-ranged then the general quantum critical behaviour would be well understood [326]. However, in ferroelectrics the motion of the atoms in optical modes leads to the emergence of electric dipoles. A good description of these long-range dipole forces is important to properly describe the ferroelectric transition; building on the self-consistent one-loop approximation of Moriya [308], the effect of long-range dipolar forces was studied first by Khmel'nitskii and Shneerson [327], and Rechester [328]. The classical ferroelectric transition was studied by Aharony and Fisher [329], who found that anisotropies associated with the dipolar interaction led to a universality class. The quantum ferroelectric phase transition in the mean-field approximation, and its universality class, was studied by Roussev and Millis [330]. However, recent experimental evidence points towards new physics that occurs close to quantum criticality, for example the coexistence of a quantum paraelectric and a quantum ferroelectric in $SrTiO_3$ provides strong evidence for a first order phase transition [68], and the inverse dielectric constant behaviour of $SrTiO_3$ that is reproduced in Fig. 8.4 which turns from $\epsilon^{-1} \sim -T$ to $\epsilon^{-1} \sim T^2$ and then to $\epsilon^{-1} \sim T$ with rising temperature. One suggestion is that new phenomena are driven by the coupling of acoustic to optical phonons [69, 331]. However, inspired by the ramifications of quantum fluctuations in ferromagnets that were described in Chp. 6 [4], another possibility is that the coupling to transverse-optic phonons could drive a first order metaelectric transition. Furthermore, we present a holistic expression for the inverse susceptibility that is consistent with recent experimental results [69, 332, 333] and demonstrate that the coupling of transverse-optic phonons could cause it to have a characteristic minimum at low temperature.
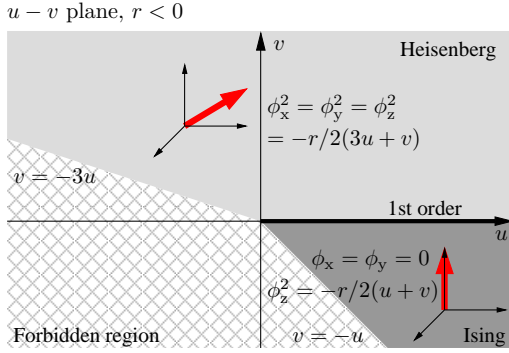
$u - v$ plane, $r < 0$

Figure 8.1: The phase diagram in the $u-v$ plane at zero temperature in the mean-field approximation. The cross-hatched forbidden region denotes where the polarisability would diverge without higher order corrections. The solid thick line highlights a first order phase boundary between the light grey region that denotes a Heisenberg polarisation, and the dark grey which labels the Ising phase. In each regime the inset axes illustrate the polarisation solution highlighted by the red vector.

8.2 Order parameter and action

We adopt a bosonic field theory to describe the soft optical phonon modes that should recover the main physical behaviour of the system. The order parameter of the theory is the local polarisation $\phi(\mathbf{x},t) = \sum_{i=1}^{n} e_i \mathbf{r}_i(\mathbf{x},t)$, which is formally defined for one unit cell at $\mathbf{x}$ containing n atoms of charge e_i each individually displaced through $\mathbf{r}_i$ by the optic mode. This order parameter describes both thermal and quantum fluctuations. Following Roussev and Millis [330] the action arises from a "soft mode" instability in which the optical phonon softens to zero. We describe the action in three-dimensional space and imaginary time via the GL phenomenology described in App. A.3

$$S = \int_0^\beta \left\{ \sum_{\mathbf{q},\alpha,\beta} \left[\left(\frac{a^2}{c^2} \partial_\tau^2 + a^2 q^2 + r + f q_\alpha^2 \right) \delta_{\alpha,\beta} + \left(g - h q^2 \right) \frac{q_\alpha q_\beta}{q^2} \right] \phi_\alpha(\mathbf{q}) \phi_\beta(-\mathbf{q}) \right.$$
$$\left. + \sum_{\alpha,\beta,\{\mathbf{q}_i\}} \left(u + v \delta_{\alpha,\beta} \right) \phi_\alpha(\mathbf{q}_1) \phi_\alpha(\mathbf{q}_2) \phi_\beta(\mathbf{q}_3) \phi_\beta(\mathbf{q}_4) \right\} d\tau, \tag{8.1}$$

where a is the lattice constant, c is the speed of the phonons, $q^2 = \sum_\alpha q_\alpha^2$, the dimensionless momenta $-\pi < q_\alpha \leq \pi$, and the second summation is carried out under the conservation of momentum $(\mathbf{q}_1 + \mathbf{q}_2 + \mathbf{q}_3 + \mathbf{q}_4 = \mathbf{0})$. Since the field ϕ describes an electric dipole, the action includes a long-range dipole interaction and also coupling to the underlying lattice through the parameters r, f, g, and h. The terms u and v that describe the local anharmonic interactions ensure that the solution remains bounded. In general these parameters are tensorial, but for simplicity we have assumed that they adopt cubic symmetry. Estimates for the

Table 8.1: Model parameters for the ferroelectrics $SrTiO_3$ and $KTaO_3$ [69].

	E_0/meV	a/Å	$\hbar c$/meV	r	f	g	h
$SrTiO_3$	4.47	3.9	5.55	5.31	55.7	0.39	5.1
$KTaO_3$	10.6	3.9	13.1	9.77	472	39.2	165

parameters were obtained from *ab initio* calculations [330, 334, 335] in the two key ferroelectrics $SrTiO_3$ and $KTaO_3$ [69], which are shown in Table 8.1. The typical energy scale of ferroelectric fluctuations along (100) is $E_0 = \hbar\pi c/a$. Using this definition we can then employ a dimensionless bosonic Matsubara frequency $\tilde{\omega} = \omega/E_0$, and a dimensionless temperature $\tilde{T} = T/E_0$. Throughout the chapter we adopt the units $a = \hbar = k_B = 1$.

To cement the connection to previous work we first consider the mean-field phase diagram that is sketched in Fig. 8.1. Making the ansatz that the low energy solution is uniform, constant, and is aligned along one direction we obtain the action $S = r\phi^2 + (u + v)\phi^4$. When $v < 0$ the polarisation $\phi_x = \phi_y = 0$, $\phi_z^2 = -r/2(u + v)$ has Ising symmetry, whereas when $v > 0$ the polarisation $\phi_x^2 = \phi_y^2 = \phi_z^2 = -r/2(3u + v)$ possesses Heisenberg symmetry. The term proportional to v controls the polarisation direction in the ferroelectric phase, whereas the u term is rotationally invariant. We note that whilst sweeping v through $v = 0$ with $u > 0$ the first order rotation of polarisation direction is accompanied with a continuous change in the magnitude of the polarisation. This is driven by a similar mechanism to the coupling of two bosonic fields described by Blume et al. [336]. Within the mean-field approximation the condition for stability is that the net quartic term is positive which translates to $u + v > 0$ when $v < 0$ and $u + v/3 > 0$ if $v > 0$. If these conditions are not fulfilled then higher order terms must be included and rather than undergo a second order transition at $r = 0$, the system might have a first order transition at mean-field level. Here we wish to investigate whether near criticality the transverse-optic modes can conspire to drive an otherwise second order transition to become first order. In order to access this behaviour we now go beyond mean-field and consider the consequences of quantum fluctuations on the system.

8.3 Propagator and fluctuations

To account for fluctuation corrections to the system Roussev and Millis [330] employed the renormalisation group phenomenology, which is tailored to study the well-established second order ferroelectric transition. However, motivated by recent experiments [68] we wish to explore the possibility of a first order metaelectric transition. Therefore, rather than considering just the corrections due to slow fluctuations encompassed by renormalisation group, we wish to consider fluctuations $\boldsymbol{\psi}$ over all length scales in the polarisation $\boldsymbol{\phi} + \boldsymbol{\psi}$ around the saddle-point solution $\boldsymbol{\phi}$. When $u \ll r^2$ we can neglect fluctuations in $\boldsymbol{\psi}$ beyond second order which reduces the action to

$$S = \tilde{\beta}\left[\left(r + \frac{g}{3}\right)\phi^2 + u\phi^4 + v\sum_\alpha \phi_\alpha^4\right] + \tilde{\beta}\sum_{\tilde{\omega},\mathbf{q}} \boldsymbol{\psi}^{\mathrm{T}}(\tilde{\omega},\mathbf{q})\mathsf{G}^{-1}\boldsymbol{\psi}(-\tilde{\omega}, -\mathbf{q})\,, \quad (8.2)$$

where $G_{\alpha,\beta}^{-1} = G_\alpha^{(\mathrm{d})-1}\delta_{\alpha,\beta} + G_{\alpha,\beta}^{(\mathrm{o})-1}$, and the diagonal inverse Green function takes the form $G_\alpha^{(\mathrm{d})-1} = \tilde{\omega}^2 + q^2 + r + fq_\alpha^2 + (g - hq^2)q_\alpha^2/q^2 + (4u + 6v)\phi_\alpha^2 + 2u\phi^2$, and the off-diagonal terms are $G_{\alpha,\beta}^{(\mathrm{o})-1} = (g - hq^2)q_\alpha q_\beta/q^2 + 4u\phi_\alpha\phi_\beta$. To proceed we note that g and h are irrelevant to the critical behaviour [330], and that the lowest order term in them would average to zero on integrating over momenta, so here we assume that $g = 0 = h$. We now employ the functional integral phenomenology described in App. A.2 and integrate over quantum fluctuations to yield

$$F = \left(r + \frac{g}{3}\right)\phi^2 + u\phi^4 + v\sum_\alpha \phi_\alpha^4 + \frac{1}{2\tilde{\beta}}\operatorname{Tr}\ln\mathsf{G}^{-1}\,. \quad (8.3)$$

Finally, we expand the inverse Green function in its off-diagonal terms which if $\boldsymbol{\phi} = \mathbf{0}$ requires $r \gg g - h\pi^2$, and if $\boldsymbol{\phi} \neq \mathbf{0}$ requires that $r \ll \pi^2$ to find

$$\begin{aligned} F = {}& \left(r + \frac{g}{3}\right)\phi^2 + u\phi^4 + v\sum_\alpha \phi_\alpha^4 \\ &+ \frac{1}{\tilde{\beta}}\sum_\alpha\left[\operatorname{Tr}\ln\sinh\left(\tilde{\beta}\xi_\mathbf{q}^\alpha/2\right) - \ln(\xi_\mathbf{0}^\alpha)\right] - \frac{1}{4\tilde{\beta}}\operatorname{Tr}\left(G_{\alpha,\alpha+1}^{(\mathrm{o})-1}G_\alpha^{(\mathrm{d})}G_{\alpha+1,\alpha}^{(\mathrm{o})-1}G_{\alpha+1}^{(\mathrm{d})}\right)\,, \end{aligned}$$
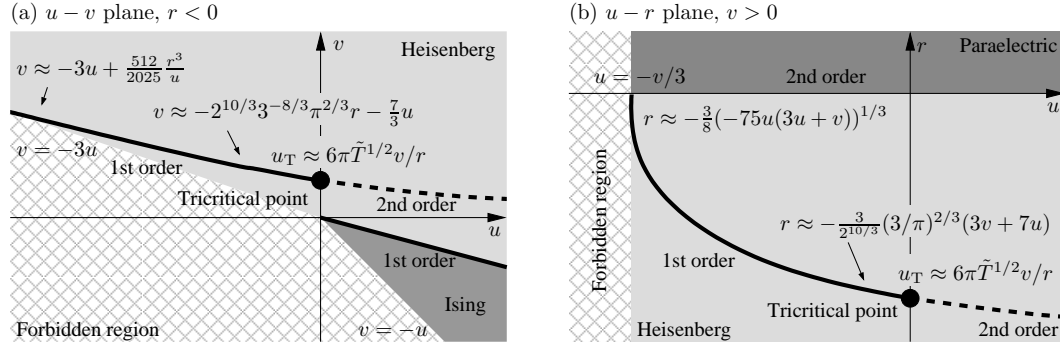$$(8.4)$$

Figure 8.2: The phase diagram at $\tilde{T} = 0$ in the (a) $u - v$ plane with $r < 0$, and (b) $u - r$ plane with $v > 0$, both at zero temperature. The cross-hatched forbidden region denotes where the polarisability would diverge without higher order corrections, the light grey denotes a Heisenberg polarisation, and the dark grey the (a) Ising phase and (b) paraelectric phase. Solid thick lines denote first order phase boundaries, dashed lines second order transitions, and the circle the tricritical point.

where $\xi_{\mathbf{q}}^{\alpha} = [q^2 + r + f q_{\alpha}^2 + (4u + 6v)\phi_{\alpha}^2 + 2u\phi^2]^{1/2}$, and $\tilde{\beta} = 1/\tilde{T}$ is the dimensionless inverse temperature. This expression, except for the final fluctuation correction term, agrees with that of Ref. [330]. The condition for stability is the same as for the mean-field case.

The momentum integrals are in general evaluated numerically. However, to further investigate the Heisenberg phase we make the approximation that the cuboid Brillouin zone boundary $(-\pi < q_{\alpha} < \pi)$ that bounds the momentum space integral can be replaced with a spherical boundary that encloses the same total phase space, so has radius $q_{\mathrm{D}} = \sqrt[3]{6\pi^2}$. In the low temperature limit the resulting integrals can then be evaluated analytically, and were found to be in good agreement with the corresponding numerical result.

8.3.1 Phase behaviour and heat capacity

The system phase behaviour is shown in Fig. 8.2. The forbidden region indicates where the action polarisability and free energy would diverge without considering higher order corrections to the original action. When considered within the framework of mean-field phenomenology, here the system could undergo a first order paraelectric-ferroelectric transition. However, the corrections due to quantum fluctuations renormalise the action, causing a metaelectric boundary to peel away from the first order transition associated with the forbidden region. This
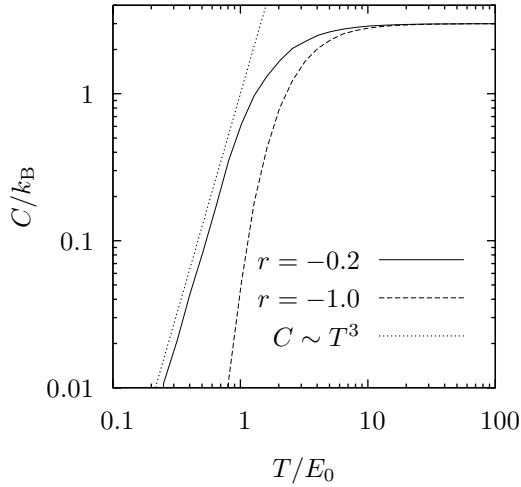
Figure 8.3: The specific heat capacity per unit cell at $v = 3$, $u = -0.98$ at two different r values either side of the first order metaelectric transition.

metaelectric transition is consistent with recent experimental evidence for a first order phase transition [68] in $SrTiO_3$. In both of the planes considered, the line of first order metaelectric transitions covers an extensive region of the phase diagram, terminating in a tricritical point at $u = 0$. The polarisation formed upon crossing this boundary is vanishingly small at $u \lesssim [224(6/\pi)^{2/3}r^2 - 225v]/1350$, being caused by a logarithmic singularity in the free energy. The first order transition at small u is destroyed at non-zero temperature, with the tricritical point moving up the line of transitions to $u \approx 6\pi\tilde{T}^{1/2}v/r$.

A further ramification of the quantum fluctuation corrections is that the rotation of the polarisation from Ising to Heisenberg-like no longer occurs where v turns negative. Though, as for the mean-field case, the magnitude of the polarisation is conserved, fluctuations have renormalised the quartic terms and shifted the phase boundary in Fig. 8.2(b). This behaviour can also be recovered by a renormalisation group analysis [330]. One experimental probe of the metaelectric transition is the changing behaviour of the heat capacity $C = -T\partial^2 F/\partial T^2$. As shown in Fig. 8.3 before the metaelectric transition (at $r = -0.2$) the relevant optic mode is "soft" and so the heat capacity follows the customary quantal form $C \sim T^3$, whereas after the metaelectric transition (at $r = -1.0$), the relevant optic modes are "stiff" and so the heat capacity has an exponential dependence on temperature. At high temperature, in both cases the heat capacity has the expected classical behaviour $C = 3k_B$.

Table 8.2: Upper: inverse susceptibility of the longitudinal-optic term in the quantum critical and paraelectric regime. Lower: inverse susceptibility of the transverse-optic term comprised of the different components of $G^{(o)-1}_{\alpha,\beta}$, in the limit of small g and h, where $R = r + g/3$ and $\gamma = q_D/R$.

Longitudinal-optic term

Quantum critical	$\frac{(5u+3v)R}{4\pi^2}(\gamma\sqrt{1+\gamma^2}-\sinh^{-1}\gamma)+R+\frac{5u+3v}{18}\tilde{T}^2$	$\tilde{T} \ll q_D/2$
	$R + \frac{(5u+3v)\sqrt{R}}{3\pi^2}(\gamma - \tan^{-1}\gamma)\tilde{T}$	$\tilde{T} \gg q_D/2$
Paraelectric	$R + \coth(\Delta/2\tilde{T})$	

Transverse-optic term

g^2	0	$\tilde{T} \ll \sqrt{g}/2$
	$\frac{5u+3v}{120}\sqrt{g}\tilde{T}$	$\tilde{T} \gg \sqrt{q}/2$
ghq^2	0	$\tilde{T} \ll \sqrt{g}/2$
	$-\frac{5u+3v}{20}\sqrt{g}h\tilde{T}$	$\tilde{T} \gg \sqrt{g}/2$
$(hq^2)^2$	$\frac{h^2(5u+3v)}{15\pi}\left(\frac{3q_D^2}{16} + \frac{\pi^2}{2}\tilde{T}^2\right)$	$\tilde{T} \ll q_D/2$
	$\frac{2q_D}{15\pi}h^2\tilde{T}$	$\tilde{T} \gg q_D/2$
$u^2\phi^4$ $gu\phi^2$ $hq^2u\phi^2$	0	All $\tilde{T}$

8.3.2 Inverse susceptibility

The inverse susceptibility provides an experimental window [69, 332, 333] onto the quantum critical properties of ferroelectrics. The inverse susceptibility $\chi^{-1} = \partial^2 F/\partial\phi^2|_{\phi_{\text{eqm}}}$ calculated from our formalism is presented in Table 8.2, where the contribution from the longitudinal-optic part of the free energy and the transverse-optic term are presented separately; for the latter term the contributions from the separate components of $G^{(o)-1}_{\alpha,\beta}$, namely $gq_\alpha q_\beta/q^2$, $-hq_\alpha q_\beta$, and $4u\phi_\alpha\phi_\beta$ are also shown individually.

In the paraelectric regime we recover the expected Barrett's formula [337] for a gapped system. In the quantum critical regime we see three characteristic types of behaviour. At low temperature the transverse-optic contribution dominates, with the linear temperature dependence due to the g^2 term giving a positive slope to the inverse susceptibility whereas the ghq^2 term would provide a negative slope. At higher temperatures the T^2 contribution from the mean-field term dominates, which is also characteristic of quantum critical behaviour and is in good agreement with recent experimental results [69]. We note that the T^2 behaviour is recovered by other models, including a diagrammatic resummation [327, 328], the quantum spherical model [338], renormalisation group studies [339, 340], and an analogy to the temporal Casimir effect [331]. The behaviour has also been observed experimentally [69,
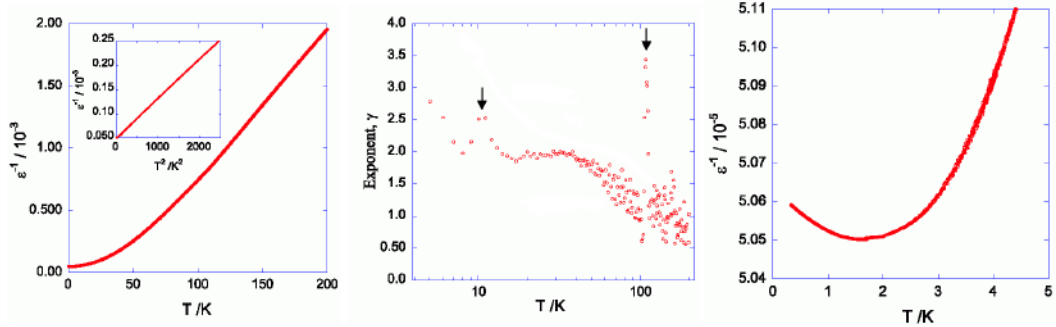
Figure 8.4: The inverse dielectric constant of $SrTiO_3$ taken from Rowley et al. [69]. The left-hand plot demonstrates the cross-over from $\epsilon^{-1} \sim T^2$ to $\epsilon^{-1} \sim T$ at $\sim 60K$, and the central plot shows the results of a power law fit $\epsilon^{-1} \sim T^\gamma$; the features marked with arrows are experimental artifacts not covered by the model. The right-hand plot highlights the low-temperature minimum in the inverse dielectric constant.

332, 333]. In both $SrTiO_3$ and $KTaO_3$ the linear negative slope $\chi^{-1} \sim -T$ and the quadratic $\chi^{-1} \sim T^2$ term conspire to cause a characteristic minimum in the inverse susceptibility. Estimated using the parameters in Table 8.1, for $SrTiO_3$ the minimum occurs at $T = 1.1K$, whereas for $KTaO_3$ the minimum is at $T = 0.8K$, which gives a good description of the recent low temperature measurements [69] that are reproduced in Fig. 8.4 and Fig. 1.11. Finally, at high temperatures a classical term $\chi^{-1} \sim T$ from the longitudinal-optic term dominates. This is predicted to be from 76K in $SrTiO_3$ and 180K in $KTaO_3$, which is again in good agreement with the experimental observations [69], that for $SrTiO_3$ are reproduced in Fig. 8.4.

8.4 Discussion

In this chapter we have found that the polar transverse-optic phonons can drive a displacive ferroelectric through a first order metaelectric transition, and also lead to a characteristic minimum in the inverse susceptibility. However, another mechanism, coupling of the soft optic modes to acoustic phonons could be significant. It has already been shown by Pálová et al. [331] that a coupling with the acoustic phonons φ of the form $-\eta(\nabla\varphi)\phi^2$ leads to a correction in χ^{-1} of $-T^4$ that could explain the characteristic minimum in the inverse susceptibility, and also has the capability of driving a first order transition [69, 331]. This work and the results presented here motivate further experimental investigations into the inverse susceptibility and

putative metaelectric transition to shed light on the quantum critical dynamics in ferroelectrics.

The low temperature behaviour of the inverse susceptibility provides a useful probe into the low-temperature symmetry of ferroelectric materials. The predicted behaviour of the inverse susceptibility $\chi^{-1} \sim T^2$ is indicative of cubic symmetry, whereas a system with tetragonal symmetry would have $\chi^{-1} \sim T^3$ [338]. Though in typical multidomain materials the effective symmetry is cubic, the current unknown symmetry of $SrTiO_3$ at low temperature poses an interesting point for further investigation. The crossover from the Barrett formula to the $\chi^{-1} \sim T^2$ behaviour seen in the quantum paraelectric phase [332, 341] should also provide a measure of the vicinity to a quantum critical point.

Long-range dipole interactions play an important role in ferroelectrics [327, 330]. The inclusion of the term $(g - hq^2)\phi^2$ in the action was pivotal in creating the correction to the inverse susceptibility $\chi^{-1} \sim -T$ that could explain the characteristic inverse susceptibility minimum [69], as well as provide important corrections to the self-consistent phonon treatment presented by Rowley et al. [69]. Though the coupling to acoustic phonons complicated the solid state system, ultracold atoms in an optical lattice with long-range dipole interactions [342] present a clean system that could provide a powerful tools to help unravel the properties of the generic Hamiltonian.

One important simplification was to model the ferroelectric with undamped dynamics. Damping would primarily arise due to free electrons, which can be introduced controllably through doping. Analogous to "avoided criticality" at a magnetic critical point which leads to non-Fermi liquid behaviour and superconductivity, ferroelectrics might also be expected to adopt novel behaviour; for example doped $SrTiO_3$ [343], and conducting in the undoped state Tin Telluride (SnTe) [344] and Germanium Telluride (GeTe) [345] both become superconducting at low temperatures. This area presents a promising avenue of research. Further open questions are to determine whether with just a change of parameters [330, 346] the same formalism be applied to order-disorder ferroelectrics, and to consider the consequences of the coupling of fluctuating polarisation and magnetisation that

could arise in Europium Titanate (EuTiO$_3$) [347].

Appendices

A.1 Scattering length

Due to the importance of the exquisite level of control of interaction strength in atomic gases, in this appendix we review the natural parameter used to express the interaction strength – the *scattering length* [37]. At large separation ultracold atoms experience each others fluctuating electric dipole so attract via a van der Waals potential $\propto r^{-6}$; whereas at short separation (a few Bohr radii) their electron clouds strongly repel leading to a "hard-core" repulsion. The atomic gases studied in experiments are typically both ultracold and ultradilute so the de Broglie wavelength and interparticle distance are much larger than the range of the interatomic potential and the details of the interatomic scattering potential are unimportant.

We start by considering elastic collisions between atoms with a central scattering potential in their centre-of-mass frame, using $\mathbf{r}$ to denote their separation. The wave function $\psi(\mathbf{r})$ is the sum of an incident plane wave $e^{i\mathbf{k}\cdot\mathbf{r}}$ and an outgoing scattered wave

$$\psi(\mathbf{r}) = e^{i\mathbf{k}\cdot\mathbf{r}} + \frac{f(\mathbf{k}',\mathbf{k})e^{ikr}}{r} \, . \tag{A.5}$$

Here $f(\mathbf{k}',\mathbf{k})$ is the scattering amplitude from the incident plane wave to a direction along $\mathbf{k}'$, and energy conservation demands that $|\mathbf{k}'| = |\mathbf{k}|$. As the potential is central, and is approximately a contact interaction, we only need to consider the zero angular momentum *s-wave scattering* component so [348]

$$f \approx \frac{1}{|\mathbf{k}|\cot\delta - i|\mathbf{k}|} \, . \tag{A.6}$$

Here δ is the scattering *phase shift* that the atomic wave function receives in a collision and governs the behaviour of the gas. Therefore, for low momentum

$$|\mathbf{k}|\cot\delta \approx -\frac{1}{a} + \frac{R_{\text{eff}}|\mathbf{k}|^2}{2} \, , \tag{A.7}$$

where R_{eff} is the effective range of the potential. In this limit the *scattering length*

is

$$a = -\lim_{|\mathbf{k}| \ll 1/R} \frac{\tan\delta}{|\mathbf{k}|} . \tag{A.8}$$

For $1/k_\mathrm{F}a < 0$ the interaction is weakly attractive and we are in the BCS regime of weakly bound Cooper pairs. At $1/k_\mathrm{F}a > 0$ the interaction is sufficiently attractive that there is a two-body bound state with energy $-\hbar^2/ma^2$ available and we are in the BEC regime of tightly bound molecules. The BEC-BCS crossover occurs at $1/k_\mathrm{F}a = 0$. The interaction strength itself is tuned using a Feshbach resonance, which was described in Sec. 1.3.1.

The scattering potential is often weak motivating the *Born approximation*. Using the Green's function for the Schrödinger equation $G(\mathbf{r}) = -\mathrm{e}^{ikr}/4\pi r$ the general solution to the scattering problem in potential $V(\mathbf{r})$ takes the form

$$\psi(\mathbf{r}) = \psi_0(\mathbf{r}) - \frac{m}{2\pi\hbar^2} \int \frac{\mathrm{e}^{ik|\mathbf{r}-\mathbf{r}'|}}{|\mathbf{r}-\mathbf{r}'|} V(\mathbf{r}')\psi(\mathbf{r}')\mathrm{d}\mathbf{r}' . \tag{A.9}$$

Next we invoke the Born approximation, which tells us that the incoming plane-wave is not substantially altered by the potential so $\psi(\mathbf{r}) \approx \psi_0(\mathbf{r})$ and therefore

$$f(\mathbf{k},\mathbf{k}') = -\frac{m}{2\pi\hbar^2} \int \mathrm{e}^{-i(\mathbf{k}-\mathbf{k}')\cdot\mathbf{r}'} V(\mathbf{r}')\mathrm{d}\mathbf{r}' . \tag{A.10}$$

Finally for the low-energy s-wave scattering occurring in ultracold atomic systems the Born approximation becomes

$$f = -\frac{m}{2\pi\hbar^2} \int V(\mathbf{r}')\mathrm{d}\mathbf{r}' , \tag{A.11}$$

and so any short-range potential acting between atoms can be approximated by a contact potential.

To close the discussion of the scattering length we note that the physical meaning of the scattering length is the intercept of $r\psi$ on the radial axis, as shown in Fig. A.5. This is positive for a wave function that curves over and is bound, whereas it is negative for a divergent unbound wave function. This visualisation means that the scattering length is sometimes called the *extrapolated Fermi intercept*.
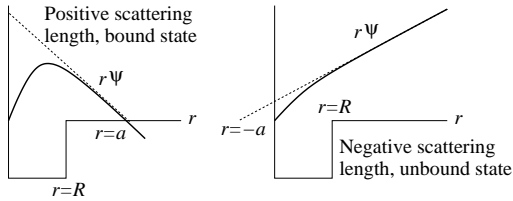
Figure A.5: The scattering length a of a wave function shown by the bold line in an attractive scattering potential radius R. The extrapolation performed to find the Fermi intercept is shown by the dashed line.

.

A.2 Path integral formulation

In this appendix we introduce the *path integral* formalism, also known as *functional integral*, *integral over trajectories*, or *continuous integral*, this is an analytical approach to solving the many-body problem. Our formalism is focused on quantum mechanics, where it was first used in 1953, however the method may be applied to many other areas [17, 349]; for example it was first used in 1921 to analyse diffusion and Brownian motion [17], and it has also been applied to model option pricing on the stock market [8, 17].

The basic premise of the functional integral is to calculate the quantum partition function – a summation over all possible states of the system. In general this is not tractable, but one approach is to focus attention on those terms which make the most significant contribution to the summation over states. First one identifies the dominant term, and then accounts for a small subset of related terms, but discards the less relevant high energy contributions. Firstly, in App. A.2.1 we construct the path integral for a single particle. Next we formulate the tools to handle many-body states in App. A.2.3 and finally the many-body formalism is developed in App. A.2.4.

A.2.1 Single-particle quantum path integral construction

Our route to develop the path integral is to start by focusing on the propagator that describes how the wavefunction changes in both space and time. In order to evolve the wave function with a time development operator [111], it is convenient to propagate the wave function forward for many successive small time intervals. To affect this the time development operator is considered as the accumulated action

of N operators [8], each with small time-step $\Delta t = t/N$,

$$e^{-i\hat{H}t} = \left(e^{-i\hat{H}\Delta t}\right)^N.$$
(A.12)

Using $\hat{H} = \hat{T} + \hat{V}$ the time development operator can be factorised as the product of kinetic $\hat{T}$ and potential $\hat{V}$ energy exponentials in the limit of small Δt $(N \gg 1)$[1]

$$e^{-i\hat{H}\Delta t} = e^{-i\hat{T}\Delta t}e^{-i\hat{V}\Delta t} + \mathcal{O}(\Delta t^2).$$
(A.13)

A complete basis set of momentum $|\mathbf{p}\rangle$ and position $|\mathbf{r}\rangle$ state vectors diagonalises the exponentials containing the time evolution of the kinetic and potential parts respectively. We also note that the *resolution of the identity* can be expressed as an integral over the state vectors

$$\hat{I} = \iint |\mathbf{r}\rangle \langle\mathbf{r}|\mathbf{p}\rangle \langle\mathbf{p}| \, d\mathbf{r}d\mathbf{p}.$$
(A.14)

A resolution of the identity is inserted between each pair of evolution operators in the factorised time development operator Eqn. (A.12) and Eqn. (A.13). We use index n to denote separate time-steps. The time development operator acting between states $|\mathbf{r}_I\rangle$ and $|\mathbf{r}_F\rangle$ is then

$$\left\langle \mathbf{r}_F \left| e^{-i\hat{H}t} \right| \mathbf{r}_I \right\rangle = \lim_{\Delta t \to 0} \left\langle \mathbf{r}_F \left| \prod_{n=1}^{N} \left(\hat{I}_n e^{-i\hat{T}\Delta t}e^{-i\hat{V}\Delta t} \right) \right| \mathbf{r}_I \right\rangle$$

$$= \lim_{\Delta t \to 0} \iint e^{-i\Delta t \sum_{n=0}^{N}(V(\mathbf{r}_n)+T(\mathbf{p}_{n+1})-\mathbf{p}_{n+1}\cdot(\mathbf{r}_{n+1}-\mathbf{r}_n)/\Delta t)}$$

$$\times \prod_{n=1}^{N-1} (d\mathbf{r}_n) \prod_{n=1}^{N-1} \left(\frac{d\mathbf{p}_n}{2\pi} \right).$$
(A.15)

In the limit of zero time-step, $\Delta t \to 0$, both position and momentum variables become continuous, $(\mathbf{r}_{n+1} - \mathbf{r}_n)/\Delta t \mapsto \dot{\mathbf{r}}|_t$, $\Delta t \sum_{n=0}^{N} \mapsto \int_0^t dt'$, and we define the

---

[1]More formally Δt is much smaller than the reciprocal of the dominant eigenvalues of the Hamiltonian.

functional integral

$$\iint \prod_{n=1}^{N-1} (\mathrm{d}\mathbf{r}_n) \prod_{n=1}^{N-1} \left(\frac{\mathrm{d}\mathbf{p}_n}{2\pi} \right) \mapsto \iint_{\substack{\mathbf{r}(t)=\mathbf{r}_\mathrm{F} \\ \mathbf{r}(0)=\mathbf{r}_\mathrm{I}}} \mathcal{D}\mathbf{r}\mathcal{D}\mathbf{p} \,, \tag{A.16}$$

that combined with Eqn. (A.15) yields the final expression for the matrix element

$$\left\langle \mathbf{r}_\mathrm{F} \left| e^{-i\hat{H}t} \right| \mathbf{r}_\mathrm{I} \right\rangle = \iint_{\substack{\mathbf{r}(t)=\mathbf{r}_\mathrm{F} \\ \mathbf{r}(0)=\mathbf{r}_\mathrm{I}}} e^{\displaystyle i \int_0^t \overbrace{\left(\mathbf{p} \cdot \dot{\mathbf{r}} - \left\langle \mathbf{p},\mathbf{r} \left| \hat{H} \right| \mathbf{p},\mathbf{r} \right\rangle \right)}^{\displaystyle \overbrace{}^{S} \; L} \mathrm{d}t'} \mathcal{D}\mathbf{r}\mathcal{D}\mathbf{p} \,. \tag{A.17}$$

By analogy with the Lagrangian formulation of classical dynamics [350], the term L represents the Lagrangian of the trajectory[2], and S is the action. From the above result for the propagator we can find the Green's function that describes a particle propagating from $\mathbf{r}_\mathrm{I}$ to $\mathbf{r}_\mathrm{F}$ in time t

$$\begin{aligned} G(\mathbf{r}_\mathrm{F},\mathbf{r}_\mathrm{I},t) &= \Theta(t) \left\langle \mathbf{r}_\mathrm{F} \left| e^{-i\hat{H}t} \right| \mathbf{r}_\mathrm{I} \right\rangle \\ &= \Theta(t) \iint_{\substack{\mathbf{r}(t)=\mathbf{r}_\mathrm{F} \\ \mathbf{r}(0)=\mathbf{r}_\mathrm{I}}} e^{i \int_0^t (\mathbf{p}\cdot\mathbf{r} - \langle \mathbf{p},\mathbf{r}|\hat{H}|\mathbf{p},\mathbf{r}\rangle)\mathrm{d}t'} \mathcal{D}\mathbf{r}\mathcal{D}\mathbf{p} \,, \end{aligned} \tag{A.18}$$

where the Heaviside function $\Theta(t)$ ensures causality since the particle cannot propagate backwards in time. By making a *Wick rotation* $t = -i\beta$ to imaginary time β, which represents temperature, we can derive the *quantum partition function*

$$\mathcal{Z} = \int \left\langle \mathbf{r} \left| e^{-\beta\hat{H}} \right| \mathbf{r} \right\rangle \mathrm{d}\mathbf{r} \,, \tag{A.19}$$

that sums over all possible particle path start and end points.

A.2.2 Path integral visualisation

A visualisation of the Feynman path integral is shown in Fig. A.6. We build up from a double slit experiment to the continuum limit. Starting with just two possible paths (a), and then in (b) several possible path combinations, by

---

[2]The mapping, for a single particle, $\mathbf{p} \mapsto \hbar\mathbf{k}$ and $E \mapsto \hbar\omega$ gives the Lagrangian $L = \hbar(\mathbf{k}\cdot\mathbf{x} - \omega)$. Hence, the action represents the total phase evolution of the particle along its path.
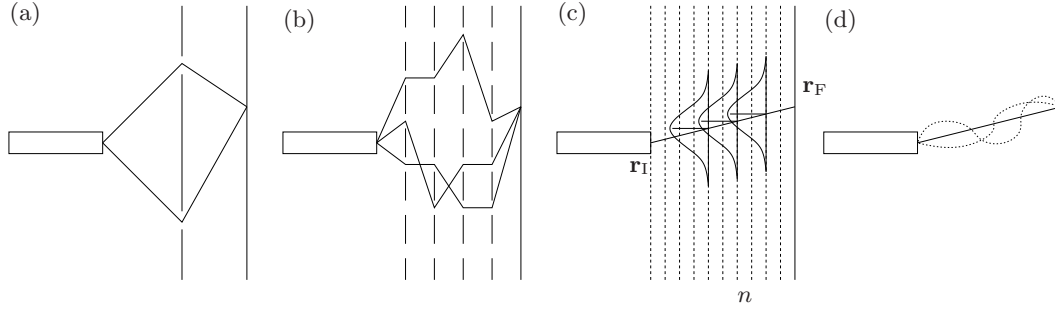
Figure A.6: The two paths from a source to screen in a double slit diffraction experiment are shown in (a). A many slit experiment is shown in (b), there are now many possible paths. In the large number of slits limit, we get the continuum empty space limit shown in (c) of the path from $\mathbf{r}_I$ to $\mathbf{r}_F$. The Gaussian probability distributions around the minimum action path are shown at successive time-steps indexed by n. The classical path chosen by the path integral is shown in (d), with possible fluctuations integrated over shown by the dotted paths.

increasing the number of screening layers and slits until one reaches an infinite number, the screens disappear and the space becomes continuous recovering an integral over paths. Distance up a particular screen corresponds to position $\mathbf{r}$, and passing through successive screen is analogous to time evolution. The Feynman path integral allows all such possible paths in phase space to be sampled. To evaluate the integral practically simplifications must be made, one approximation is to focus on the contributions around the stationary path that minimises the action is found. Paths around it, which correspond to quantum fluctuations, are then evaluated by expanding to quadratic order, and contributions from more distant paths will deconstructively interfere so are neglected. The path weights are then the Gaussian distributions shown. The Gaussian weight $\sim \mathrm{e}^{-r_i^2/2\sigma_i^2}$ at each time-step, corresponding to which slit has just been passed through is then integrated over at subsequent time-step (corresponding to the nth slit) resulting from the $\mathcal{D}\mathbf{r} = \prod_n \mathrm{d}\mathbf{r}_n$ to recover the total action associated with the path. This action can renormalise the saddle point path, which must then be re-evaluated.

A.2.3   Coherent states

We would now like to extend the path integral to deal with a many-particle system. To do this we take advantage of the already well-established creation and annihilation operator formalism within the framework of second quantisation and formulate a field theoretic representation. To follow this prescription we first

need to analyse the properties of the creation and annihilation operators, chiefly the annihilation operator eigenstates, known as *coherent states* [8]. As a coherent state is unaffected by a measurement (written in terms of an operator containing a and $a^\dagger$) they are the quantum states that are most like classical states. The creation operators cannot posses eigenstates[3], however annihilation operators do. The bosonic coherent states are

$$|\phi\rangle \equiv e^{\sum_i \phi_i a_i^\dagger} |\Omega\rangle \, . \tag{A.20}$$

The elements ϕ_i are *complex numbers* that are the eigenvalues of the annihilation operator, that is $a_i|\phi\rangle = \phi_i|\phi\rangle$. Therefore, the probability of detecting a second particle is the same as the probability of detecting the first, a prerequisite for Poisson statistics. In a similar fashion, the fermionic coherent states are

$$|\eta\rangle \equiv e^{-\sum_i \eta_i c_i^\dagger} |\Omega\rangle \, . \tag{A.21}$$

The elements η_i are the annihilation operator eigenvalues $c_i|\eta\rangle = \eta_i|\eta\rangle$. Since the fermionic field operators obey anticommutation relations, elements η_i are *Grassmann numbers*. They obey Grassman algebra, for example they anticommute, $\eta_i\eta_j = -\eta_j\eta_i$, obey the Pauli exclusion principle as $\eta_i\eta_i = 0$, and have the rules of calculus[4] $\partial_{\eta_j}\eta_i = \delta_{i,j}$, $\int d\eta = 0$, and $\int \eta d\eta = 1$.

Whilst the annihilation operator has eigenstates, when the creation operator

---

[3]If the minimum number particles to describe state $|\phi\rangle$ is n then the minimum number required to describe $a^\dagger|\phi\rangle$ is $n+1$. These requirements are inconsistent so a contradiction arises, the creation operator cannot have eigenstates. This issue does not arise with the annihilation operator.

[4]The *Berezin integration* [351] rules of calculus are consistent with the requirement that Grassmann calculus be linear

$$\int aA(\eta) + bB(\eta)d\eta = \int aA(\eta)d\eta + \int bB(\eta)d\eta \, , \tag{A.22}$$

and obey the partial integration formula

$$\int f(\eta)\left(\frac{\partial g(\eta)}{\partial\eta}\right)d\eta = \int \left(\frac{\partial f(\eta)}{\partial\eta}\right)g(\eta)d\eta \, , \tag{A.23}$$

from which it follows that

$$\int \frac{\partial f(\eta)}{\partial\eta}d\eta = 0 \, . \tag{A.24}$$

The fact that differentiation is identical to integration is consistent with the identity $\eta^2 = 0$, so the rules uniquely define a map as variables are either constant or linear.

acts on a coherent state, it behaves as a differential operator, $a_i^\dagger \left| \phi \right\rangle = \partial_{\phi_i} \left| \phi \right\rangle$, and $c_i^\dagger \left| \eta \right\rangle = -\partial_{\eta_i} \left| \eta \right\rangle$. It can be shown that the overlap between coherent states is $\left\langle \phi' | \phi \right\rangle = \exp(\sum_i \bar{\phi}'_i \phi_i)$, and $\left\langle \eta' | \eta \right\rangle = \exp(\sum_i \bar{\eta}'_i \eta_i)$. From these relations appropriate normalisation for a resolution of the identity operator immediately follows, where both bosonic and fermionic coherent states form overcomplete sets of states in Fock space. Finally, to lay the foundations on which to build the functional integral formulation we note that for complex number variables, Gaussian integrals can be extended to

$$\int e^{-\phi^\dagger \mathsf{A} \phi} \mathcal{D}\left(\phi^\dagger, \phi \right) = \pi^N \det \mathsf{A}^{-1} , \tag{A.25}$$

whereas in the Grassmann variable case, Gaussian integration gives

$$\int e^{-\bar{\eta}^T \mathsf{A} \eta} \mathcal{D}\left(\bar{\eta}, \eta \right) = \det \mathsf{A} . \tag{A.26}$$

A.2.4 Many-body quantum path integral construction

Now that we have developed an efficient many-body representation we can proceed with the quest to find the many-body quantum partition function. It is possible to re-write the Hamiltonian in terms of creation and annihilation operators. Using the ideas from the single particle case, it is therefore possible to formulate [8] a functional integral for a many-body system using coherent states. We start with the quantum partition function that is defined as

$$\mathcal{Z} = \sum_n \left\langle n \left| e^{-\beta(\hat{H} - \mu \hat{N})} \right| n \right\rangle . \tag{A.27}$$

The summation over n extends over states $\{|n\rangle\}$ containing n particles, giving a complete Fock space. The quantum partition function is therefore in the *grand canonical ensemble* [352].

We insert a resolution of the identity $\hat{I} = \int e^{-\sum_i \bar{\psi}_i \psi_i} |\psi\rangle\langle\psi| d[\bar{\psi},\psi]$ [5] so

$$\mathcal{Z} = \int e^{-\sum_i \bar{\psi}_i \psi_i} \sum_n \langle n|\psi\rangle \left\langle \psi \left| e^{-\beta(\hat{H} - \mu\hat{N})} \right| n \right\rangle d[\bar{\psi},\psi]. \qquad (A.28)$$

A sign difference arises when the element $\langle n|\psi\rangle$ is now commuted through the expression, we take the positive for bosons $\langle n|\psi\rangle\langle\psi|n\rangle = \langle\psi|n\rangle\langle n|\psi\rangle$, and negative for fermions $\langle n|\psi\rangle\langle\psi|n\rangle = -\langle\psi|n\rangle\langle n|\psi\rangle$ giving the $\pm$ factor in

$$\mathcal{Z} = \pm \int e^{-\sum_i \bar{\psi}_i \psi_i} \sum_n \left\langle \psi \left| e^{-\beta(\hat{H} - \mu\hat{N})} \right| n \right\rangle \langle n|\psi\rangle d[\bar{\psi},\psi]. \qquad (A.29)$$

We use the resolution of the identity $\sum_n |n\rangle\langle n| = \hat{I}$ to remove the dependence on number states

$$\mathcal{Z} = \pm \int e^{-\sum_i \bar{\psi}_i \psi_i} \left\langle \psi \left| e^{-\beta(\hat{H} - \mu\hat{N})} \right| \psi \right\rangle d[\bar{\psi},\psi]. \qquad (A.30)$$

We then follow the method prescribed in the single particle case Sec. A.2.1; consider small time steps, insert resolution of the identity operators written in terms of the new coherent state basis, and let the time-steps tend to zero[6]. We finally get

$$\mathcal{Z} = \int e^{-\int_0^\beta \bar{\psi}\partial_\tau \psi + H(\bar{\psi},\psi) - \mu N(\bar{\psi},\psi) d\tau} \mathcal{D}\left(\bar{\psi},\psi\right). \qquad (A.31)$$

Here the Hamiltonian and number operators may be written in terms of creation and annihilation operators. For example the number of electrons in a state with wave vector $\mathbf{k}$ is $\langle\psi|\hat{n}_\mathbf{k}|\psi\rangle/\langle\psi|\psi\rangle = \langle\psi|c_\mathbf{k}^\dagger c_\mathbf{k}|\psi\rangle/\langle\psi|\psi\rangle = \bar{\psi}_\mathbf{k}\psi_\mathbf{k}$. The fields ψ and $\bar{\psi}$ represent the interacting particle states, which could be visualised in terms of

---

[5]The field ψ is a complex number whose real and imaginary parts are separate variables which must be integrated over independently, therefore we use $d[\bar{\psi},\psi] = d\Re(\psi)d\Im(\psi)$.

[6]By construction, as a result of discretisation analogous to Eqn. (A.15), the field $\bar{\psi}$ is evaluated infinitesimally later than field ψ. Therefore a multiplicative factor $\exp(-i\omega\delta)$ should be associated with every $\bar{\psi}$, with δ an infinitesimal interval of time. This term may ensure convergence in Matsubara frequency summations, notably the otherwise divergent $\sum_\omega G_0(\omega,C) = \lim_{\delta\to 0^+} \sum_\omega 1/(-i\omega\exp(-i\omega\delta) + C) = n_F(C)$.

Though Heisenberg's uncertainty principle [353, 354] indicates that $\delta \sim 1/\max(\omega)$, this does not prevent the exponent from tending to zero. This is ensured by a careful choice of oblong integration contour, with its major axis along the complex axis defining the maximum frequency and so minimum δ, and minor axis along the real axis giving that frequency which multiplies the time-step [355].

154

Feynman diagrams.

The functional integral Eqn. (A.31) is currently in the time representation. However, one could make the fields periodic, $\psi(\tau) = \psi(\tau + \beta)$ for bosons and $\eta(\tau) = -\eta(\tau + \beta)$ for fermions so that they could be expressed in terms of a Fourier series [356]. This representation is often more convenient if the Hamiltonian is time independent. We would then have to sum over the *Matsubara frequencies*,

$$
\omega_n = \begin{cases} 2n\pi/\beta & \text{bosons,} \\ (2n+1)\pi/\beta & \text{fermions,} \end{cases} \quad n \in \mathbb{Z}, \tag{A.32}
$$

whose values reflect boson (fermion) particle exchange symmetry (antisymmetry).

In evaluating the coherent state part integral, the terms in the field can be divided into two different types, as shown in Table A.3. First is the *classical* term in which the field is constant in time. They are classical since they are akin to what is seen in the Feynman path integral where time evolution is not necessary since the momentum and space operators commute (the classical limit corresponds to $\hbar \to 0$). Second are those terms that do evolve with time which lie in the *quantum sector*. These two sectors can be further divided into those terms that do and do not vary in space where the former can change the total number of particles, and the latter shift them around. Finally, we note that the constant homogeneous field, which often corresponds to the saddle point solution for the field, is still integrated over despite the saddle point approximation. This is because the coherent state path integral operates within the grand canonical regime where the chemical potential is fixed, but the total number of particles is not. However, the inclusion of a path integral over variations in this field can lead to problems, chiefly because the action will contain a term of the form $\phi_0\phi_{fl}$, where ϕ_0 is the saddle point field and ϕ_{fl} variation around it. The dogmatic solution is to neglect the variations ϕ_{fl}, with the consequence that the coherent state path integral accounts for the majority of the terms in the summation of the grand partition function, and assume that the variations in ϕ_{fl} are just one of an infinite multitude of terms and therefore can be neglected. The alternative pragmatic solution is to sidestep the problem and ignore the term $\phi_0\phi_{fl}$, but include variations of the type ϕ_{fl}^2.

Table A.3: The consequences of time (frequency ω) and spatial (wave vector $\mathbf{q}$) fields in a a coherent state path integral.

	$\mathbf{q} = \mathbf{0}$	$\mathbf{q} \neq \mathbf{0}$
	Classical sector	
$\omega = 0$	Changes total number of particles, often the saddle point solution	Spatial fluctuations at constant total number of particles
	Quantum sector	
$\omega \neq 0$	Fluctuations change total number of particles	Full quantum fluctuations in space and time

A.2.5   Hubbard-Stratonovich transformation

The Hubbard-Stratonovich transformation can be used to decouple an interaction term $\bar{\psi}\bar{\psi}\psi\psi$ that is quartic in the field ψ and make it quadratic at expense of introducing an auxiliary field ϕ. Once the action is quadratic in ψ we can integrate over that variable. The transformation is based on the identity $1 = \int \exp(-\frac{1}{4}\phi_i V_{ij}^{-1}\phi_j)\mathcal{D}\phi$ where we have then mapped $\phi_i \mapsto \phi_i + 2\mathrm{i}V_{ij}\hat{\rho}_j$ to get

$$\exp\left(-\hat{\rho}_i V_{ij}\hat{\rho}_j\right) = \int \exp\left(-\frac{1}{4}\phi_i V_{ij}^{-1}\phi_j - \mathrm{i}\phi_i\hat{\rho}_j\right)\mathcal{D}\phi\,, \qquad (A.33)$$

where i and j are indices of some generalised basis set, and the density operator is $\rho \sim \bar{\psi}\psi$. The Hubbard-Stratonovich transformation should be deployed whenever the particles form characteristic *pairs*, for example Cooper pairs in superconductors or spin pairs in ferromagnetism. It should not be used to, for example, decouple the quartic interaction term in describing BEC, where the ground state particles are not paired and so should not be forced to do so by the mathematical formulation.

A difficulty arises as there is a choice in how to decouple the original field ψ, in momentum space there are three main choices or channels for the decoupling:

Direct channel: We use $\hat{\rho}_\mathbf{q} = \sum_\mathbf{p} \bar{\psi}_{\sigma\mathbf{p}}\psi_{\sigma\mathbf{p}+\mathbf{q}}$. The parameter $\mathbf{q}$ represents how far from the Fermi surface the particles are excited from/to. This is tailored for analysing problems involving the Coulomb interaction of charge in the normal phase.

Exchange channel: Here $\hat{\rho}_\mathbf{q} = \sum_\mathbf{p} \bar{\psi}_{\sigma\mathbf{p}}\psi_{\sigma'\mathbf{p}+\mathbf{q}}$. The parameter $\mathbf{q}$ represents how far from the Fermi surface the particles are excited from/to. This channel is similar to the direct except that it also carries spin structure, making it

Scheme	$n_\uparrow(\mathbf{r})n_\downarrow(\mathbf{r}) =$	Rotational invariance	Hartree-Fock	References
i	$\frac{1}{2}\rho(\mathbf{r}) - 2S_z^2(\mathbf{r})$	✗	✓	[291, 357]
ii	$\frac{1}{4}\rho^2(\mathbf{r}) - \frac{1}{3}\mathbf{S}^2(\mathbf{r})$	✓	✗	[358–361]
iii	$\frac{1}{4}\rho^2(\mathbf{r}) - (\mathbf{e}_z \cdot \mathbf{S}(\mathbf{r}))^2$	✗	✓	[362, 363]
iv	$\frac{1}{4}\rho^2(\mathbf{r}) - (\boldsymbol{\phi}(\mathbf{r}) \cdot \mathbf{S}(\mathbf{r}))^2$	✓	✓	[293, 294]

Table A.4: Approximation schemes used in the Hubbard-Stratonovich decomposition of the interacting term $gn_\downarrow(\mathbf{r})n_\uparrow(\mathbf{r})$, where $\rho(\mathbf{r}) = n_\uparrow(\mathbf{r}) + n_\downarrow(\mathbf{r})$, $S_z(\mathbf{r}) = n_\uparrow(\mathbf{r}) - n_\downarrow(\mathbf{r})$, and $\mathbf{S}(\mathbf{r})$ is the total particle spin. Whether the scheme obeys rotational invariance and gives the correct Hartree-Fock result is indicated. Previous uses of each scheme are referenced.

suitable for problems with magnetism. It can itself be split into three channels representing the three magnetisation directions.

Cooper channel: In this case $\hat{\rho}_\mathbf{q} = \sum_\mathbf{p} \bar{\psi}_{\sigma\mathbf{p}}\bar{\psi}_{\sigma'\mathbf{q}-\mathbf{p}}$. The parameter $\mathbf{q}$ represents the deviation from a true Cooper pair with no centre of mass motion. This is suited to problems involving superconductivity.

Whichever decoupling channel we choose, the Hubbard-Stratonovich transformation is exact, but the choice is influenced by what further approximations will be necessary to do the functional integral over the auxiliary field. In each case a suitable decoupling channel will generate an auxiliary field that depends on a small momentum $\mathbf{q}$, meaning the interaction has overall low energy, facilitating an expansion in the auxiliary field. The other two momenta involved in the problem are on the same scale as the Fermi momentum since the particles involved in the interaction and excitations are typically near the Fermi surface. If following the Hubbard-Stratonovich transformation just a mean-field analysis is performed on the auxiliary field, the scheme generates the Hartree-Fock approximation (HF) terms. The Gaussian fluctuations in the auxiliary field can be included by a further functional integral. This generates a ring of RPA-like contributions and a more accurate estimate of the ground-state properties. Essentially the choice of decoupling channel determines which terms are included in the summation for the quantum partition function.

A.2.6   Choice of Hubbard-Stratonovich transformation

As a case study of choosing an appropriate Hubbard-Stratonovich transformation
we look at the contact interaction studied in Chp. 6 and Chp. 7, where the goal was
to study itinerant ferromagnetism. The interaction term in the Hamiltonian takes
the form

$$H = g \int n_\uparrow(\mathbf{r}) n_\downarrow(\mathbf{r}) \mathrm{d}\mathbf{r}, \tag{A.34}$$

for spin-up density $n_\uparrow$ and spin-down density $n_\downarrow$. We decouple the interaction,
quartic in fields, using a Hubbard-Stratonovich transformation in the exchange
channel as we are searching for ferromagnetism. There are several possibilities even
for the decomposition in this channel, making the method ambiguous. Though any
decomposition is exact, approximations made following a decomposition to continue
the analysis can lead to different results as contrasting contributions are included
in the approximation for the partition function. There are myriads of possibilities,
four characteristic types that have been used in previous studies are outlined in
Table A.2.6.

The first approach (i) has a field with just a single component along the z-axis.
The initial rotational symmetry is lost which implies a physical deficiency with this
scheme. The second method (ii) contains a scalar product of a vector form for the
spin and so is rotationally invariant. However, if the analysis is continued through
in the mean-field limit it does not give the correct Hartree-Fock equations for the
Hamiltonian, but instead maps the interaction parameter $g \mapsto g/3$. Therefore, the
scheme does not properly comply with the Pauli exclusion principle. The third (iii)
and fourth (iv) approaches feature a choice of vector $\boldsymbol{\phi}$. If a single component
is chosen, for example along the z-axis, in approach (iii), then much like in the
first scheme (i) the rotational symmetry is lost. However, in approach (iv) the
choice of axis is functionally integrated over so rotational invariance is preserved.
The fourth method also gives the correct Hartree-Fock equations; it is the simplest
scheme to both preserve rotational invariance and obey Pauli exclusion, motivating
its deployment in Chp. 6 and Chp. 7.

A.3 Phase transitions

Phase transitions [56] play an important rôle in the universe. Large scale structure in the cosmos formed in phase transitions soon after the Big Bang; later phase transitions shaped galaxies and stars. In our lives the transition of water between ice, liquid, and vapour play an important part in shaping our world. The ice-liquid and liquid-vapour phase transitions of water are both *first-order*, meaning that *latent heat* is released as the substance temperature changes infinitesimally across the transition (at 0°C and 100°C respectively). Those transitions which do not involve latent heat, known as *continuous* or *second-order* (or higher) transitions are interesting as the typical length and time scales diverge on approaching the phase boundary. The phase transitions that we observe in everyday life are driven by *thermal fluctuations* in the *classical* limit. However, at low temperatures *quantum phase transitions* are driven by *quantum fluctuations* which can lead to novel and unexpected phases that are the subject of cutting edge research. We now present a general approach to analyse phase transitions that can be applied to a vast range of systems.

A.3.1 Landau mean-field theory

The degrees of freedom that usually describe phase transitions are long-range collective excitations [8]. We can therefore increase the resolved length-scales by *coarse-graining* the system and represent the average of a system property around a point in space by an *order parameter*. A suitable coarse-grained Hamiltonian obeys:

Locality: The Hamiltonian depends only on the local order parameter and the short range interactions described by its gradients.

Rotational symmetry: Without an external field the Hamiltonian must be invariant under a rotation of the order parameter.

Translational and rotational symmetry in the position variable: This allows us to write the Hamiltonian in terms of a power expansion in the order parameter and its gradients.

Any Hamiltonian falling in this class is a *Ginzburg-Landau Hamiltonian*. Using $\mathbf{m}$ to represent the order parameter (magnetisation) and $\mathbf{h}$ the external (magnetic) field the *Ginzburg-Landau free energy density* is

$$f(m,h) = \frac{\beta F}{V} = \frac{t}{2}m^2 + um^4 + vm^6 + \frac{K}{2}(\nabla m)^2 + \frac{L}{2}(\nabla^2 m)^2 + \frac{N}{2}m^2(\nabla m)^2 - hm\,.$$
(A.35)

We keep only the lowest order terms in the expansion since at the critical point $\bar{m}$ is often small, and to ensure stability we require the coefficient of the highest order term be positive, meaning that here $v > 0$.

The more general *Ginzburg-Landau* phenomenology accounts for a spatially varying order parameter. If it is assumed that spatial variation always costs energy then the order parameter can be assumed to be uniform, and the gradient terms can be dropped, which gives the *Landau mean-field theory*. The quantum partition function for the system is

$$\mathcal{Z}[\beta,\mathbf{H}] = \int e^{-\beta H[\mathbf{m},\mathbf{H}]}\mathcal{D}\mathbf{m}\,.$$
(A.36)

By minimising the free energy density with respect to its order parameter we can find the saddle point solution for the quantum partition function. This provides a *mean-field* approximation for the quantum partition function

$$\mathcal{Z}[\beta,\mathbf{H}] = e^{-\beta\overbrace{\min_{\mathbf{m}}(H[\mathbf{m},\mathbf{H}])}^{F[\mathbf{H}]}}\,.$$
(A.37)

The behaviour, with $h = 0$ is shown in Fig. A.7. We see second order transitions are associated with the quadratic term turning negative; first order transitions occur where the quartic term becomes negative. Finally, we note that at a first order transition the free energy has two degenerate minima, which necessarily move differently with temperature resulting in latent heat $T\Delta S = T\partial f/\partial T$ being emitted. At the first-second order transition crossover at $t = 0 = u$ there is a *tricritical point* where the free energy curve has *three* degenerate minima.
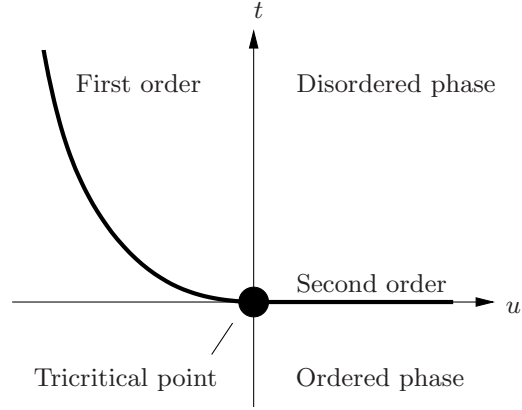
Figure A.7: For the system with free energy density Eqn. (A.35), the bold line shows the phase boundary in the t,u plane, and the circle highlights the tricritical point.

A.4 Quantum Monte Carlo background

In this appendix we introduce the *ab initio* QMC computational technique employed in this thesis to examine strongly correlated states. This powerful stochastic method enables investigators to not only study otherwise intractable many-body problems, but it is also formally exact (except for the fixed-node approximation), and so is used to study many-body theory with an accuracy that is usually not achievable with analytical methods. The QMC method calculates the energy via a Monte Carlo integral, and then employs the variational principle to minimise the energy and determine the ground state, using an algorithm that is outlined below.

A.4.1 Variational principle

The Ritz variational principle [354] states that the expectation value of the Hamiltonian operator $\hat{H}$ in the state $|\psi\rangle$ is greater than or equal to the Hamiltonian ground eigenstate energy E_0. Equality occurs if and only if $|\psi\rangle$ is the ground eigenstate $|\psi_0\rangle$,

$$E = \frac{\langle\psi|\,\hat{H}\,|\psi\rangle}{\langle\psi|\,\psi\rangle} \geq \frac{\langle\psi_0|\,\hat{H}\,|\psi_0\rangle}{\langle\psi_0|\,\psi_0\rangle} = E_0\,. \tag{A.38}$$

This principle places an upper bound on the ground-state energy E_0. To implement this principle in VMC, we re-write the energy as

$$E = \frac{\int |\psi(\mathbf{R})|^2 E_{\mathrm{L}}(\mathbf{R})\mathrm{d}\mathbf{R}}{\int |\psi(\mathbf{R})|^2\mathrm{d}\mathbf{R}}\,. \tag{A.39}$$

Here $E_{\mathrm{L}}(\mathbf{R}) = \psi^{-1}(\mathbf{R})\hat{H}\psi(\mathbf{R})$ denotes the *local energy*, where $\mathbf{R} = \{\mathbf{r}_i\}$ denotes the positions $\mathbf{r}$ of all of the N particles in the system. The energy E can now be minimised with respect to free parameters in the trial wave function ψ to find the ground-state ψ_0.

A.4.2 Monte Carlo integration

To evaluate a d-dimensional integral $I = \int f \mathrm{d}V$, a conventional quadrature method might distribute points in a d-dimensional cubic mesh of N points, evaluate the function at each point and apply a Newton-Cotes formula, for example Simpson's rule [356]. The error in the Simpson's rule estimate scales as $N^{-4/d}$. As the number of dimensions increases, the error decays more slowly with N so the problem becomes intractable. A typical system studied using QMC might be three-dimensional and contain 100 electrons; therefore to use Eqn. (A.39) to calculate the energy, a $3 \times 100 = 300$ dimensional integral $\int \mathrm{d}\mathbf{R} = \int \prod_{i=1}^{100} \mathrm{d}\mathbf{r}_i$ needs to be evaluated. Due to its high dimensionality, rather than use a conventional quadrature method, this problem is perfectly suited to Monte Carlo integration.

A Monte Carlo algorithm [356] samples the integrand f at N pseudo-random points $\{\mathbf{R}_n\}$ within the integral boundaries (which define an integration volume V). In QMC, a particular point $\{\mathbf{R}_n\}$ is known as a *configuration*, *walker*, or *psip* [15]. The estimate of the integral is then

$$I = \frac{V}{N} \sum_{n=1}^{N} f(\mathbf{R}_n) \equiv V \langle f \rangle, \tag{A.40}$$

where $\langle f \rangle$ is the sample mean of the integrand. The variance of this estimate is

$$\sigma^2 = \frac{V}{N(N-1)} \sum_{n=1}^{N} (f(\mathbf{R}_n) - \langle f \rangle)^2. \tag{A.41}$$

The error in the estimate for the integral decreases as $\sim N^{-1/2}$, a substantial improvement over Simpson's rule. An *importance sampling transformation* [15] can improve the estimate still further by focusing the sampling to where the integral changes most rapidly. We re-write $f(\mathbf{R}_n) = w(\mathbf{R}_n)g(\mathbf{R}_n)$ where the unnormalised

probability distribution $w(\mathbf{R}_n)$ is chosen to make $g(\mathbf{R}_n)$ as smooth as possible. The integral is then

$$I = \frac{\int wg\mathrm{d}V}{\int w\mathrm{d}V} \,, \tag{A.42}$$

which may be evaluated as

$$I = \frac{V}{N} \sum_{n=1}^{N} g(\mathbf{R}_n) \,. \tag{A.43}$$

The configurations are now sampled according to $w/\int w\mathrm{d}V$. The variance of the estimate reduces with a good choice of unnormalised probability distribution. To estimate the energy Eqn. (A.39) we take $w = |\psi|^2 / \int |\psi|^2 \mathrm{d}\mathbf{R}$ [15], and use the local energy density $g(\mathbf{R}_n) = E_\mathrm{L}(\mathbf{R}_n)$.

To implement the importance sampling transformation the distribution w must be normalised, which requires its integral to be known, the very quantity we are trying to evaluate. The *Metropolis rejection algorithm* [129] overcomes this difficulty, allowing the distribution to be sampled directly without its normalisation. A single configuration starts at a random position, at a later step i the configuration is $\mathbf{R}_i$. A move sampled from a Gaussian centred on the current configuration to $\mathbf{R}_i'$ is proposed, and then if $|\psi(\mathbf{R}_i')/\psi(\mathbf{R}_i)|^2$ is less than some random number between zero and one the move is accepted. After many steps, the distribution of configurations will asymptotically approach $\psi(\mathbf{R})$.

A.4.3 Wave function optimisation

Minimising the variance of the local energy with respect to the free parameters $\{\alpha\}$ is sometimes more robust than minimisation of the total energy [364–366]. Using E_VMC to denote the average QMC energy, the variance in the local energy E_L is

$$\sigma_{E_\mathrm{L}}^2 = \frac{\int \left(E_\mathrm{L}^{\{\alpha\}} - E_\mathrm{VMC}^{\{\alpha\}}\right)^2 \left|\psi^{\{\alpha\}}(\mathbf{R})\right|^2 \mathrm{d}\mathbf{R}}{\int \left|\psi^{\{\alpha\}}(\mathbf{R})\right|^2 \mathrm{d}\mathbf{R}} \,, \tag{A.44}$$

which is zero if the trial wave function is exact and positive otherwise. Therefore, the trial wave function may be optimised by changing the free parameters $\{\alpha\}$ to minimise the variance of the local energy.

The variance should be computed for each parameter set. However, this is computationally expensive and unstable due to statistical noise. To circumvent this the *correlated sampling* approach fixes the configurations according to some initial set of parameters $\{\alpha_0\}$ and then calculates the variance as the parameters are varied. To compensate for the fixed configurations, a *re-weighted variance* formula is used

$$\sigma_{E_{\mathrm{L}}}^2 = \frac{\int \left(E_{\mathrm{L}}^{\{\alpha\}} - E_{\mathrm{VMC}}^{\{\alpha\}}\right)^2 W_{\{\alpha_0\}}^{\{\alpha\}}(\mathbf{R}) \left|\psi^{\{\alpha_0\}}(\mathbf{R})\right|^2 \mathrm{d}\mathbf{R}}{\int W_{\{\alpha_0\}}^{\{\alpha\}}(\mathbf{R}) \left|\psi^{\{\alpha_0\}}(\mathbf{R})\right|^2 \mathrm{d}\mathbf{R}}, \qquad (\mathrm{A}.45)$$

where the VMC energy is

$$E_{\mathrm{VMC}}^{\{\alpha\}} = \frac{\int E_{\mathrm{L}}^{\{\alpha\}} W_{\{\alpha_0\}}^{\{\alpha\}}(\mathbf{R}) \left|\psi^{\{\alpha_0\}}(\mathbf{R})\right|^2 \mathrm{d}\mathbf{R}}{\int W_{\{\alpha_0\}}^{\{\alpha\}}(\mathbf{R}) \left|\psi^{\{\alpha_0\}}(\mathbf{R})\right|^2 \mathrm{d}\mathbf{R}}, \qquad (\mathrm{A}.46)$$

and in general the weights are

$$W_{\{\alpha_0\}}^{\{\alpha\}} = \left(\frac{\psi^{\{\alpha\}}}{\psi^{\{\alpha_0\}}}\right)^2. \qquad (\mathrm{A}.47)$$

The re-weighted variance is minimised at the true ground state for any arbitrary positive weights. If fixed at unity ($W_{\{\alpha_0\}}^{\{\alpha\}} = 1$) we get the *unreweighted variance*, which we used for the VMC calculations presented in this thesis.

A.4.4   Slater-Jastrow wave functions

Every QMC calculation requires a trial wave function that not only obeys the appropriate particle exchange statistics, but ideally will also contain optimisable parameters. The two-component of a Slater determinant and a Jastrow factor implemented here is well-established as the perfect vehicle to use within QMC. For a system of N fermions at positions $\mathbf{R} = (\mathbf{r}_1,...,\mathbf{r}_N)$, the trial wave function $\psi(\mathbf{R})$

must be antisymmetric under particle exchange. A straightforward way to achieve antisymmetry for a system of spin-up and spin-down electrons is to use a Slater determinant of single particle orbitals $\phi_j^{\uparrow\downarrow}(\mathbf{r}_i)$ [354],

$$
\psi(\mathbf{R}) = \begin{vmatrix} \phi_1^{\uparrow}(\mathbf{r}_1^{\uparrow}) & \cdots & \phi_1^{\uparrow}(\mathbf{r}_{N_\uparrow}^{\uparrow}) \\ \vdots & \ddots & \vdots \\ \phi_{N_\uparrow}^{\uparrow}(\mathbf{r}_1^{\uparrow}) & \cdots & \phi_{N_\uparrow}^{\uparrow}(\mathbf{r}_{N_\uparrow}^{\uparrow}) \end{vmatrix} \begin{vmatrix} \phi_1^{\downarrow}(\mathbf{r}_1^{\downarrow}) & \cdots & \phi_1^{\downarrow}(\mathbf{r}_{N_\downarrow}^{\downarrow}) \\ \vdots & \ddots & \vdots \\ \phi_{N_\downarrow}^{\downarrow}(\mathbf{r}_1^{\downarrow}) & \cdots & \phi_{N_\downarrow}^{\downarrow}(\mathbf{r}_{N_\downarrow}^{\downarrow}) \end{vmatrix} \equiv D^{\uparrow} D^{\downarrow} . \quad \text{(A.48)}
$$

The single particle orbitals may be derived using Hartree-Fock theory [111] or DFT [11], and for a uniform periodic system would be plane waves. The Hamiltonian is spin independent so the wave function can be written as a product of separate spin up $(D_\uparrow)$ and down $(D_\downarrow)$ determinants. The expense to evaluate a $N \times N$ determinant scales as $\mathcal{O}(N^3)$ [367] so this factorisation reduces computational effort. If the electron gas has ν flavours this idea can be extended, the many-body wave function may be written as the product of 2ν determinants, each representing a different spin and flavour combination.

Because of the variational principle, Sec. A.4.1, the ground state energy can be reduced by varying free parameters in the trial wave function using VMC (Sec. A.4.3). The standard method is to consider a Slater-Jastrow wave function that has a single Slater determinant multiplied by a Jastrow factor [15, 132] $J(\mathbf{R})$, which contains the free parameters

$$
\psi_{\mathrm{T}}(\mathbf{R}) = \mathrm{e}^{J(\mathbf{R})} \prod_{i=1}^{\nu} D_i^{\uparrow} D_i^{\downarrow} . \quad \text{(A.49)}
$$

As $J(\mathbf{R})$ is real, the factor is non-negative so the wave function generated is explicitly antisymmetric under particle exchange. Also, the Slater-Jastrow wave function and Slater wave function have identical nodal surfaces. Because of the variational principle (Sec. A.4.1), a suitable Jastrow factor will always reduce the ground state energy, that difference is (part of) the *correlation energy* [111].

The HF wave function is explicitly antisymmetric, so it generates an exchange hole which ensures that electrons with the same spin cannot occupy the same point in space. The HF wave function does not however account for correlations due to

Coulomb repulsion between electrons with different spins. A two-body term $u(\mathbf{r}_{ij})$ in the Jastrow factor could reduce the wave function where two electrons i and j come close to each other. The trial wave function should have near constant local energy density, $E_{\mathrm{L}} = \psi^{-1}\hat{H}\psi$ but the Coulomb interaction between electrons separated by $\mathbf{r}$ diverges as $\sim 1/|\mathbf{r}|$. Therefore as the electrons approach the wave function needs a cusp [134], which we attribute to the u term. To generate this cusp places constraints on u, differing if the two electrons obey the Pauli exclusion principle,

$$\left.\frac{\mathrm{d}u}{\mathrm{d}r}\right|_{\mathbf{r}=\mathbf{0}} = \begin{cases} -\frac{1}{2} & \text{for opposite spins,} \\ -\frac{1}{4} & \text{for parallel spins.} \end{cases} \tag{A.50}$$

A suitable form for the u term is a series expansion of the powers of its arguments [133]. The u term cannot act outside of the simulation cell so therefore has a cutoff length that can be optimised. The maximum allowed value is the Wigner-Seitz radius[7] in supercell calculations, which avoids the need for an Ewald sum.

The u terms act over a spherical region so cannot act at the corner of the simulation cell. Therefore, a plane-wave expansion $p(\mathbf{r}_{ij})$ can be included in the Jastrow factor to provide additional freedom. If a periodic potential is applied then a periodic $q(\mathbf{r}_i)$ term with the form of an expansion of cosine of the scalar product of position and a suitable wave vector can be included.

A.4.5   Variational Monte Carlo

In order to go beyond the HF wave function, optimisable parameters were introduced via a Jastrow factor into the trial wave function. In order to determine suitable values for these parameters, the well-established method is to calculate the total energy with QMC and then minimise is within the framework of VMC. The standard VMC algorithm is outlined in Fig. A.8. Following initial setup, the configurations are randomly distributed. During the equilibration phase, for each electron in a configuration a move is proposed that is accepted or rejected according to the Metropolis algorithm (Sec. A.4.3), but the local energy is not accumulated at this

---

[7]The Wigner-Seitz radius is defined as the radius of the largest sphere that fits inside the simulation supercell [9].
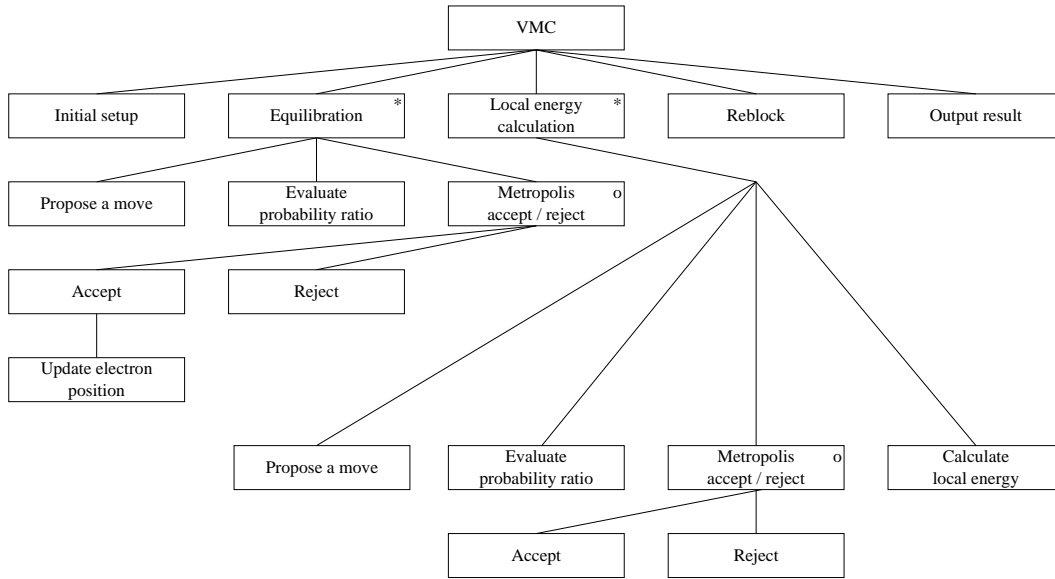
Figure A.8: Jackson structure chart of the VMC algorithm.

stage. Once the local energy no longer drifts the configurations correctly sample the distribution $|\psi_T|^2$. In the second stage the configurations continue to move according to the Metropolis algorithm but the local energy is accumulated. This process is repeated many times during variance minimisation (Sec. A.4.3) as the wave function parameters are adjusted. The reblocking analysis that is used to get the final result is described in Sec. A.4.6.

The VMC time-step controls how far configurations move each time-step. It is chosen to minimise the correlation period of the local energy. If the time-step is too long the move rejection probability is high, and configurations do not move leading to serial correlation. If the time-step is short then the configuration step length is small and so only one part of the wave function is sampled, again resulting in serial correlation. At the optimal time-step the rejection probability should be $\sim 50\%$.

The VMC algorithm may be parallelised. The general scheme is for each node to be assigned a set of configurations which it equilibrates and calculates their local energy density. At the end of the calculation the *master node* collates the results and determines the mean total energy.

A.4.6 Diffusion Monte Carlo

The wave function optimisation in the VMC framework is limited by the freedom permitted by the terms within the Jastrow factor. To imbue complete freedom in the wave function we employ the DMC method [15, 131] that is formally exact except for the fixed node approximation. DMC is a stochastic method that projects the wave function $\phi(\mathbf{R},t)$ onto configurations and solves the imaginary-time many-body Schrödinger equation,

$$\partial_t \phi(\mathbf{R},t) = (\hat{H} - E_{\mathrm{T}})\phi(\mathbf{R},t)\,. \tag{A.51}$$

Here $\mathbf{R}$ is a $3N$ dimensional vector of the positions of all N electrons, t is a real variable describing imaginary time, and E_{T} is the trial energy. The Green's function is the propagator

$$G(\mathbf{R} \leftarrow \mathbf{R}',\tau) = \left\langle \mathbf{R}' \left| \mathrm{e}^{-\tau(\hat{H}-E_{\mathrm{T}})} \right| \mathbf{R} \right\rangle\,. \tag{A.52}$$

This satisfies the initial condition $G(\mathbf{R} \leftarrow \mathbf{R}',\tau) = \delta(\mathbf{R} - \mathbf{R}')$ and obeys the same Schrödinger equation as the wave function ϕ

$$\partial_\tau G(\mathbf{R} \leftarrow \mathbf{R}',\tau) = (\hat{H}(\mathbf{R}') - E_{\mathrm{T}})G(\mathbf{R} \leftarrow \mathbf{R}',\tau)\,. \tag{A.53}$$

A spectral expansion allows us to express the Green's function as

$$G(\mathbf{R} \leftarrow \mathbf{R}',\tau) = \sum_i \psi_i(\mathbf{R}')\mathrm{e}^{-\tau(E_i-E_T)}\psi_i^*(\mathbf{R})\,, \tag{A.54}$$

where ψ_i and E_i are the eigenfunctions and eigenvalues of $\hat{H}$. This formalism then allows us to write the wave function at a later time $t+\tau$ in terms of the propagator,

$$\begin{aligned}
\phi(\mathbf{R}',t+\tau) &= \int G(\mathbf{R} \leftarrow \mathbf{R}',\tau)\phi(\mathbf{R},t)\mathrm{d}\mathbf{R} \\
&= \sum_i \psi_i(\mathbf{R}')\mathrm{e}^{-\tau(E_i-E_T)} \left\langle \psi_i \right| \phi(t=0)\rangle\,.
\end{aligned} \tag{A.55}$$

As the interval becomes large ($\tau \to \infty$), if $E_T = E_0$ the higher energy states decay exponentially in magnitude projecting out the ground state,

$$\lim_{\tau \to \infty} \phi(\mathbf{R}, t + \tau) = \lim_{\tau \to \infty} \psi_0(\mathbf{R}) e^{-\tau(E_0 - E_T)} \langle \psi_0 | \phi(t = 0) \rangle . \qquad (A.56)$$

To maintain a mean number of configurations the trial energy is actively varied[8], which allows configurations to be created or destroyed; an example of the propagation of walkers is shown in Fig. A.9. Electrons in configurations are allowed to diffuse with step-length according to a Gaussian distribution with a width controlled by a characteristic DMC time-step. We note that the Schrödinger equation Eqn. (A.53) has the same form as a diffusion equation

$$\partial_\tau \phi(\mathbf{R}, \tau) = -\left(\frac{1}{2} \nabla^2 + \hat{V}(\mathbf{R}) - E_T \right) \phi(\mathbf{R}, \tau) , \qquad (A.57)$$

where $E_T - \hat{V}(\mathbf{R})$ is a rate term describing branching. Therefore, this equation may be simulated by a diffusion process. The Green's function solution [130] of it

$$G(\mathbf{R} \leftarrow \mathbf{R}', \tau) = \frac{1}{(2\pi\tau)^{3N/2}} e^{-(\mathbf{R} - \mathbf{R}')^2/2\tau} e^{-\tau(V(\mathbf{R}) + V(\mathbf{R}') - 2E_T)/2} \qquad (A.58)$$

can be interpreted as a transition probability density for the configurations.

The above analysis assumes that the wave function ψ is everywhere positive as it is interpreted as a probability. Electrons however have Fermi antisymmetry so a many-body wave function must have positive and negative spatial regions. If these regions are allowed to encroach then the wave function becomes unstable, and one region would grow exponentially [127]. To overcome this a trial nodal surface is derived using HF or DFT. The *fixed-node* DMC [130] method rejects moves between positive and negative regions, as if there were an infinite potential that ensures the regions remain fixed. Though not exact, this approximation gives energies which satisfy the variational principle and is stable in large systems. Around the nodal surface the wave function is small so makes only a small contribution to the energy,

---

[8]A VMC simulation may be regarded as a DMC calculation without branching of electrons. Without branching each configuration evolves independently without any drift-diffusion, so the form of the wave function does not change.
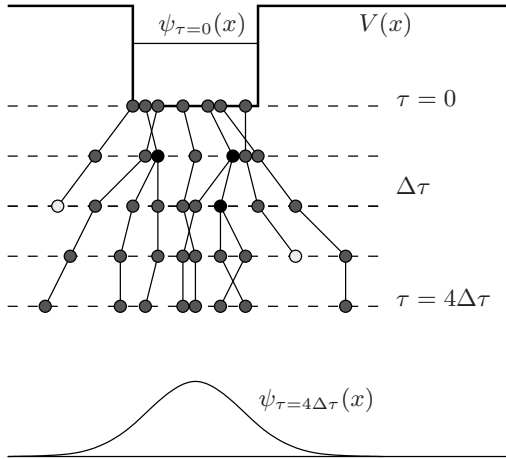
Figure A.9: The wave function is confined by a one-dimensional finite square well $V(x)$ shown by the bold line. The trial wave function $\psi_{\tau=0}(x)$ at $\tau = 0$ is uniform and shown by the solid line. It is represented by walkers shown by grey shaded circles. The horizontal dashed lines show DMC walker propagation during imaginary time-steps $\Delta\tau$. After propagation the distribution converges to the true ground state at $\tau = 4\Delta\tau$. Black circles represent configuration birth, empty configuration death.

hence any error in the nodal surface makes only a small difference to the ground state energy prediction. If the wave function is complex then the fixed-node approximation may be generalised to the *fixed-phase* approximation, which requires the trial and DMC wave function has everywhere the same phase.

In the DMC algorithm shown in Fig. A.10, firstly configurations are initialised according to the probability density given by configurations from a VMC simulation. Each electron within a configuration diffuses one step, if it crosses a node the move is rejected. To avoid divergences due to the Coulomb interaction we use importance sampling. We actually propagate the distribution $f(\mathbf{R},t) = \psi(\mathbf{R})\phi(\mathbf{R},t)$, where ψ is the trial wave function generated from VMC and ϕ is the DMC wave function. The weight for the move is

$$W(\mathbf{R}',\mathbf{R}) = \frac{|\psi(\mathbf{R}')|^2 G(\mathbf{R}',\mathbf{R},\tau)}{|\psi(\mathbf{R})|^2 G(\mathbf{R},\mathbf{R}',\tau)} \ . \tag{A.59}$$

The move is accepted with probability $P = \min(1,W(\mathbf{R}',\mathbf{R}))$. The branching probability for the configuration is

$$P = \mathrm{e}^{-\tau((E_{\mathrm{L}}(\mathbf{R}')+E_{\mathrm{L}}(\mathbf{R}))/2 - E_{\mathrm{T}})} \ . \tag{A.60}$$

Then $\mathrm{int}(P + \zeta)$ copies of the configuration are made, where ζ is a random number between zero and one, and hence this algorithm allows configuration death. The configuration energy is then accumulated, the best estimate of the ground-state

energy E_{best} is updated during equilibration after each block of moves as

$$E_{\mathrm{best}}(\mu) = \frac{3}{4} \langle E_{\mathrm{L}} \rangle (\mu) + \frac{1}{4} E_{\mathrm{best}}(\mu - 1) , \qquad (A.61)$$

where $\langle E_{\mathrm{L}} \rangle (\mu)$ is the average of the local energy over block μ. During statistics accumulation E_{best} is instead recalculated after each move using the expectation value of the local energy at that time-step. The adjustable energy E_{T} that controls the number of configurations is

$$E_{\mathrm{T}}(\mu + 1) = E_{\mathrm{best}}(\mu) - \frac{A}{\tau_{\mathrm{eff}}(m)} \ln \left(\frac{N(\mu)}{N_0} \right) , \qquad (A.62)$$

where $A = \min(1, \tau c_{E_{\mathrm{T}}})$ with constant $c_{E_{\mathrm{T}}}$ usually set equal to unity; A^{-1} is the number of time-steps over which the weight has attempted to return the number of configurations $N(\mu)$ to the target population N_0. When calculating the branching factor we wish to use as a time-step the actual distance diffused [130], this varies between particles as some moves are rejected. The effective time-step is

$$\tau_{\mathrm{eff}}(m) = \tau \frac{\sum_i p_i \Delta r_{d,i}^2}{\sum_i \Delta r_{d,i}^2} , \qquad (A.63)$$

where p_i is the move acceptance probability, and $\Delta r_{i,d}$ is the diffusive displacement. The DMC process is then repeated until equilibrium is reached and statistical uncertainty reduced to a satisfactory level.

The DMC algorithm is intrinsically parallel. The configurations can be spread across all the nodes of the parallel machine. Each node performs the diffusion, drift and creation/annihilation of its configurations. Following a block of time-steps, the mean energy of all the configurations can be found. Configurations can then be redistributed across all the nodes to ensure *load balance*. A typical DMC calculation requires approximately an order of magnitude greater more Central Processing Unit (CPU) time than the equivalent VMC calculation. Most of the VMC calculations in this thesis were therefore done on single machines, whilst the DMC was done on parallel machines, either the High Perfomance Computing Service (HPCS) or a 32-node cluster.
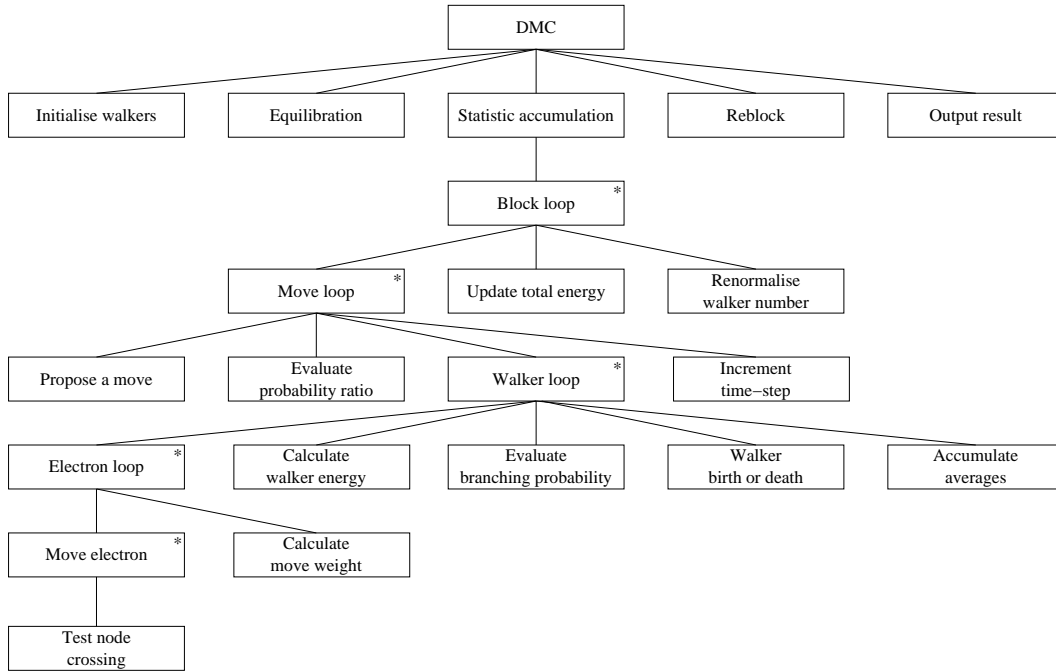
Figure A.10: Jackson structure chart of the DMC algorithm.

Though formally exact (except for the fixed node approximation), the practical implementation of DMC is reliant on further approximations that when relaxed make the calculation infeasible. The key approximations and extrapolation schemes that surmount the errors introduced are addressed briefly below.

Population-control bias

We derived the DMC Green's function Eqn. (A.54) assuming that E_T is constant, however, continual adjustment of E_T during DMC biases the system. This effect can be mitigated by using a large population of configurations, or alternatively to avoid extrapolating to infinite N, we follow the method of Umrigar et al. [131] for evaluating mixed estimators that eliminates the population-control bias.

Finite size corrections

The QMC simulations were performed inside finite sized simulation cells. This limits the range of the electron-electron correlation function and so the accuracy of the calculation. To overcome this error we could extrapolate using successively larger

Figure A.11: The allowed wave vectors in successive energy shells. The lowest energy shell containing one allowed electron is shown by the light grey point, successive shells containing 6, 12 and 8 points are shown by progressively darker shades.
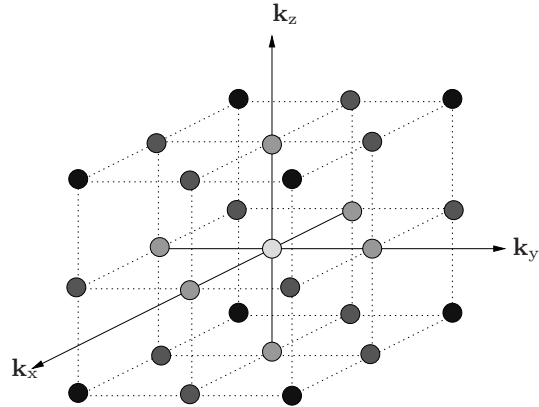
systems as shown in Fig. A.11, or alternatively one could average the calculation over the Brillouin zone. One method of doing this is to shift the origin of the free orbitals used over the Brillouin zone, that is use Twisted Boundary Conditions (TBC) and then average over the results [368]. A cheaper solution is to use the mean-value point in the Brillouin zone, also known as the Baldereschi point [369–371].

Finite time-step

During DMC the small but finite time-step is assumed to be zero. This approximation introduces a *time-step bias* that is corrected by performing simulations at two or more different time-steps and then extrapolating to zero time-step.

Serial correlation

Successive VMC and DMC configurations are produced from a previous configuration with small changes in electron position. The consecutive local energies therefore suffer from *serial correlation*, which is eliminated with a *reblocking algorithm* [372]. As shown in Fig. A.12, a reblocking transformation is repeated until just the average energy remains. The estimated standard deviation of a set of energies $\tilde{\sigma}_{\bar{E}}^{n}$ tends to a limit that will equal the true standard deviation $\sigma_{\bar{E}}$.

A.4.7 Blip basis set

The single particle orbitals that enter the Slater determinant are often plane waves. These pose the distinct disadvantage that they are delocalised so every basis function

$$\underbrace{E_1^{(0)} \ E_2^{(0)}}_{} \ \underbrace{E_3^{(0)} \ E_4^{(0)}}_{} \ \underbrace{E_5^{(0)} \ E_6^{(0)}}_{} \ \underbrace{E_7^{(0)} \ E_8^{(0)}}_{} \quad \rightarrow \quad \tilde{\sigma}_{\bar{E}}^{(0)}$$

Figure content:

Figure A.12: A reblocking transformation, with blocks of $\gamma = 2$ energy elements E. The energy subscript is the sequential element number, and the superscript is the number of accrued reblocking transformations. The standard deviation in the estimate of the mean energy is $\{\sigma_{\bar{E}}^n\}$, less than the true standard deviation $\sigma_{\bar{E}}$.

in every orbital must be summed over for each electron and hence the time to carry out a configuration move scales as $\mathcal{O}(N^3)$. One important alternative is to employ localised blip functions [169], which is particularly useful in a non-periodic system. The orbitals now need to be evaluated only about the electron, so the time taken for a configuration move scales as $\mathcal{O}(N^2)$. Blip wave functions are localised to a regular grid of spacing unity, and are zero beyond two grid increments. They are cubic splines of the form [168]

$$\phi(r) = \begin{cases} 1 - \frac{3}{2}r^2 + \frac{3}{4}r^3 & 0 \le r < 1\,, \\ \frac{1}{4}(2-r)^3 & 1 \le r < 2\,, \\ 0 & r \ge 2\,, \end{cases} \tag{A.64}$$

where r is the distance from the blip function's grid point. The function and its first two derivatives are continuous. A blip basis set is superior to other localised basis sets such as Gaussians [373] because they are *unbiased*[9] and their accuracy is systematically improvable by increasing the number of grid points.

A.4.8 Spin states of the Slater determinant

The Slater determinant is a practical trial wave function to use in QMC calculations. In the calculation of magnetic properties it is important to understand the spin state

---

[9]If an orbital is truncated introducing a small discontinuity this results in a Dirac delta function in the kinetic energy integrand. This cannot be sampled so the contribution to the energy is lost and the system is biased.

of a trial wave function with different numbers of up and down spin particles – is it singlet or triplet in character? If it were singlet then the total in-plane magnetisation is zero, if triplet then there could be a significant magnetic moment perpendicular to the axis, fundamentally changing the magnetisation of the state. To answer this important question we consider the Slater determinant in second quantised notation

$$|n_\uparrow, n_\downarrow\rangle = \prod_{i=1}^{n_\uparrow} c_{\uparrow,i}^\dagger \prod_{i=1}^{n_\downarrow} c_{\downarrow,i}^\dagger |\Omega\rangle \,, \tag{A.65}$$

where $n_\uparrow$ is the number of up-spin particles, $n_\downarrow$ is the number of down-spin particles, and without loss of generality we assume that $n_\uparrow \geq n_\downarrow$. Furthermore, during the construction of the wave function we assume that for each spin species the lowest single particle energy states are occupied, so for example for free particles these would be the allowed momentum states within a spherical Fermi surface.

In order to determine the spin expectation values of the Slater determinant wave function we use the *total spin operator* given by

$$\hat{\mathbf{S}} = \frac{1}{2} \begin{pmatrix} c_\uparrow^\dagger & c_\downarrow^\dagger \end{pmatrix} \boldsymbol{\sigma} \begin{pmatrix} c_\uparrow \\ c_\downarrow \end{pmatrix} \,, \tag{A.66}$$

where $\boldsymbol{\sigma} = (\sigma_x, \sigma_y, \sigma_z)$ represents a vector of the Pauli spin matrices. This has an expectation value for the total spin of

$$\left\langle \hat{\mathbf{S}} \right\rangle = \begin{pmatrix} 0 \\ 0 \\ (n_\uparrow - n_\downarrow)/2 \end{pmatrix} \,, \tag{A.67}$$

and the estimate for the root mean square in-plane spin is

$$\left\langle \hat{S}_{\perp,\mathrm{RMS}} \right\rangle \equiv \sqrt{\left\langle \hat{S}_x^2 + \hat{S}_y^2 \right\rangle} = \frac{\sqrt{n_\uparrow + n_\downarrow}}{2} \,. \tag{A.68}$$

In the limit of many particles this shows that with a population imbalance the majority of the spin magnetic moment is aligned along the z-axis, $\langle \hat{S}_{\perp,\mathrm{RMS}} \rangle \ll \langle \hat{\mathbf{S}} \rangle$, and so the Slater determinant wave function mostly has singlet rather than triplet

initialisation
repeat loop over time steps
    foreach *configuration in the simulation* **do**
        foreach *electron in the configuration* **do**
            propose move of electron; changes a single column of D
            calculate ratio $\Psi(\mathbf{R}_{new},\mathbf{S})/\Psi(\mathbf{R}_{old},\mathbf{S})$
            perform Metropolis accept/reject step
            if *move is accepted* **then** update cofactor matrix and determinant
            propose spin flip of electron; changes a single column of D
            calculate ratio $\Psi(\mathbf{R},\mathbf{S}_{new})/\Psi(\mathbf{R},\mathbf{S}_{old})$
            perform Metropolis accept/reject step
            if *flip is accepted* **then** update cofactor matrix and determinant
        end
    end
    accumulate local energy
until *end of simulation*
reblock
output

Algorithm 1: Pseudocode of the noncollinear VMC algorithm

character. Its magnetic moment is therefore approximately given by that along the z-axis, $(n_\uparrow - n_\downarrow)/2$. If one considers the spin states summed over during the construction of the Slater determinant then, akin to the central limit theorem, there are many more contributing low than high spin states and so the overall in-plane spin would be expected to be small relative to the total spin.

A.4.9 Noncollinear spin states

To address the possibility of a spin spiral using QMC we must extend beyond standard algorithms that are restricted to *collinear* systems. The capability to study *noncollinear* spins is well-established in DFT, and here we outline how, for the first time, to make noncollinear states accessible within the framework of VMC [315].

The wave function $\Psi(\mathbf{R},\mathbf{S}) = \exp(J(\mathbf{R}))D(\mathbf{R},\mathbf{S})$ is represented by a single Slater determinant $D(\mathbf{R},\mathbf{S})$, containing both up and down-spin electrons, and also contains a Jastrow factor $J(\mathbf{R})$ that depends only on position to ensure that the spin spiral orientation is not changed from that fixed by the determinant. The number of up and down spin orbitals in the determinant is set by the magnetisation. The noncollinear

VMC algorithm is represented through pseudocode in Alg. 1, where the novel point is that whilst in standard VMC only position varies, here both position and spins are allowed to vary and flip to maintain ergodicity and explore all of the orbitals in the determinant. Within this algorithm the position moves and spin flips are separated for efficiency; positions are proposed and accepted as before, whilst spin flips are accepted with a probability of 50%.

A.5   Density functional theory

In this appendix we outline the theorems of DFT that can be used to find the ground-state properties of a system without considering the many-particle wave function. This makes the method inherently faster than QMC, but it requires an energy functional meaning that the method is not *ab initio*. We start by proving the Hohenberg-Kohn theorems that show how the ground-state electron density is uniquely defined by the external potential and vice-versa, before demonstrating how these enable the Kohn-Sham equations to be used to derive the ground-state electron density.

A.5.1   Hohenberg-Kohn theorems

The Hamiltonian of N electrons in a solid with ions Z_α at positions $\mathbf{r}_\alpha$ is

$$\hat{H} = \underbrace{-\frac{1}{2}\sum_i \nabla_i^2 + \frac{1}{2}\sum_{i,j\neq i}\frac{1}{|\mathbf{r}_i - \mathbf{r}_j|}}_{\hat{F}} + \underbrace{\sum_{i,\alpha}\frac{Z_\alpha}{|\mathbf{r}_i - \mathbf{r}_\alpha|}}_{\hat{V}_{\text{ext}}} . \tag{A.69}$$

The operator $\hat{F}$ is the same for all systems, whereas the static external potential $\hat{V}_{\text{ext}}$ varies between systems. The Hamiltonian is therefore characterised by the number of electrons present and the external potential. The ground state for this system $|\psi_0\rangle$ has a ground-state electron density of

$$n_0(\mathbf{r}) = \langle \psi_0 |\hat{n}| \psi_0\rangle = \int |\psi_0(\mathbf{r},\mathbf{r}_2,\mathbf{r}_3,\ldots,\mathbf{r}_N)|^2 \prod_{i=2}^{N} \mathrm{d}\mathbf{r}_i . \tag{A.70}$$

We may regard the ground-state wave function and the corresponding density as functionals of the number of electrons and the external potential. Hohenberg and Kohn [120] formulated two theorems about this system.

First theorem

The first Hohenberg-Kohn theorem shows that the external potential $V_{\text{ext}}(\mathbf{r})$ is uniquely determined by the ground-state electronic density $n(\mathbf{r})$ (the corresponding wave function is $|\psi\rangle$), to within an additive constant. This is proven by *reductio ad absurdum*. We introduce a second external potential $V'_{\text{ext}}(r)$ with ground-state $|\psi'\rangle$ that has the same density $n(\mathbf{r})$. The ground-state energies are $E_0 = \langle\psi|\hat{H}|\psi\rangle$ and $E'_0 = \langle\psi'|\hat{H}'|\psi'\rangle$. We then use the ground-state wave function for each potential as a trial wave function for the Hamiltonian containing the other potential. The variational principle then implies

$$
\begin{aligned}
E_0 < \left\langle \psi' \left| \hat{H} \right| \psi' \right\rangle &= \left\langle \psi' \left| \hat{H}' \right| \psi' \right\rangle + \left\langle \psi' \left| \hat{H} - \hat{H}' \right| \psi' \right\rangle \\
&= E'_0 + \int \left(V_{\text{ext}} - V'_{\text{ext}} \right) n(\mathbf{r})\mathrm{d}\mathbf{r},
\end{aligned}
\tag{A.71}
$$

and

$$
\begin{aligned}
E'_0 < \left\langle \psi \left| \hat{H}' \right| \psi \right\rangle &= \left\langle \psi \left| \hat{H} \right| \psi \right\rangle + \left\langle \psi \left| \hat{H}' - \hat{H} \right| \psi \right\rangle \\
&= E_0 + \int \left(V'_{\text{ext}} - V_{\text{ext}} \right) n(\mathbf{r})\mathrm{d}\mathbf{r}.
\end{aligned}
\tag{A.72}
$$

Adding these two results leads to the contradiction

$$
E_0 + E'_0 < E_0 + E'_0,
\tag{A.73}
$$

and therefore an external potential is uniquely determined by a ground-state electronic density.

Second theorem

The second Hohenberg-Kohn theorem shows that the electron density that minimises the total energy is the exact ground state density. A given density $n(\mathbf{r})$ has its own

external potential $V_{\text{ext}}(\mathbf{r})$ and ground state $|\psi\rangle$. This wave function is then used as the trial state for a Hamiltonian with external potential $V'(\mathbf{r})$ (with corresponding but different ground state $|\psi'\rangle$ and energy E'). Then by the variational principle

$$\left\langle \psi \left| \hat{H} \right| \psi \right\rangle \geq \left\langle \psi \left| \hat{H}' \right| \psi \right\rangle = E' \,, \tag{A.74}$$

and therefore a given density has its own external potential.

A.5.2   The Kohn-Sham equations

Having shown that for a given external potential the ground-state electron density is uniquely defined, we can be confident that if we develop a formalism in terms of density then we will recover the correct ground-state density. Our starting point is the variational problem for the Hohenberg-Kohn density-functional

$$\delta \left[T_{\text{s}}[n] + \frac{1}{2} \int \frac{n(\mathbf{r})n(\mathbf{r}')}{|\mathbf{r} - \mathbf{r}'|} \mathrm{d}\mathbf{r} + E_{\text{xc}}[n] + \int V_{\text{ext}}(\mathbf{r})n(\mathbf{r})\mathrm{d}\mathbf{r} \right.$$
$$\left. -\mu \left(\int n(\mathbf{r})\mathrm{d}\mathbf{r} - N \right) \right] = 0 \,, \tag{A.75}$$

where the terms are respectively: the kinetic energy, the electron-electron Coulomb energy, the exchange-correlation energy, the external potential, and the Lagrange multiplier μ that constrains the total number of electrons to be N; physically μ represents the chemical potential. This gives an equation of motion for a non-interacting system of electrons moving in an external potential. We then have to solve the Schrödinger equation for $N/2\nu$ single-particle states $|\psi_i\rangle$ with energy E_i

$$\left(-\frac{1}{2}\nabla^2 + \int \frac{n(\mathbf{r}')}{|\mathbf{r} - \mathbf{r}'|} \mathrm{d}\mathbf{r}' + V_{\text{xc}}(\mathbf{r}) + V_{\text{ext}}(\mathbf{r}) \right) \psi_i(\mathbf{r}) = E_i \psi_i(\mathbf{r}) \,, \tag{A.76}$$

here $V_{\text{xc}}(\mathbf{r}) = \delta E_{\text{xc}}[n]/\delta n(\mathbf{r})$. The potential felt by each electron depends on the density $n(\mathbf{r}) = 2\nu \sum_{i=1}^{N/2\nu} |\psi_i(\mathbf{r})|^2$, the factor of 2ν accounts for spin and flavour degeneracy. A typical implementation of DFT requires an exchange-correlation potential V_{xc} that is derived using another method, typically with QMC calculations. From this starting point the ground-state electron density can then be found self-consistently from the above equation. This typically proceeds much quicker than

QMC and so more complicated systems can be analysed. However, the improved speed comes with the cost that one must invoke the approximation that the exchange-correlation potential V_{xc} can be applied in situations where electron density is spatially varying even though it applies only for uniform systems.

The energy of the non-interacting system is the sum of the particle energy eigenvalues. Compared to the interacting system this double-counts the Hartree energy and incorrectly accounts for the exchange correlation energy. When compensated for this gives

$$E = 2\nu \sum_{i=1}^{N/2\nu} \varepsilon_i - \frac{1}{2} \int \int \frac{n(\mathbf{r})n(\mathbf{r}')}{|\mathbf{r} - \mathbf{r}'|} \mathrm{d}\mathbf{r}\mathrm{d}\mathbf{r}' - \int n(\mathbf{r})V_{xc}(\mathbf{r})\mathrm{d}\mathbf{r} + E_{xc}[n]\,, \qquad (A.77)$$

which is in agreement with the energy calculated directly using a uniform charge density n.

A.6 Many-flavour perturbation expansion

In this appendix we demonstrate which Feynman diagrams dominate in the many-flavour limit. Our starting point is the work of Andryushin et al. [71] and Keldysh and Onishchenko [72], who summed over all orders of Green's function contributions to derive an exact expression for the interacting energy per particle pair

$$E_{\mathrm{int}} = \frac{1}{2n} \int_0^1 \frac{\mathrm{d}\lambda}{\lambda} \int\int \left(\frac{4\pi\chi}{1 + 4\pi\chi} - 4\pi\chi_0 \right) \frac{\mathrm{d}\omega\mathrm{d}^3 q}{(2\pi)^4}\,, \qquad (A.78)$$

where $\chi(\mathbf{q},\omega,\lambda)$ is the polarisability of the system of electrons and holes of concentration n and charge $\mp\sqrt{\lambda}$. Here, λ is a coupling constant, the integral increases the strength of the electron-electron interaction from $\lambda = 0$ up to the full strength at $\lambda = 1$. After expanding out the denominator of the fraction, we can

use a diagrammatic visualisation to represent the exact interaction energy

$$\text{(A.79)}$$

where a shaded loop represents a sum over all possible irreducible polarisation operators. An irreducible operator is one that cannot be split in two by breaking one single interaction line. The irreducible polarisation operator is therefore the summation

$$\text{(A.80)}$$

There are two possible diagrams in λ^2, that is with four electron-photon vertices. The alternative electron flavours in these diagrams are labelled ν_1, ν_2 and ν_3

$$\text{(A.81)}$$

The matrix element G for each diagram is proportional to the number of possible flavours. In the many-flavour limit $\nu \gg 1$ the first diagram, having a matrix element proportional to ν^2 dominates over the second diagram with a matrix element proportional to ν. Physically this corresponds to the increased likelihood of interactions between electrons of different flavours. The left-hand diagram contains two empty electron loops, in the many flavour limit these empty loops therefore dominate. The many-flavour limit means we can replace each filled loop in the

expansion Eqn. (A.79) by a subclass of diagrams with only empty electron loops

$$+ \cdots . \qquad (A.82)$$

The perturbation expansion now sums over the same diagrams as in the RPA limit[10]. Reducing the expansion to just the empty loop diagrams is equivalent to demanding that the principal contribution to χ is χ_0; that is the polarisation function found in Sec. 2.1.1 represents the first term in the perturbation theory expansion justifying the subscript "0" attached to it. The link to the path integral analysis of Sec. 2.2.2 is made by replacing $\chi \mapsto \chi_0 = -\lambda e^2 \Pi_0 / q^2$.

The final term of Eqn. (A.78) $(-4\pi\chi_0)$ corresponds the self-energy of an electron

$$. \qquad (A.83)$$

This cancels following the expansion of the first term. The cancellation verifies the assertion that the term † in Eqn. (2.6) removes the interaction of the electron with itself.

A.7   BEC wave function and potential regularisation

In this appendix we determine the non-interacting pair wave function for a contact interaction, suitable to describe BEC molecules, and confirm the regularisation of the contact interaction potential strength, Eqn. (4.6). The pair wave function with

---

[10]The RPA theory has a dense electron gas [8] which increases the probability of different electrons partaking in the interaction. Therefore, diagrams with more distinct electrons are favoured.

contact interaction strength g in two dimensions is

$$-\frac{1}{r}\frac{\mathrm{d}}{\mathrm{d}r}\left(r\frac{\mathrm{d}\psi}{\mathrm{d}r}\right) + g\frac{\delta(r)}{\pi r}\psi(r) = E_{\mathrm{b}}\psi(r)$$

$$r\frac{\mathrm{d}^2\psi(r)}{\mathrm{d}r^2} + \frac{\mathrm{d}\psi(r)}{\mathrm{d}r} - \frac{g}{\pi}\delta(r)\psi(r) - k^2 r\psi(r) = 0\,, \tag{A.84}$$

where the energy wave vector $-k^2 = E_{\mathrm{b}}$ is negative since the state is bound and we use $\delta(r)/\pi r$ to represent the two-dimensional contact interaction [374]. The normalised wave function that satisfies the boundary condition $\psi(r) \to 0$ as $r \to \infty$ is

$$\psi(r) = \frac{\sqrt{\pi}}{2}k\Re\left(Y_0(\mathrm{i}kr)\right)\,, \tag{A.85}$$

where Y_n represents Bessel's function of the second kind [356] that gives the large radius behaviour $\psi(r) \sim \mathrm{e}^{-kr}/\sqrt{kr}$. The imaginary part of the Bessel function Y_0 cancels with a Bessel function of the first kind J_0. This solution gives an expected particle radius, the Bohr radius, of

$$a_0 \equiv \langle r \rangle = \frac{0.616854}{k}\,. \tag{A.86}$$

At the origin, $r = 0$, the wave function has to obey the boundary condition imposed by the contact potential of

$$\frac{r}{\psi(r)}\frac{\mathrm{d}\psi(r)}{\mathrm{d}r}\bigg|_{r \to r_{\mathrm{c}}} = \frac{g}{\pi}\,. \tag{A.87}$$

The right-hand side of this expression tends to zero logarithmically, which is consistent with the regularisation Eqn. (4.6) of the contact interaction strength g with a cutoff length r_{c}. The consistency means that

$$\frac{1}{g}\frac{r}{\psi(r)}\frac{\mathrm{d}\psi(r)}{\mathrm{d}r}\bigg|_{r \to r_{\mathrm{c}}} = \int_0^{E_{\mathrm{c}}}\frac{1}{2E + E_{\mathrm{b}}}\mathrm{d}E\, \frac{r}{\psi(r)}\frac{\mathrm{d}\psi(r)}{\mathrm{d}r}\bigg|_{r \to 0^+} = \frac{1}{\pi}\,. \tag{A.88}$$

The energy cutoff is related to the cutoff length scale through $E_{\mathrm{c}} \sim \hbar^2/mr_{\mathrm{c}}^2$. Using $E_{\mathrm{F}} = \hbar^2/(2mr_{\mathrm{s}}^2)$ and $E_{\mathrm{b}} = \hbar^2 k^2/(2m)$ we can therefore relate the ratio of the binding
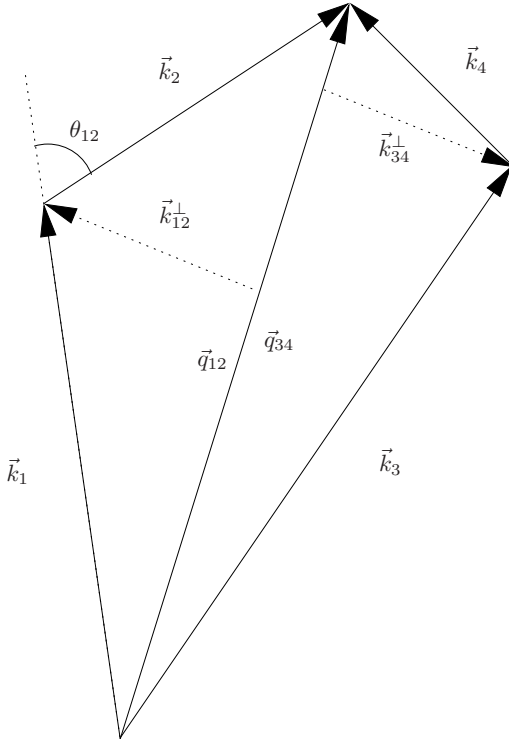
Figure A.13: The re-parameterisation of momenta used to ensure momentum conservation. $\mathbf{k}_{1,2,3,4}$ represent the momenta appearing in the original integral, whose separate sums are $\mathbf{q}_{12} = \mathbf{k}_1 + \mathbf{k}_2$ and $\mathbf{q}_{34} = \mathbf{k}_3 + \mathbf{k}_4$, which the Dirac delta function in Eqn. (A.90) will ensure that $\mathbf{q}_{12} = \mathbf{q}_{34}$. θ_{12} represents the angle between $\mathbf{k}_1$ and $\mathbf{k}_2$, $\mathbf{k}_{12}^{\perp}$ is the vector perpendicular from $\mathbf{q}_{12}$ to $\mathbf{k}_1$ and $\mathbf{k}_2$, and $\mathbf{k}_{34}^{\perp}$ is similarly defined.

energy and Fermi energy to Bohr radius and scale radius through

$$\frac{E_{\mathrm{b}}}{E_{\mathrm{F}}} = 0.380509 \left(\frac{r_{\mathrm{s}}}{a_0}\right)^2 . \tag{A.89}$$

A.8 Momentum space integral evaluation

The pivotal integral Eqn. (6.12) of the analysis presented in Chp. 6 is of the form

$$\iiiint F(|\mathbf{k}_1|,|\mathbf{k}_2|,|\mathbf{k}_3|,|\mathbf{k}_4|)\delta(\mathbf{k}_1 + \mathbf{k}_2 - \mathbf{k}_3 - \mathbf{k}_4)\mathrm{d}\mathbf{k}_1\mathrm{d}\mathbf{k}_2\mathrm{d}\mathbf{k}_3\mathrm{d}\mathbf{k}_4 . \tag{A.90}$$

To evaluate this integral one could substitute $\mathbf{k}_4 = \mathbf{k}_1 + \mathbf{k}_2 - \mathbf{k}_3$, and then integrate over three parameters representing the lengths of vectors $\mathbf{k}_1$, $\mathbf{k}_2$, and $\mathbf{k}_3$, and a minimum of three relative angles between these vectors, giving a total of six integration parameters. However, numerical integration generally becomes more prohibitive with increasing number of dimensions. Since the function F depends only on the magnitude of the momentum, the scheme outlined below allows us to perform the angular integration separately of the function and leave a numerical integral over just the four dimensions of the vector lengths.

The integral can however be re-parameterised according to Fig. A.13, $\mathbf{q}_{12} = \mathbf{k}_1 + \mathbf{k}_2$ and $\mathbf{q}_{34} = \mathbf{k}_3 + \mathbf{k}_4$, the vector perpendicular from $\mathbf{q}_{12}$ to $\mathbf{k}_1$ and $\mathbf{k}_2$ is $\mathbf{k}_{12}^\perp$ which has length

$$k_{12}^\perp = \frac{1}{2q}\sqrt{2q^2\left(k_1^2 + k_2^2\right) - q^4 - \left(k_1^2 - k_2^2\right)^2}\,, \qquad (A.91)$$

and $\mathbf{k}_{34}^\perp$ is similarly defined. We first concentrate on calculating the angular component just of the integral over $\mathbf{k}_1$ and $\mathbf{k}_2$, where the angle between these vectors is θ_{12}. The phase space volume of the angular integral is

$$\sin\theta_{12}\mathrm{d}\theta_{12} = \frac{k_{12}^\perp}{k_1 k_2}\left(2 + \sqrt{\frac{k_1^2 - k_{12}^{\perp 2}}{k_2^2 - k_{12}^{\perp 2}}} + \sqrt{\frac{k_2^2 - k_{12}^{\perp 2}}{k_1^2 - k_{12}^{\perp 2}}}\right)\mathrm{d}k_{12}^\perp = -\frac{q_{12}}{k_1 k_2}\mathrm{d}q_{12}\,, \quad (A.92)$$

where $|k_1 - k_2| \le q_{12} \le k_1 + k_2$. The total number density integrated over two momenta can then be found using

$$\int_0^\pi 4\pi k_1^2 2\pi k_2^2 \sin\theta_{12}\mathrm{d}\theta_{12} = \int_{|k_1-k_2|}^{k_1+k_2} 4\pi k_1 2\pi k_2 q_{12}\mathrm{d}q_{12} = 4\pi k_1^2 4\pi k_2^2\,, \qquad (A.93)$$

which is the expected result. A similar procedure is used to parameterise the separate integral over the angular components of $\mathbf{k}_3$ and $\mathbf{k}_4$ into $\mathbf{q}_{34}$.

The original integral Eqn. (A.90) is now re-written in terms of the parameters q_{12} and q_{34} using Eqn. (A.93). Momentum conservation is required by the presence of the Dirac delta function $\delta(\mathbf{k}_1 + \mathbf{k}_2 - \mathbf{k}_3 - \mathbf{k}_4) = \delta(\mathbf{q}_{12} - \mathbf{q}_{34})$, however the q_{12} and q_{34} parameters introduced are just scalar quantities. The momentum conservation requirement is implemented by demanding that the two scalar integration parameters are equal, which sets the two integration parameters equal, $q_{12} = q_{34} = q$ so that there is just one integral over parameter q remaining. However, this introduces an extra angular degree of freedom (the angle between $\mathbf{q}_{12}$ and $\mathbf{q}_{34}$). In order to compensate the integrand is divided by the extra phase space volume of the angular integration, $4\pi q^2$. We then obtain our final result

$$16\pi^3 \iiiint F(k_1, k_2, k_3, k_4) k_1 k_2 k_3 k_4 \times$$

$$\max\left(0, \min(k_1 + k_2, k_3 + k_4) - \max\left(|k_1 - k_2|, |k_3 - k_4|\right)\right)\mathrm{d}k_1\mathrm{d}k_2\mathrm{d}k_3\mathrm{d}k_4\,. \quad (A.94)$$

This integral is better suited to computational evaluation since it is four-dimensional [rather than the six-dimensional Eqn. (A.90)] and the term introduced to compensate for the angular integral has a relatively simple form. Physically the introduction of the max and min functions can be understood in terms of the available phase space at the Fermi surface following a particle-hole transformation.

A.9 Acronyms and abbreviations

The acronyms and abbreviations used in this thesis are listed alphabetically below:

ac   Alternating Current

$BaTiO_3$ Barium Titanate

BCS   Bardeen, Cooper, and Schrieffer

BEC   Bose-Einstein Condensation

$Ca_3Ru_2O_7$ Calcium Ruthenate

$CePd_2Si_2$ Cerium Palladium Silicon

CoS_2   Cobalt (II) Sulphide

CPU   Central Processing Unit

Cr   Chromium

DFT   Density-Functional Theory

DMC   Diffusion Monte Carlo

DMFT   Dynamical Mean Field Theory

DOS   Density of States

EPSRC   Engineering and Physical Sciences Research Council

$EuTiO_3$ Europium Titanate

FFLO   Fulde-Ferrel-Larkin-Ovchinnikov

FP   Fully Polarised

GaAs   Gallium(III) Arsenide

Ge   Germanium

GeTe   Germanium Telluride

GL   Ginzburg-Landau

GW   GW

^{3}He   Helium-3

HF   Hartree-Fock approximation

HPCS   High Perfomance Computing Service

K   Potassium

KTaO$_3$ Potassium Tantalate

LDA   Local Density Approximation

MFEG   Many-Flavour Electron Gas

MnSi   Manganese Silicide

NbFe$_2$ Iron-Niobium

OL   Optical Lattice

PP   Partially Polarised

PS   Phase Separated

QMC   Quantum Monte Carlo

RPA   Random-Phase Approximation

SF   Superfluid

Si   Silicon

SnTe   Tin Telluride

Sr$_3$Ru$_2$O$_7$ Strontium Ruthenate

SrRuO$_3$ Strontium Ruthenium Oxide

SrTiO$_3$ Strontium Titinate

STLS   Singwi, Tosi, Land & Sjölander

TBC   Twisted Boundary Conditions

TCM   Theory of Condensed Matter

TOF   Time of Flight

UGe$_2$ Uranium Digermanide

UV   Ultraviolet

VMC   Variational Monte Carlo

YbRh$_2$Si$_2$ Ytterbium-Rhodium-Silicon

ZP   Zero Particles

ZrZn$_2$ Zirconium 2-Zinc

Bibliography

[1]   G.J. Conduit. *Phys. Rev. B*, **78**:035111, 2008.

[2]   G.J. Conduit and P.D. Haynes. *Phys. Rev. B*, **78**:195310, 2008.

[3]   G.J. Conduit, P.H. Conlon, and B.D. Simons. *Phys. Rev. A*, **77**:053617, 2008.

[4]   G.J. Conduit and B.D. Simons. Itinerant ferromagnetism in an atomic Fermi gas: Influence of population imbalance. 2009.

[5]   R.M. Martin. *Electronic Structure: Basic Theory and Practical Methods.* Cambridge University Press, 2004.

[6]   L. Solymar and D. Walsh. *Lectures on the Electrical Properties of Materials.* Oxford University Press, 1993.

[7]   G. Csányi, T. Albaret, G. Moras, Payne M.C., and A. De Vita. *J. Phys.: Condens. Matter*, **17**:691, 2005.

[8]   A. Altland and B. Simons. *Condensed Matter Field Theory.* Cambridge University Press, 2006.

[9]   C. Kittel. *Introduction to Solid State Physics.* Wiley, 2004.

[10]   M.O. Steinhauser. *Computational Multiscale Modeling of Fluids and Solids: Theory and Applications.* Springer, 2007.

[11]   M.C. Payne, M.P. Teter, D.C. Allan, T.A. Arias, and J.D. Joannopoulos. *Rev. of Modern Phys.*, **64**:1045, 1992.

[12] K. Held, I.A. Nekrasov, G. Keller, V. Eyert, N. Blümer, A.K. McMahan, R.T. Scalettar, Th. Pruschke, V.I. Anisimov, and D. Vollhardt. *Psi-k Newsletter*, **243**:2599, 2006.

[13] P. Garca-González and R.W. Godby. *Computer Physics Communications*, **137**:108, 2001.

[14] S. Doniach and E. Sondheimer. *Green's Functions for Solid State Physics*. Imperial College Press, 1998.

[15] W.M.C. Foulkes, L. Mitas, R.J. Needs, and G. Rajagopal. *Rev. of Modern Phys.*, **73**:33, 2001.

[16] N. Nagaosa. *Quantum Field Theory in Condensed Matter Physics*. Springer, 1999.

[17] H. Kleinert. *Path Integrals in Quantum Mechanics, Statistics, and Polymer Physics, and Financial Markets*. World Scientific, 2004.

[18] G. Grosso and G.P. Parravicini. *Solid State Physics*. Academic Press, 2000.

[19] J.E. Ortega and F.J. Himpsel. *Phys. Rev. B*, **47**:2130, 1993.

[20] X. Zhu and S.G. Louie. *Phys. Rev. B*, **43**:14142, 1991.

[21] J.P. Wolfe, W.L. Hansen, E.E. Haller, R.S. Markiewicz, C. Kittel, and C.D. Jeffries. *Phys. Rev. Lett.*, **34**:1292, 1975.

[22] M.H. Anderson, J.R. Ensher, M.R. Matthews, C.E. Wieman, and E.A. Cornell. *Science*, **269**:198, 1995.

[23] C.C. Bradley, C.A. Sackett, J.J. Tollett, and R.G. Hulet. *Phys. Rev. Lett.*, **75**: 1687, 1995.

[24] K.B. Davis, M.-O. Mewes, M.R. Andrews, N.J. van Druten, D.S. Durfee, D.M. Kurn, and W. Ketterle. *Phys. Rev. Lett.*, **75**:3969, 1995.

[25] P. Courteille, R.S. Freeland, D.J. Heinzen, F.A. van Abeelen, and B.J. Verhaar. *Phys. Rev. Lett.*, **81**:69, 1998.

[26]   S. Inouye, M.R. Andrews, J. Stenger, H.-J. Miesner, D.M. Stamper-Kurn, and W. Ketterle. *Nature*, **392**:151, 1998.

[27]   J. Stenger, S. Inouye, M.R. Andrews, H.-J. Miesner, D.M. Stamper-Kurn, and W. Ketterle. *Phys. Rev. Lett.*, **82**:2422, 1999.

[28]   D.S. Petrov, C. Salomon, and G.V. Shlyapnikov. *Phys. Rev. Lett.*, **93**:090404, 2004.

[29]   T. Loftus, C.A. Regal, C. Ticknor, J.L. Bohn, and D.S. Jin. *Phys. Rev. Lett.*, **88**:173201, 2002.

[30]   K.M. O'Hara, S.L. Hemmer, M.E. Gehm, S.R. Granade, and J.E. Thomas. *Science*, **298**:2179, 2002.

[31]   T. Bourdel, J. Cubizolles, L. Khaykovich, K.M.F. Magalhaes, S.J.J.M.F. Kokkelmans, G.V. Shlyapnikov, and C. Salomon. *Phys. Rev. Lett.*, **91**:020402, 2003.

[32]   S.L. Cornish, N.R. Claussen, J.L. Roberts, E.A. Cornell, and C.E. Wieman. *Phys. Rev. Lett.*, **85**:1795, 2000.

[33]   I. Bloch. *Nature Physics*, **1**:23, 2005.

[34]   W. Ketterle, D.S. Durfee, and D.M. Stamper-Kurn. *arXiv:cond-mat/9904034 v2*, 1999.

[35]   R. Feynman. *Optical News*, **11**:11, 1985.

[36]   R. Feynman. *Found. Phys.*, **16**:507, 1986.

[37]   W. Ketterle and M.W. Zwierlein. *arXiv:cond-mat/0801.2500 [cond-mat.other]*, 2008.

[38]   C.A. Regal and D.S. Jin. *Phys. Rev. Lett.*, **90**:230404, 2003.

[39]   G.E. Astrakharchik, J. Boronat, J. Casulleras, and S. Giogini. *Phys. Rev. Lett.*, **93**:200404, 2004.

[40] M. Bartenstein, A. Altmeyer, S. Riedl, S. Jochim, R. Geursen, C. Chin, J. Hecker Denschlag, and R. Grimm. *arXiv:cond-mat/0412712v1 [cond-mat.other]*, 2004.

[41] B.S. Chandrasekhar. *Appl. Phys. Lett.*, **1**:7, 1962.

[42] A.M. Clogston. *Phys. Rev. Lett.*, **9**:266, 1962.

[43] P. Fulde and R.A. Ferrell. *Phys. Rev.*, **135**:A550, 1964.

[44] A.I. Larkin and Y.N. Ovchinnikov. *Soviet Phys. JETP*, **20**:762, 1965.

[45] K. Kubo. *J. Phys. Jpn.*, **77**:043702, 2008.

[46] J. Flouquet and A. Buzdin. *Phyiscs World*, 2002.

[47] M. Uhlarz, C. Pfleiderer, and S.M. Hayden. *Phys. Rev. Lett.*, **93**:256404, 2004.

[48] M. Uhlarz, C. Pfleiderer, and S.M. Hayden. *Physica B*, **359-361**:1174, 2005.

[49] A. Huxley, I. Sheikin, and D. Braithwaite. *Physica B*, **284-288**:1277, 2000.

[50] C. Pfleiderer, S.R. Julian, and G.G. Lonzarich. *Nature (London)*, **414**:427, 2001.

[51] W. Yu, F. Zamborszky, J.D. Thompson, J.L. Sarrao, M.E. Torelli, Z. Fisk, and S.E. Brown. *Phys. Rev. Lett.*, **92**:086403, 2004.

[52] M. Otero-Leal, F. Rivadulla, M. Garcia-Hernandez, A. Pineiro, V. Pardo, D. Baldomir, and J. Rivas. *arXiv:cond-mat/0806.2819v1 [cond-mat.str-el]*, 2008.

[53] M. Shimizu. *Proc. Phys. Soc. London*, **84**:397, 1964.

[54] D. Belitz, T.R. Kirkpatrick, and T. Vojta. *Phys. Rev. B*, **55**:9452, 1997.

[55] D. Belitz, T.R. Kirkpatrick, and T. Vojta. *Phys. Rev. Lett.*, **82**:4707, 1999.

[56] T. Vojta. *Ann. Phys. (Leipzig)*, **9**:403, 2000.

[57] D. Belitz and T.R. Kirkpatrick. *Phys. Rev. Lett.*, **89**:247202, 2002.

[58] D. Belitz, T.R. Kirkpatrick, and J. Rollbühler. *Phys. Rev. Lett.*, **94**:247205, 2005.

[59] A.J. Schofield. *Contemorary Physics*, **40**:95, 1999.

[60] S.R. Julian, C. Pfleiderer, F.M. Grosche, N.D. Mathur, G.J. McMullan, A.J. Diver, I.R. Walker, and G.G. Lonzarich. *J. Phys.: Condens. Matter*, **8**:9675, 1996.

[61] N.D. Mathur, F.M. Grosche, S.R. Julian, I.R. Walker, D.M. Freye, R.K.W. Haselwimmer, and G.G. Lonzarich. *Nature (London)*, **394**:39, 1998.

[62] O.K. Rice. *J. of Chem. Phys.*, **22**:1535, 1954.

[63] C.W. Garland and R. Renard. *J. of Chem. Phys.*, **44**:1120, 1966.

[64] A.I. Larkin and S.A. Pikin. *Journal of Experimental and Theoretical Physics*, **29**:891, 1969.

[65] S.A. Grigera, P. Gegenwart, R.A. Borzi, F. Weickert, A.J. Schofield, R.S. Perry, T. Tayama, T. Sakakibara, Y. Maeno, A.G. Green, and A.P. Mackenzie. *Science*, **306**:1154, 2004.

[66] D. Saint-James, G. Sarma, and E.J. Thomas. *Type II superconductivity.* Pergamon, New York, 1969.

[67] A.I. Buzdin and H. Kachkachi. *arXiv:cond-mat/9611153v1 [cond-mat.supr-con]*, 1996.

[68] H. Taniguchi, M. Itoh, and T. Yagi. *Phys. Rev. Lett.*, **99**:017602, 2007.

[69] S.E. Rowley, L.J. Spalek, R.P. Smith, M.P.M. Dean, G.G. Lonzarich, J.F. Scott, and S.S. Saxena. *arXiv:cond-mat/0810.1907v2 [cond-mat.mtrl-sci]*, 2009.

[70] C.D. Jeffries and L.V. Keldysh. *Electron-hole droplets in semiconductors.* North-Holland, 1983.

[71] E.A. Andryushin, V.S. Babichenko, L.V. Keldysh, Y.A. Onishchenko, and A.P. Silin. *Pis'ma Zh. Eksp. Teor. Fiz.*, **24**:210, 1976.

[72] L.V. Keldysh and T.A. Onishchenko. *Pis'ma Zh. Eksp. Teor. Fiz.*, **24**:70, 1976.

[73] T. Story, G. Karczewski, L. Świerkowski, and R.R. Galazka. *Phys. Rev. B*, **42**:10477, 1990.

[74] W.F. Brinkman and T.M. Rice. *Phys. Rev. B*, **7**:1508, 1973.

[75] P. Vashishta, P. Bhattacharyya, and K.S. Singwi. *Phys. Rev. B*, **10**:5108, 1974.

[76] Y.E. Pokrovsky and K.I. Svistunova. The Electric Charge of the Electron-Hole Drops in Ge. In M.H. Pilkhun, editor, *Proceedings of the twelfth International Conference on the Physics of Semiconductors*, page 71, Stuttgart, Germnay, 1974.

[77] P. Vashishta and S.G. Das. *Phys. Rev. Lett.*, **33**:911, 1974.

[78] R.K. Kalia and P. Vashishta. *Phys. Rev. B*, **17**:2655, 1978.

[79] J.P. Wolfe, R.S. Markiewicz, S.M. Kelso, J.E. Furneaux, and C.D. Jeffries. *Phys. Rev. B*, **18**:1479, 1978.

[80] H. h. Chou and G.K. Wong. *Phys. Rev. Lett.*, **41**:1677, 1978.

[81] J. Wagner, A. Forchel, and R. Sauer. *Solid State Communications*, **38**:991, 1981.

[82] P.L. Gourley and J.P. Wolfe. *Phys. Rev. B*, **24**:5970, 1981.

[83] A. Forchel, B. Laurich, J. Wagner, W. Schmid, and T.L. Reinecke. *Phys. Rev. B*, **25**:2730, 1982.

[84] J.C. Culbertson and J.E. Furneaux. *Phys. Rev. Lett.*, **49**:1528, 1982.

[85] A.H. Simon, F.M. Steranka, and J.P. Wolfe. *Phys. Rev. B*, **40**:4003, 1989.

[86] K. Thonke, R. Schliesing, N. Teofilov, H. Zacharias, R. Sauer, A.M. Zaitsev, H. Kanda, and T.R. Anthony. *Diamond and Related Materials*, **9**:428, 2000.

[87] J.H. Jiang, M.W. Wu, M. Nagai, and M. Kuwata-Gonokami. *Phys. Rev. B*, **71**:035215, 2005.

[88] N. Naka, J. Omachi, and M. Kuwata-Gonokami. *Phys. Rev. B*, **76**:193202, 2007.

[89] L.M. Sander, H.B. Shore, and L.J. Sham. *Phys. Rev. B*, **31**:533, 1973.

[90] T.M. Rice. *Phys. Rev. B*, **9**:1540, 1974.

[91] T.M. Rice. *Solid State Physics*, **32**:1, 1977.

[92] R.S. Markiewicz, H. Hurwitz, and R.S. Likes. *Phys. Rev. B*, **18**:2780, 1978.

[93] R.S. Markiewicz. *Phys. Rev. B*, **18**:5573, 1978.

[94] T.L. Reinecke, M.C. Lega, and S.C. Ying. *Phys. Rev. B*, **20**:1562, 1979.

[95] G. Zaránd, T. Costi, A. Jerez, and N. Andrei. *Phys. Rev. B*, **65**:134416, 2002.

[96] K.S. Kim. *Phys. Rev. B*, **72**:245106, 2005.

[97] C.J. Bolech and A. Iucci. *Phys. Rev. Lett.*, **96**:056402, 2006.

[98] H. Eskes, O.Y. Osman, R. Grimberg, W. vanSaarloos, and J. Zaanen. *Phys. Rev. B*, **58**:6963, 1998.

[99] G.F. Giuliani and J.J. Quinn. *Surface Science*, **170**:316, 1986.

[100] D.C. Marinescu, J.J. Quinn, and G.F. Giuliani. *Phys. Rev. B*, **61**:7245, 2000.

[101] C. Honerkamp and W. Hofstetter. *Phys. Rev. Lett.*, **92**:170403, 2004.

[102] C. Honerkamp and W. Hofstetter. *Phys. Rev. B*, **70**:094521, 2004.

[103] R.W. Cherng, G. Refael, and E. Demler. *Phys. Rev. Lett.*, **99**:130406, 2007.

[104] A. Gold. *Phys. Rev. B*, **50**:4297, 1994.

[105] M.L. Cohen. *Phys. Rev.*, **134**:A511, 1964.

[106] S.J. Clark, M.D. Segall, C.J. Pickard, P.J. Hasnip, M.J. Probert, K. Refson, and M.C. Payne. *Zeitschrift für Kristallographie*, **220**:567, 2005.

[107] J. Kanamori. *Prog. Theor. Phys.*, **30**:275, 1963.

[108] J. Hubbard. *Proc. R. Soc. London*, **276**:238, 1963.

[109] E.P. Wohlfarth and P. Rhodes. *Philos. Mag.*, **7**:1817, 1962.

[110] G. Fabricius, A.M. Llois, and H. Dreyssé. *Phys. Rev. B*, **48**:6665, 1993.

[111] N.W. Ashcroft and N.D. Mermin. *Solid State Physics*. Holt Saunders, 2001.

[112] G. Beni and T.M. Rice. *Phys. Rev. B*, **18**:768, 1978.

[113] H. Kleinert. *Fortschritte der Physik*, **26**:565, 1978.

[114] M. Gell-Mann and K.A. Brueckner. *Phys. Rev.*, **106**:364, 1957.

[115] A. Gold. *Z. Phys. B*, **89**:1, 1992.

[116] P. Vashishta and R.K. Kalia. *Phys. Rev. B*, **25**:6492, 1982.

[117] D. Ceperley. *Phys. Rev. B*, **18**:3126, 1978.

[118] D.M. Ceperley and B.J. Alder. *Phys. Rev. Lett.*, **45**:566, 1980.

[119] R.O. Jones and O. Gunnarsson. *Rev. of Modern Phys.*, **61**:689, 1989.

[120] P. Hohenberg and W. Kohn. *Phys. Rev.*, **136**:B864, 1964.

[121] C.F. von Weizsäcker. *Z. Phys.*, **96**:431, 1935.

[122] K.S. Singwi, M.P. Tosi, R.H. Land, and A. Sjölander. *Phys. Rev.*, **176**:589, 1968.

[123] K.S. Singwi and M.P. Tosi. *Solid State Physics*, **36**:177, 1981.

[124] C. Bulutay, I. Al-Hayek, and M. Tomak. *Phys. Rev. B*, **56**:15115, 1997.

[125] B.L. Hammond, W.A. Lester Jr., and P.J. Reynolds. *Monte Carlo Methods in Ab Initio Quantum Chemistry.* World Scientific, 1994.

[126] W.A. Lester. *Recent Advances in Quantum Monte Carlo Methods Part II.* World Scientific, 1997.

[127] M.P. Nightingale and C.J. Umrigar. *Quantum Monte Carlo Methods in Physics and Chemistry.* Kluwer Academic Publishers, 1999.

[128] G.D. Mahan. *Many-Particle Physics.* Plenum Press, 1993.

[129] N. Metropolis, M.N. Rosenbluth, A.H. Teller, and E. Teller. *J. of Chem. Phys.*, **21**:1087, 1953.

[130] P.J. Reynolds, D.M. Ceperley, B.J. Alder, and W.A. Lester. *J. of Chem. Phys.*, **77**:5593, 1982.

[131] C.J. Umrigar, M.P. Nightingale, and K.J. Runge. *J. of Chem. Phys.*, **99**:2865, 1993.

[132] R. Jastrow. *Phys. Rev.*, **98**:1479, 1955.

[133] N.D. Drummond, M.D. Towler, and R.J. Needs. *Phys. Rev. B*, **70**:235119, 2004.

[134] R.T. Pack and W. Byers-Brown. *J. of Chem. Phys.*, **45**:556, 1966.

[135] G. Ortiz and P. Ballone. *Phys. Rev. B*, **50**:1391, 1994.

[136] R.J. Needs, M.D. Towler, N.D. Drummond, and P. López Ríos. *CASINO version 2.0 User Manual.* Cambridge University, 2006.

[137] D.B. Hyun, J.S. Hwang, T.S. Oh, J.D. Shim, and N.V. Kolomoets. *J. Phys. and Chem. Solids*, **59**:1039, 1998.

[138] S. Lee and P. von Allmen. *Appl. Phys. Lett.*, **88**:022107, 2006.

[139] H.-J. Noh, H. Koh, S.-J. Oh, J.-H. Park, H.-D. Kim, J.D. Rameau, T. Valla, T.E. Kidd, P.D. Johnson, Y. Hu, and Q. Li. *Europhys. Lett.*, **81**:57006, 2008.

[140] P. Noziéres and D. Pines. *The Theory of Quantum Liquids.* Perseus Books, Cambridge, Mass., 1999.

[141] G. Sugiyama, C. Bowen, and B.J. Alder. *Phys. Rev. B*, **46**:13042, 1992.

[142] S. Moroni, D.M. Ceperley, and G. Senatore. *Phys. Rev. Lett.*, **69**:1837, 1992.

[143] C. Bowen, G. Sugiyama, and B.J. Alder. *Phys. Rev. B*, **50**:14838, 1994.

[144] S. Moroni, D.M. Ceperley, and G. Senatore. *Phys. Rev. Lett.*, **75**:689, 1995.

[145] L. Bányai and S.W. Koch. *Semiconductor Quantum Dots.* World Scientific, 1993.

[146] S.M. Reimann and M. Manninen. *Rev. of Modern Phys.*, **74**:1283, 2002.

[147] E.L. Pollock and S.W. Koch. *J. of Chem. Phys.*, **94**:6776, 1991.

[148] A. Harju, V.A. Sverdlov, R.M. Nieminen, and V. Halonen. *Phys. Rev. B*, **59**: 5622, 1999.

[149] F. Bolton. *Phys. Rev. B*, **54**:4780, 1996.

[150] Yu.E. Lozovik and V.A. Mandelshtam. *Phys. Lett. A*, **165**:469, 1992.

[151] C.H. Mak, R. Egger, and H. Weber-Gottschick. *Phys. Rev. Lett.*, **81**:4533, 1998.

[152] R. Egger, W. Häusler, C.H. Mak, and H. Grabert. *Phys. Rev. Lett.*, **82**:3320, 1999.

[153] M. Eto. *Jpn. J. Appl. Phys.*, **36**:3924, 1997.

[154] L.X. Benedict, A. Puzder, A.J. Williamson, J.C. Grossman, G. Galli, J.E. Klepeis, J.Y. Raty, and O. Pankratov. *Phys. Rev. B*, **68**:085310, 2003.

[155] A.J. Williamson, J.C. Grossman, R.Q. Hood, A. Puzder, and G. Galli. *Phys. Rev. Lett.*, **89**:196803, 2002.

[156] A. Puzder, A.J. Williamson, F.A. Reboredo, and G. Galli. *Phys. Rev. Lett.*, **91**:157405, 2003.

[157] F. Pederiva, C.J. Umrigar, and E. Lipparini. *Phys. Rev. B*, **62**:8120, 2000.

[158] A. Ghosal, A.D. Güçlü, C.J. Umrigar, D. Ullmo, and H.U. Baranger. *Nature Physics*, **2**:336, 2006.

[159] M. Ferconi and G. Vignale. *Phys. Rev. B*, **50**:14722, 1994.

[160] M. Koskinen, M. Manninen, and S.M. Reimann. *Phys. Rev. Lett.*, **79**:1389, 1997.

[161] K. Hirose and N.S. Wingreen. *Phys. Rev. B*, **59**:4604, 1999.

[162] S. Tarucha, D.G. Austing, T. Honda, R.J. van der Hage, and L.P. Kouwenhoven. *Phys. Rev. Lett.*, **77**:3613, 1996.

[163] S. Sasaki, D.G. Austinga, and S. Taruchaa. *Physica B*, **256-258**:157, 1998.

[164] R.C. Ashoori. *Nature (London)*, **379**:413, 1996.

[165] L.P. Kouwenhoven, T.H. Oosterkamp, M.W.S. Danoesastro, M. Eto, D.G. Austing, T. Honda, and S. Tarucha. *Science*, **278**:1788, 1997.

[166] B. Reusch. *Quantum Simulations for Semiconductor Quantum Dots: From Artificial Atoms to Wigner Molecules*. PhD thesis, Heinrich-Heine-Universität Düsselforf, 2003.

[167] N. Hine. *DOTDFT: Density Functional Calculations for Quantum Dots*. Imperial College, London, 2005.

[168] E. Hernández, M.J. Gillan, and C.M. Goringe. *Phys. Rev. B*, **55**:13485, 1997.

[169] D. Alfè and M.J. Gillan. *Phys. Rev. B*, **70**:161101(R), 2004.

[170] J.P. Perdew and A. Zunger. *Phys. Rev. B*, **23**:5048, 1981.

[171] R.M. Dreizler and E.K.U. Gross. *Density Functional Theory: An Approach to the Quantum Many-Body Problem*. Springer-Verlag, 2001.

[172] S. Kalliakos, M. Rontani, V. Pellegrini, C.P. Garcǐa, A. Pinczuk, G. Goldoni, E. Molinari, L.N. Pfeiffer, and K.W. West. *Nature Physics*, **4**:467, 2008.

[173] G. Giuliani and G. Vignale. *Quantum Theory of the Electron Liquid.* Cambridge University Press, 2005.

[174] Yu.E. Lozovik and V.A. Mandelshtam. *Phys. Lett. A*, **145**:269, 1990.

[175] F. Bolton and U. Rössler. *Superlattices and Microstructures*, **13**:139, 1993.

[176] G. Date, M.V.N. Murthy, and R. Vathsan. *J. Phys.: Condens. Matter*, **10**: 5875, 1998.

[177] S.Y. Shiau, S. Chutia, and R. Joynt. *Phys. Rev. B*, **75**:195345, 2007.

[178] S.Y. Shiau and R. Joynt. *Phys. Rev. B*, **76**:205314, 2007.

[179] Y. Hada and M. Eto. *Phys. Rev. B*, **68**:155322, 2003.

[180] D. Ahn. *J. Appl. Phys.*, **98**:033709, 2005.

[181] V.A. Belyakov and V.A. Burdov. *Phys. Rev. B*, **76**:045335, 2007.

[182] C. Yannouleas and U. Landman. *Rep. Prog. Phys*, **70**:2067, 2007.

[183] C.A. Regal, M. Greiner, and D.S. Jin. *Phys. Rev. Lett.*, **92**:040403, 2004.

[184] M.W. Zwierlein, C.A. Stan, C.H. Schunck, S.M.F. Raupach, A.J. Kerman, and W. Ketterle. *Phys. Rev. Lett.*, **92**:120403, 2004.

[185] T. Loftus, C.A. Regal, C. Ticknor, J.L. Bohn, and D.S. Jin. *Phys. Rev. B*, **88**: 173201, 2002.

[186] K.E. Strecker, G.B. Partridge, and R.G. Hulet. *Phys. Rev. Lett.*, **91**:080406, 2003.

[187] S. Gupta, M.W. Hadzibabic, Z. Zwierlein, C.A. Stan, 1 K. Dieckmann, C.H. Schunck, E.G.M. van Kempen, B.J. Verhaar, and W. Ketterle. *Science*, **300**: 1723, 2003.

[188] C. Chin, M. Bartenstein, A. Altmeyer, S. Riedl, S. Jochim, J. Hecker Denschlag, and R. Grimm. *Science*, **305**:1128, 2004.

[189] M. Greiner, C.A. Regal, and D.S. Jin. *Nature*, **426**:537, 2003.

[190] P.F. Bedaque, H. Caldas, and G. Rupak. *Phys. Rev. Lett.*, **91**:247002, 2003.

[191] A. Sedrakian, J. Mur-Petit, A. Polls, and H. Müther. *Phys. Rev. A*, **72**:013613, 2005.

[192] J. Kinnunen, L.M. Jensen, and P. Törmä. *Phys. Rev. Lett.*, **96**:110403, 2006.

[193] F. Chevy. *Phys. Rev. Lett.*, **96**:130401, 2006.

[194] P. Pieri and G.C. Strinati. *Phys. Rev. Lett.*, **96**:150404, 2006.

[195] C.-H. Pao, S.-T. Wu, and S.-K. Yip. *Phys. Rev. B*, **73**:132506, 2006.

[196] T.N. De Silva and E.J. Mueller. *Phys. Rev. A*, **73**:051602(R), 2006.

[197] J. Dukelsky, G. Ortiz, S.M.A. Rombouts, and K. Van Houcke. *Phys. Rev. Lett.*, **96**:180404, 2006.

[198] H. Hu and X.-J. Liu. *Phys. Rev. A*, **73**:051603(R), 2006.

[199] D.E. Sheehy and L. Radzihovsky. *Phys. Rev. Lett.*, **96**:060401, 2006.

[200] M. Haque and H.T.C. Stoof. *Phys. Rev. A*, **74**:011602(R), 2006.

[201] X.-J. Liu and H. Hui. *Europhys. Lett.*, **75**:364, 2006.

[202] K. Machida, T. Mizushima, and M. Ichioka. *Phys. Rev. Lett.*, **97**:120407, 2006.

[203] M. Iskin and C.A.R. Sá de Melo. *Phys. Rev. Lett.*, **97**:100404, 2006.

[204] J. Tempere, M. Wouters, and J.T. Devreese. *Phys. Rev. B*, **75**:184526, 2007.

[205] W. Zhang and L.-M. Duan. *Phys. Rev. A*, **76**:042710, 2007.

[206] C.-H. Pao, S.-T. Wu, and S.-K. Yip. *Phys. Rev. A*, **76**:053621, 2007.

[207] M. Rizzi, M. Polini, M.A. Cazalilla, M.R. Bakhtiari, M.P. Tosi, and R. Fazio. *arXiv:cond-mat/0712.3364v1 [cond-mat.str-el]*, 2007.

[208] L. He and P. Zhuang. *arXiv:cond-mat/0801.3127v1 [cond-mat.supr-con]*, 2008.

[209] S. Inouye, J. Goldwin, M.L. Olsen, C. Ticknor, J.L. Bohn, and D.S. Jin. *Phys. Rev. Lett.*, **93**:183201, 2004.

[210] C.A. Stan, M.W. Zwierlein, C.H. Schunck, S.M.F. Raupach, and W. Ketterle. *Phys. Rev. Lett.*, **93**:143001, 2004.

[211] C. Ospelkaus, S. Ospelkaus, L. Humbert, P. Ernst, K. Sengstock, and K. Bongs. *Phys. Rev. Lett.*, **97**:120402, 2006.

[212] F. Ferlaino, C. D'Errico, G. Roati, M. Zaccanti, M. Inguscio, G. Modugno, and A. Simoni. *Phys. Rev. A*, **73**:040702(R), 2006.

[213] M. Zaccanti, C. D'Errico, F. Ferlaino, G. Roati, M. Inguscio, and G. Modugno. *Phys. Rev. A*, **74**:041605(R), 2006.

[214] M. Iskin and C.A.R. Sá de Melo. *Phys. Rev. A*, **77**:013625, 2008.

[215] T. Gottwald and P.G.J. van Dongen. *Eur. Phys. J. B*, **61**:277, 2008.

[216] E. Wille, F.M. Spiegelhalder, G. Kerner, D. Naik, A. Trenkwalder, G. Hendl, F. Schreck, R. Grimm, T.G. Tiecke, J.T.M. Walraven, S.J.J.M.F. Kokkelmans, E. Tiesinga, and P.S. Julienne. *Phys. Rev. Lett.*, **100**:053201, 2008.

[217] M.M. Parish, F.M. Marchetti, A. Lamacraft, and B.D. Simons. *Nature Physics*, **3**:124, 2007.

[218] W.V. Liu and F. Wilczek. *Phys. Rev. Lett.*, **90**:047002, 2003.

[219] T. Mizushima, K. Machida, and M. Ichioka. *Phys. Rev. Lett.*, **94**:060404, 2005.

[220] J. Carlson and S. Reddy. *Phys. Rev. Lett.*, **95**:060401, 2005.

[221] D.T. Son and M.A. Stephanov. *e-print*, page 050758, 2005.

[222] G.G. Batrouni, M.H. Huntley, V.G. Rousseau, and R.T. Scalettar. *arXiv:cond-mat/0710.1353v1 [cond-mat.str-el]*, 2007.

[223] Y. Chen, Z.D. Wang, F.C. Zhang, and C.S. Ting. *arXiv:cond-mat/0710.5484v1 [cond-mat.supr-con]*, 2007.

[224] T.K. Koponen, T. Paananen, J.-P. Martikainen, M.R. Bakhtiari, and P. Törmä. *arXiv:cond-mat/0711.4065v2 [cond-mat.supr-con]*, 2007.

[225] Y. Yanase. *arXiv:cond-mat/0805.1450v1 [cond-mat.supr-con]*, 2008.

[226] A. Bianchi, R. Movshovich, C. Capan, P.G. Pagliuso, and J.L. Sarrao. *Phys. Rev. Lett.*, **91**:187004, 2003.

[227] S.-T. Wu and S. Yip. *Phys. Rev. A*, **67**:053603, 2003.

[228] Y. Shin, M.W. Zwierlein, C.H. Schunck, A. Schirotzek, and W. Ketterle. *Phys. Rev. Lett.*, **97**:030401, 2006.

[229] X. Zhu, P.B. Littlewood, M.S. Hybertsen, and T.M. Rice. *Phys. Rev. Lett.*, **74**:1633, 1995.

[230] P. Pieri, D. Neilson, and G.C. Strinati. *Phys. Rev. B*, **75**:113301, 2007.

[231] T. Hakioğlu and M. Şahin. *Phys. Rev. Lett.*, **98**:166405, 2007.

[232] R. Combescot and C. Mora. *Eur. Phys. J. B*, **44**:189, 2005.

[233] B.P. Anderson and M.A. Kasevich. *Science*, **282**:1686, 1998.

[234] S. Burger, F.S. Cataliotti, C. Fort, F. Minardi, M. Inguscio, M.L. Chiofalo, and M.P. Tosi. *Phys. Rev. Lett.*, **86**:4447, 2001.

[235] F.S. F. S. Cataliotti, S. Burger, C. Fort, P. Maddaloni, F. Minardi, A. Trombettoni, A. Smerzi, and M. Inguscio. *Science*, **293**:843, 2001.

[236] J.K. Chin, D.E. Miller, Y. Liu, C. Stan, W. Setiawan, C. Sanner, K. Xu, and W. Ketterle. *Nature (London)*, **443**:961, 2006.

[237] J.-P. Martikainen and H.T.C. Stoof. *Phys. Rev. A*, **68**:013610, 2003.

[238] M. Wouters, J. Tempere, and J.T. Devreese. *Phys. Rev. A*, **70**:013616, 2004.

[239] W. Zhang, G.-D. Lin, and L.-M. Duan. *arXiv:cond-mat/0801.2500v1 [cond-mat.str-el]*, 2008.

[240] J.A. Bowers and K. Rajagopal. *Phys. Rev. D*, **66**:065002, 2002.

[241] V.N. Efimov. *Phys. Lett. B*, **33**:563, 1970.

[242] V.N. Efimov. *Nuclear Physics A*, **210**:157, 1973.

[243] M.A. Baranov, C. Lobo, and G.V. Shlyapnikov. *arXiv:cond-mat/0801.1815v1 [cond-mat.other]*, 2008.

[244] Q. Chen, J. Stajic, S. Tan, and K. Levin. *Physics Reports*, **412**:1, 2005.

[245] W. Yi and L.M. Duan. *Phys. Rev. A*, **73**:063607, 2006.

[246] J. Zhang and H. Zhai. *Phys. Rev. A*, page 041602(R), 2005.

[247] M. Randeria, J.-M. Duan, and L.-Y. Shieh. *Phys. Rev. B*, **41**:327, 1990.

[248] R. Casalbuoni and G. Nardulli. *Rev. of Modern Phys.*, **76**:263, 2004.

[249] H. Burkhardt and D. Rainer. *Ann. Phys. (Leipzig)*, **3**:181, 1994.

[250] H. Shimahara. *Phys. Rev. B*, **50**:12760, 1994.

[251] G.B. Partridge, W. Li, R.I. Kamar, Y. Liao, and R.G. Hulet. *Science*, **311**: 503, 2006.

[252] G.B. Partridge, W. Li, Y.A. Liao, R.G. Hulet, M. Haque, and H.T.C. Stoof. *Phys. Rev. Lett.*, **97**:190407, 2006.

[253] A. Imambekov, C.J. Bolech, M. Lukin, and E. Demler. *Phys. Rev. A*, **74**: 053626, 2006.

[254] T. Gottwald and P.G.J. van Dongen. *arXiv:cond-mat/0708.3161v1 [cond-mat.str-el]*, 2007.

[255] E. Wille, F.M. Spiegelhalder, G. Kerner, D. Naik, A. Trenkwalder, G. Hendl, F. Schreck, R. Grimm, T.G. Tiecke, J.T.M. Walraven, S.J.J.M.F. Kokkelmans, E. Tiesinga, and P.S. Julienne. *arXiv:cond-mat/0711.2916v1 [cond-mat.other]*, 2007.

[256] R. Combescot, M. Yu. Kagan, and S. Stringari. *Phys. Rev. A*, **74**:042717, 2006.

[257] M. Iskin and C.A.R. Sá de Melo. *arXiv:cond-mat/0606624v2 [cond-mat.supr-con]*, 2006.

[258] I. Kosztin, Q. Chen, Y.-J. Kao, and K. Levin. *Phys. Rev. B*, **61**:11662, 2000.

[259] A. Minguzzi, G. Ferrari, and Y. Castin. *Eur. Phys. J. D*, **17**:49, 2001.

[260] N. Andrenacci, P. Pieri, and G.C. Strinati. *Phys. Rev. B*, **68**:144507, 2003.

[261] H.P. Büchler, P. Zoller, and W. Zwerger. *Phys. Rev. Lett.*, **93**:080401, 2004.

[262] P. Pieri, L. Pisani, and G.C. Strinati. *Phys. Rev. B*, **70**:094508, 2004.

[263] D.S. Petrov and G.V. Shlyapnikov. *Phys. Rev. A*, **64**:012706, 2001.

[264] J.F. Annett. *Superconductivity, Superfluids, and Condensates.* Oxford University Press, 2004.

[265] F. Pistolesi and G.C. Strinati. *Phys. Rev. B*, **53**:15168, 1996.

[266] Y. Ohashi and A. Griffin. *Phys. Rev. A*, **67**:063612, 2003.

[267] M. Bartenstein, A. Altmeyer, S. Riedl, S. Jochim, C. Chin, J. Hecker Denschlag, and R. Grimm. *Phys. Rev. Lett.*, **92**:203201, 2004.

[268] J. Kinast, A. Turlapov, and J.E. Thomas. *Phys. Rev. Lett.*, **94**:170404, 2005.

[269] M.A. Baranov and D.S. Petrov. *Phys. Rev. A*, **62**:041601, 2000.

[270] G.M. Bruun and B.R. Mottelson. *Phys. Rev. Lett.*, **87**:270403, 2001.

[271] S. Stringari. *Phys. Rev. Lett.*, **77**:2360, 1996.

[272] R. Haussmann. *Self-consistent Quantum-Field Theory and Bosonization for Strongly Correlated Electron Systems.* Springer, 1999.

[273] W.C. Stwalley. *Phys. Rev. Lett.*, **37**:1628, 1976.

[274] E. Tiesinga, B.J. Verhaar, and H.T.C. Stoof. *Phys. Rev. A*, **47**:4114, 1993.

[275] E.C. Stoner. *Proc. R. Soc. London*, **165**:372, 1937.

[276] J.M. Ziman. *Principles of the Theory of Solids*. Cambridge University Press, 1979.

[277] Y.J. Uemura, T. Goko, I.M. Gat-Malureanu, J.P. Carlo, P.L. Russo, A.T. Savici, A. Acze, G.J. MacDougall, J.A. Rodriguez, G.M. Luke, S.R. Dunsiger, A. McCollam, J. Arai, Ch. Pfleiderer, P. Böni, K. Yoshimura, E. Baggio-Saitovitch, M.B. Fontes, J. Larrea, Y.V. Sushko, and J. Sereni. *Nature (London)*, **3**:29, 2007.

[278] M. Otero-Leal, F. Rivadulla, S.S. Saxena, K. Ahilan, and J. Rivas. *Phys. Rev. B*, **79**:060401(R), 2009.

[279] A.E. Petrova, V.N. Krasnorussky, T.A. Lograsso, and S.M. Stishov. *Phys. Rev. B*, **79**:100401(R), 2009.

[280] T. Misawa, Y. Yamaji, and M. Imada. *J. Phys. Jpn.*, **77**:093712, 2008.

[281] J.J. Hamlin, S. Deemyad, J.S. Schilling, M.K. Jacobsen, R.S. Kumar, A.L. Cornelius, G. Cao, and J.J. Neumeier. *Phys. Rev. B*, **76**:014432, 2007.

[282] R. Combescot. Introduction to FFLO phases and collective mode in the BEC-BCS crossover. In M. Inguscio, W. Ketterle, and C. Salomon, editors, *Ultracold Fermi Gases*, volume 164, page 697. IOS Press, 2007.

[283] D.E. Sheehy and L. Radzihovsky. *Ann. Phys. (Leipzig)*, **322**:1790, 2007.

[284] T. Sogo and H. Yabu. *Phys. Rev. A*, **66**:043611, 2002.

[285] R.A. Duine and A.H. MacDonald. *Phys. Rev. Lett.*, **95**:230403, 2005.

[286] A. Huxley, I. Sheikin, E. Ressouche, N. Kernavanois, D. Braithwaite, R. Calemczuk, and J. Flouquet. *Phys. Rev. B*, **63**:144519, 2001.

[287] S. Watanabe and K. Kiyake. *J. Phys. and Chem. Solids*, **63**:1465, 2002.

[288] K. Kitagawa, K. Ishida, R.S. Perry, T. Tayama, T. Sakakibara, and Y. Maeno. *Phys. Rev. Lett.*, **95**:127001, 2005.

[289] I. Berdnikov, P. Coleman, and S.H. Simon. *arXiv:0805.3693v1 [cond-mat.str-el]*, 2008.

[290] H. Keiter. *Phys. Rev. B*, **2**:3777, 1970.

[291] W.E. Evenson, J.R. Schrieffer, and S.Q. Wang. *J. Appl. Phys.*, **41**:1199, 1970.

[292] G. Morandi, E. Galleani d'Agliano, F. Napoli, and C.F. Ratto. *Adv. Phys.*, **23**:867, 1974.

[293] J. Hubbard. *Phys. Rev. B*, **19**:2626, 1979.

[294] R.E. Prange and V. Korenman. *Phys. Rev. B*, **19**:4691, 1979.

[295] A.A. Abrikosov and I.M. Khalatnikov. *Soviet Phys. JETP*, **6**:888, 1958.

[296] R.E. Prange and V. Korenman. *Phys. Rev. B*, **19**:4698, 1979.

[297] R.K. Pathria. *Statistical Mechanics*. Butterworths, London, 1996.

[298] D.E. Sheehy and L. Radzihovsky. *Phys. Rev. B*, **75**:136501, 2007.

[299] F. Baumberger, N.J.C. Ingle, N. Kikugawa, M.A. Hossain, W. Meevasana, R.S. Perry, K.M. Shen, D.H. Lu, A. Damascelli, A. Rost, A.P. Mackenzie, Z. Hussain, and Shen Z.-X. *Phys. Rev. Lett.*, **96**:107601, 2006.

[300] J.A. Hertz. *Phys. Rev. B*, **14**:1165, 1976.

[301] P. Coleman and A.J. Schofield. *Nature (London)*, **433**:226, 2005.

[302] D.V. Efremov, J.J. Betouras, and A. Chubukov. *arXiv:cond-mat/0804.2736v1 [cond-mat.str-el]*, 2008.

[303] D.L. Maslov and A.V. Chubukov. *arXiv:cond-mat/08111732v2 [cond-mat.str-el]*, 2008.

[304] M.R. Crook and R. Cywinski. *Journal of Magnetism and Magnetic Materials*, **140**:71, 1995.

[305] R.B. Laughlin, G.G. Lonzarich, P. Monthoux, and D. Pines. *Adv. Phys.*, **50**:361, 2001.

[306] T.D. Lee and C.N. Yang. *Phys. Rev.*, **117**:897, 1960.

[307] F. Mohling. *Phys. Rev.*, **122**:1062, 1960.

[308] T. Moriya. *Spin fluctuations in itinerant electron magnetism*. Springer-Verlag, 1985.

[309] A.J. Millis. *Phys. Rev. B*, **48**:7183, 1993.

[310] J. Rech, C. Pépin, and A.V. Chubukov. *Phys. Rev. B*, **74**:195126, 2006.

[311] D.L. Maslov, A.V. Chubukov, and R. Saha. *Phys. Rev. B*, **74**:220402(R), 2006.

[312] R.J. Needs, M.D. Towler, N.D. Drummond, and P. López Ríos. *CASINO version 2.3 User Manual*. Cambridge University, 2008.

[313] G. Ortiz, M. Harris, and P. Ballone. *Phys. Rev. Lett.*, **82**:5317, 1999.

[314] F.H. Zong, C. Lin, and D.M. Ceperley. *Phys. Rev. E*, **66**:036703, 2002.

[315] Z. Radnai and R. Needs. Noncollinear spins in Variational Monte Carlo. Unpublished, 2009.

[316] P. López Ríos, A. Ma, N.D. Drummond, M.D. Towler, and R.J. Needs. *Phys. Rev. E*, **74**:066701, 2006.

[317] S. Flügge. *Practical Quantum Mechanics*. Springer, 1994.

[318] J. Carlson, S.Y. Chang, V.R. Pandharipande, and K.E. Schmidt. *Phys. Rev. Lett.*, **91**:050401–1, 2003.

[319] S.Y. Chang, V.R. Pandharipande, J. Carlson, and K.E. Schmidt. *Phys. Rev. A*, **70**:043602, 2004.

[320] C. Pfleiderer and A.D. Huxley. *Phys. Rev. Lett.*, **89**:147005, 2002.

[321] K. Sandeman, G. Lonzarich, and A. Schofield. *Phys. Rev. Lett.*, **90**:167005, 2003.

[322] A.M. Berridge, A.G. Green, S.A. Grigera, and B.D. Simons. *Phys. Rev. Lett.*, 2008.

[323] Kee H.-Y. and Y.B. Kim. *Phys. Rev. B*, **71**:184402, 2005.

[324] E. Fradkin, S.A. Kivelson, and V. Oganesyan. *Science*, **315**:196, 2007.

[325] J.W. Kim, S.Y. Hamm, Y.S. Oh, S. Park, S.-W. Cheong, P.A. Sharma, M. Jaime, N. Harrison, J.H. Han, G.-S. Jeon, P. Coleman, and K.H. Kim. *arXiv:cond-mat/0810.1907v2 [cond-mat.mtrl-sci]*, 2008.

[326] S. Sachdev. *Quantum Phase Transitions*. Cambridge University Press, 2000.

[327] D.E. Khmel'nitskii and V.L. Shneerson. *Sov. Phys. Solid State*, **13**:687, 1971.

[328] A.B. Rechester. *Journal of Experimental and Theoretical Physics*, **33**:423, 1971.

[329] A. Aharony and M.E. Fisher. *Phys. Rev. B*, **8**:3323, 1973.

[330] R. Roussev and A.J. Millis. *Phys. Rev. B*, **67**:014105, 2003.

[331] L. Pálová, P. Chandra, and P. Coleman. *Phys. Rev. B*, **79**:075101, 2009.

[332] D. Rytz, U.T. Höchli, and H. Bilz. *Phys. Rev. B*, **22**:359, 1980.

[333] P. Coleman. *Physica B*, **378-380**:1160, 2006.

[334] C.H. Perry, R. Currat, H. Buhay, R.M. Migoni, W.G. Stirling, and J.D. Axe. *Phys. Rev. B*, **39**:8666, 1989.

[335] C. LaSota, C.Z. Wang, R. Yu, and H. Krakauer. *arXiv:cond-mat/9703240v1 [cond-mat.mtrl-sci]*, 1997.

[336] M. Blume, V.J. Emery, and R.B. Griffiths. *Phys. Rev. A*, **4**:1071, 1971.

[337] J.H. Barrett. *Phys. Rev.*, **86**:118, 195.

[338] T. Schneider, H. Beck, and E. Stoll. *Phys. Rev. B*, **13**:1123, 1976.

[339] D. Schmeltzer. *Phys. Rev. B*, **28**:459, 1983.

[340] S. Sachdev. *Phys. Rev. B*, **55**:142, 1996.

[341] K.A. Müller and H. Burkard. *Phys. Rev. B*, **19**:3593, 1979.

[342] M. Baranov, L. Dobrek, K. Goral, L. Santos, and M. Lewenstein. *Physica Scripta*, **102**:74, 2002.

[343] J.F. Schooley, W.R. Hosler, E. Ambler, J.H. Becker, M.L. Cohen, and C.S. Koonce. *Phys. Rev. Lett.*, **14**:305, 1965.

[344] K.L.I. Kobayashi, Y. Kato, Y. Katayama, and K.F. Komatsubara. *Phys. Rev. Lett.*, **37**:772, 1976.

[345] A.A. Bahgat, E.A. Mahmoud, A.S. Abd Rabo, and I.A. Mahdy. *Physica B*, **382**:271, 2006.

[346] A.N. Rubtsov and T. Janssen. *Phys. Rev. B*, **63**:172101, 2001.

[347] L.J. Spalek, M. Shimuta, S.E. Rowley, T. Katsufuji, O.A. Petrenko, S.S. Saxena, and C. Panagopoulos. Quantum criticality in magnetic and ferroelectric systems. In *Proceedings of SCES'08*, 2008.

[348] L.D. Landau and E.M. Lifshitz. *Quantum Mechanics (non-relativistic theory)*. Butterworths, London, 1981.

[349] M. Chaichian and A. Demichev. *Path Integrals in Physics*. Institute of Physics, 2001.

[350] H. Goldstein, C.P. Poole, and J.L. Safko. *Classical Mechanics (3rd Edition)*. Addison Wesley, 2001.

[351] F.A. Berezin. *The Method of Second Quantization*. Academic Press, 1966.

[352] F. Mandl. *Statistical Physics*. Wiley, 1988.

[353] E. Merzbacher. *Quantum Mechanics*. Wiley, 1997.

[354] S. Gasiorowicz. *Quantum Physics*. Wiley, 2003.

[355] A.O. Silver. Private communication, 2008.

[356] K.F. Riley, M.P. Hobson, and S.J. Bence. *Mathematical Methods for Physics and Engineering*. Cambridge University Press, 2006.

[357] M. Cyrot. *Phys. Rev. Lett.*, **25**:871, 1970.

[358] D.R. Hamann. *Phys. Rev. Lett.*, **23**:95, 1969.

[359] K.K. Murata and S. Doniach. *Phys. Rev. Lett.*, **29**:285, 1972.

[360] A.A. Gomes and P. Lederer. *J. de Phys.*, **38**:231, 1977.

[361] J.A. Hertz and M.A. Klenin. *Physica B*, **91**:49, 1977.

[362] M. Cyrot. *J. de Phys.*, **33**:125, 1972.

[363] P. Lacour-Gayet and M. Cyrot. *J. Phys. C: Solid State Phys.*, **7**:400, 1974.

[364] C.J. Umrigar, K.G. Wilson, and J.W. Wilkins. *Phys. Rev. Lett.*, **60**:1719, 1988.

[365] P.R.C. Kent, R.J. Needs, and G. Rajagopal. *Phys. Rev. B*, **59**:12344, 1999.

[366] N.D. Drummond and R.J. Needs. *Phys. Rev. B*, **72**:085124, 2005.

[367] W.H. Press, S.A. Teukolsky, W.T. Vetterling, and B.P. Flannery. *Numerical Recipies in Fortran 90*. Cambridge University Press, 1996.

[368] C. Lin, F.H. Zong, and D.M. Ceperley. *Phys. Rev. E*, **64**:016702, 2001.

[369] A. Baldereschi. *Phys. Rev. B*, **7**:5212, 1973.

[370] G. Rajagopal, R.J. Needs, A. James, S.D. Kenny, and W.M.C. Foulkes. *Phys. Rev. B*, **51**:10591, 1995.

[371] P.R.C. Kent, R.Q. Hood, A.J. Williamson, R.J. Needs, W.M.C. Foulkes, and G. Rajagopal. *Phys. Rev. B*, **59**:1917, 1999.

[372] H. Flyvbjerg and H.G. Peterson. *J. of Chem. Phys.*, **91**:461, 1989.

[373] F.F. Assaad, P. Werner, P. Corboz, E. Gull, and M. Troyer. *Phys. Rev. B*, **72**:224518, 2005.

[374] R.N. Bracewell. *The Fourier Transform & Its Applications*. McGraw-Hill, 1999.